The Role of Elevator Modes in Double-Diffusive Convection

Thomas James Goodfellow

University of Leeds

School of Computing and School of Mathematics

Submitted in accordance with the requirements for the degree of

Doctor of Philosophy

May, 2020

Intellectual Property Statement

The candidate confirms that the work submitted is his own and that appropriate credit has been given where reference has been made to the work of others.

Acknowledgements

I would first and foremost like to express my deepest love and adoration for my wife, Tanya Goodfellow, who has been unwavering in her encouragement, motivation and support in helping me realise my dreams. I would not be where I am today without her. I'm ready, and excited, to begin the next chapter of our lives—I can't wait for the next big adventure.

Secondly, I would like to express my sincere gratitude to my supervisors: Prof. David Hughes, Dr. Stephen Griffiths, and Prof. Peter Jimack, for their continual support throughout my doctoral studies. Their knowledge and guidance has been invaluable in developing my skills as a researcher and scientist. I would also like to thank Prof. Alastair Rucklidge and Dr. Oliver Kerr for their insightful comments, questions and discussions during the viva, and for their valuable suggestions for improving the thesis.

Thirdly, I include here my closest friends, who have been both a welcome distraction and an emotional crutch throughout my journey. Their humour, commitment and affection continue to enrich my life on a daily basis. They know who they are. Thank you for being you.

My appreciation extends to the wonderful students and staff in the Centre for Doctoral Training in Fluid Dynamics, who have made my time at the University of Leeds unforgettable. I have built lifelong friendships and I wish everyone the best for the future. I would also like to thank the EPSRC for funding my research and making all of this possible.

Finally, I would like to say a very special thank you to Andrea and Graham for taking me in and looking after me as I pursued my goals. I am eternally grateful for their love, patience and understanding. They really are two of a kind.

Abstract

Double-diffusive convection arises in fluids comprising two diffusive elements that compete to influence the density of the fluid, such as heat and salt in the ocean. Instabilities in such systems have previously been shown to lead to the formation of layered structures, known as ‘density staircases’. We are interested in the modal interactions that lead to the formation of such layers. Specifically, we begin by constructing highly truncated models of double-diffusive convection comprising horizontally uniform ‘elevator modes’, which are thought to be critical in the formation of layers. We study the interactions of modes in the truncated modes, and show that we can obtain layered structures in systems having as few as nine modes.

In view of the importance of elevator modes in layer formation, we then proceed to study the stability of the elevator modes themselves. That is, we apply perturbations to an initial state comprising fully developed elevator modes to determine the fastest growing secondary modes. We first study the stability of steady elevator modes, before extending our analysis to elevator modes that are oscillatory in time. We discover that form of the dominant secondary mode in each case is highly dependent on the amplitude of the elevator mode. Furthermore, this dependency is influenced by the parameters governing the background basic state and the fluid itself.

Interestingly, the secondary modes arising from oscillatory elevator modes are similar in structure to those arising from steady elevator modes, except that the former modes are oscillatory in time. The fastest-growing secondary modes in the oscillatory case are found to be similar to those that lead to layer formation in our truncated models. This suggests that the elevator modes may first become unstable to secondary modes, which then interact with the elevator modes to generate layering modes. The layering modes then grow in amplitude to eventually dominate and form a layered state.

This constitutes a relatively simple mechanism describing the initial formation of a layered state from a stably-stratified background density gradient.

We compare our results with those of a purely hydrodynamic system, to show that large amplitude elevator modes appear to become unstable to a hydrodynamic, rather than a diffusive instability. We conclude that, although diffusive effects are vital for the formation of the primary instability, the system may eventually become driven, at least in part, by viscous shear effects, providing the elevator modes grow to a sufficient amplitude.

CONTENTS

1 Introduction 1

1.1 Introduction 2

1.2 Double-Diffusive Convection 6

1.3 Layer Formation 9

1.3.1 Experiments 10

1.3.2 Numerical Simulations 11

1.4 Theories and Mechanisms 13

1.4.1 Thermohaline Intrusions 13

1.4.2 Stability of Salt Fingers 14

1.4.3 Gamma Instability 15

1.4.4 Thermohaline-Shear Instability 16

1.4.5 Stability and Interactions of Elevator Modes 17

2 Formulation of the Problem 19

2.1 Introduction 20

2.2 Governing Equations 20

2.2.1 Continuity equation 20

2.2.2 Momentum equation 21

2.2.3 Thermal Energy Equation 22

2.2.4 Boussinesq Approximation 22

2.3 Mathematical Formulation 24

2.3.1 Boundary Conditions 24
2.3.2 Basic State 26
2.3.3 Perturbation Equations 27
2.3.4 Non-dimensionalisation 27
2.3.5 Streamfunction Formulation 28
2.3.6 Linear stability analysis 29
2.3.7 Salt Finger Instability 33
2.3.8 Oscillatory Instability 34
2.4 Bounded Domain 35

3 Truncated Models **39**
3.1 Introduction 40
3.2 Lorenz System 42
3.3 Fifth-order Model 42
3.4 Higher Order Systems 45
3.4.1 Noguchi and Niino Study 46
3.4.2 Novel Systems 52
3.4.3 Implementation 58
3.5 Verification 59
3.5.1 Da Costa et al. System 59
3.5.2 Ninth-order system 64
3.5.3 Tenth-order system 71
3.5.4 Seventeenth-order system 74
3.6 Evolution of Modes in Truncated Systems 76
3.6.1 Ninth-Order System 76
3.6.2 Tenth-order system 109
3.6.3 Seventeenth-order system 121
3.7 Equilibrium Points 127
3.7.1 Veronis System 127

3.7.2 Stability of Equilibrium Points 128
3.8 Discussion 134

4 Instabilities of Non-Oscillatory Elevator Modes 137
4.1 Introduction 138
4.2 Secondary Instabilities 141
4.2.1 Floquet Theory 142
4.2.2 Application to the Quasi-Steady Equations 143
4.3 Numerical Implementation and Convergence 145
4.3.1 Solver 146
4.3.2 Convergence 147
4.4 Parametric Study 158
4.4.1 Heat-Salt System 160
4.4.2 Fastest growing elevators with $k_x = k_x*$ 171
4.4.3 Effect of the Prandtl Number 179
4.4.4 Salt-Sugar System 181
4.5 Role of Heat and Salt 184
4.5.1 Beaumont Results 185
4.6 Shear-free System 189
4.7 Conclusions 192

5 Instabilities of Oscillatory Elevator Modes 193
5.1 Introduction 194
5.2 Secondary Instabilities 196
5.2.1 Floquet Theory 197
5.3 Numerical Implementation and Convergence 201
5.3.1 Solver 202
5.3.2 Convergence 203
5.3.3 Accuracy 204
5.3.4 Comparison with Holyer 207

5.4 Parametric Study 209
5.4.1 Sweep over A_ψ 209
5.4.2 Sweep over R_ρ^{-1} 214
5.4.3 Sweep over Pr 215
5.4.4 $k_x = k_x^*$ 219
5.5 The Role of Heat and Salt 227
5.5.1 Unsteady Kolmogorov Results 229
5.5.2 High-Pr System 230
5.6 Conclusions 232

6 Conclusions **235**
6.1 Discussion 236
6.2 Development and future work 238

References **240**

List of Figures

1.1 Schematic diagram of a vertical density profile resembling a 'staircase', for example as might be observed in the Ocean in the form of a 'thermohaline staircase'. 3

1.2 Schematic diagram of fluid velocity, **u**, representing an elevator mode in a two-dimensional domain. 5

1.3 A field of salt fingers in an experiment whereby salt solution is poured on top of a fluid having a stable temperature gradient. Taken from Huppert and Turner (1981). 7

1.4 Formation and decay of layers in a salt-sugar system susceptible to fingering convection. Taken from Stern and Turner (1969). 11

1.5 Two-dimensional direct numerical simulation of fingering convection with periodic horizontal and vertical boundaries, showing the formation and evolution of layers. Instantaneous temperature (T) fields are shown for (a) $t = 50$, (b) $t = 400$ and (c) $t = 800$. Each unit of time, t is scaled to represent thermal diffusion time on a finger width. Red corresponds to high values of T, and blue corresponds to low values ot T. Taken from Radko (2003) 12

1.6 Two-dimensional direct numerical simulation of diffusive convection with periodic horizontal and vertical boundaries, showing the formation and evolution of layers. Taken from Prikasky (2007). 13

LIST OF FIGURES

2.1 A schematic of the behaviour of a blob of fluid in a double-diffusive system in which the slower-diffusing component (salt) has a stabilising effect (i.e. $\mathrm{sgn}(T_Z) = \mathrm{sgn}(S_Z) = 1$). 29

2.2 A schematic of the behaviour of a blob of fluid in a system susceptible to salt fingering, in which the slower-diffusing component (salt) has a destabilising effect (i.e. $\mathrm{sgn}(T_z) = \mathrm{sgn}(S_z) = 1$). 30

2.3 Contours showing the growth rate of perturbations as a function of R_ρ^{-1} and k_x for $\mathrm{sgn}(T_z) = \mathrm{sgn}(S_z) = 1$, i.e. in the salt-fingering regime, when $Pr = 7$ and $\tau = 0.01$. 33

2.4 Growth rate of perturbations as a function of R_ρ^{-1} and k_x for $\mathrm{sgn}(T_z) = \mathrm{sgn}(S_z) = -1$; i.e. in the oscillatory regime. 34

2.5 A schematic diagram of a diffusively stratified fluid vertically bounded by upper and lower rigid horizontal boundaries separated by a distance d. The upper and lower boundaries are maintained at a constant temperature and salinity. The temperature T and salinity S in the fluid domain are each linearly stratified with gradient $T_z = \frac{\Delta T}{d}$ and $S_z = \frac{\Delta S}{d}$. 35

2.6 Schematic diagram of instability in a bounded system as a function of R_T and R_S, optimised over k_x. 37

2.7 Schematic diagram of the regions of instability in an unbounded system as a function of αT_Z and βS_Z, optimised over k_x, wherein the stability characteristics are unchanging along lines of constant αT_Z / βS_Z. 38

3.1 Wavenumber lattice, showing the potential higher-harmonics. 44

3.2 Snapshots of net density distribution at four different times in the DNS simulation of Noguchi and Niino (2010a), showing the formation of discrete layers. Corresponds to Figure 9 in Noguchi and Niino (2010a) . . . 48

3.3 Schematic diagrams showing contours of streamfunction, psi for LEFT: a $(1, 0)$ elevator mode; MIDDLE: a $(1, 1)$ cellular mode; and RIGHT: a $(0, 1)$ layering mode (a $(0, 2)$ layering mode looks the same as a $(0, 1)$ layering mode but with half the vertical wavenumber). 49

3.4 Time evolution of the amplitude of the temperature perturbation in the system studied by Noguchi and Niino (2010a) 51

3.5 Variation of modes in the system of Da Costa et al. (1981) corresponding to Figure 2 thereof, wherein $\gamma = 4$, $r_T = 0.5$ and $r_S = 2.0$. 61

3.6 Comparison of LHS and RHS of the energy equation (3.9), over time for the Da Costa et al. (1981) system with $r_S = 0.5$ and $r_T = 2.0$. 62

3.7 Relative error on a logarithmic scale between the LHS and RHS of the energy equation (3.9) for the Da Costa et al. (1981) system with $r_s = 0.5$ and $r_T = 2.0$. 62

3.8 Locations of error peaks on a plot of the LHS of equation (3.9) vs. time for the system of Da Costa et al. (1981) with $r_s = 0.5$ and $r_T = 2.0$. Black circles represent the locations of error spikes. 63

3.9 Evolution of the streamfunction perturbation in the 9th-order system when $\gamma = 0.9$ ($R_\rho^{-1} = 1.11$), $Pr = 7$, $\tau = 0.01$ and $(k, m) = (0.19, 0.09)$. We use tolerances of RelTol $= 10^{-6}$, AbsTol $= 10^{-9}$. 64

3.10 Relative error between the LHS and RHS of the energy balance equation (3.10) in the 9th-order system when $\gamma = 0.9$, $Pr = 7$, $\tau = 0.01$, $(k, m) = (0.19, 0.09)$, RelTol $= 10^{-6}$, and AbsTol $= 10^{-9}$. 66

3.11 Change in time step δt over time t in the simulation used to produce Figure 3.9, when $\gamma = 0.9$, $Pr = 7$, $\tau = 0.01$ and $(k, m) = (0.19, 0.09)$. Results were obtained using RelTol $= 10^{-6}$ and AbsTol $= 10^{-9}$. 67

3.12 Relative error between the LHS and RHS of equation 3.10 in the 9th-order system with $\gamma = 0.9$, $Pr = 7$, $\tau = 0.01$, and $(k, m) = (0.19, 0.09)$. The results were obtained using fixed $\delta t = 0.01$ as the order of the Runge-Kutta scheme was increased from 2 to 4. 68

3.13 Relative error over time t in simulations of the 9th-order system, when $\gamma = 0.9$, $Pr = 7$, $\tau = 0.01$, and $(k, m) = (0.19, 0.09)$. The results were obtained using a 4th-order Runge-Kutta scheme. δt is reduced from $\delta t = 0.1$ to $\delta t = 0.0001$. 69

3.14 Maximum and average error against δt in the 9th-order system, with $\gamma = 0.9$, $Pr = 7$, $\tau = 0.01$, and $(k, m) = (0.19, 0.09)$. The results were obtained using a 4th-order Runge-Kutta scheme. 71

3.15 Temperature evolution in the 10th-order system with $\gamma = 0.9$, $Pr = 7$, $\tau = 0.01$, and $(k, m) = (0.19, 0.09)$. The results on the left and right sides were obtained using different tolerances. 72

3.16 Relative error in the 10th-order simulation with $\gamma = 0.9$, $Pr = 7$, $\tau = 0.01$, and $(k, m) = (0.19, 0.09)$. The results on the left and right sides were obtained using different tolerances. 73

3.17 Change in time-step in the 10th-order system with $\gamma = 0.9$, with $\gamma = 0.9$, $Pr = 7$, $\tau = 0.01$, and $(k, m) = (0.19, 0.09)$. The results were obtained with RelTol $= 10^{-9}$ and AbsTol $= 10^{-12}$ over the period a) $t = 0$ to $t = 1000$, and b) $t = 600$ to $t = 800$. 73

3.18 Evolution of the streamfunction modes, ψ', in the 17th-order system when $\gamma = 0.9$, $Pr = 7$, $\tau = 0.01$, and $(k, m) = (0.19, 0.09)$. The results were obtained using a fourth-order Runge Kutta scheme having a constant time-step of $\delta t = 10^{-3}$. 74

3.19 Maximum and average error in the 17th-order system, simulated using $\gamma = 0$, $Pr = 7$, $\tau = 0.01$, and $(k, m) = (0.19, 0.09)$. over two different ranges of time t. 75

3.20 Growth rates of perturbations to a static basic state in wavenumber (k, m) space when $\gamma = 0.9$ ($R_\rho^{-1} = 1.11$), $Pr = 7$ and $\tau = 0.01$. The uncontoured white region represents stable wavenumbers (i.e. those with negative growth rates). 78

3.21 Modal decomposition of ψ', T', S' and ρ' perturbations in the 9th-order system, when $\gamma = 0.9$ ($R_\rho^{-1} = 1.11$), $Pr = 7$, $\tau = 0.01$, and $(k, m) = (0.257, 0.129)$. 79

3.22 Unscaled modal decomposition of ψ', T', S' and ρ' perturbations in the 9th-order system between $t = 0$ and $t = 1000$ when $\gamma = 0.9$ ($R_\rho^{-1} = 1.11$), $Pr = 7$, $\tau = 0.01$, and $(k, m) = (0.257, 0.129)$. 80

3.23 Amplitudes of terms in equations (3.6) for the growth rates of the a_3 (layering) and b_2 (cellular) modes in the 9th-order system during the 'accelerated growth' phase. Here, $\gamma = 0.9$ ($R_\rho^{-1} = 1.11$), $Pr = 7$, $\tau = 0.01$, and $(k, m) = (0.257, 0.129)$. 83

3.24 Top: Amplitudes of the $(1, 0)$ elevator modes in ψ,T and S; Bottom: Amplitudes of the $(1, 1)$ cellular modes in ψ,T and S. The results are shown around the 'first peak', taking $\gamma = 0.9$ ($R_\rho^{-1} = 1.11$), $Pr = 7$, $\tau = 0.01$, and $(k, m) = (0.257, 0.129)$. 86

3.25 Amplitudes of terms in the equation for the growth rate of the b_3 (layering) mode in the 9th-order system (3.6) around the 'first peak'. Here, $\gamma = 0.9$ ($R_\rho^{-1} = 1.11$), $Pr = 7$, $\tau = 0.01$, and $(k, m) = (0.257, 0.129)$ . . . 87

3.26 Amplitudes of terms in the equations for the growth rates of the a_2 and b_2 (cellular) modes in the 9th-order system (3.6) during the 'second growth' phase. Here, $\gamma = 0.9$ ($R_\rho^{-1} = 1.11$), $Pr = 7$, $\tau = 0.01$, and $(k, m) = (0.257, 0.129)$. 88

3.27 Amplitudes of terms in the equations for the growth rates of the a_1 and b_1 (elevator) modes in the 9th-order system (3.6). Here, $\gamma = 0.9$ ($R_\rho^{-1} = 1.11$), $Pr = 7$, $\tau = 0.01$, and $(k, m) = (0.257, 0.129)$. 90

3.28 Contours of T at successive time intervals within one oscillation period, from Figure 6 of Howard and Krishnamurti (1986). 94

3.29 Contours of T at successive time intervals within one oscillation period during the 'layering' phase, starting from $t = 278$. The abscissa shows a horizontal extent (x) of π/k, while the ordinate shows a vertical extend of πm, to match the plots shown in Figure 6 of Howard and Krishnamurti (1986). Here, $\gamma = 0.9$ ($R_\rho^{-1} = 1.11$), $Pr = 7$, $\tau = 0.01$, and $(k, m) = (0.257, 0.129)$. 95

3.30 Contour plots of the streamfunction perturbation, ψ', at different times in the 9th-order system, using $\gamma = 0.9$ ($R_\rho^{-1} = 1.11$), $Pr = 7$, $\tau = 0.01$, and $(k, m) = (0.257, 0.129)$. The box is two horizontal and vertical wavelengths in size. 96

3.31 Contour plots of the temperature perturbation, T', at different times in the 9th-order system, using $\gamma = 0.9$ ($R_\rho^{-1} = 1.11$), $Pr = 7$, $\tau = 0.01$, and $(k, m) = (0.257, 0.129)$. The box is two horizontal and vertical wavelengths in size. 97

3.32 Contour plots of the salinity perturbation, S', at different times in the 9th-order system, using $\gamma = 0.9$ ($R_\rho^{-1} = 1.11$), $Pr = 7$, $\tau = 0.01$, and $(k, m) = (0.257, 0.129)$. The box is two horizontal and vertical wavelengths in size. 98

3.33 Contour plots of the total density, ρ_T, at different times in the 9th-order system, using $\gamma = 0.9$ ($R_\rho^{-1} = 1.11$), $Pr = 7$, $\tau = 0.01$, and $(k, m) = (0.257, 0.129)$. The box is two horizontal and vertical wavelengths in size. The total density is given by adding the density perturbation ρ' to the linear background gradient. 99

3.34 The horizontally-averaged total density, ρ_T, plotted on the abscissa as a function of height in the domain. This figure shows the evolution of a density ‘staircase’. 100

3.35 Evolution of modes in the streamfunction perturbation for different wavenumbers when $\gamma = 0.9$ ($R_\rho^{-1} = 1.11$), $Pr = 7$ and $\tau = 0.01$. LEFT: $(k, m) = (0.257, 0.05)$. RIGHT: $(k, m) = (0.257, 0.02)$. 102

3.36 Evolution of modes in the streamfunction perturbation when $\gamma = 0.9$ ($R_\rho^{-1} = 1.11$), $Pr = 7$, $\tau = 0.01$ and $(k, m) = (0.2, 0.205)$. 103

3.37 Evolution of modes in the 9th-order system when $\gamma = 0.88$ ($R_\rho^{-1} = 1.11$), $Pr = 7$, $\tau = 0.01$, and $(k, m) = (0.187, 0.09)$. 104

3.38 Evolution of modes in the 9th-order system when $\gamma = 0.99$, ($R_\rho^{-1} = 1.01$), $Pr = 7$, $\tau = 0.01$, and $(k, m) = (0.232, 0.116)$ 105

3.39 Evolution of modes in the 10th-order system with Simulated using $\gamma = 0.9$, $Pr = 7$, $\tau = 0.01$, $(k, m) = (0.187, 0.09)$, RelTol $= 10^{-6}$ and AbsTol $= 10^{-9}$. 110

3.40 Schematic diagrams showing interactions of misaligned (left) and aligned (right) elevator and cellular modes in the streamfunction perturbation ψ'. The arrows show the direction of fluid flow along streamlines of constant ψ'. The aligned modes correspond to those in the 9th-order system, while the misaligned modes correspond to those in the 10th-order system. 112

3.41 Evolution of modes in the tenth-order system with $\gamma = 0.9$, $Pr = 7$, $\tau = 0.01$, $(k, m) = (0.187, 0.09)$, RelTol $= 10^{-6}$ and AbsTol $= 10^{-9}$. . . 115

3.42 Evolution of modes in the streamfunction ψ' perturbation in the 10th-order system between $t = 435$ and $t = 470$, showing highly oscillatory cellular modes. Simulated using $\gamma = 0.9$, $Pr = 7$, $\tau = 0.01$, $(k, m) = (0.187, 0.09)$, RelTol $= 10^{-6}$ and AbsTol $= 10^{-9}$. 116

3.43 Evolution of modes in the temperature T' perturbation in the 10th-order system between $t = 424$ and $t = 450$, showing highly oscillatory cellular and layering modes. Simulated using $\gamma = 0.9$, $Pr = 7$, $\tau = 0.01$, $(k, m) = (0.187, 0.09)$, RelTol $= 10^{-6}$ and AbsTol $= 10^{-9}$. 117

3.44 Evolution of modes in the streamfunction ψ' perturbation in the 10th-order system, highlighting points where the elevator (top) and cellular modes (bottom) pass through zero. Simulated using $\gamma = 0.9$, RelTol $= 10^{-6}$, AbsTol $= 10^{-9}$. 118

3.45 **Top:** Number of zero-crossings (‘nPoints’) of the cellular mode between a pair of zero-crossings of an elevator mode in the 10th-order system as a function of time, t. **Bottom:** Maxmimum value of the ψ' elevator mode in the 10th-order system over time. Results shown between $t = 0$ and $t = 700$, and simulated using $\gamma = 0.9$, RelTol $= 10^{-6}$, AbsTol $= 10^{-9}$. . 119

3.46 Evolution of modes in the ψ', T', S' and ρ' perturbations in the 17th-order system when $\gamma = 0.9$. 122

3.47 Evolution of modes between $t = 0$ and $t = 2000$ in the 17th-order system which has been reduced to a 9th-order system by appropriate initialisation of modes, when $\gamma = 0.9$. An ‘aligned’ elevator mode in ψ' has been initialised as a small-amplitude perturbation. 124

3.48 Evolution of modes between $t = 2000$ and $t = 4000$ in the 17th-order system which has been reduced to a 9th-order system by appropriate initialisation of modes, when $\gamma = 0.9$. An ‘aligned’ elevator mode in ψ' was initialised as a small-amplitude perturbation, and has generated other modes which have grown to eventually constitute the 17th-order system. 125

3.49 rates of Veronis equilibrium points as a function of k and m in LEFT: the 5th-order system and RIGHT: the 9th-order system. The top and bottom rows show the results at first and second ‘sets’ of equilibrium points. The results were obtained using $R_\rho^{-1} = 1.11$, $Pr = 7$, and $\tau = 0.01$, which correspond to the values used in our simulations of the 9th-order system. 131

3.50 Growth rates of Veronis equilibrium points as a function of R_ρ^{-1} and Pr in LEFT: the 5th-order system and RIGHT: the 9th-order system. The top and bottom rows show the results at $(k, m = 0.2, 0.4)$ and $(k, m) = (0.2, 0.1)$, respectively. 132

3.51 Growth rates of Veronis equilibrium points as a function of R_ρ^{-1} and Pr in the 9th-order system. Values of $m = 0.001$, $Pr = 7$ and $\tau = 0.01$ were employed in this case. 133

4.1 Growth rate of secondary modes along (a) the $k_z = 0$ axis, and (b) the $f = 0$ axis with $Pr = 10$, $\tau = 0.01$, $R_\rho^{-1} = 0.02$ and $A_\psi = 4$. The value of N has little effect on the calculated growth rates when $k_z = 0$; however, N does impact the growth rates calculated when $f = 0$. 148

4.2 Results from Holyer (1984) showing the growth rate of secondary modes along (a) the $k_z = 0$ axis, and (b) the $f = 0$ axis with $Pr = 10$, $\tau = 0.01$, $R_\rho^{-1} = 0.02$ and $A_\psi = 4$. The dashed lines are approximate solutions described in the paper. Note the transformation of coordinates from (f, k_z) in our notation to (k, m) in Holyer's notation. 148

4.3 Comparison of the growth rate of the linear solution (computed using equations (4.11)–(4.13) with $k_z = 0$) with the contributions from solutions of (4.15) at $n = -1$, $n = 0$, and $n = 1$. 150

4.4 Heat flux vs. R_ρ for various values of C obtained from our simulations. . 152

4.5 Heat flux vs. R_ρ for various values of C from Radko and Smith (2012), Figure 5. 152

4.6 (a) Growth rate, λ, and (b) Absolute error, E, for $N = 3$, when $R_\rho^{-1} = 0.02$, $\tau = 0.01$ and $Pr = 10$. 154

4.7 (a) Growth rate, λ, and (b) Absolute error, E, for $N = 6$, when $R_\rho^{-1} = 0.02$, $\tau = 0.01$ and $Pr = 10$. 154

4.8 (a) Growth rate, λ and (b) Absolute error, E, for $N = 9$, when $R_\rho^{-1} = 0.02$, $\tau = 0.01$ and $Pr = 10$. 154

4.9 (a) Variation of the growth rate λ with level of truncation N, and (b) the associated error E as a function of N, for the fastest growing secondary mode $(f, k_z) = (0, 0.32)$. Here, $(R_\rho^{-1}, A_\psi, Pr, \tau) = (0.02, 4, 10, 0.01)$ . . . 156

4.10 (a) Variation of the growth rate λ with level of truncation N, and (b) the associated error E as a function of N, for the mode $(f, k_z) = (0.1, 0.45)$. Here, $(R_\rho^{-1}, A_\psi, Pr, \tau) = (0.02, 4, 10, 0.01)$ 156

4.11 Spectral decompositions of eigenfunctions with the largest growth rate in: (a) the fastest growing mode, $(f, k_z) = (0, 0.33)$; and (b) the mode $(0.1, 0.45)$. The y-axis is scaled as $\log_{10} |\psi_n|$. 158

4.12 Growth rate of the primary elevator mode λ_0 as a function of the background density gradient ratio R_ρ^{-1} and the basic-state wavenumber k_x for the heat-salt system ($Pr = 10$, $\tau = 0.01$). The black lines are contours of $\lambda_0 = [0, 10^{-3}, 10^{-2}, 10^{-1}]$. 161

4.13 Real and imaginary part of the growth rates of secondary instabilities λ in the heat-salt system with $R_\rho^{-1} = 0.02$, $Pr = 10$, $\tau = 0.01$ and $A_\psi = [10^{-2}, 10^{-1}, 1, 10]$. 162

4.14 Wavenumbers f and k_z of the fastest growing secondary mode vs. A_ψ for the heat-salt system with $R_\rho^{-1} = 0.02$. 164

4.15 Perturbations and total values of streamfunction and density for the fastest growing mode $(f, k_z) = (0.5, 0.486)$ in the heat-salt system with $R_\rho^{-1} = 0.02$ and $A_\psi = 0.17$. This corresponds to an R1 mode of Figure 4.14. The amplitudes are normalised w.r.t. A_ψ. 165

4.16 Perturbations and total values of streamfunction and density for the fastest growing mode $(f, k_z) = (0, 0.4)$ in the heat-salt system with $R_\rho^{-1} = 0.02$ and $A_\psi = 10$. This corresponds to an R2 mode of Figure 4.14. The amplitudes are are normalised w.r.t. A_ψ. 165

4.17 Growth rate λ of the fastest growing secondary modes as a function of A_ψ for the heat-salt system with $R_\rho^{-1} = 0.02$. Regimes 1 and 2 correspond to those shown in Figure 4.14. 166

4.18 Value of N required to achieve convergence at each point in (f, k_z)-space for two different values of A_ψ. 167

4.19 Relative growth rate and wavenumber of the fastest-growing secondary mode for $R_\rho^{-1} = 0.17$, $Pr = 10$ and $\tau = 0.01$. 169

4.20 Relative growth rate and wavenumber of the fastest-growing secondary mode for $R_\rho^{-1} = 0.5$, $Pr = 10$ and $\tau = 0.01$. 169

4.21 Relative growth rate and wavenumber of the fastest growing mode for $R_\rho^{-1} = 0.9$, $Pr = 10$ and $\tau = 0.01$. 169

4.22 Critical values of A_ψ as a function of R_ρ^{-1} for the heat-salt system, which has $Pr = 10$ and $\tau = 0.01$. 171

4.23 Relative growth rate and wavenumber of the FGSM for $R_\rho^{-1} = 0.02$, $Pr = 10$ and $\tau = 0.01$. 172

4.24 Perturbations and total values of streamfunction and density for the fastest growing mode $(f, k_z) = (0.5, 0.47)$ in the heat-salt system with $R_\rho^{-1} = 0.02$, $A_\psi = 0.035$ and $k_x = k_x^*$. This corresponds to a point in R1 in Figure 4.23. 174

4.25 Perturbations and total values of streamfunction and density for the fastest growing mode $(f, k_z) = (0.0, 0.511)$ in the heat-salt system with $R_\rho^{-1} = 0.02$, $A_\psi = 0.08$ and $k_x = k_x^*$. This corresponds to a point in R1 in Figure 4.23. 174

4.26 Relative growth rate and wavenumber of the FGSM for $R_\rho^{-1} = 0.2$, $Pr = 10$ and $\tau = 0.01$. 176

4.27 Relative growth rate and wavenumber of the FGSM for $R_\rho^{-1} = 0.5$, $Pr = 10$ and $\tau = 0.01$. 176

4.28 Relative growth rate and wavenumber of the fastest growing mode for $R_\rho^{-1} = 0.991$, $Pr = 10$ and $\tau = 0.01$. 176

4.29 Relative growth rate and wavenumber of the fastest growing mode for $R_\rho^{-1} = 0.991$, $Pr = 10$ and $\tau = 0.01$, presented at low A_ψ to capture the collective instability 178

4.30 Relative growth rate and wavenumber of the fastest growing mode for $R_\rho^{-1} = 0.991$, $Pr = 10$ and $\tau = 0.01$, presented at low A_ψ to capture the collective instability 178

4.31 Critical values of A_ψ as a function of R_ρ^{-1} for $Pr = [0.1, 10, 100]$ and $\tau = 0.01$. 180

4.32 Growth rate of the primary elevator mode λ_0 as a function of the background density gradient ratio R_ρ^{-1} and the basic-state wavenumber k_x for the salt-sugar system ($Pr = 1000$, $\tau = 1/3$). The black lines are contours of $\lambda_0 = [0, 10^{-3}, 10^{-2}, 10^{-1}]$. 182
4.33 Real and imaginary parts of the growth rate of secondary modes in the salt-sugar system when $R_\rho^{-1} = 0.91$, $Pr = 1000$, $\tau = 0.01$ and $A_\psi = 100$. 182
4.34 Wavenumber of the FGSM vs. A_ψ in the salt-sugar system, when $R_\rho^{-1} = 0.91$ 183
4.35 Growth rate of secondary instabilities in steady Kolmogorov flow with $Re = 10$. 186
4.36 Growth rate of secondary instabilities in steady Kolmogorov flow with $Re = 20$. 186
4.37 Growth rate of secondary modes in the Kolmogorov system when $Pr = 10$ and, **Top:** $A_\psi = 10$; **Middle:** $A_\psi = 12$; and **Bottom:** $A_\psi = 15$. . . . 188
4.38 Real and imaginary part of the growth rates of secondary instabilities λ in the shear-free heat-salt system with $R_\rho^{-1} = 0.02$, $Pr = 10$, $\tau = 0.01$ and $A_\psi = [10^{-2}, 10^{-1}, 1, 10]$. 191

5.1 Growth rate of elevator modes, highlighting the values chosen in our test-case. 203
5.2 Growth rate of secondary modes in the test case, where $R_\rho^{-1} = 1.11$, $Pr = 10$, $\tau = 0.01$ and $A_\psi = 10$. 204
5.3 Spectrum of $\psi_{n,m}$ with $(f, k_z) = (0, 0.225)$ when N = M = 3. 206
5.4 Spectrum of $\psi_{n,m}$ with $(f, k_z) = (0, 0.225)$ when $N = M = 7$. 206
5.5 Sparsity of the matrix A in the salt-finger regime using **Left:** the steady system, and **Right:** the unsteady system. 208
5.6 Reproducing the results of Holyer (1984) using **Left:** the steady system, and **Right:** the unsteady system. 208
5.7 Growth rate of modes in wavenumber space for increasing A_ψ, when $R_\rho^{-1} = 1.106$ 210

5.8 Wavenumber of the fastest growing mode when $R_\rho^{-1} = 1.06$ between $A_\psi = 1$ and $A_\psi = 6$. 212

5.9 Contours of ψ and ρ of the fastest-growing secondary mode having $(f, k_z = 0.225)$ when $R_\rho^{-1} = 1.06$ and $A_\psi = 10$ in the heat-salt system. 213

5.10 Contours of ψ and ρ of the fastest-growing secondary mode having $(f, k_z = 0.225)$ when $R_\rho^{-1} = 1.06$ and $A_\psi = 10$ in the heat-salt system. 213

5.11 Wavenumber of the fastest growing mode with increasing A_ψ for $R_\rho^{-1} = [1.06, 1.07, 1.08]$ in the heat-salt system. 215

5.12 Wavenumber of the fastest growing mode with increasing A_ψ for $R_\rho^{-1} = [1.09, 1.10, 1.11]$ in the heat-salt system. 216

5.13 Wavenumber of the fastest growing mode with increasing A_ψ for $R_\rho^{-1} = [2.5, 4.5, 6.5, 8.5]$, when $Pr = 0.1$. 217

5.14 Caption 218

5.15 Wavenumber of the fastest growing mode with increasing A_ψ for $R_\rho^{-1} = [1.002, 1.004, 1.006, 1.008]$, when $Pr = 10$. 220

5.16 **Left:** Relative growth rates, and **Right:** frequencies of secondary modes arising from the fastest-growing elevator mode in the heat-salt system when $R_\rho^{-1} = 1.01$, and $A_\psi = \{1, 11, 21, 31, 41\}$. 223

5.17 Growth rates and wavenumbers of fastest growing modes secondary modes arising from fastest-growing, oscillatory elevator modes with $R_\rho^{-1} = 1.01$ – 1.05, $Pr = 10$ and $\tau = 0.01$. 226

5.18 Growth rate of secondary modes in unsteady Kolmogorov flow, taking $k_x = 0.515$ and $\omega = 0.$. These correspond to a value of $R_\rho^{-1} = 1.06$ in the heat-salt system. 229

5.19 Imaginary part of the growth rate λ_I in unsteady Kolmogorov flow, taking $k_x = 0.515$ and $\omega = 0.$. These correspond to a value of $R_\rho^{-1} = 1.06$ in the heat-salt system. 230

Abbreviations

DDC	Double-Diffusive Convection
FGM	Fastest Growing Mode
MHD	Magnetohydrodynamics
ODDC	Oscillatory Double-Diffusive Convection
FGSM	Fastest Growing Secondary Mode
DNS	Direct Numerical Simulation

CHAPTER 1

Introduction

1.1 Introduction

Fluid dynamical systems with the tendency to form patterns have been the subject of much scientific interest over the years (Hoyle, 2006). One of the most interesting patterns is that of layers or 'staircases', which appear to form from a disordered turbulent state. The term 'staircase' is the given to stepped vertical density profiles, such as that shown in Figure 1.1. Thermohaline staircases, for instance, are found in the oceans as mixed, almost neutrally stratified layers of salinity and temperature with steep gradient interfaces. These homogeneous layers can be tens to hundreds of metres high and persist for several years or more (Johannessen and Lee, 1974, Molcard and Tait, 1977).

Double-diffusive convection (DDC) is thought to play a prominent role in the formation of such layers. In classical convection the behaviour of a system depends on one component—heat—whereas double-diffusive systems rely on two competing elements, such as heat and a compositional gradient. In an oceanic context, the two competing elements are heat and salt, and such systems may be referred to as 'thermohaline' systems (Radko, 2013). In contrast to purely thermal convection, instabilities can arise in double-diffusive systems even with a stable background density stratification. The mechanism behind this instability is explored further in Chapter 2.

Outside the oceanic context, well-defined layers have been observed in igneous rocks, which motivated early studies of double-diffusive convection in magma chambers (Turner, 1980). In stellar cores, an unstable chemical composition and destabilizing thermal gradient can lead to diffusive convection, known in this case as semiconvection. Semiconvection is thought to play a fundamental role in the evolution of giant stars and planets. Furthermore, in solar physics, the density of the magnetic gas is influenced by the magnetic field through magnetic pressure (Hughes and Weiss, 1995, Spiegel and Weiss, 1982). Since this quantity diffuses, this system is also double-diffusive and has been the subject of numerical studies which draw parallels with diffusive convection in

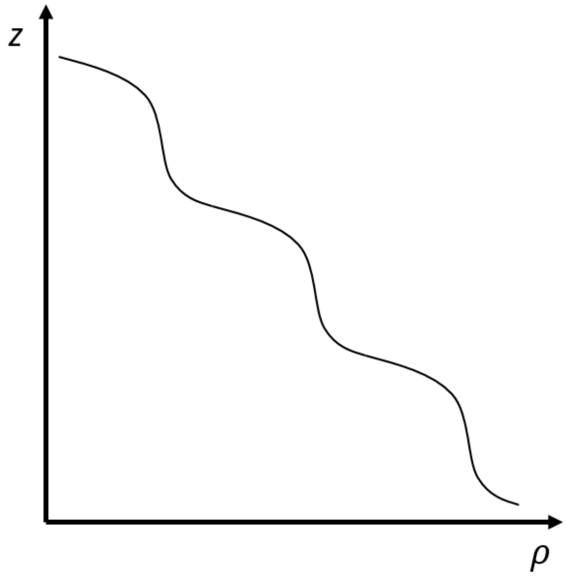

Figure 1.1: Schematic diagram of a vertical density profile resembling a ‘staircase’, for example as might be observed in the Ocean in the form of a ‘thermohaline staircase’.

the Ocean (Knobloch et al., 1981, Rosenblum et al., 2011, Wood et al., 2013).

Another, ostensibly different system is rotating turbulence in which a staircase of potential vorticity is formed, manifested by strong jets. A striking example of potential vorticity layering is on the surface of Jupiter. It is clear that layering can occur in a wide variety of systems; as such it is desirable to study and understand the nature of staircase formation.

Staircase formation has been most widely studied in the thermohaline system, largely due to its origins in oceanography and the abundance of experimental data. Therefore, one of the main focuses of the project is to gain a better understanding of layering in such systems. A summary of work in this area was produced by Merryfield (2000), in which numerous hypotheses concerning the origin of thermohaline staircases were reviewed. These include: the collective instability of salt fingers, in which collections of fingers excite gravity waves; metastable equilibria, in which the layered structures would persist indefinitely if property jumps across layers were maintained; and thermohaline intrusions, giving rise to inclined finger-like intrusions reminiscent of layering. More recent studies (Radko, 2003, Stellmach et al., 2011) have suggested that a so-called γ-instability could be responsible for layer formation. The γ-instability describes the growth of secondary, large-scale γ-modes, which take the form of exponentially growing, horizontally invariant perturbations in density. We provide an overview of the γ-instability mechanism later in this chapter.

The nature of staircase formation is not yet fully understood. In this thesis, we seek to address some of the outstanding questions by building on the work of previous authors. In Chapter 1, we present a summary of the literature surrounding double-diffusive convection, particularly that relating to layer formation. We discuss in more detail some of the theories and mechanisms for layering which are outlined above.

In Chapter 2, we lay the groundwork in terms of the mathematical background pertaining to thermal convection and double-diffusive convection. We develop, from first principles, the equations governing double-diffusive convection, and discuss the stability of the mathematical systems which thereby arise. We then go on to develop the mathematical basis for the models employed throughout the thesis.

In Chapter 3, we build on the methods of previous authors in producing a limited representation of a double-diffusive system (Da Costa et al., 1981, Noguchi and Niino, 2010a, Veronis, 1965). The limited representations are used to generate low-order models of double-diffusive convection. These are then employed in an attempt to identify which basic modes are vital for the formation of layers. In particular, we ask how many such modes are necessary for a system to exhibit layer-like behaviour. Our models appear to support an idea that so-called ‘elevator’ modes play an important, or even critical, role in the formation of layers. Elevator modes appear as adjacent columns of vertically alternating fluid velocity, as shown in the schematic of Figure 1.2.

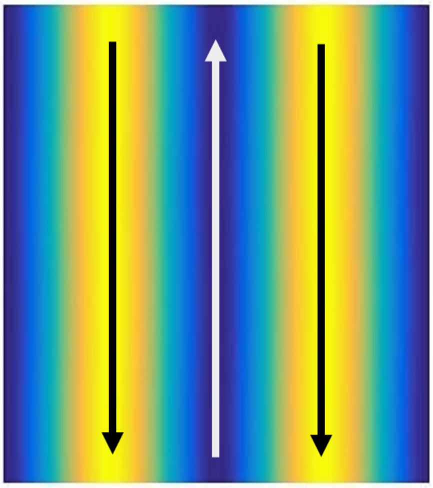

Figure 1.2: Schematic diagram of fluid velocity, $\mathbf{u}$, representing an elevator mode in a two-dimensional domain.

We then depart slightly from our original motivation of studying the formation of layers, *per se*, and instead go deeper into studying the elevator modes themselves. If, as seems likely, the elevator modes are important in layering dynamics, then it is very important to understand their stability properties. This issue has not been fully addressed to date. There appears to be scope to extend, and build upon, certain models employed in the literature.

Therefore, in Chapters 4 and 5 we extend the work of previous authors in determining the form of secondary modes that destabilise a basic state consisting entirely of elevator modes (Holyer, 1984, Radko, 2016). Over the course of the two Chapters, we identify the form of secondary modes arising from two distinct double-diffusive systems. We attempt to address certain unanswered questions, for instance: how do the basic state parameters affect the form of secondary modes that are generated; how do the secondary modes differ between the two distinct systems; and to what extent do the background heat and salt gradients impact the form of the secondary modes, when compared to a purely hydrodynamic system?

We conclude by drawing together and discussing the findings from each Chapter. In this way, we build a picture of how the elevator modes alone may begin to generate, and subsequently interact with, other modes in order to initiate the formation of layers. We also discuss some of the limitations of our models and highlight areas which may be of interest for further study.

1.2 Double-Diffusive Convection

We begin by reviewing the history and background of double-diffusive convection (DDC), particularly exploring the research surrounding layer formation and outlining some of the key theories. This will lead into a discussion of low-order models and linear theory, both of which are of particular relevance to this research project.

In thermohaline convection, such as that observed in the ocean, perturbations to an initially static basic state may grow by virtue of the diffusivity of heat being greater than that of salt (Stern, 1960). Consider a parcel of fluid in a system with a stable salinity gradient (i.e. salinity increases in the direction of gravity) and an unstable temperature gradient (i.e. temperature increases downwards). If the parcel is perturbed upwards, the heat in the parcel rapidly diffuses into the surrounding colder fluid, and the parcel becomes heavier as it cools. The salt content of the parcel, however, is generally retained, as salt diffuses much more slowly than heat. Therefore, the parcel ends up heavier than the surrounding fluid, causing the parcel to sink.

If the destabilising temperature field is strong enough, then the parcel may cool enough to overshoot its original position and continue to travel downwards into warmer and saltier fluid. The parcel will heat up as it descends and may eventually become lighter than its surroundings, due to a lower salt content in the parcel. This will cause the parcel to rise back up to begin the cycle again. This type of regime is known as the ‘diffusive’ regime. The behaviour may be expressed as steady or growing oscillations

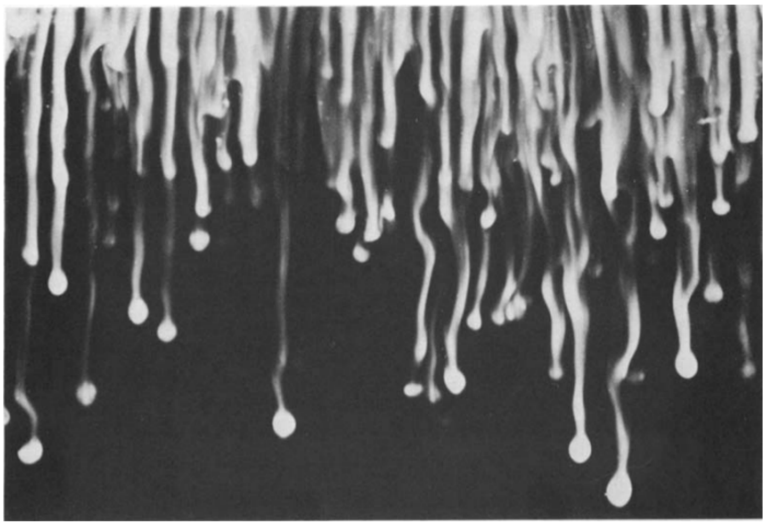

Figure 1.3: A field of salt fingers in an experiment whereby salt solution is poured on top of a fluid having a stable temperature gradient. Taken from Huppert and Turner (1981).

(Radko, 2013), with growing oscillations being the signature of instability.

If the basic stratification is reversed, such that the system is solutally unstable (saltier at the top) and thermally stable (colder at the bottom), then a direct (non-oscillatory) instability may occur. In this case, a parcel perturbed downwards into colder, less salty surroundings will diffuse both its heat and its salt, thereby continually increasing in weight. In this way, the stable thermal gradient is eroded much more quickly than the destabilising solutal gradient, so the system becomes increasingly unstable. This behaviour results in the emergence of long, thin cells, known as salt fingers, and is hence referred to as the ‘fingering’ regime. Figure 1.3 shows an example of salt fingers observed in an experiment by Huppert and Turner (1981). The respective stability regimes are discussed further in Chapter 2.

The polar regions of the Arctic Ocean, for example, are susceptible to diffusive convection and layers have been observed in such locations Schmitt et al. (1987). In such regions, cold, fresh water from melting surface ice overlies warmer, saltier water below.

Salt fingering regimes may be observed, for example, in the Mediterranean, and particularly the Mediterranean outflow. Here, evaporation of water on the surface of the Mediterranean Sea leaves the water relatively warm and salty. This warm, salty water flows over the cooler, fresher water of the Atlantic, leading to conditions conducive to salt fingering (Schmitt, 1994). The diffusive and salt fingering regimes will be discussed in more detail in Chapter 2.

The linear stability of double-diffusive systems has been well-studied. Initially noted as an ‘oceanographic curiosity’ (Stommel et al., 1956), the onset of instability was first studied in Stern (1960) and expanded upon in Walin (1964). Stommel et al. (1956) derived a thought experiment in which a pipe was suspended vertically with one end in warmer salty water (above) and the other in cool, fresh water (below). Pumping fluid upwards in the pipe would result in the cooler water increasing in temperature as it rose, while maintaining its freshness, thereby becoming more buoyant than its surroundings. This would continue in a perpetual ‘Salt Fountain’ if pumping was removed. Stern noted that since the diffusivity of salt is much lower than that of heat, the pipe is not necessary and indeed this should not merely be a curiosity, but an expected occurrence in the ocean.

Stern proceeded to investigate the linear stability of this system in two dimensions, unbounded in the horizontal direction and bounded by rigid horizontal plates in the vertical direction (Stern, 1960). Stern determined the criterion for marginal stability in terms of a ‘thermohaline Rayleigh number’, so named as the criterion was found to be analogous to that of bounded Rayleigh-Bénard convection. In the same paper, Stern then determined stability criteria in a three-dimensional domain, again in the presence of boundaries in the vertical direction. Walin extended the work of Stern to study instabilities in a completely unbounded system, thereby determining a set of criteria that complemented those of Stern (Walin, 1964). The fastest growing mode in each case was found to take the form of vertical columns, though the planforms may take any shape, such as squares, rectangles or sheets.

The above linear theories surrounding marginal stability of double-diffusive systems set the groundwork for future studies of nonlinear behaviour. Veronis (1965, 1968) performed finite amplitude studies of the nonlinear instabilities in double-diffusive systems, focusing on marginally unstable cases in vertically-bounded systems. Later studies extended this work to study larger parameter ranges (Huppert and Moore, 1976). These studies are discussed further, particularly in Chapter 3, when we employ similar methods to study vertically-unbounded systems.

1.3 Layer Formation

Since the discovery and initial theoretical studies of double-diffusive convection in the late '50s and early '60s, it quickly became clear from experiments that, following mixing by salt fingers, a state may emerge consisting of stacked layers of constant density separated by thin interfaces with steep gradients (Stern and Turner, 1969, Turner, 1967). This layered state was found to be characterised by a stepped density gradient, leading to the coining of the term ‘density staircase’. Although the early experiments (and indeed most experiments since) comprised salt and sugar as the diffusive components, similar long-lived ‘staircases’ were observed and generally accepted to exist in the Oceans at around the same time (Cooper and Stommel, 1968, Tait and Howe, 1968). Double-diffusive layering is observed in both the salt fingering and diffusive regimes.

Theoretical arguments, for example in (Radko, 2005), suggest that layers form in a matter of days, but equilibrate over a time-scale of decades. Thus, oceanographic observations, although useful in studying the long-term behaviour of layered systems, are of limited use in studying the *formation* of layers in such systems. For this reason, much research on layer formation typically comprises mathematical, numerical and/or laboratory experiments.

We also note here that, although not the subject of this thesis, following the initial formation of layers, the layers have been observed to merge in so-called 'layer-merging events'. This phenomenon been observed and studied in various physical and numerical experiments (Stellmach et al., 2011, Stern and Turner, 1969). It is typically observed in such studies that the scale of the initial layer formation is relatively small, and adjacent layers merge to form larger-scale layers (Noguchi and Niino, 2010b). It is the larger scale layers, formed over many decades, which are typically observed in the Ocean. In many numerical experiments, the layers continue to merge until a single layer interface is present in the system. In other experiments, we see that layers stop merging once a height of the layers reaches an equilibrium value. Radko et al. (2014b) determined this equilibrium height of layers, and showed that inhomogeneities within the layers are responsible for stabilising the density staircases.

1.3.1 Experiments

Experiments were initially performed using heat and salt as the diffusing components (Turner, 1967). Figure 1.3 above, for example, shows the onset of fingering initiated by setting up a stable temperature gradient and pouring salt solution on the top (Huppert and Turner, 1981). It was later found that certain issues with the heat-salt experiments could be resolved by instead employing salt and sugar as the faster- and slower-diffusing components, respectively (Stern and Turner, 1969). One issue was that heat in the system was readily lost through side-walls. Salt-sugar experiments also revealed more defined salt fingers, and gradients were able to be maintained for longer periods of time (such as weeks). The latter point is important for any study of layering, as the generation of salt fingers occurs on a much shorter time scale than the formation of layers (Radko, 2013).

Early experiments presented in Turner (1968) showed that layers could form in diffusive systems. It was later shown by experiments in Stern and Turner (1969) that

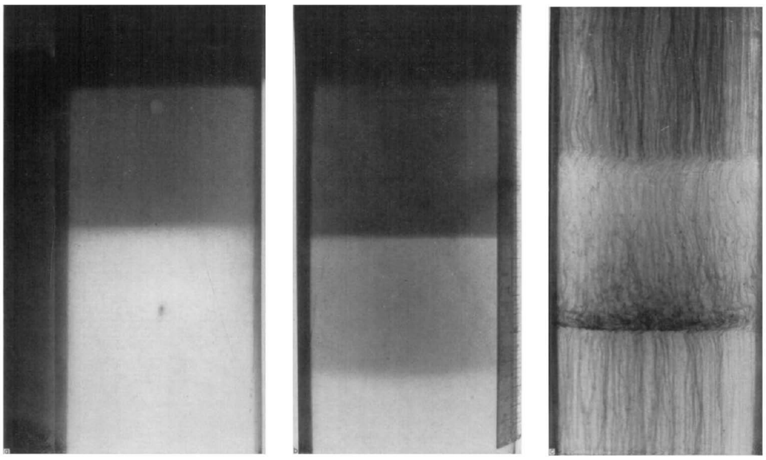

Figure 1.4: Formation and decay of layers in a salt-sugar system susceptible to fingering convection. Taken from Stern and Turner (1969).

layers may also form in diffusive systems. Figure 1.4 highlights a set of results from the latter paper, which show (a) a convective layer formed between a dark layer of sugar mixture (dyed) and a lighter layer of salt mixture; (b) a second layer formed below the first layer, around an hour after (a); and (c) a decay of the convecting layers, three days after beginning the experiment.

1.3.2 Numerical Simulations

Improvements in computing power over the years have led to direct numerical simulations of double-diffusive systems becoming increasingly feasible. Numerical experiments are able to forego some of the limitations and challenges of physical experiments, such as maintaining constant background gradients, and eliminating boundary effects. Numerical experiments have been performed by numerous authors throughout the years. Many of the more recent models have reproduced layering. Figure 1.5, for example shows the formation of layers in a two-dimensional Direct Numerical Simulation (DNS) from a basic state consisting of uniform heat and salt gradients in a domain comprising periodic boundaries in both directions (Radko, 2003). Specifically, the perturbations are periodic on the boundaries, while the basic state comprises a constant linear back-

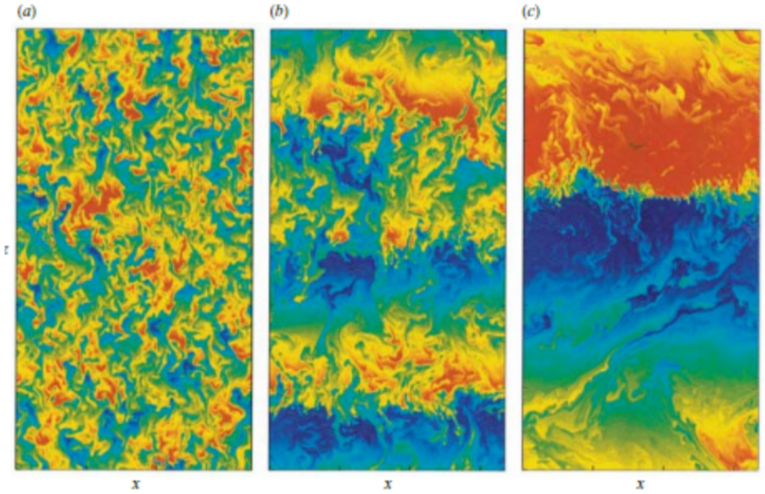

Figure 1.5: Two-dimensional direct numerical simulation of fingering convection with periodic horizontal and vertical boundaries, showing the formation and evolution of layers. Instantaneous temperature (T) fields are shown for (a) $t = 50$, (b) $t = 400$ and (c) $t = 800$. Each unit of time, t is scaled to represent thermal diffusion time on a finger width. Red corresponds to high values of T, and blue corresponds to low values ot T. Taken from Radko (2003)

ground density gradient. It can be seen that the basic state gives way to salt fingers, which mix the fluid. Layers then appear to emerge spontaneously from the chaotic mixing fluid. Figure 1.6 shows similar behaviour obtained from DNS in the diffusive regime (Prikasky, 2007).

Notably, numerical experiments in both two- and three- dimensions appear to show that layers typically form in vertically unbounded domains (Radko et al., 2014a,b). Indeed, in the Ocean, layering tends to occur far from any physical boundaries. This appears to suggest that certain modes are permitted in vertically unbounded domains which would not be permitted otherwise, and that these modes are important in layer formation (Noguchi and Niino, 2010a). Our results support this idea, showing that vertically-independent ‘elevator modes’ play an important role in the formation of layers. We note that in certain models, layers are observed to form in the presence of physical boundaries, though vertically-independent structures, such as salt fingers, are

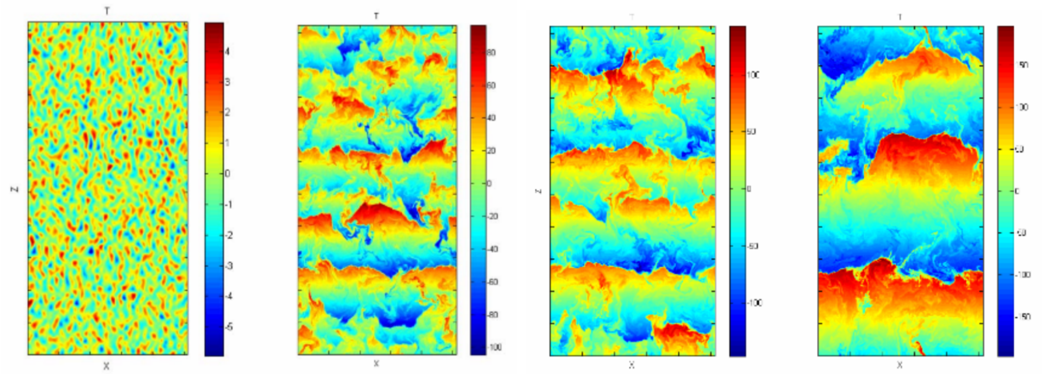

Figure 1.6: Two-dimensional direct numerical simulation of diffusive convection with periodic horizontal and vertical boundaries, showing the formation and evolution of layers. Taken from Prikasky (2007).

generally included in such models(Paparella and Hardenberg, 2014).

1.4 Theories and Mechanisms

An explanation for the mechanism(s) behind layer formation, particularly in a 'diffusive' system, has remained elusive. We here summarise some of the prevailing theories, as identified and discussed in a review of the literature in Merryfield (2000), and further in Radko (2013).

1.4.1 Thermohaline Intrusions

Thermohaline intrusions, initially predicted by Stern (1967), consist of quasi-horizontal structures which spread across lateral temperature and salinity fronts (Radko, 2013). This theory pertains to both the salt-fingering and diffusive regimes. Merryfield (2000) argued using linear theory that conventional intrusions are not the only outcome of lateral gradients, and that a staircase-like structure can be obtained. Indeed, experiments and observations in the ocean have shown the presence of stepped structures in regions of strong lateral gradients. However, whilst this mechanism is likely to be relevant for some oceanic observations, layering is observed in simulations and experiments in which T and S gradients are entirely vertical, and such systems are the focus of this thesis.

1.4.2 Stability of Salt Fingers

A second class of ideas suggests that lateral gradients are not required, and instead that layering is inherent to the dynamics of fingering convection (Stellmach et al., 2011). The stability of salt fingers was first investigated by Stern (1969), who discovered that laminar salt-fingers were unstable to long-wavelength perturbations, which he called the 'collective instability'. He obtained the criterion for instability (Stern, 1975),

$$\frac{\beta F_S - \alpha F_T}{\nu(\alpha T_z - \beta S_z)} > 1, \tag{1.1}$$

where F_S and F_T are the heat and salt fluxes of the fingers, and α and β are coefficients of expansion due to heat and salt, respectively. The collective instability is characterised by an excitation of large-scale internal gravity waves by a fully developed and initially homogeneous field of salt fingers (Radko, 2013). These waves were observed in experiments just before the formation of density staircases, and so were initially thought to be directly linked to the formation of layers (Stern and Turner, 1969). It was later shown that this is perhaps not the case (Stellmach et al., 2011).

Stern (1969) had made assumptions about the coupling of large and small-scale motions, namely that the salt fingers would rotate with the collective instability, and that the heat and salt flux would remain constant. A later study by Holyer (1981) showed that the fluxes actually increase due to the effects of the collective instability, leading to a modified criterion for instability,

$$\frac{\beta F_S - \alpha F_T}{\nu(\alpha T_z - \beta S_z)} > 1/3. \tag{1.2}$$

This was achieved by separating the small-scale finger motions from the long-scale internal wave perturbations. As noted above, it was initially thought that staircase structures could be the result of salt fingers becoming unstable to the collective instability which disrupts the fingers (Merryfield, 2000). This would cause convection to set in, driven by buoyancy fluxes from the remaining salt finger interfaces. Direct evidence for this hypothesis was obtained from qualitative observations in salt sugar experiments by Stern and Turner (1969)

Holyer (1984) later studied the system under perturbations of all wavelengths. This was motivated by the findings of other salt-sugar experiments performed around the same time, which showed a stability parameter about two orders of magnitude less than that predicted by (1.2). The perturbed equations used in the study exhibited periodic coefficients and Floquet theory was used to analyse the system. It was found that small-scale zigzag modes generally grow faster than collective gravity waves, so the collective instability may not be the primary mechanism for layer formation from a homogeneous state. Indeed, the aforementioned experiments by Stern and Turner only exhibited layering when either a sharp interface was present initially, or disturbances were induced during the filling process that triggered convection; carefully set-up experiments showed vertically uniform fingering (Merryfield, 2000). Subsequent numerical experiments aiming to investigate the evolution of gravity waves excited by the collective instability also failed to produce layering (Stellmach et al., 2011).

1.4.3 Gamma Instability

This led Radko (2003) to propose the γ-instability as the mechanism by which a layered state may emerge from an initially homogeneous salt-fingering field. His initial 2D-simulations seemed to support the idea that a large-scale, horizontally invariant secondary mode, termed the γ-mode, grows exponentially and eventually disrupts the salt-fingers, transforming the basic density gradient into a stepped structure consisting of salt finger interfaces sandwiched between the nearly homogeneous layers. Specifically, a linear stability analysis shows that a density gradient defined by uniform T and S gradients is unstable to the γ-instability providing the flux-ratio $\gamma = \overline{wT}/\overline{wS}$ is a decreasing function of the density ratio R_ρ. Here, w is a vertical velocity, the overbar indicates a horizontal average, and R_ρ is a measure of the strength of the background stratification, as will be described in Chapter 2.

The γ-mode is observed in 3D direct numerical simulations, such as those performed by Stellmach et al. (2011) and Radko et al. (2014a). In these simulations, a collective instability is first obesrved to emerge, following a growth of salt fingers. The collective instability does not appear to influence the formation of layers; rather, the γ-mode grows exponentially in the background, and eventually reaches a sufficiently large amplitude to cause localised overturning in regions of large local density gradient. This leads to the formation and self-reinforcement of layers in the system. It should be noted, however, that the γ-instability grows fastest as the vertical wavenumber, $k_z \to \infty$ (Radko, 2003), and so the instability cannot be said to predict the larger vertical wavelengths of layers that are observed in these simulations.

Furthermore, the theory of the γ-instability theory is not limited to fingering convection and may be applied to diffusive convection. We show in Chapter 3 that the layers in diffusive systems may form at relatively small scales, on the order of the wavelength of the primary instability. This is supported by direct numerical simulations of Noguchi and Niino (2010a) and Noguchi and Niino (2010b), and is perhaps contrary to the idea that layers form on the scale of the γ-instability which, in the 3D DNS simulatons described above, is significantly larger (such as 10 to 20 times larger, according to Radko (2013)) than the wavelength of the primary instability. It may be that the γ-instability represents only a part of the story, and that layer formation in certain systems is influenced by—or even predominantly driven by—other mechanisms, as explored in this thesis.

1.4.4 Thermohaline-Shear Instability

Much of the recent work on double-diffusive convection has stemmed from a paper by Radko (2016) who showed, importantly, that a system consisting of both a dynamically stable shear flow and a diffusively stable stratification could become unstable. The results are relevant to ocean dynamics, wherein phenomena associated with instabilities (such as layering) are observed in regions with linearly stable temperature and salt gradients. Radko (2016) showed that a dynamically stable shear flow can cause a statically stable double-diffusive system to become unstable. More recently, Brown and Radko (2019) and Radko (2019) have studied the initiation of diffusive convection by time-dependent shear. The authors show, using linear stability analysis, that conditions for thermohaline-shear instability are met in most ocean regions where temperature and salinity concurrently increase downward, even if that region is double-diffusively stable. A summary of the work done so far in studying the thermohaline-shear instability is provided by Garaud et al. (2019).

1.4.5 Stability and Interactions of Elevator Modes

Although staircase formation remains the general motivation for this research project, we have approached the problem initially by studying the interactions of elevator modes with secondary instabilities. Similar studies have been performed by previous authors, and have been shown to be quite informative with regard to diffusive convection and layering dynamics (Da Costa et al., 1981, Noguchi and Niino, 2010a, Veronis, 1965). In addition, since elevator modes are seemingly vital in the formation of layers, it is of great importance to study and understand their stability properties. This has been the subject of previous study (Holyer, 1984, Radko, 2016, Veronis, 1987), though there is scope to expand on this work. For example, we here build on the work of the previous authors by further exploring the parameter space, and studying the stability of oscillatory elevator modes using so-called ‘floquet theory’, which has not yet been done. Further critical discussions of the literature are reserved for the relevant chapters.

In the chapters that follow, we first derive, in Chapter 2, the governing equations of double-diffusive systems and perform linear stability analyses of the systems. This provides a general introduction to some of the mathematical principles we rely upon throughout the thesis. We then derive specific models in later chapters that are used to study the weakly nonlinear dynamics of double-diffusive systems. The general aim of each of Chapters 3 to 5 is to gain a deeper understanding of the underlying mechanics leading to layering. We conclude each Chapter by comparing our results with prevailing theories and previous studies, in an attempt to place our work in the wider context of diffusive convection. Chapter 6 provides a general overview of our findings and poses further questions which may be of interest for further research.

CHAPTER 2

Formulation of the Problem

2.1 Introduction

The equations governing double-diffusive convection are obtained as an extension to those governing Rayleigh-Bénard convection, the derivation of which was discussed in great detail by Chandrasekhar (1961). For completeness, we derive here the governing equations by way of first-principle expressions for the conservation of mass, momentum and energy. We then define a set of boundary conditions and basic states constituting the systems to be studied in later chapters, and express our equations in terms of perturbations to the basic states. Appropriate scales are introduced to express the equations in dimensionless form, thereby providing a set of parameters which influence the resulting dynamics. In anticipation of the analyses in subsequent chapters, we manipulate the equations into several useful forms.

2.2 Governing Equations

2.2.1 Continuity equation

The mass of fluid contained within an arbitrary fixed volume V is given by the integral of the density $\rho \equiv \rho(\mathbf{x}, t)$,

$$\int_V \rho \, \mathrm{d}V, \tag{2.1}$$

where $\mathrm{d}V = \mathrm{d}x\mathrm{d}y\mathrm{d}z$ is a volume element. The mass of fluid inside the volume can only vary by passing fluid through its boundary. Hence we define the rate of change of mass as the total velocity flux through the surface, i.e.

$$\frac{\mathrm{d}}{\mathrm{d}t} \int_V \rho \, \mathrm{d}V = - \int_S \rho \mathbf{u} \cdot \mathrm{d}\mathbf{S}, \tag{2.2}$$

where $\mathbf{u}$ is the fluid velocity, and $\mathbf{dS} = \hat{\mathbf{n}} \cdot \mathrm{d}S$ is the outward pointing normal associated with a surface element $\mathrm{d}S$. Making use of the divergence theorem, and noting that the fluid volume is fixed, we express the conservation of mass as

$$\int_V \left(\frac{\partial \rho}{\partial t} + \nabla \cdot (\rho \mathbf{u}) \right) \mathrm{d}V = 0, \tag{2.3}$$

which holds for any arbitrary volume V. Hence the integrand equals zero:

$$\frac{\partial \rho}{\partial t} + \nabla \cdot (\rho \mathbf{u}) = 0. \tag{2.4}$$

This is the general expression for conservation of mass, which, on the assumption of incompressibility (i.e. density is materially conserved, meaning $\frac{\partial \rho}{\partial t} + \nabla \rho = 0$), reduces to the continuity equation

$$\nabla \cdot \mathbf{u} = 0. \tag{2.5}$$

2.2.2 Momentum equation

Newton's second law concerns the conservation of momentum in a system, and it holds true in fluids. In this context, the forces acting on a fluid parcel per unit volume are equated to the product of the acceleration of the fluid parcel and its mass per unit volume (density). This is expressed mathematically as

$$\rho \frac{D\mathbf{u}}{Dt} = \rho \left(\frac{\partial \mathbf{u}}{\partial t} + (\mathbf{u} \cdot \nabla)\mathbf{u} \right) = \mathbf{F} + \nabla \cdot \boldsymbol{\sigma}, \tag{2.6}$$

where $\mathbf{F}$ represents external body forcing, and the *stress tensor* $\boldsymbol{\sigma}$ represents internal stresses acting on a fluid parcel. In convective systems, we are typically concerned with gravitational buoyancy forcing only, i.e. $\mathbf{F} = \rho \mathbf{g}$, with $\mathbf{g} = -g\hat{\mathbf{e}}_{\mathbf{z}}$. Examples in which other forces are also of significance include rotating convection, in which the system rotates with angular velocity $\boldsymbol{\Omega}$ and is subject to a *Coriolis* force $\mathbf{F}_C = -2\rho \boldsymbol{\Omega} \times \mathbf{u}$ (Pedlosky, 2013); and Magneto-convection, in which the fluid is electrically conducting, and convective motion generates a Lorenz force which acts on the fluid (Weiss and Proctor, 2014).

The stress tensor arises as a result of pressure and microscopic shear. It is written in tensor notation as

$$\sigma_{i,j} = -P\delta_{i,j} + \tau_{i,j}, \tag{2.7}$$

where $i = 1, 2, 3$, P is the (scalar) pressure acting normal to each face of a fluid element, and the *viscous stress tensor* $\tau_{i,j}$ is the i^{th} component of shear stress on a face with unit normal in the j direction. Shear stress is a direct result of energy transfer across a velocity gradient, so a stationary fluid exhibits zero shear stress; the pressure, on the other hand, may be entirely hydrostatic. We are concerned with Newtonian fluids, in which the viscous stress is linearly proportional to the local strain rate. The viscous shear stress tensor is related to the rate of strain tensor as

$$\tau_{i,j} = \mu \left(\frac{\partial u_i}{\partial x_j} + \frac{\partial u_j}{\partial x_i} \right) - \frac{2}{3}\mu \frac{\partial u_k}{\partial x_k}, \tag{2.8}$$

where μ is the dynamic viscosity, which is here assumed to be constant and δ is the Kronecker delta. Substituting (2.8) into (2.7) and (2.6) results in the momentum equation for a Newtonian fluid, given by

$$\rho \left(\frac{\partial \mathbf{u}}{\partial t} + (\mathbf{u} \cdot \nabla)\mathbf{u} \right) = -\nabla P + \rho \mathbf{g} + \mu \nabla^2 \mathbf{u} + \frac{1}{3}\mu \nabla (\nabla \cdot \mathbf{u}), \tag{2.9}$$

2.2.3 Thermal Energy Equation

The rate of change of energy in a fluid system is given by (e.g. Spiegel and Veronis (1960)):

$$\rho C_v \left(\frac{\partial}{\partial t} + \mathbf{u} \cdot \nabla \right) T + P \nabla \cdot \mathbf{u} = k \nabla^2 T + Q + \mu \nabla \cdot (\mathbf{u} \cdot \nabla \mathbf{u}) - \frac{2}{3}\mu (\nabla \cdot \mathbf{u})^2, \tag{2.10}$$

where T is the temperature, Q represents a radiation source, and the coefficients C_v and k are taken to be constant. Terms multiplied by μ represent viscous heating, the Laplacian term $k\nabla^2 T$ represents diffusive heating, and the remaining terms represent convective heating.

2.2.4 Boussinesq Approximation

Momentum Equation

We here derive the governing equations under what is known as the Boussinesq approximation, in which density variations are assumed to have a negligible effect except in the bouyancy term. We first take the density field to comprise a reference density and a deviation from the reference density, i.e.

$$\rho = \rho_0 + \delta \rho. \tag{2.11}$$

Substituting this into the momentum equation gives,

$$(\rho_0 + \delta\rho)\left(\frac{\partial \mathbf{u}}{\partial t} + (\mathbf{u} \cdot \nabla)\mathbf{u}\right) = -\nabla P + (\rho_0 + \delta\rho)\mathbf{g} + \mu\nabla^2\mathbf{u} + \frac{1}{3}\mu\nabla(\nabla \cdot \mathbf{u}). \tag{2.12}$$

We note that in a fluid at rest with only the reference density, the momentum equation reduces to the hydrostatic equation,

$$0 = -\nabla P + \rho_0\mathbf{g}. \tag{2.13}$$

Therefore, we can take hydrostatic pressure out of the equation by defining a new pressure, say P', which is the difference between the actual pressure and the hydrostatic pressure,

$$\nabla P' = \nabla P + \rho_0 g. \tag{2.14}$$

Substituting this into our momentum equation gives,

$$(\rho_0 + \delta\rho)\left(\frac{\partial \mathbf{u}}{\partial t} + (\mathbf{u} \cdot \nabla)\mathbf{u}\right) = -\nabla P' + \delta\rho\mathbf{g} + \mu\nabla^2\mathbf{u} + \frac{1}{3}\mu\nabla(\nabla \cdot \mathbf{u}). \tag{2.15}$$

It is apparent from 2.15 that for a small change in density from the reference density, i.e. when $\delta\rho \ll \rho_0$, there is little change to the inertial terms, but a large change to the gravity term, which disappears entirely when $\delta\rho = 0$. In other words, the fluid is ‘almost incompressible’, meaning that small variations in density generally affect only the gravitational buoyancy term. This is the Boussinesq approximation, which holds only when $\delta\rho \ll \rho_0$. Thus, assuming the fluid is generally incompressible (i.e. $\nabla \cdot \mathbf{u} = 0$)) for small changes in density, we may represent the momentum equation as,

$$\frac{\partial \mathbf{u}}{\partial t} + (\mathbf{u} \cdot \nabla)\mathbf{u} = -\frac{\nabla P'}{\rho_0} + \frac{\delta\rho}{\rho_0}\mathbf{g} + \nu\nabla^2\mathbf{u}, \tag{2.16}$$

where $\nu = \mu/\rho_0$ is the kinematic viscosity. Note that under this approximation, the continuity equation reduces to that shown in equation (2.5)

Energy Equation

Viscous heating is typically neglected under the Boussinesq approximation, because it is argued that it should be small (Spiegel and Veronis, 1960). We note that there may be exceptions to this, such as mantle convection (McKenzie and Jarvis, 1980). Neglecting viscous heating, assuming a lack of radiative heating and accepting that the fluid is incompressible except for in relation to gravitational terms (i.e. $\nabla \cdot \mathbf{u} = 0$), the energy equation 2.10 reduces to the advection-diffusion heat equation (herein, the 'heat equation'),

$$\left(\frac{\partial}{\partial t} + \mathbf{u} \cdot \nabla\right) T = \kappa_T \nabla^2 T, \tag{2.17}$$

where $\kappa_T = k/\rho C_v$ is the (constant) diffusivity of heat. Again, small changes in density are assumed to have a negligible affect on the diffusivity.

Heretofore, we have considered a fluid having only a single diffusive component. We are interested, however, in double-diffusive convection, in which instabilities are driven by competing diffusive components such as heat and salt. We obtain an advection-diffusion equation for salt (or any other diffusive component) in a similar way as for the heat equation. The 'salt equation' is thus,

$$\left(\frac{\partial}{\partial t} + \mathbf{u} \cdot \nabla\right) S = \kappa_S \nabla^2 S, \tag{2.18}$$

where S is the concentration of salt, and κ_S is the (constant) diffusivity of salt.

2.3 Mathematical Formulation

2.3.1 Boundary Conditions

The choice of boundary conditions greatly affects the resulting dynamics in double-diffusive convection. Classically, the problem was studied à la Rayleigh-Bénard convection; that is, by investigating a two-dimensional fluid layer sandwiched between two infinite and perfectly conducting horizontal boundaries. In this case, one may induce differential heating by maintaining a constant temperature on both boundaries; similarly, fixing the concentration of a solute (such as salt) on the boundaries induces a compositional gradient across the domain. The distance between the two plates represents a readily available length scale for non-dimensionalisation. It will later be seen that in such a system we obtain two dimensionless Rayleigh numbers—one for temperature, and one for composition—expressing the strength of the two background gradients.

An alternative configuration that has been widely employed in studies of this nature over the past few decades utilises periodic boundaries in both the horizontal and vertical directions. The rationale behind such an approximation is that phenomena associated with double-diffusive convection, such as layering, tend to occur far from any physical boundaries. As noted in Chapter 1, layers are generally not observed in numerical simulations with impermeable boundaries. They are, however, observed in oceans (Johannessen and Lee, 1974, Molcard and Tait, 1977). A second motivation for the use of a periodic domain is that it permits the presence of so-called ‘elevator’ modes as the form of the primary instability of a static basic state. Elevator modes manifest as horizontally independent shear modes with infinite vertical extent, and are thought to be important in the formation of layers. Since the core focus of this study is the stability of elevator modes, periodic boundaries will be employed throughout – except when reproducing results obtained in previous studies.

In a doubly-periodic system, there is no externally imposed lengthscale with which to non-dimensionalise the governing equations, and hence the lengthscale must emerge from the intrinsic fluid properties. In line with previous studies of this nature (Holyer, 1984, Noguchi and Niino, 2010a, Radko and Smith, 2012), we choose a length scale defined in terms of the coefficient thermal expansion α, the diffusivity of heat, κ_T, the kinematic viscosity ν, gravitational acceleration g, and the background temperature gradient T_z, i.e.

$$\delta = \left| \frac{g\alpha T_z}{\kappa_T \nu} \right|^{-\frac{1}{4}} \tag{2.19}$$

This distance is that of the theoretical salt-finger width found by Stern (1960). Scaling in this way gives an undisturbed (background) temperature gradient of unity, leading to a single non-dimensional parameter governing the relative strength of background gradients. This proves useful as it effectively reduces the number of degrees of freedom of the system. In this section, we begin by deriving the governing equations for a horizontally and vertically periodic system, before proceeding to do the same with horizontal rigid boundaries. We then discuss how the two systems relate.

2.3.2 Basic State

We take an infinite, two-dimensional, thermally and compositionally stratified fluid domain, with linear vertical temperature and salinity gradients T_z and S_z respectively. The Navier-Stokes equations are written in Boussinesq form as

$$\frac{\partial \mathbf{u}}{\partial t} + (\mathbf{u} \cdot \nabla)\mathbf{u} = -\frac{1}{\rho_0}\nabla p + \frac{\rho}{\rho_0}\mathbf{g} + \nu\nabla^2\mathbf{u}, \tag{2.20}$$

$$\nabla.\mathbf{u} = 0 \tag{2.21}$$

$$\frac{\partial T}{\partial t} + (\mathbf{u} \cdot \nabla)T = \kappa_T \nabla^2 T, \tag{2.22}$$

$$\frac{\partial S}{\partial t} + (\mathbf{u} \cdot \nabla)S = \kappa_S \nabla^2 S. \tag{2.23}$$

The density is represented as a linear function of temperature and salinity:

$$\rho = \rho_0[1 - \alpha(T - T_0) + \beta(S - S_0)], \tag{2.24}$$

where T_0, S_0 and ρ_0 are (constant) reference values of temperature, salinity and density respectively. There exists a static ($\mathbf{u} = 0$) basic state with,

$$\begin{aligned} T &= T_0 + T_z z, \qquad (2.25)\\ S &= S_0 + S_z z,\\ \rho &= \rho_0[1 - (\alpha T_z - \beta S_z)z],\\ p &= p_0 - g\rho_0[1 - (\alpha T_z - \beta S_z)z^2/2], \end{aligned}$$

where T_z and S_z represent constant background gradients.

2.3.3 Perturbation Equations

We consider perturbations to this basic state of the form $T = T_0 + T_z z + \tilde{T}(x, z, t)$, where tilde denotes a perturbed variable. This leads to the perturbation equations,

$$\frac{\partial \tilde{\mathbf{u}}}{\partial t} + (\tilde{\mathbf{u}}.\nabla)\tilde{\mathbf{u}} = -\frac{1}{\rho_0}\nabla\tilde{p} - \frac{\tilde{\rho}}{\rho_0}g\hat{\mathbf{z}} + \nu\nabla^2\tilde{\mathbf{u}}, \tag{2.26}$$

$$\frac{\partial \tilde{T}}{\partial t} + (\tilde{\mathbf{u}}.\nabla)\tilde{T} + wT_z = \kappa_T\nabla^2\tilde{T}, \tag{2.27}$$

$$\frac{\partial \tilde{S}}{\partial t} + (\tilde{\mathbf{u}}.\nabla)\tilde{S} + wS_z = \kappa_S\nabla^2\tilde{S}, \tag{2.28}$$

$$\tilde{\rho} = \rho_0(-\alpha\tilde{T} + \beta\tilde{S}), \tag{2.29}$$

$$\nabla.\tilde{u} = 0, \tag{2.30}$$

where w is the vertical velocity and perturbations are not assumed to be small. We eliminate $\tilde{\rho}$ by substituting for $\tilde{\rho}$ in terms of $\tilde{T}$ and $\tilde{S}$ from (2.29) into (2.26):

$$\frac{\partial \tilde{\mathbf{u}}}{\partial t} + (\tilde{\mathbf{u}}.\nabla)\tilde{\mathbf{u}} = -\frac{1}{\rho_0}\nabla\tilde{p} + g(\alpha\tilde{T} - \beta\tilde{S})\hat{\mathbf{z}} + \nu\nabla^2\tilde{u}. \tag{2.31}$$

2.3.4 Non-dimensionalisation

As noted above, in the absence of physical boundaries we non-dimensionalise with an internal lengthscale related to the theoretical width of salt fingers. That is, we define a length of:

$$\delta = \left|\frac{g\alpha T_z}{\kappa_T\nu}\right|^{-\frac{1}{4}}. \tag{2.32}$$

Hence, we scale time with δ^2/κ_T, velocity with κ_T/δ, temperature and salinity with $|T_z|\delta$ and $|S_z|\delta$, and pressure with $\rho u^2 = \rho_0\kappa_T^2/\delta^2$. This results in the non-dimensional perturbation equations (dropping tildes),

$$\frac{\partial \mathbf{u}}{\partial t} + (\mathbf{u}.\nabla)\mathbf{u} = -\nabla p + Pr(T - S)\hat{\mathbf{z}} + Pr\nabla^2 u, \tag{2.33}$$

$$\frac{\partial T}{\partial t} + (\mathbf{u}.\nabla)T + \mathrm{sgn}(T_z)w = \nabla^2 T, \tag{2.34}$$

$$\frac{\partial S}{\partial t} + (\mathbf{u}.\nabla)S + \mathrm{sgn}(S_z)R_\rho^{-1}w = \tau\nabla^2 S, \tag{2.35}$$

where Pr is the Prandtl number, $Pr = \nu/\kappa_T$, and τ is the ratio of diffusivities $\tau = \kappa_S/\kappa_T$. Typical values in the ocean are $Pr = 7$ and $\tau = 0.01$, and we use these values throughout this thesis. Furthermore, $R_\rho = \alpha|T_z|/\beta|S_z|$ is the density gradient ratio, pertaining to the strength of the background stratification, whilst the two sgn$(\cdot)$ terms (which are either $+1$ or -1 depending on the sign of T_Z and S_Z) pertain to the nature of the stratification: positive (negative) T_z and S_z places the system in the fingering (diffusive) regime.

As an aside: for typical parameter values in the ocean ($\alpha \sim 10^{-4}\mathrm{K}^{-1}$, $g \sim 9.81$ ms^{-2}, $T_z \sim 0.02$ K m^{-1}, $\nu \sim 1.8\times10^{-6}$ m^{2}s^{-1}, $\kappa_T \sim 1.38\times10^{-7}$m^{2}s^{-1}) we see that $\delta \sim 0.01m$. Thus the characteristic timescale and velocity for temperature and diffusion are $t \sim 818$s and $u \sim 1.3 \times 10^{-5}$ ms^{-1}.

Density

We also scale the density, as it can provide a useful means of interpreting results. We recognise that the total density is the sum of a background gradient (2.25) and perturbation (2.29):

$$\rho_T = \rho_0(1 - (\alpha T_z - \beta S_z)z - (\alpha\tilde{T} - \beta\tilde{S})). \tag{2.36}$$

We then scale T, S and z as before, and scale ρ with $\rho_0\alpha|T_z|\delta$. This gives, after dropping any dashes and tildes, the dimensionless equation for total density:

$$\rho_T = -(\mathrm{sgn}(T_z) - R_\rho^{-1}\mathrm{sgn}(S_z))z - (T - R_\rho^{-1}S) + C, \tag{2.37}$$

where C is a constant reference density, $C = (\alpha|T_z|\delta)^{-1}$.

2.3.5 Streamfunction Formulation

In this study we will be concerned primarily with 2-dimensional systems. As such, it is desirable to investigate the behaviour of the fluid in terms of a stream function. Taking the curl of (2.33) eliminates pressure and leads to the vorticity equation, which is expressed in the y-direction only. That is,

$$\frac{\partial\omega}{\partial t} + (\mathbf{u}.\nabla)\omega = -Pr\,(T_x - S_x) + Pr\nabla^2\omega. \tag{2.38}$$

We now introduce the stream function, ψ such that

$$\mathbf{u} = \left(-\frac{\partial \psi}{\partial z}, 0, \frac{\partial \psi}{\partial x}\right) \qquad \text{and} \qquad \omega = -\nabla^2 \psi.$$

This yields the governing, nonlinear, dimensionless Boussinesq equations for perturbations to the basic state,

$$\left(\frac{\partial}{\partial t} - Pr\nabla^2\right)\nabla^2\psi = -J(\psi, \nabla^2\psi) + Pr\left(\frac{\partial T}{\partial x} - \frac{\partial S}{\partial x}\right), \tag{2.39}$$

$$\left(\frac{\partial}{\partial t} - \nabla^2\right)T + \operatorname{sgn}(T_z)\frac{\partial \psi}{\partial x} = -J(\psi, T), \tag{2.40}$$

$$\left(\frac{\partial}{\partial t} - \tau\nabla^2\right)S + \operatorname{sgn}(S_z)R_\rho^{-1}\frac{\partial \psi}{\partial x} = -J(\psi, S), \tag{2.41}$$

where all nonlinear terms are captured in the Jacobian, $J(a,b) = \partial_x a \partial_z b - \partial_z a \partial_x b$.

2.3.6 Linear stability analysis

The stability of the static basic state may be considered in terms of the behaviour of a parcel of fluid within the domain. Figure 2.1 shows the behaviour of a blob of fluid in a background state consisting of a stable compositional (salt) gradient and a destabilising thermal gradient. The top and bottom boundaries are periodic and the T and S gradients are linear in z. This configuration is found for instance in the Arctic Ocean, in which cold fresh water from glacial outflows lies over warmer (but still cold) salty water from the Atlantic Ocean.

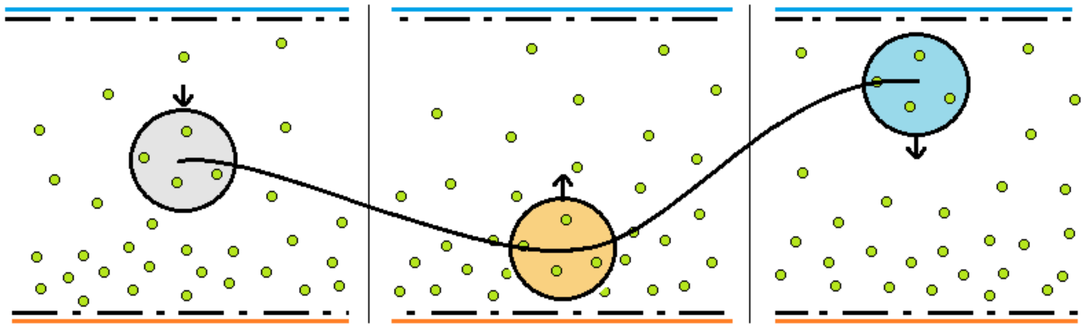

Figure 2.1: A schematic of the behaviour of a blob of fluid in a double-diffusive system in which the slower-diffusing component (salt) has a stabilising effect (i.e. $\operatorname{sgn}(T_Z) = \operatorname{sgn}(S_Z) = 1$).

As heat diffuses quicker than salt ($\tau \ll 1$), a parcel displaced downwards will rapidly heat up and return to its original position while maintaining its salt content. The parcel may then be warmer than its surroundings, and thus lighter, leading to an overshoot. If overshoot occurs, the parcel will rapidly cool to the surrounding temperature, again maintaining its salt content. The parcel will then be heavier than its surroundings and sink, restarting the cycle and leading to oscillations which may grow, depending on the strength of the background stratification. We refer to this phenomenon as 'oscillatory double-diffusive convection', or simply 'diffusive convection'.

The gradients are reversed in areas such as the Mediterranean ocean, in which surface evaporation leaves warm, salty water above the cold, fresh outflow from rivers. This configuration is shown in Figure 2.2. A parcel of fluid displaced downwards will cool down more quickly than it will lose its salt content, and so it will become heavier as it continues to sink. A blob of fluid displaced upwards will also continue its motion, becoming warmer and lighter as it rises. This instability is known as 'salt-fingering', which lends its name to this configuration of T and S.

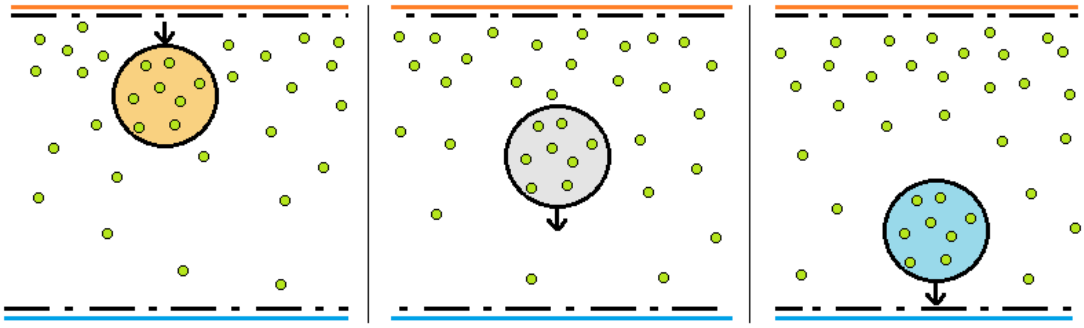

Figure 2.2: A schematic of the behaviour of a blob of fluid in a system susceptible to salt fingering, in which the slower-diffusing component (salt) has a destabilising effect (i.e. $\text{sgn}(T_z) = \text{sgn}(S_z) = 1$).

The static basic state is shown to be unstable to growing perturbations of the form,

$$\psi = A_\psi e^{\lambda_0 t} \cos(k_x x), \quad T = A_T e^{\lambda_0 t} \sin(k_x x), \quad S = A_S e^{\lambda_0 t} \sin(k_x x), \tag{2.42}$$

where k_x is a horizontal wave number. These are commonly referred to as 'elevator' modes. Equations (4.24) - (4.26) are nonlinear, but the Jacobian terms are zero on the substitution of such perturbations as 2.42, since $\partial_z(\psi, T, S) = 0$. Hence elevator solutions satisfy the linear equations

$$\begin{aligned} &A_T(\lambda_0 + k_x^2) = \operatorname{sgn}(T_z) k_x A_\psi, \\ &A_S(\lambda_0 + \tau k_x^2) = \operatorname{sgn}(S_z) k_x R_\rho^{-1} A_\psi, \\ &\frac{A_\psi k_x}{Pr}(\lambda_0 + Pr k_x^2) = -(A_T - A_S), \end{aligned} \tag{2.43}$$

which correspond to Equations (2.22) in Holyer (1984) when $k_x = 1$ and $\operatorname{sgn}(T_z) = \operatorname{sgn}(S_z) = 1$. Solving the simultaneous equations (2.43), we obtain a cubic equation for the growth rate of perturbations, λ_0:

$$(\lambda_0 + k_x^2)(\lambda_0 + Pr k_x^2)(\lambda_0 + \tau k_x^2) + Pr(\operatorname{sgn}(T_z)(\lambda_0 + \tau k_x^2) - \operatorname{sgn}(S_z) R_\rho^{-1}(\lambda_0 + k_x^2)) = 0. \tag{2.44}$$

Since equation (2.44) is a cubic with real coefficients, then the roots are either all real, or one real and two complex conjugates. Hence instability can occur as overstable oscillations (when a pair of complex roots crosses the imaginary axis), or as an exchange of stabilities (when one of the roots equals zero).

We determine the stability boundary by expanding (2.44) and setting $\lambda_0 = \sigma + i\omega$ in

$$\lambda_0^3 + a\lambda_0^2 + b\lambda_0 + c = 0, \tag{2.45}$$

with

$$\begin{aligned} a &= k_x^2(Pr + \tau + 1), \\ b &= k_x^4(\tau Pr + Pr + \tau) \pm Pr(1 - R_\rho^{-1}), \\ c &= k_x^6 \tau Pr \pm k_x^2 Pr(\tau - R_\rho^{-1}). \end{aligned}$$

Here, ± denotes positive or negative T_z and S_z—positive for salt fingering, negative for diffusive convection. In the present study, we are primarily interested in oscillatory double-diffusive convection, for which the signs of T_z and S_z are negative. We first seek the direct non-oscillatory instability, where $\sigma = \omega = 0$. Hence, in this case, $c = 0$ and so

$$\begin{aligned} k_x^4 \tau Pr &= \mp Pr(\tau - R_\rho^{-1}), \\ \implies R_\rho^{-1} &= \tau(1 \pm k_x^4). \end{aligned} \tag{2.46}$$

We can also find oscillatory solutions, where $\sigma = 0$ and ω is real and non-zero, i.e.

$$\mp i\omega^3 \mp a\omega^2 \pm ib\omega + c = 0. \tag{2.47}$$

Here, $\omega^2 = b$ and $\omega^2 = c/a$. Eliminating ω^2 gives $c = ab$. However, this is only a line of marginal stability if $b > 0$. If $b < 0$ then ω is imaginary and the solution is stable.

Since a is always positive, and b is positive for an oscillatory instability, then c is also positive. Oscillatory solutions occur when $\mathrm{sgn}(T_z) = \mathrm{sgn}(S_z) = -1$; hence, the frequency of marginal instabilities is given by

$$\omega^2 = k_x^4(\tau Pr + Pr + \tau) - Pr(1 - R_\rho^{-1}). \tag{2.48}$$

We find the boundary of the instability by setting $ab = c$.

$$k_x^6(Pr+\tau+1)(Pr+\tau+\tau Pr) - k_x^2(Pr+\tau+1)(Pr(1-R_\rho^{-1})) = k_x^6 \tau Pr - k_x^2 Pr(\tau - R_\rho^{-1})$$

$$\implies R_\rho^{-1} = \frac{(Pr+1)}{(Pr+\tau)}\left(1 - k_x^4(1+\tau)(1+\frac{\tau}{Pr})\right) \tag{2.49}$$

Examining the total density equation (2.37) we can observe that the background density gradient

$$\rho_B = \pm(R_\rho^{-1} - 1)z \tag{2.50}$$

is always unstable if: $R_\rho^{-1} \geq 1$ in the fingering (+) configuration; or $R_\rho^{-1} \leq 1$ in the oscillatory (−) configuration. Putting everything together we can see that the system is unstable to salt-fingers (+) if

$$1 \geq R_\rho^{-1} \geq \tau(1k_x^4), \tag{2.51}$$

and unstable to oscillatory double-diffusive convection (ODDC) $(-)$ when

$$1 \leq R_\rho^{-1} \leq \frac{(Pr+1)}{(Pr+\tau)}\left(1 - k_x^4(1+\tau)(1+\frac{\tau}{Pr})\right), \tag{2.52}$$

providing $b > 0$, i.e.

$$k_x^4(\tau Pr + Pr + \tau) = Pr(1 - R_\rho^{-1}). \tag{2.53}$$

2.3.7 Salt Finger Instability

We determine the growth rate of instabilities by finding the three roots λ_0 of the cubic equation (2.44). Calculating the roots in the salt-finger regime (with T_z and S_z both positive) as a function of R_ρ^{-1} and k_x results in the plot of growth rates shown in Figure (2.3).

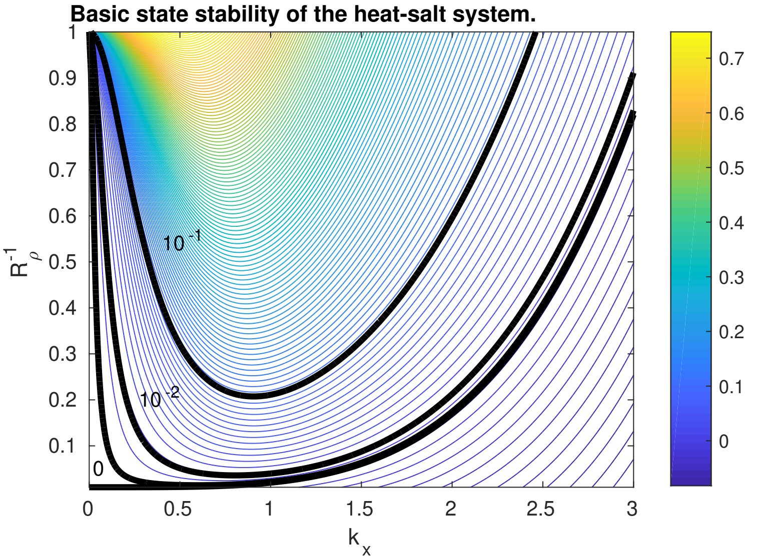

Figure 2.3: Contours showing the growth rate of perturbations as a function of R_ρ^{-1} and k_x for $\mathrm{sgn}(T_z) = \mathrm{sgn}(S_z) = 1$, i.e. in the salt-fingering regime, when $Pr = 7$ and $\tau = 0.01$.

The solid line showing zero growth rate matches the curve given by the lower bound of equation (2.51), wherein the curve meets the ordinate at a value of $R_\rho^{-1} = \tau$. We can thus use equation (2.51) to determine the wavenumber for a given R_ρ^{-1} to give marginal stability, or vice versa.

Alternatively, for a given R_ρ^{-1} we may solve the cubic (2.44) to find the wavenumber of the fastest growing mode, k_x.

2.3.8 Oscillatory Instability

We may also solve (2.44) to obtain three roots describing the growth rate and frequency of perturbations in the oscillatory regime. Figure (2.4) shows the growth rate (maximum real part) of perturbations as a function of R_ρ^{-1} and k_x in the oscillatory case.

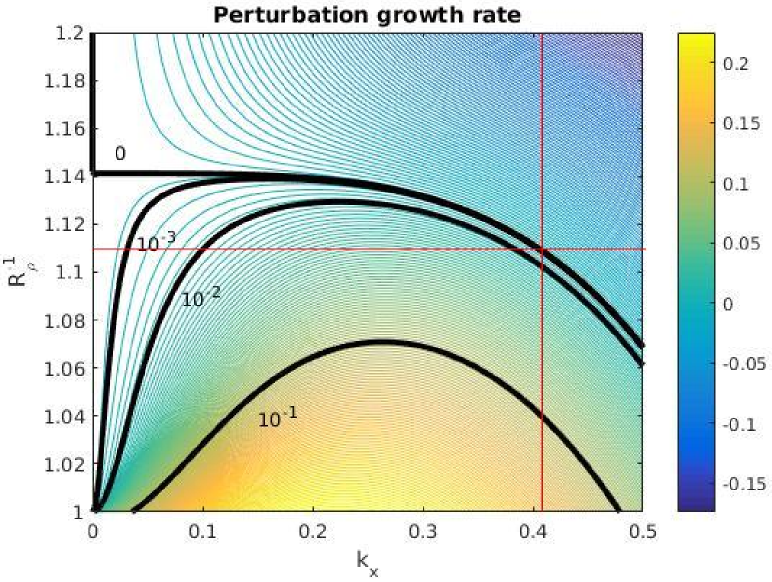

Figure 2.4: Growth rate of perturbations as a function of R_ρ^{-1} and k_x for $\mathrm{sgn}(T_z) = \mathrm{sgn}(S_z) = -1$; i.e. in the oscillatory regime.

The solid line showing zero growth rate matches the curve given by equation (2.52) so that the curve meets the ordinate at $R_\rho^{-1} = (Pr + 1)/(Pr + \tau)$, highlighting boundary of instability. Hence we can use (2.52) to determine the wavenumber for a given R_ρ^{-1} at marginal stability (as indicated by the red lines in Figure 2.4), or vice-versa, with frequency given by (2.48). Alternatively for a given R_ρ^{-1} we may solve the cubic equation

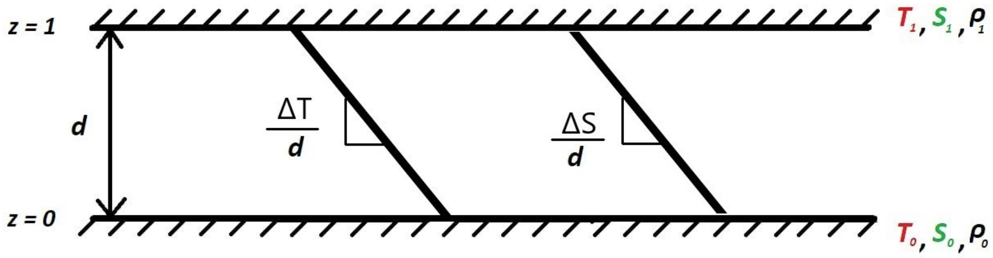

Figure 2.5: A schematic diagram of a diffusively stratified fluid vertically bounded by upper and lower rigid horizontal boundaries separated by a distance d. The upper and lower boundaries are maintained at a constant temperature and salinity. The temperature T and salinity S in the fluid domain are each linearly stratified with gradient $T_z = \frac{\Delta T}{d}$ and $S_z = \frac{\Delta S}{d}$.

(2.44) to find the wavenumber of the fastest growing mode, k_x^* and the corresponding frequency of oscillations.

2.4 Bounded Domain

In preparation for a brief study of a bounded system in Chapter 3, we here derive the governing equations in a domain with rigid, horizontal upper and lower boundaries. Figure 2.5 shows a schematic diagram of this configuration. The lower boundary is maintained at a fixed temperature $T = T_0$ and salinity $S = S_0$. The temperature and salinity differences between the top and bottom plates are denoted ΔT and ΔS respectively so that the top plate has temperature $T = T_0 + \Delta T$ and salinity $S = S_0 + \Delta S$. The distance between the two plates is d, so linear temperature and salinity gradients in the fluid may be defined as $T_z = \frac{\Delta T}{d}$ and $S_z = \frac{\Delta S}{d}$, respectively. As in the unbounded case, the gradients may be either positive or negative—a positive δT gives a stable temperature gradient, and vice versa, while a positive δS gives in unstable salinity gradient, and vice versa.

The boundaries are considered impermeable, stress-free and perfectly conducting (having fixed temperature and salinity), which may be expressed as

$$\psi = \frac{\partial^2 \psi}{\partial z^2} = T = S = 0, \tag{2.54}$$

on each boundary, where ψ is as defined hereinbefore. Taking the governing Navier-Stokes equations (2.20–2.23), perturbing the variables as before, and nondimensionalising using the length scale d results in the following non-dimensional governing equations (cf. Baines and Gill (1969) and Da Costa et al. (1981)):

$$\left(\frac{\partial}{\partial t} - Pr\nabla^2\right)\nabla^2\psi = -J(\psi, \nabla^2\psi) + Pr\left(\frac{R_T \partial T}{\partial x} - R_S\frac{\partial S}{\partial x}\right), \tag{2.55}$$

$$\left(\frac{\partial}{\partial t} - \nabla^2\right)T + \operatorname{sgn}(T_z)\frac{\partial \psi}{\partial x} = -J(\psi, T), \tag{2.56}$$

$$\left(\frac{\partial}{\partial t} - \tau\nabla^2\right)S + \operatorname{sgn}(S_z)\frac{\partial \psi}{\partial x} = -J(\psi, S), \tag{2.57}$$

where $R_T = g\alpha\Delta T d^3/\nu\kappa_T = g\alpha T_z d^4/\nu\kappa_T$ is a thermal Rayleigh number, and $R_S = g\beta\Delta S d^3/\nu\kappa_T = g\beta S_z d^4/\nu\kappa_T$.

Note that we may combine R_T and R_S into a density gradient ratio, $R_\rho = \frac{R_T}{R_S} = \frac{\alpha T_z}{\beta S_Z}$, as with the unbounded system. Furthermore, we may recover the governing equations pertaining to an unbounded system by taking $d = \delta = \left|\frac{g\alpha T_z}{\kappa_T \nu}\right|^{-\frac{1}{4}}$, which gives a thermal Rayleigh number of unity, so that,

$$\left(\frac{\partial}{\partial t} - Pr\nabla^2\right)\nabla^2\psi = -J(\psi, \nabla^2\psi) + Pr\left(\frac{\partial T}{\partial x} - R_\rho^- 1\frac{\partial S}{\partial x}\right), \tag{2.58}$$

$$\left(\frac{\partial}{\partial t} - \nabla^2\right)T + \operatorname{sgn}(T_z)\frac{\partial \psi}{\partial x} = -J(\psi, T), \tag{2.59}$$

$$\left(\frac{\partial}{\partial t} - \tau\nabla^2\right)S + \operatorname{sgn}(S_z)\frac{\partial \psi}{\partial x} = -J(\psi, S). \tag{2.60}$$

The density gradient ratio R_ρ is, here, located in the streamfunction equation; however,

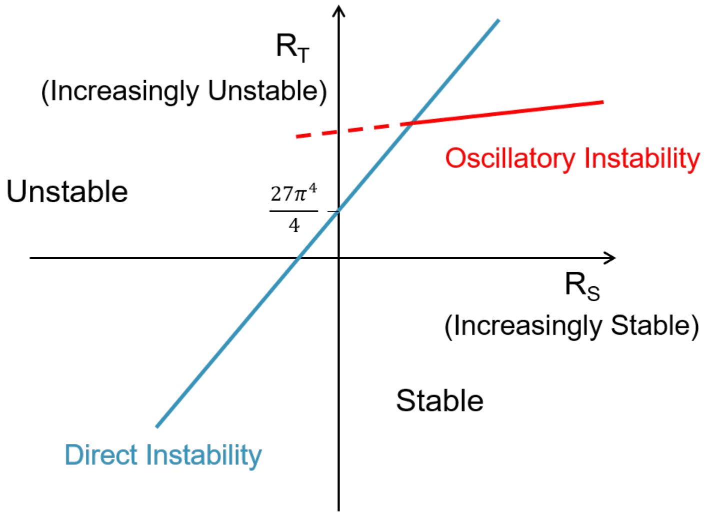

Figure 2.6: Schematic diagram of instability in a bounded system as a function of R_T and R_S, optimised over k_x.

it may equally be comprised in the salinity equation, as in equations (4.24–4.26). Notably, the stability of the system in the bounded domain is dependent on the values of both R_T and R_S. The schematic diagram of Figure 2.6 shows the regions of instability on a plot of R_T vs R_S (Huppert and Moore, 1976, Veronis, 1965). It is clear from Figure 2.6 that for a given choice of R_T and R_S, the bounded system may be either stable, marginally unstable, or fully unstable.

The stability of the unbounded system, in contrast, is the same along lines of constant $R_\rho = R_T/R_S = \frac{\alpha T_z}{\beta S_Z}.Thisisbecause,intheboundeddomain,thediffusiveeffectsof\kappa_T$ and κ_S each play a part in the stability of the system. In the unbounded system, we have non-dimensionalised using δ as defined in equation 2.19, which includes κ_T. Thus, non-dimensionalising the equations using δ gives a thermal Rayleigh number, R_T, of 1; hence, the stability is dependent only on R_ρ. Figure 2.7 shows the stable, oscillatory, salt-fingering, and unstably stratified ($R_\rho^{-1} > 1$) regions as a function of αT_Z and βS_Z, where the boundaries for stability have been optimised over k_x.

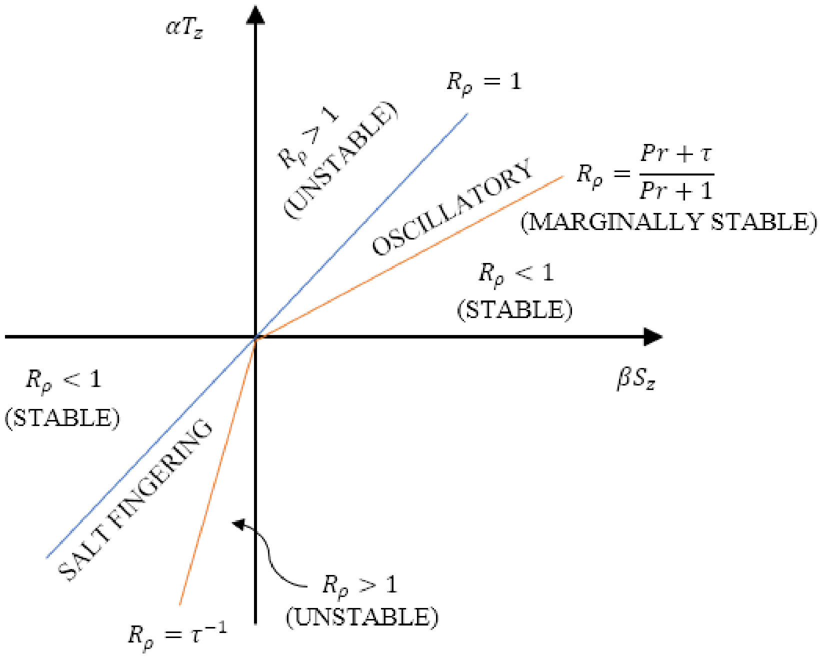

Figure 2.7: Schematic diagram of the regions of instability in an unbounded system as a function of αT_Z and βS_Z, optimised over k_x, wherein the stability characteristics are unchanging along lines of constant αT_Z / βS_Z.

In Chapter 3, we discuss the bounded and unbounded systems in more detail with respect to the work of Veronis (1965), Veronis (1968), Da Costa et al. (1981) and Noguchi and Niino (2010a). For this reason, in Chapter 3 we refer to the Prandtl number Pr using the symbol σ, and the density gradient ratio R_ρ using γ, to permit a more direct comparison with the work of these authors. The symbols Pr and R_ρ are used in Chapters 4 and 5 to permit comparisons with the work of other authors such as Stellmach et al. (2011) and Radko (2013).

CHAPTER 3

Truncated Models

3.1 Introduction

Truncated Fourier expansions have seen numerous applications in the modelling of convective systems. Perhaps the most notable example is that of the heavily truncated Lorenz system (Lorenz, 1963), in which velocity and temperature fields are represented by a total of three different modes. Truncating in this way permits the formulation of a time-dependent system of ODEs, which can then be solved to analyse modal interactions of the three basic modes and gain insight into the non-linear behaviour of such systems. We discuss the Lorenz system in section 3.2.

Other examples exist of truncated systems used to model double-diffusive convection. Such a truncated system was obtained by Veronis (1965), and was later used by Da Costa et al. (1981) to study modal interactions in double-diffusive convection. In each of these studies, two extra modes were included to account for the concentration of salt. These studies will be described in section 3.3. The systems studied by Veronis (1965) and Da Costa et al. (1981) were constrained to a bounded domain, so no elevator modes were present in the truncation. A further study was therefore performed by Noguchi and Niino (2010a) who used a truncated Fourier expansion in a doubly-periodic domain to study the effects of elevator modes. This study is discussed in section 3.4

Heavily truncated, low-order models provide certain advantages when used to study convective systems. Firstly, it is possible, with a reduced-order system, to directly study the interactions of individual modes with one another. This can help to bring out the important physical processes that are responsible for the behaviour of interest. Secondly, within the truncated equations, equilibrium solutions can be easily found and their stability readily computed. This can be valuable to determine whether there are any parameter ranges at which stable solutions exist.

There are, however, certain disadvantages to using heavily truncated models. Specifically, as the amplitude of each mode increases, additional modes may be generated through further nonlinear interactions. These additional modes would be unaccounted for by a heavily truncated Fourier series. Thus, behaviour we observed at anything other than small amplitudes is likely to be unreliable. For this reason, care must be taken in drawing conclusions from such models, particularly as modal amplitudes increase. Nevertheless, we here analyse the behaviour of the modes at larger amplitudes in order to gain further insight into the persistence of layering modes which can be observed in such heavily truncated models.

This chapter starts with an overview of the truncated systems used by previous authors to model both convection and double-diffusive convection, detailing some of the understandings gained. We then investigate how these studies may be extended by including additional modes. Specifically, we study the effects of introducing elevator modes in heavily truncated systems. In this way, we obtain a system of equations that is of lower-order than that studied by Noguchi and Niino (2010a), but that can be used to obtain many of the same findings. We also derive two higher-order systems to study the effects of different configurations of the elevator modes. We verify and use these models to study the system after modal amplitudes become large, thereby further extending the work of 3.4.

In § 3.6, we use our findings to explain how the interactions between low-order modes can lead to the formation (and eventual collapse) of persistent vertical density structures, which are reminiscent of double-diffusive layers. We then study, in § 3.7, the stability of equilibrium points identified and studied by Veronis (1965) and Da Costa et al. (1981) in the presence of elevator modes. We conclude by contrasting our findings with knowledge gained by other authors through large-scale direct numerical simulations of the governing equations, particularly in relation to the formation of density layers.

3.2 Lorenz System

Lorenz (1963) employed a heavily truncated ODE system to study the chaotic behaviour of bounded thermal convection. The perturbations in ψ and T are approximated by a heavily truncated Fourier expansion, or 'minimal representation', of the form

$$\begin{aligned}\psi &= A_\psi \sin(kx)\cos(mz),\\ T &= A_T \cos(kx)\sin(mz) + A_T \sin(2mz),\end{aligned}$$

where k and m are horizontal and vertical wavenumbers, respectively. Substituting these approximate solutions into the governing equations and retaining only terms of the same spatial form, results in a 3rd-order system of ODEs, which, in contrast to the governing PDE system, is readily numerically integrated. We do not here cover the Lorenz (1963) system in detail, as there is a wide array of literature discussing this topic (Sparrow, 1982). Rather, it is more instructive to discuss an extension and application of this method to a double-diffusive system, as in the following section.

3.3 Fifth-order Model

A similar minimal representation as employed by Lorenz (1963) can be constructed to study the weakly non-linear behaviour of double-diffusive systems. As in the Lorenz system, a heavily truncated Fourier series solution is employed to convert the governing system of PDEs (2.20–2.22) into a solvable low-order system of ODEs. We can then study modal interactions by way of numerical simulation, thereby providing insight into the system as amplitudes become too large for a linear stability analysis to be valid.

Such a minimal representation was first suggested by Veronis (1965), and was later investigated thoroughly by Da Costa et al. (1981). In each study, the fluid domain is bounded between two impermeable horizontal plates, as described in Chapter 2. The minimal representation of the streamfunction (ψ), temperature (T) and salinity (S) perturbations in the Da Costa et al. (1981) study are taken to be

$$\psi = a(t^*)2(2p)^{\frac{1}{2}}\frac{\lambda}{\pi}\sin\frac{\pi x}{\lambda}\sin\pi z, \tag{3.1}$$

$$T = b(t^*)2\left(\frac{2}{p}\right)^{\frac{1}{2}}\cos\frac{\pi x}{\lambda}\sin\pi z - c(t^*)\frac{1}{\pi}\sin 2\pi z, \tag{3.2}$$

$$S = d(t^*)2\left(\frac{2}{p}\right)^{\frac{1}{2}}\cos\frac{\pi x}{\lambda}\sin\pi z - e(t^*)\frac{1}{\pi}\sin 2\pi z, \tag{3.3}$$

where $t^* = pt$, $p = \pi^2(1 + 1/\lambda^2)$, and the coefficients are selected to scale and simplify the resulting system of ODEs. In this case, the wavenumbers $(k, m) = (\pi/\lambda, \pi)$. We here define wavenumbers as (Kk, Mm), where $K, M \in \mathbb{Z}$. In this way, we may identify harmonics independently of their respective wavenumbers as (K, M). The above system thus comprises the modes $(1, 1)$ and $(0, 2)$.

Suppose that only the $(1, 1)$ modes are taken initially; the $(0, 2)$ mode is then generated through nonlinear interactions in the Jacobian terms of the governing equations in a bounded system (2.58–2.60), and so is included in the minimal representation. Indeed, if this process is repeated then further higher harmonics are generated. One must thus choose when to truncate the system; that is, to choose which generated terms are neglected and which are kept. Consider the lattice in Figure (3.1) showing possible modal combinations of K and M, from Veronis (1966). It could be said that this system is truncated as a triangular array—any additional harmonics generated which lie below the dashed line in Figure (3.1) are retained, while those above are discarded. Using the notation previously introduced, this is equivalent to ensuring $K + M = 2$. The resulting system of ODEs, after substituting the above minimal representation into the

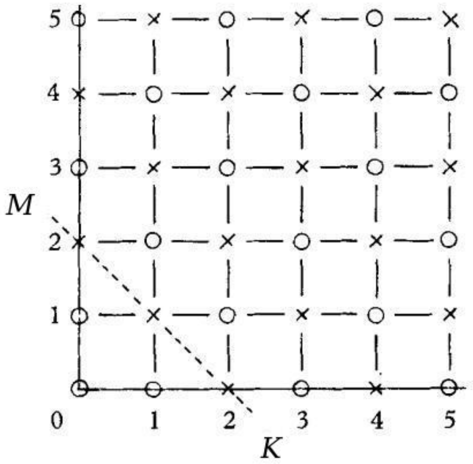

Figure 3.1: Wavenumber lattice, showing the potential higher-harmonics.

governing equations (2.58–2.60) neglecting such higher harmonics, is

$$\begin{aligned} a' &= \sigma[-a + r_T b - r_S d], \\ b' &= -b + a(1-c), \\ c' &= \varpi[-c + ab], \\ d' &= -\tau d + a(1-e), \\ e' &= \varpi[-\tau e + ad], \end{aligned} \tag{3.4}$$

where

$$\varpi = \frac{4\pi^2}{p}, \qquad r_T = \frac{\pi^2}{\lambda^2 p^3} R_T, \qquad r_S = \frac{\pi}{\lambda^2 p^3} R_S,$$

and $'$ symbolises a time-derivative. Note that by removing the salinity terms, i.e. setting $d = e = 0$, this reduces to the well-known Lorenz (1963) system. Furthermore, the presence of impenetrable boundaries limits the system to a $\sin(n\pi z)$ dependence and so no ‘elevator’ $(1, 0)$ mode can be included.

Linearising the system about the trivial static solution $a = b = c = d = e = 0$ admits solutions that vary as $e^{\sigma t^*}$ (Da Costa et al., 1981). The initial instability is an oscillatory standing wave solution; however, it should be noted that a weakly non-linear analysis by Bretherton (1981) predicted travelling-wave solutions begin to dominate when nonlinearity becomes important (i.e. with large-amplitude disturbances). Da Costa et al. (1981) show that results from nonlinear simulations of this system corresponded quite closely to those obtained by Huppert and Moore (1976) for the full system.

Knobloch et al. (1981) developed equations governing the problem of magneto-convection, which resembled those of double-diffusive convection studied here. Hughes and Weiss (1995) successfully applied reduced order models similar to those of Veronis (1965) and Da Costa et al. (1981) to the equations derived by Knobloch et al. (1981). The wide-ranging use of low-order models by previous authors is exemplary of the success of such models in providing insight into a variety of convective systems.

The linear stability analysis presented in Chapter 2 shows that the fastest growing mode for a system having periodic boundaries is an elevator mode of the form $(1, 0)$, corresponding to infinitely long vertical columns. Elevator modes are not permitted in the system (3.4) owing to the presence of upper and lower rigid boundaries. In a natural context, salt fingering and staircase formation tend to occur far away from any physical boundaries and so it is important to minimise any boundary effects (Stellmach et al., 2011). This suggests that in order to observe layers, the vertical distance between boundaries must be significantly large, or else periodic boundaries must be used.

3.4 Higher Order Systems

We are interested in extending the system studied by Veronis (1965) and by Da Costa et al. (1981) to include elevator modes, which are thought to play a critical role in the formation of layers. This requires the use of periodic boundary conditions, as described in Chapter 2. A similar study was performed by Noguchi and Niino (2010a), who studied a truncated system to investigate modal interactions during the formation of layers in two-dimensional double-diffusive convection. The truncation in the Noguchi and Niino (2010a) paper was very specific—the authors performed a direct numerical simulation (DNS) of the full 2D system and identified from the results which modes should be included in the low-order model based on their apparent importance.

This is a different approach to that of Lorenz (1963) and Veronis (1965), who include only first-order modes generated through nonlinear interactions of the basic modes. It may be the case that Noguchi and Niino (2010a) (herein referred to as NN) included more modes in their model than was necessary to observed layer formation. In this chapter, we derive a low-order model of double-diffusive convection, by extending the system and method of Veronis (1965) to include elevator modes. The model is used to study the modal interactions which lead to layering. we see that the model is able to produce results similar to those of NN, but using fewer modes.

Furthermore, NN did not monitor the behaviour of the modes after all modes had reached the same amplitude as one another. This is because when the lower-order modes reach a similar amplitude to one another, higher-order modes may no longer be considered negligible. Such higher-order modes would likely be generated through further nonlinear interactions, which are excluded in our model by virtue of the heavy truncation. Nevertheless, we find it instructive to study the behaviours and interactions of the modes in our lower-order model even after the modes reach a similar order of magnitude as one another.

3.4.1 Noguchi and Niino Study

We here provide a brief overview of the findings of NN, with the aim of providing a background with with to compare our novel system. As stated previously, NN studied the system using Direct Numerical Simulation (DNS) to identify modes thought to be important to staircase formation. We first provide a brief overview of the findings from the DNS, before discussing the truncated system of NN.

Direct Numerical Simulation

In order to determine which modes were responsible for layer formation, NN ran a two-dimensional direct numerical simulation of the equations governing double-diffusive convection in the 'diffusive' state. A marginally supercritical value of $\gamma = 0.88$ ($R_\rho^{-1} = 1.136$) was used in the simulation. The calculation was made on a square domain that was about 20 times larger than the wavelength of the fastest growing mode elevator mode predicted by linear theory. Periodic boundary conditions were imposed at horizontal and vertical boundaries, and the system was initialised with a low-amplitude white-noise disturbance.

The authors monitored the kinetic energy throughout the simulation (see Figure 5 in NN). They found that, following a brief period of total energy decrease, which was attributed to the damping of disturbances with negative growth rates, the initial random perturbations started to grow exponentially with time. The growth rate was comparable to that of the fastest-growing elevator mode from linear theory. This exponential growth was followed by an 'explosive growth' phase, in which the kinetic energy increased by three orders of magnitude in a relatively short space of time. When the amplitudes reached $\mathcal{O}(1)$, the growth rate slowed down and was no longer exponential. Interestingly, a sudden formation of layered structures was observed following the explosive growth phase.

In Figure 3.2 we show the plots of Figure 9 of NN. These plots show the formation and evolution of layered structures in the system over time. The vertical density profile was observed to remain almost constant during the linear growth phase, but gave way to small-wavelength modulations during the exponential growth phase. These modulations then rapidly developed into step-like structures having a thickness that was close to the horizontal wavelength of the fastest-growing mode. Over time, horizontal disturbances in each layer became visible, the disturbances having the same horizontal

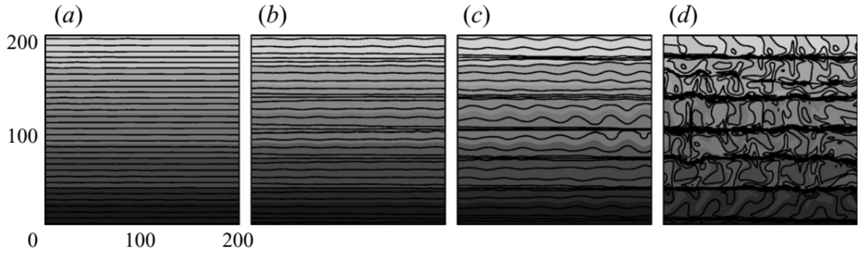

Figure 3.2: Snapshots of net density distribution at four different times in the DNS simulation of Noguchi and Niino (2010a), showing the formation of discrete layers. Corresponds to Figure 9 in Noguchi and Niino (2010a)

wavelength as that of the fastest-growing elevator modes. The amplitudes of these disturbances continued to grow and eventually resulted in overturning and subsequent mixing within the layers. Note that this produced strongly stratified interfaces between the layers. Over time, the layers were observed to merge into successively larger layers, each being supported by convective motions within the layer that resembled Rayleigh-Bénard convection.

The nonlinear interactions of modes in the DNS were analysed to find a set of modes that play principal roles in the formation of layers. That is, the governing equations were Fourier-transformed and used to determine ‘energy transfer functions’ which represented nonlinear-interactions between modes. These were evaluated in the exponential growth phase, just before the explosive growth phase.

The first mode to emerge during the exponential growth phase corresponded to the fastest-growing elevator mode from linear theory. The elevator mode is entirely horizontally dependent, so we refer to it herein as a $(1, 0)$ mode. This $(1, 0)$ elevator mode was observed to interact with a $(1, 1)$ ‘cellular mode’, and a $(0, 1)$ ‘layering’ mode. The $(1, 1)$ cellular mode had horizontal and vertical structure, while the $(0, 1)$ layering mode had entirely vertical structure. A fourth mode—the $(0, 2)$ layering mode—was observed to interact only with the $(0, 1)$ cellular mode.

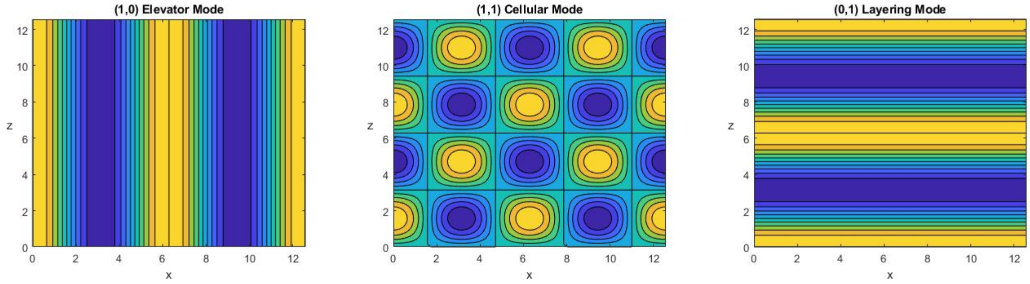

Figure 3.3: Schematic diagrams showing contours of streamfunction, psi for LEFT: a $(1, 0)$ elevator mode; MIDDLE: a $(1, 1)$ cellular mode; and RIGHT: a $(0, 1)$ layering mode (a $(0, 2)$ layering mode looks the same as a $(0, 1)$ layering mode but with half the vertical wavenumber).

Figure 3.3 shows schematic diagrams of these modes in terms of the streamfunction perturbation, ψ (though the shapes of the contours equally apply to the temperature, T, and salinity, S perturbations). The $(1, 0)$ elevator mode looks like columnar convection, with adjacent 'elevators' travelling in opposite directions. The $(1, 1)$ cellular mode is so named as it comprises cells of rotating fluid (or, equally, of T and S hotspots). The $(0, 1)$ layering mode comprises layers of horizontally-moving jets (or banded regions of T and S). The $(0, 2)$ layering mode is the same but with half the wavelength. It is worth noting here that the resolution of modes is insufficient to produce well-defined interfaces between layers in the $(0, 1)$ and $(0, 2)$ layering modes, or in combinations thereof. This is addressed in § 3.6 when we discuss the modal evolutions in our novel systems.

Figure 7 of NN shows that the $(1, 0)$ elevator mode was dominant soon after initiation of the simulation. This eventually gave way to the $(1, 1)$ cellular and $(0, 1)$ and $(0, 2)$ layering modes, which dominated at the start of the exponential growth phase. We note that the wavelength of the $(0, 2)$ layering mode was found to match the layer depth after the explosive growth phase shown in Figure 3.2(d). This means that the emergence of a $(0, 2)$ mode in a low-order model of the system may be indicative of layer formation in the system.

Truncated Spectral Model

A truncated spectral model was then produced by NN considering only the four modes identified. The form of the truncation was not explicitly stated but appears to be given by

$$\eta = A(t)e^{i(kx)} + B(t)e^{i(kx+mz)} + C(t)e^{i(mz)} + D(t)e^{i(2mz)} + c.c. \tag{3.5}$$

where *c.c.* stands for complex conjugate. In this way, each combination of trigonometric functions was included in the formulation. For instance, the formulation includes two elevator modes, $\cos(kx) + \sin(kx)$, four cellular $(1, 1)$ modes, and so on, leading to a potential maximum of 30 modes. This is in contrast to system (3.4), in which only the $\cos(kx)\sin(mz)$ term was included for the streamfunction and the system had a maximum of 5 modes.

In email correspondence, Noguchi, one of the authors of the NN paper, noted to us that many of the 30 modes are actually degenerate, resulting in a 12th-order system of equations. As we show later, it may not be necessary even to include all 12 of these modes to reproduce behaviour observed in numerical simulations.

The wavenumbers (k, m) of these modes were taken from the results of the DNS when $\gamma = 0.88$ ($R_\rho^{-1} = 1.136$): $(0.19, 0)$ for the $(1, 0)$ elevator mode; $(0.19, 0.09)$ for the $(1, 1)$ cellular mode; $(0, 0.09)$ for the $(0, 1)$ layering mode; and $(0, 0.18)$ for the $(0, 2)$ layering mode. Note that the value of $k = 0.19$ in the $(1, 0)$ elevator mode is the same as that of the fastest-growing elevator mode when $\gamma = 0.8$, as would be expected. The $(0, 2)$ layering mode has a value of $m = 0.18$, which is approximately the same as the horizontal wavelength of the $(0, 1)$ elevator mode. Intial conditions for $|A| = 10^{-1}$ and $|B| = 10^{-3}$ were taken from the DNS simulation at the start of the exponential growth stage, while $|C| = |D| = 0$ since they are decaying modes according to linear theory and do not exist at the initial time.

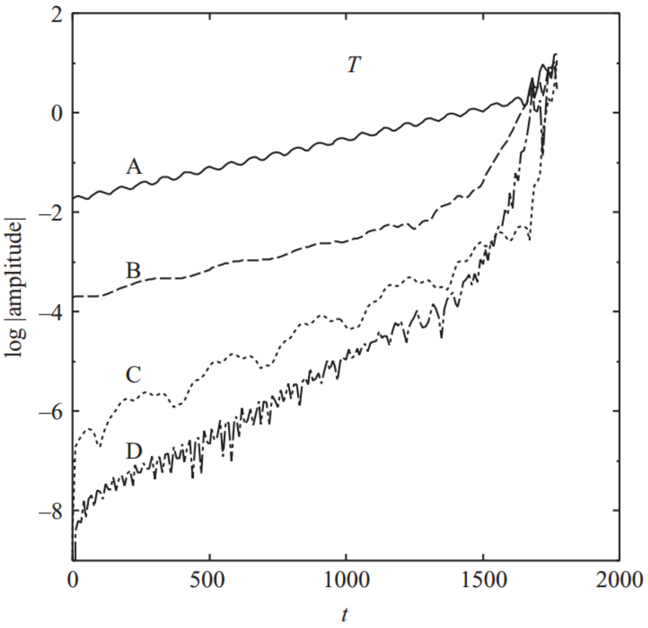

Figure 3.4: Time evolution of the amplitude of the temperature perturbation in the system studied by Noguchi and Niino (2010a)

NN solved the resulting ODE system and obtained the plot shown in Figure 3.4. This plot shows the amplitude of modes in the temperature perturbation over time. Initially, the $(0, 1)$ elevator mode (mode 'A' in Figure 3.4) and the $(1, 1)$ cellular mode (mode 'B'in Figure 3.4) grow at nearly the same rate as that predicted by linear theory, whereas the $(0, 1)$ and $(0, 2)$ layering modes (modes 'C' and 'D' in Figure 3.4) are excited through nonlinear interactions and grow faster than the $(1, 0)$ elevator and $(1, 1)$ cellular modes.

Eventually, the $(0, 1)$ and $(0, 2)$ layering modes grow rapidly to reach the same order of amplitude as the $(0, 1)$ elevator and $(1, 1)$ cellular modes. It is not clear from Figure 3.4, but, according to the authors, the $(0, 2)$ layering mode is eventually observed to overtake the other modes to become the dominant mode.

3.4.2 Novel Systems

We here use similar methods to those employed by Veronis (1965) and, subsequently, (Da Costa et al., 1981), to obtain novel low-order systems which behave in a similar way to the system modelled by NN. In contrast to (Veronis, 1965), we here start with a baseline cellular $(1,1)$ mode in each of the perturbations and introduce an elevator $(1,0)$ mode of the form given by equation (2.42), i.e.

$$\begin{aligned} \psi &= a_1 \cos(kx) + a_2 \sin(kx)\sin(mz), \\ T &= b_1 \sin(kx) + b_2 \cos(kx)\sin(mz), \\ S &= c_1 \sin(kx) + c_2 \cos(kx)\sin(mz), \end{aligned}$$

The $(1,0)$ elevator modes are represented by either $\cos(kx)$ or $\sin(kx)$. The remaining modes are $(1,1)$ cellular modes. The addition of elevator modes changes how the modes interact nonlinearly in the governing equaions. That is, on substitution of the above perturbations into the governing equations (4.24)–(4.26), nonlinear interactions in the Jacobian terms generate higher harmonics. We limited the higher harmonics to those arising within the 'triangular' truncation of $K+M = 2$, as described hereinbefore.

In each perturbation, the baseline elevator mode can optionally be 'aligned' or 'misaligned' with the x-component of the respective cellular mode. In the case above, the streamfunction elevator mode takes the form $\psi_E = \sin(kx)$, while the corresponding cellular mode takes the form $\psi_C = \cos(kx)$, and hence this system is 'misaligned'.

This choice heavily influences the form of the resulting truncated system. Indeed, we see that when both aligned and misaligned modes are included, the resulting behaviour is most similar to the misaligned system, which suggests that this is the preferred arrangement.

This will be discussed further in the following sections, in which we detail the systems arising from the different truncations. These include: a ninth-order order system generated using misaligned modes; a tenth-order system generated using aligned modes; and a 17th-order system generated using a combination of aligned and mis-aligned modes.

Ninth-order system

We begin by noting that, in this Chapter, we employ notation which is similar to that employed by Da Costa et al. (1981) and Noguchi and Niino (2010a), for convenience and ease of comparison. Thus, we here make the following substitutions to the notation used in Chapter 2 (and subsequently in Chapters 4 and 5): $R_\rho = \gamma$; $Pr = \sigma$; $k_x = k$; and $k_z = m$, where k_x and k_z are horizontal (x) and vertical (z) wavenumbers, respectively. We also define $r_T = 1$ and $r_S = \gamma$, in order to facilitate a comparison of our equations with those of Veronis (1965) and Da Costa et al. (1981).

Substituting the misaligned perturbations above into the governing equations (4.24)–(4.26), we obtain the following set of expansions, using the above notation:

$$\begin{aligned}
\psi &= a_1 \cos(kx) + a_2 \sin(kx)\sin(mz) + a_3 \cos(mz), \\
T &= b_1 \sin(kx) + b_2 \cos(kx)\sin(mz) + b_3 \sin(2mz), \\
S &= c_1 \sin(kx) + c_2 \cos(kx)\sin(mz) + c_3 \sin(2mz).
\end{aligned}$$

This set of equations comprises 9 modes. The modes coloured red correspond to those used in the Veronis system. Note that unlike in the NN system, no $(0, 2)$ layering mode is generated here in the streamfunction expansion, and no $(0, 1)$ layering mode appears in the temperature or salinity expansions. Substituting these modal equations back into the non-dimensional system and neglecting higher harmonics results in the following ninth-order system of ODEs:

$$
\begin{aligned}
a_1' &= -\frac{\sigma}{k}(r_T b_1 - r_S c_1 + a_1 k^3) - \frac{1}{2}kma_2a_3,\\
a_2' &= \frac{1}{p}(\sigma(r_T k b_2 - r_S k c_2 - p^2 a_2) + (k^3 m - km^3)a_1a_3),\\
a_3' &= -\sigma m^2 a_3 + \frac{1}{2}kma_1a_2,\\
\\
b_1' &= -b_1k^2 + \frac{1}{2}kma_3b_2 - ka_1,\\
b_2' &= km(a_2b_3 - a_3b_1) - pb_2 + ka_2,\\
b_3' &= -4b_3m^2 - \frac{1}{2}kma_2b_2,\\
\\
c_1' &= -\tau c_1k^2 + \frac{1}{2}kma_3c_2 - ka_1,\\
c_2' &= km(a_2c_3 - a_3c_1) - \tau pc_2 + ka_2,\\
c_3' &= -4\tau c_3m^2 - \frac{1}{2}kma_2c_2,
\end{aligned}
\tag{3.6}
$$

where $p = (k^2 + m^2)$.

Tenth-order system

The form of the perturbations in the ‘aligned’ system is as follows:

$$
\begin{aligned}
\psi &= a_1\cos(kx) + a_2\cos(kx)\sin(mz),\\
T &= b_1\sin(kx) + b_2\sin(kx)\sin(mz),\\
S &= c_1\sin(kx) + c_2\sin(kx)\sin(mz).
\end{aligned}
$$

Substituting these modal equations into the governing equations (4.24)–(4.26) results in the generation of a $(0,1)$ mode and a $(0,2)$ mode in the T and S perturbations, but no layering modes at all in the ψ perturturbation:

$$
\begin{aligned}
\psi &= a_1 \sin(kx) + a_2 \sin(kx) \sin(mz), \\
T &= b_1 \cos(kx) + b_2 \cos(kx) \sin(mz) + b_3 \cos(mz) + b_4 \sin(2mz), \\
S &= c_1 \cos(kx) + c_2 \cos(kx) \sin(mz) + c_3 \cos(mz) + c_4 \sin(2mz).
\end{aligned}
$$

Again, the modes coloured in red are those present in the Veronis system. Substituting the 10 modes above into the non-dimensional system and neglecting higher harmonics results in the tenth-order system of ODEs shown below, with $p = (k^2 + m^2)$.

$$
\begin{aligned}
a_1' &= \frac{\sigma}{k}(r_T b_1 - r_S c_1 - a_1 k^3), \\
a_2' &= \frac{1}{p}(\sigma(r_T k b_2 - r_S k c_2 - p^2 a_2),
\end{aligned}
$$

$$
\begin{aligned}
b_1' &= -b_1 k^2 - \frac{1}{2} k m a_2 b_3 + k a_1, \\
b_2' &= -km(a_2 b_4 + a_1 b_3) - p b_2 + k a_2, \\
b_3' &= -b_3 m^2 + \frac{1}{2} km(a_1 b_2 + a_2 b_1), \\
b_4' &= -4 b_4 m^2 + \frac{1}{2} k m a_2 b_2,
\end{aligned}
$$

$$
\begin{aligned}
c_1' &= -\tau c_1 k^2 - \frac{1}{2} k m a_2 c_3 + k a_1, \\
c_2' &= -km(a_2 c_4 + a_1 c_3) - \tau p c_2 + k a_2, \\
c_3' &= -\tau c_3 m^2 + \frac{1}{2} km(a_1 c_2 + a_2 c_1). \\
c_4' &= -4\tau c_4 m^2 + \frac{1}{2} k m a_2 c_2,
\end{aligned}
$$

17th-order system

Including both $\cos(kx)$ and $\sin(kx)$ terms in combination with a single cellular term in each of the ψ, T and S perturbations results in the generation of additional cellular $(1,1)$ and layering $(0,1)$, $(0,2)$ modes. The resulting expansions are as follows:

$$\psi = a_1\cos(kx) + a_2\sin(kx) + a_3\cos(kx)\sin(mz) + a_4\sin(kx)\sin(mz) \\ + a_5\cos(mz) + a_6\sin(2mz),$$

$$T = b_1\cos(kx) + b_2\sin(kx) + b_3\cos(kx)\sin(mz) + b_4\sin(kx)\sin(mz) \\ + b_5\cos(mz) + b_6\sin(2mz),$$

$$S = c_1\cos(kx) + c_2\sin(kx) + c_3\cos(kx)\sin(mz) + c_4\sin(kx)\sin(mz) \\ + c_5\cos(mz) + c_6\sin(2mz).$$

The modes coloured red are present in the Veronis system. The grey-coloured $(0, 2)$ layering mode in the streamfunction perturbation emerges only as a result of nonlinear interactions with even higher-order modes, which are excluded in our truncation. Thus, this mode makes no contribution to the overall dynamics..

Computing the resulting ODE system from the above equations is a relatively lengthy and potentially error-prone process. Therefore, we developed a 'Maple' program which first identifies any additional terms that are generated for a given level of truncation (e.g. $K + M = 2$ in this case), and then computes the resulting system of ODEs.

The output of the Maple program may be copied and pasted directly into MATLAB. This has the benefit that, if desired, we may include more terms in the original truncation, for example a $(0, 2)$ mode in the streamfunction expansion which is never generated otherwise. Furthermore, we are now able to quickly and reliably obtain ODE systems of 17th-order and higher. The Maple program was verified against hand-calculated versions of the Da Costa et al. system, the 9th-order system and the 10th-order system derived here.

The resulting 17th-order system is is follows:

$$\begin{aligned}
a_1' &= \frac{\sigma}{k}(r_T b_2 - r_S c_2 - a_1 k^3) - \frac{1}{2}kma_4a_5,\\
a_2' &= -\frac{\sigma}{k}(r_T b_1 - r_S b_2 + a_2 k^3) + \frac{1}{2}kma_3a_5,\\
a_3' &= \frac{1}{p}(\sigma(r_T k b_4 - r_S k c_4 - Qa_3) - (mk^3 - km^3)a_2a_5,\\
a_4' &= -\frac{1}{p}(\sigma(r_T k b_3 - r_S k c_3 - Qa_4) - (mk^3 - km^3)a_1a_5),\\
a_5' &= -\sigma m^2 a_5 + \frac{1}{2}km(a_1a_4 - a_2a_3),
\end{aligned}$$

$$\begin{aligned}
b_1' &= -b_1k^2 + \frac{1}{2}km(a_4b_5 - a_5b_4) - ka_2,\\
b_2' &= -b_2k^2 + 12km(a_5b_4 - a_3b_5) + ka_1,\\
b_3' &= km(a_2b_5 - a_5b_2 + a_4b_6) - pb_3 - ka_4,\\
b_4' &= km(-a_1b_5 + a_5b_1 - a_3b_6) - pb_4 + ka_3,\\
b_5' &= -b_5m^2 + \frac{1}{2}km(a_1b_4 - a_2b_3 + a_3b_2 - a_4b_1),\\
b_6' &= -4b_6m^2 + \frac{1}{2}km(a_3b_4 - a_4b_3),
\end{aligned}$$

$$\begin{aligned}
c_1' &= -\tau c_1k^2 + \frac{1}{2}km(a_4c_5 - a_5c_4) - ka_2,\\
c_2' &= -\tau c_2k^2 + 12km(a_5c_4 - a_3c_5) + ka_1,\\
c_3' &= km(a_2c_5 - a_5c_2 + a_4c_6) - \tau pc_3 - ka_4,\\
c_4' &= km(-a_1c_5 + a_5c_1 - a_3c_6) - \tau pc_4 + ka_3,\\
c_5' &= -\tau c_5m^2 + \frac{1}{2}km(a_1c_4 - a_2c_3 + a_3c_2 - a_4c_1),\\
c_6' &= -\tau 4c_6m^2 + \frac{1}{2}km(a_3c_4 - a_4c_3),
\end{aligned}$$

where $p^2 = (k^2 + m^2)$. The 17th-order system reduces to the 9th- and 10th-order systems when the amplitudes of approriate modes are neglected. For example, we may obtain the 9th-order system by setting a_1, a_3, b_2, b_4, b_5, c_2, c_4, and c_5 to zero.

3.4.3 Implementation

We integrate the above sets of ODEs using MATLAB. The function '`ode45`' integrates a given ODE system using a variable time step, 4th/5th order Runge-Kutta method. Relative and absolute tolerances can be defined which adjust the time step based on the solution at a given point. That is, the time step is adjusted automatically based on errors calculated at each step of the simulation, and the tolerances can be changed to improve the accuracy of the simulation. For our solutions, the default relative ('RelTol') and absolute ('AbsTol') tolerances are $\mathrm{RelTol} = 10^{-3}$ and $\mathrm{AbsTol} = 10^{-6}$.

We have developed a MATLAB program which solves the different sets of equations over a user-selected parameter range, primarily using `ode45`. In the following section (§3.5), we initially check that our results are sensible by comparing the growth rate of the elevator modes with the growth rate obtained using linear theory. Further verification is achieved by comparing the results against an analytical model which we derive in §3.5. We also study the effects of changing the timestep, the simulation tolerance, and the order of the Runge-Kutta method used to solve the equations.

3.5 Verification

We derive a set of equations describing an energy balance in each the system, which we can use to verify our MATLAB code, and to check the accuracy of the MATLAB `ode45` solver. We first derive such a model for the simpler Da Costa et al. (1981) system to ensure that this method is appropriate.

3.5.1 Da Costa et al. System

To recap, the Da Costa et al. system is given by,

$$\begin{aligned}
a' &= \sigma[-a + r_T b - r_S d], \\
b' &= -b + a(1-c), \\
c' &= \varpi[-c + ab], \\
d' &= -\tau d + a(1-e), \\
e' &= \varpi[-\tau e + ad].
\end{aligned} \tag{3.7}$$

For the LHS of the above equations, we multiply each variable by itself and a constant, before summing the respective terms together. The result can be reformulated using the chain rule to get,

$$Aaa' + Bbb' + Ccc' + Ddd' + Eee' = \frac{1}{2}\frac{d}{dt}[Aa^2 + Bb^2 + Cc^2 + Dd^2 + Ee^2], \tag{3.8}$$

where A, B, C, D and E are constants. This represents, essentially, a rate of change of energy in the system and can be evaluated numerically based on the values of variables at each step in the simulation. The RHS of equations (3.4) becomes:

$$\begin{aligned}
RHS = {} & (-\sigma Aa^2 + \sigma r_T Aab - \sigma r_S Aad) \\
& + (-Bb^2 + Bab - Babc) \\
& + (-\varpi Cc^2 + \varpi Cabc) \\
& + (-\tau Dd^2 + Dad - Dade) \\
& + (-\tau\varpi Ee^2 + \tau\varpi Eade).
\end{aligned}$$

We here define the constants A, B, C, D and E in such a way as to obtain a single equation for the rate of change of energy in the system. That is, we take,

$$A = -\frac{B}{\sigma r_T}, \qquad C = \frac{B}{\varpi}, \qquad D = -\gamma B, \qquad E = -\gamma B/\varpi,$$

where $\gamma = r_S/r_T$, to obtain the result

$$\frac{1}{2}\frac{d}{dt}[-\frac{1}{\sigma r_T}a^2 + b^2 + \frac{1}{\varpi}c^2 - \gamma d^2 - \frac{\gamma}{\varpi}e^2] = \frac{1}{rt}a^2 - b^2 - c^2 + \tau\gamma d^2 + \tau\gamma e^2. \tag{3.9}$$

Evaluating, *numerically*, the LHS and RHS of (3.9) at each time step in the simulation, we are able to plot the LHS and RHS against each other, over time. Qualitatively, this should yield a straight line (i.e. $LHS = RHS$). A more quantitative approach includes evaluating an error between the LHS and RHS over time.

We evaluate the time-derivative in the RHS of equation (3.9) using the so-called 'Fornberg Method'. This is a 4th-order finite difference scheme developed by Fornberg (1998) which assigns different weights to calculate derivatives of any order on both structured and unstructured grids using a relatively inexpensive algorithm.

Results

We simulated the governing equations of the Da Costa et al. (1981) system using `ode45`, taking RelTol $= 10^{-6}$ and AbsTol $= 10^{-9}$. Note that these tolerances are stricter than the MATLAB default of RelTol $= 10^{-3}$ and AbsTol 10^{-6}. This is because the Da Costa et al. (1981) system is, computationally, relatively inexpensive to simulate, so we may reasonably seek more accurate solutions.

The amplitudes of individual modes are plotted over time in Figure 3.5, reproducing the results found in the original paper by Da Costa et al. (1981). That is, we take $r_S = 0.5$, $r_T = 2.0$, where r_T and r_S are scaled thermal and solutal Rayleigh numbers R_T and R_S. This gives a value of $\gamma = 4$ and thus $R_\rho^{-1} = 0.25$ in our notation for a corresponding unbounded system. We see that our results are at least qualitatively

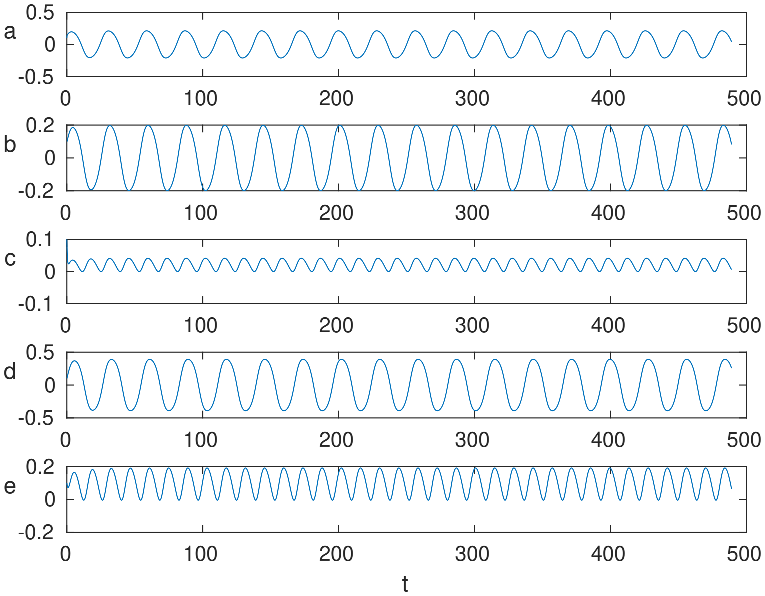

Figure 3.5: Variation of modes in the system of Da Costa et al. (1981) corresponding to Figure 2 thereof, wherein $\gamma = 4$, $r_T = 0.5$ and $r_S = 2.0$.

similar to those of Figure 2(a) in Da Costa et al. (1981); that is, the frequencies and amplitudes match in each case. Though not shown here, we reproduced other plots in the Da Costa et al. (1981) paper showing similarly good agreement.

Over the same period of time presented in Figure 3.5 we may evaluate the LHS and RHS of equation (3.9) and plot the results against one another, as shown in Figure (3.6). The straight line indicates that the LHS and RHS are equal, and that the simulation is accurate. We can quantify this by looking at the relative error,

$$E = \frac{LHS - RHS}{RHS}.$$

Figure (3.7) shows the error associated with the comparison plotted over time. We observe the average error to be around 10^{-6}, though at certain points in the simulation the error exceeds 10^{-3}. In order to determine the cause of these peaks, we overlay the location of each peak on a plot of the LHS over time in Figure (3.8).

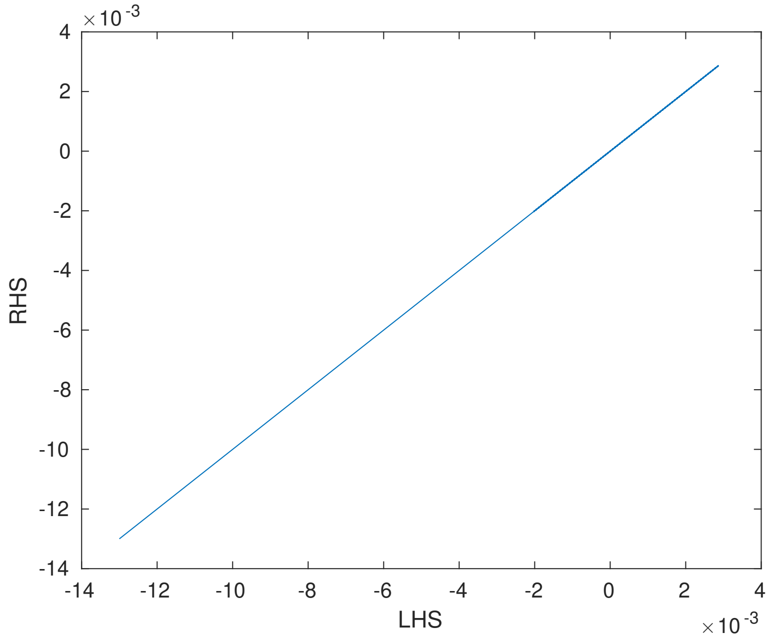

Figure 3.6: Comparison of LHS and RHS of the energy equation (3.9), over time for the Da Costa et al. (1981) system with $r_S = 0.5$ and $r_T = 2.0$.

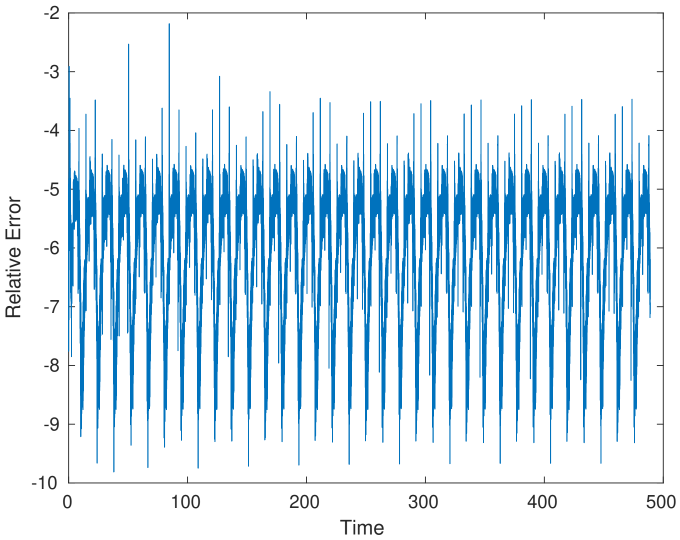

Figure 3.7: Relative error on a logarithmic scale between the LHS and RHS of the energy equation (3.9) for the Da Costa et al. (1981) system with $r_s = 0.5$ and $r_T = 2.0$.

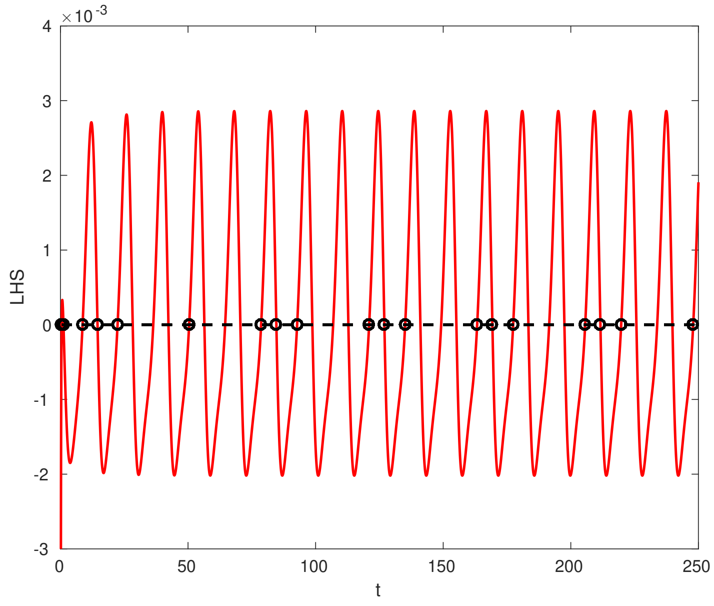

Figure 3.8: Locations of error peaks on a plot of the LHS of equation (3.9) vs. time for the system of Da Costa et al. (1981) with $r_s = 0.5$ and $r_T = 2.0$. Black circles represent the locations of error spikes.

A shorter period of time is shown here, for clarity. We see that the peaks only occur when both the LHS and RHS are relatively small, or close to zero. This means that the peaks in the relative error are likely more representative of the sensitivity of results when dividing by a small number, and are not especially representative of the accuracy of the simulation as a whole.

The relative and absolute tolerances employed by the `ode45` solver may be adjusted to study the effects on the error; however, this is later performed extensively in relation to the higher order systems and is not reproduced here.

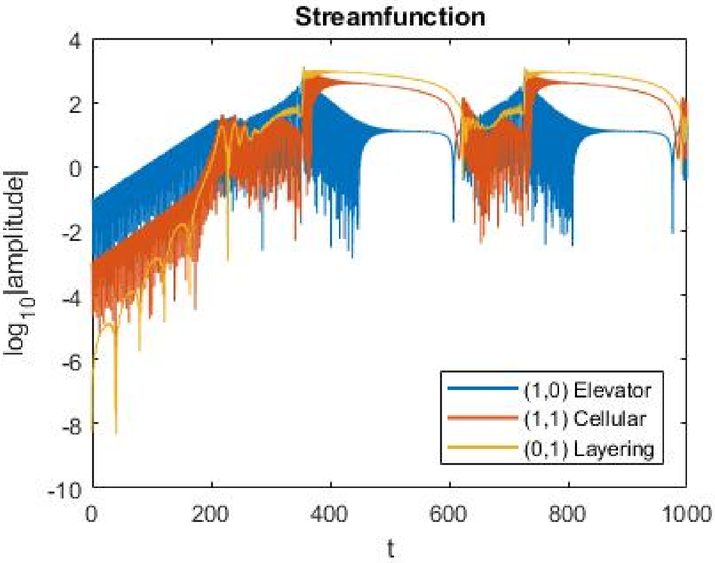

Figure 3.9: Evolution of the streamfunction perturbation in the 9th-order system when $\gamma = 0.9$ ($R_\rho^{-1} = 1.11$), $Pr = 7$, $\tau = 0.01$ and $(k, m) = (0.19, 0.09)$. We use tolerances of $\mathrm{RelTol} = 10^{-6}$, $\mathrm{AbsTol} = 10^{-9}$.

3.5.2 Ninth-order system

In order to validate the 9th-order system, we first run an initial simulation at a supercritical value of $\gamma = 0.9$. That is, we take $r_T = 1$ and $r_S = R_\rho^{-1} = 1/\gamma = 1.11$ in equations 3.6. This value of γ is taken to ensure that the system is fully unstable, and that we can investigate the accuracy of the simulation when amplitudes are large. The initial conditions and wavenumbers are the same as those used in NN; that is: $(k, m) = (0.19, 0.09)$; $a_1 = 10^{-1}$; $a_2 = 10^{-3}$; $\{b_1, c_1\} = 10^{-1.7}$; and $\{b_2, c_2\} = 10^{-2.7}$. These values were taken from the DNS simulation as the modes began to emerge at $t = 50$. The layering modes are initialised with zero amplitude.

Figure (3.9) shows the evolution of the amplitude of streamfunction modes over a time-period of $t = 1000$, with $\mathrm{RelTol} = 10^{-6}$, $\mathrm{AbsTol} = 10^{-9}$. A discussion of the behaviour of the modes is provided in § 3.6—at present, we are merely interested in the accuracy of the MATLAB ODE suite in modelling our equations. To summarise

Figure 3.9, the $(1,0)$ elevator and $(1,1)$ cellular modes begin by growing linearly and interact to excite the initially zero-amplitude $(0,1)$ layering mode. Once the modes reach substantially the same amplitude as one another, we see a rapid growth in the amplitudes of all modes, following which point the $(0,1)$ layering mode grows and dominates for around 250 non-dimensional units of time, t. The modes are then disrupted and the cycle repeats. Thus, we can reasonably limit our analysis here to just the first two 'peaks'.

The ninth-order system (3.6) was manipulated using the methods described in §3.5 to obtain a pseudo-energy equation for the system:

$$\begin{aligned}
&\frac{1}{2}\frac{d}{dt}[k^2a_1^2 + \frac{p}{2}a_2^2 \\
&\quad - \sigma r_T b_1^2 - \frac{\sigma r_T}{2}b_2^2 - \sigma r_T b_3^2 - \sigma r_T b_4^2 \\
&\quad - \sigma r_S c_1^2 + \frac{\sigma r_S}{2}c_2^2 + \sigma r_S c_3^2 + \sigma r_S c_4^2] = \\
&\quad - \sigma k^4 a_1^2 - \frac{\sigma p^2}{2}a_2^2 \\
&\quad + \sigma r_T k^2 b_1^2 + \frac{\sigma r_T p}{2}b_2^2 + 4\sigma r_T m^2 b_3^2 + \sigma r_T m^2 b_4^2 \\
&\quad - \tau\sigma r_S k^2 c_1^2 - \frac{\tau\sigma r_S p}{2}c_2^2 - 4\tau\sigma r_S m^2 c_3^2 - \tau\sigma r_S m^2 c_4^2
\end{aligned} \tag{3.10}$$

We can compare the LHS and RHS of equation (3.10) over time to investigate the error in the system. We can also investigate the effects of lower- and higher-order Runge-Kutta methods on the results, along with the effect of changing the time step and the tolerances.

Figure (3.10) shows a comparison of the LHS and RHS of equation (3.10) for the simulation shown in Figure (3.9), along with a plot of the relative error between the two calculations. The comparison plot shows a linear relationship between the two sides of the energy balance equation, indicating good agreement. The error plot shows that the average error is of $\mathcal{O}(10^{-5})$ during the exponential growth phase. As the solutions grow in amplitude and the layering mode overtakes at approximately $t = 350$, the error

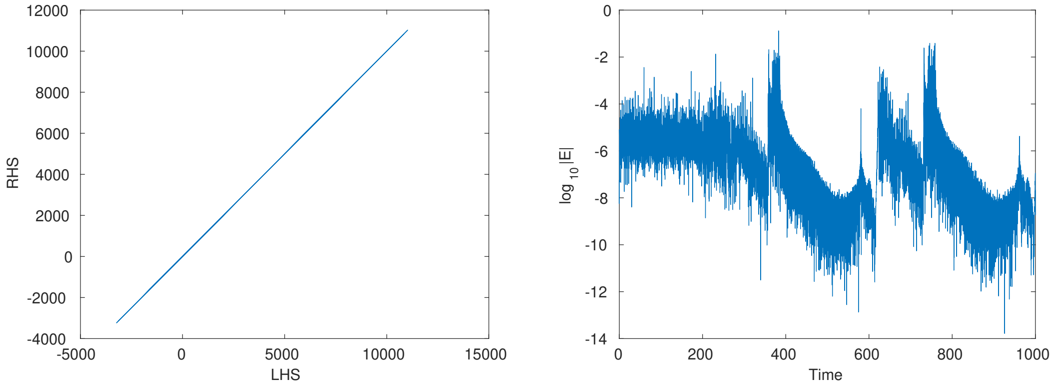

Figure 3.10: Relative error between the LHS and RHS of the energy balance equation (3.10) in the 9th-order system when $\gamma = 0.9$, $Pr = 7$, $\tau = 0.01$, $(k, m) = (0.19, 0.09)$, RelTol $= 10^{-6}$, and AbsTol $= 10^{-9}$.

jumps to approximately $\mathcal{O}(10^{-2})$. The lowest errors occur during the 'layering' stage, as modal amplitudes reduce and the error drops below 10^{-8}.

Figure (3.11) shows the change in the time-step, δt, throughout the simulation. The smallest time-step observed is $\delta t = 0.001$, which occurs during periods of largest modal amplitude (and maximum relative error). The time step is unable to reduce below this value in the variable-order scheme using the prescribed tolerances. Although not shown here, if we tighten the tolerances to RelTol $= 10^{-9}$ and AbsTol $= 10^{-12}$, the minimum time step is reduced to $\delta t = 0.0005$ and increases the accuracy accordingly.

In another example, we more directly study the effects of reducing the time-step, along with the effect of changing the order of the Runge-Kutta (RK) method, by temporarily employing a fixed time-step solver. That is, we take a relatively low, fixed time-step of $\delta t = 0.01$ and then reproduce the 9th-order simulation shown in Figure 3.9 using four different Runge-Kutta schemes of 2nd-order (RK2), 3rd-order (RK3), 4th-order (RK4) and 5th-order (RK5). Figure (3.12) shows the error between the LHS vs. RHS of the energy balance equation (3.10) for the RK2, RK3, RK4, and RK5 simulations. We

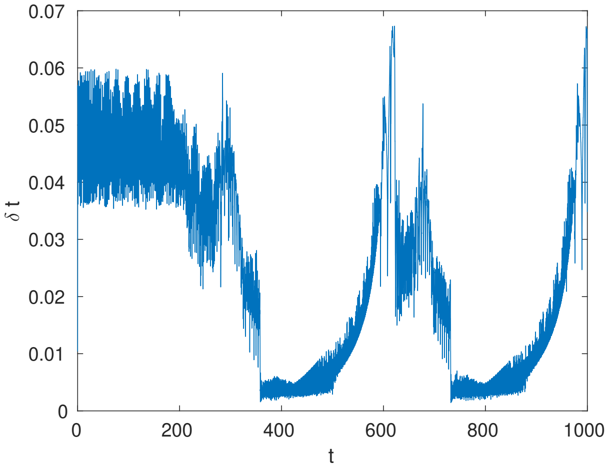

Figure 3.11: Change in time step δt over time t in the simulation used to produce Figure 3.9, when $\gamma = 0.9$, $Pr = 7$, $\tau = 0.01$ and $(k, m) = (0.19, 0.09)$. Results were obtained using RelTol $= 10^{-6}$ and AbsTol $= 10^{-9}$.

see that simulations using RK2 and RK3 are not sufficiently accurate when $\delta t = 0.01$, as both have $\mathcal{O}(10)$ errors at the point when the layering mode first dominates (the 'peak'). However, in the linear phase and the layered phase the errors are still relatively low. This suggests that the most difficult part to simulate is when the solutions 'peak'.

Increasing the order from RK4 to RK5 has very little impact on the solution at this time step. Taking RK4 as a baseline, Figure (3.13) shows the results as the time-step is reduced from 10^{-1} to 10^{-4} using the RK4 method. We see that as the time-step is reduced, the simulation becomes more accurate, as would be expected. Taking $\delta t = 0.1$, the peaks in the relative error are of the order 10^4, while the mean error during the exponential growth phase remains relatively low, at an order of 10^{-4}. At $\delta t = 0.01$, the amplitude of each error peak has reduced, but the errors are still unacceptably large. At $\delta t = 0.001$, the error peaks each drop below 10^{-4}, which we consider appropriate for an accurate simulation. Reducing the time-step further has little effect on the solution, most likely because the lowest error is now approaching machine precision.

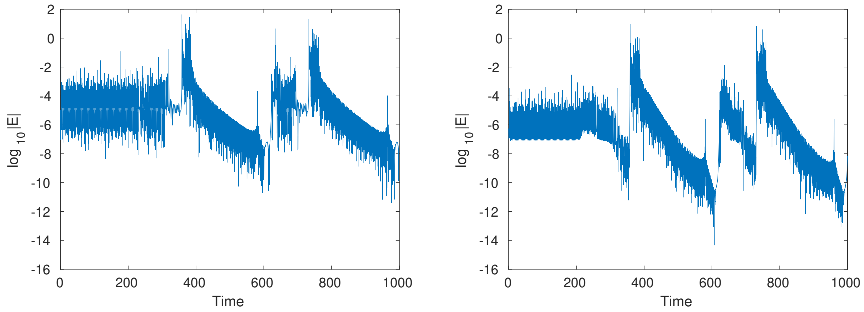

(a) RK2 (b) RK3

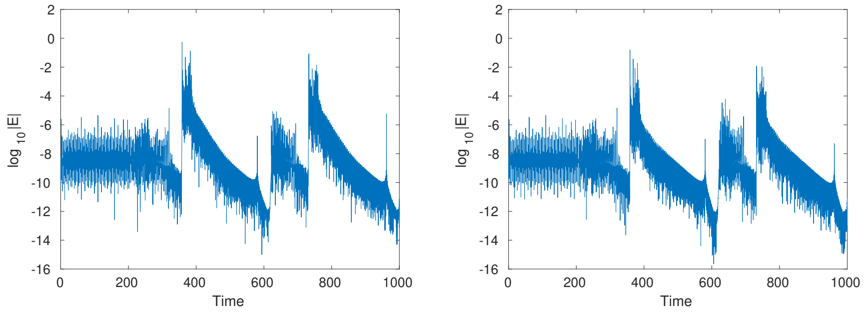

(c) RK4 (d) RK5

Figure 3.12: Relative error between the LHS and RHS of equation 3.10 in the 9th-order system with $\gamma = 0.9$, $Pr = 7$, $\tau = 0.01$, and $(k, m) = (0.19, 0.09)$. The results were obtained using fixed $\delta t = 0.01$ as the order of the Runge-Kutta scheme was increased from 2 to 4.

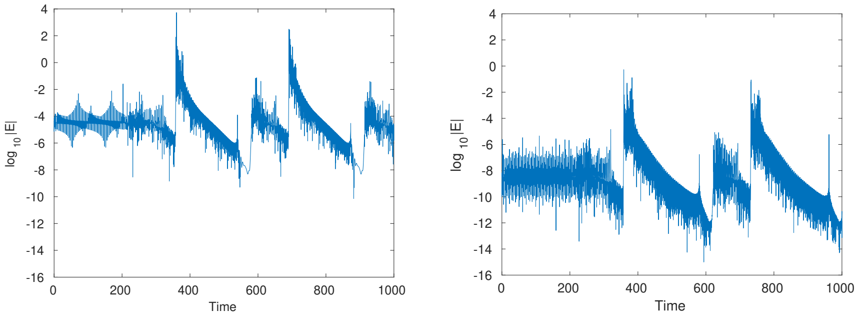

(a) $\delta t = 0.1$ (b) $\delta t = 0.01$

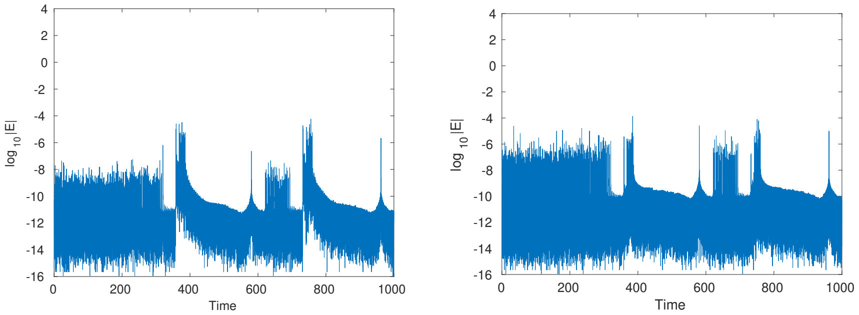

(c) $\delta t = 0.001$ (d) $\delta t = 0.0001$

Figure 3.13: Relative error over time t in simulations of the 9th-order system, when $\gamma = 0.9$, $Pr = 7$, $\tau = 0.01$, and $(k, m) = (0.19, 0.09)$. The results were obtained using a 4th-order Runge-Kutta scheme. δt is reduced from $\delta t = 0.1$ to $\delta t = 0.0001$.

We note that the error fluctuations in Figure (3.13d), i.e. when $\delta t = 0.001$, are generally of greater amplitude than when larger time steps are taken. This is likely due to an increased number of steps, leading to an increased likelihood that a solution will pass closer to zero on each oscillation.

It is useful to look at both the average error and the maximum error over the entire simulation for numerous values of δt. These are shown in Figure 3.14. The curves exhibit a comparable reduction in error with reduced time-step size. The average error begins to level out at $\delta t = 10^{-2.5}$, which is consistent with the plots in Figure (3.13), and indicates that the error approaches that of machine precision at this point. The error associated with the RK4 method is given by:

$$E = A(\delta t^4)$$

where A is a constant. Thus, taking logs of both sides, the error should be,

$$\log_{10} E = \log_{10} A + 4 \log_{10} \delta t,$$

and hence the gradient in Figure (3.14) should be 4. We find that, in the straight portion of the ‘average’ curve, the gradient is 3.78, which is relatively near. The difference may be attributed to the regular peaks observed in the numerical data as the values of LHS and RHS pass close to zero. More of these peaks exist as the time step is reduced, and hence the average is slightly higher than it should be at lower time steps.

As a final note on this topic, the simulations for $\delta t = 10^{-3}$ take approximately 10 seconds to run. Reducing the time step to $\delta t = 10^{-4}$ increases run-time by a factor of 10, as there are 10 times the number of calculation steps. However, we see that the largest errors are only observed during peaks, and the solutions obtained during the linear phase and layered phases were seen to be fairly accurate even when using a large time-step. Therefore, we herein use the more efficient variable time-step, variable order RK4/5 method for our simulations, and adjust the tolerances accordingly.

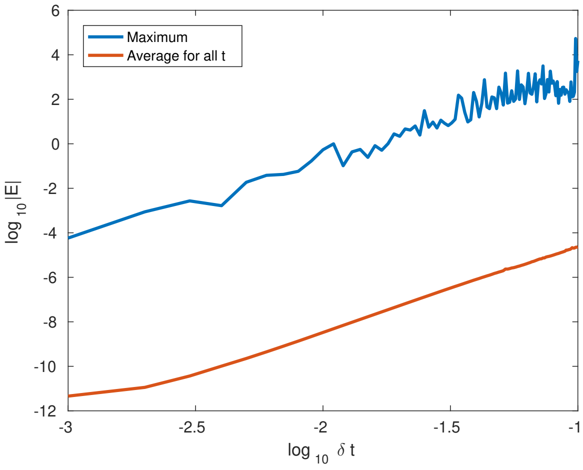

Figure 3.14: Maximum and average error against δt in the 9th-order system, with $\gamma = 0.9$, $Pr = 7$, $\tau = 0.01$, and $(k, m) = (0.19, 0.09)$. The results were obtained using a 4th-order Runge-Kutta scheme.

3.5.3 Tenth-order system

The tenth-order system, given by the equations in Section 3.4.2, was manipulated in the same way as the ninth-order system. The energy equation resulting from the manipulation was found to be,

$$\begin{aligned}\frac{1}{2}\frac{d}{dt}[k^2a_1^2 + \frac{p}{2}a_2^2 - \sigma r_T b_1^2 - \frac{\sigma r_T}{2}b_2^2 - \sigma r_T b_3^2 - \sigma r_T b_4^2 - \sigma r_S c_1^2 + \frac{\sigma r_S}{2}c_2^2 + \sigma r_S c_3^2 + \sigma r_S c_4^2]\\ = -\sigma k^4 a_1^2 - \frac{\sigma Q}{2}a_2^2 + \sigma r_T k^2 b_1^2 + \frac{\sigma r_T p}{2}b_2^2 + 4\sigma r_T m^2 b_3^2 + \sigma r_T m^2 b_4^2\\ - \tau\sigma r_S k^2 c_1^2 - \frac{\tau\sigma r_S p}{2}c_2^2 - 4 - \tau\sigma r_S m^2 c_3^2 - \tau\sigma r_S m^2 c_4^2. \qquad (3.11)\end{aligned}$$

We show in Figure (3.15) two examples of the modal evolution of temperature perturbation at $\gamma = 0.9$, using a) default tolerances of RelTol $= 10^{-6}$, AbsTol $= 10^{-9}$, and b) tighter tolerances of RelTol $= 10^{-9}$, AbsTol $= 10^{-12}$. The more accurate simulation, on the right, shows different behaviour following each peak than that on the left.

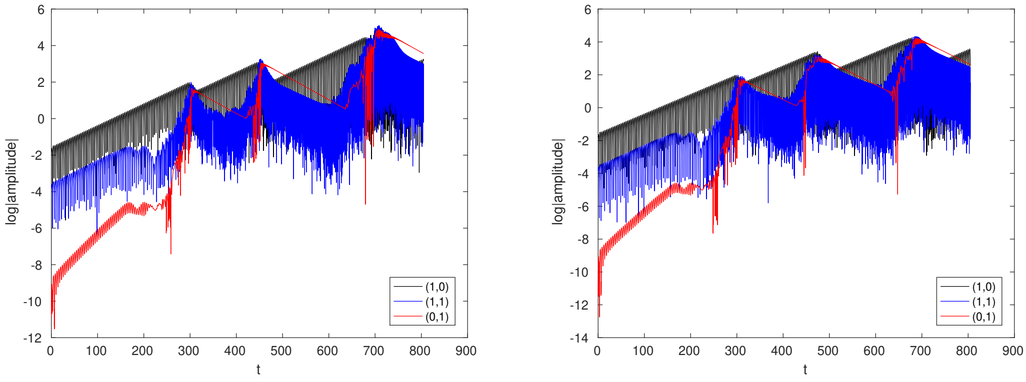

(a) RelTol $= 10^{-6}$, AbsTol $= 10^{-9}$ (b) RelTol $= 10^{-9}$, AbsTol $= 10^{-12}$

Figure 3.15: Temperature evolution in the 10th-order system with $\gamma = 0.9$, $Pr = 7$, $\tau = 0.01$, and $(k, m) = (0.19, 0.09)$. The results on the left and right sides were obtained using different tolerances.

We show in Figure (3.16) plots of the error between LHS and RHS of equation (3.11) corresponding to the results shown in Figures 3.15a and 3.15b. Firstly, we notice that the 10th-order system behaves quite differently to the 9th-order system, which will be discussed further in § 3.6. Secondly, we see that the relative error at certain times reaches almost 10^4 when using default tolerances, and exceeds 10^{-2} even when using the tighter tolerances. This was initially thought to be because the modal amplitudes exceed $\mathcal{O}(10^4)$ in this case, whereas in the 9th-order system the amplitudes of modes reached a maximum of order 10^3. Indeed, we see that in the 10th-order system the error increases at each successively larger peak, implying that the errors are higher at higher amplitudes; however, this phenomenon may be specific to the 10th-order system. As we discuss further in § 3.6.2, we find that the error is caused by an oscillatory mode whose frequency appears to increase monotonically with the amplitude of other modes.

Figure (3.17) shows the change in time-step δt for the simulation shown in Figure 3.15b using the stricter tolerances, along with a plot highlighting the change in time step from $t = 600$ to $t = 800$ in more detail. It can be seen that the time step reduces

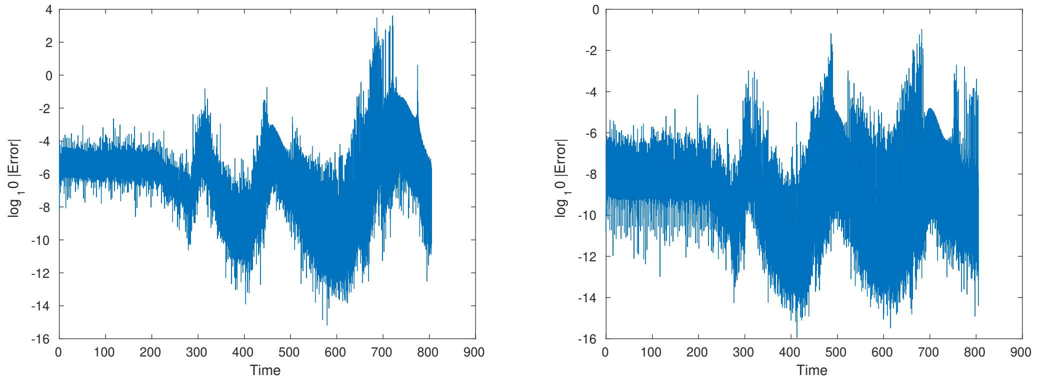

(a) RelTol = 10^{-6}, AbsTol = 10^{-9} (b) RelTol = 10^{-9}, AbsTol = 10^{-12}

Figure 3.16: Relative error in the 10th-order simulation with $\gamma = 0.9$, $Pr = 7$, $\tau = 0.01$, and $(k, m) = (0.19, 0.09)$. The results on the left and right sides were obtained using different tolerances.

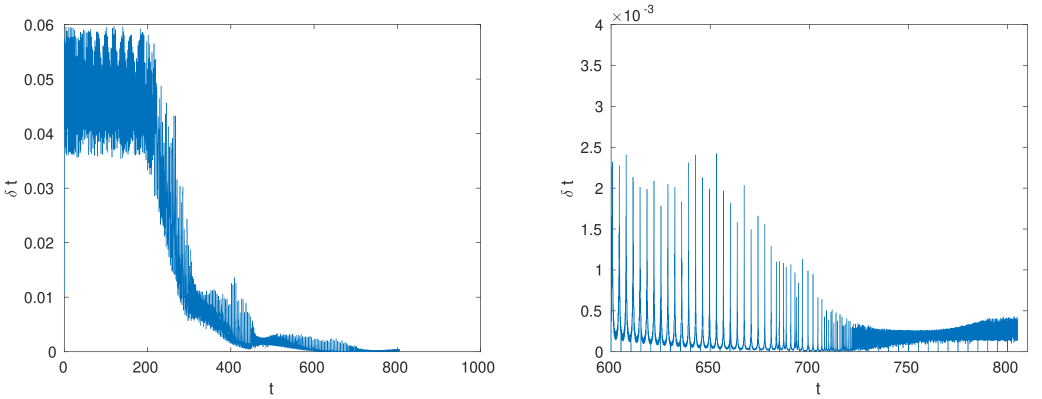

Figure 3.17: Change in time-step in the 10th-order system with $\gamma = 0.9$, with $\gamma = 0.9$, $Pr = 7$, $\tau = 0.01$, and $(k, m) = (0.19, 0.09)$. The results were obtained with RelTol = 10^{-9} and AbsTol = 10^{-12} over the period a) $t = 0$ to $t = 1000$, and b) $t = 600$ to $t = 800$.

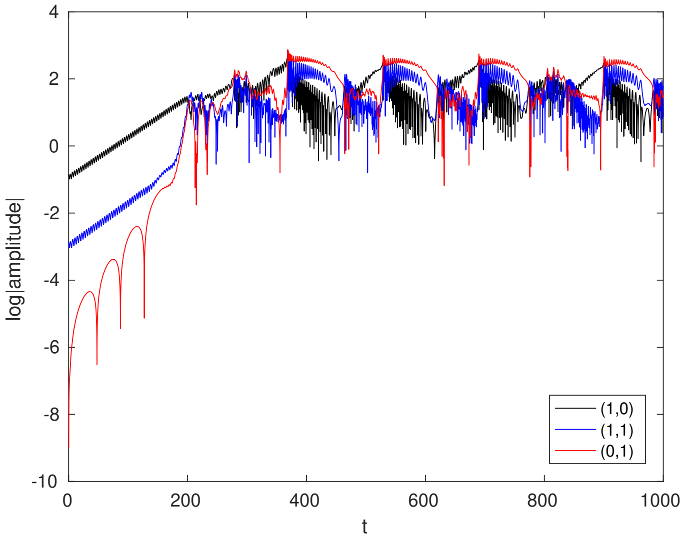

Figure 3.18: Evolution of the streamfunction modes, ψ', in the 17th-order system when $\gamma = 0.9$, $Pr = 7$, $\tau = 0.01$, and $(k, m) = (0.19, 0.09)$. The results were obtained using a fourth-order Runge Kutta scheme having a constant time-step of $\delta t = 10^{-3}$.

until it reaches its limit, given the tolerances. The minimum value is $\delta t = 10^{-4}$, and this value persists for a majority of the simulation. Again, this is likely caused by a highly oscillatory mode in the system. We find that a different solver, employing a higher-order Runge-Kutta scheme, is able to overcome this issue, as will be discussed in § 3.6.2. Thus, the results shown hereinafter for the 10th-order system are obtained using the higher-order scheme.

3.5.4 Seventeenth-order system

The 17th-order system was simulated using the RK4 method with δt ranging from 10^{-1} to 10^{-3}, as above. Figure (3.18) shows the modal evolution of the streamfunction perturbation, ψ' at $\delta t = 10^{-3}$. It can be seen that this solution more closely resembles the solution to the 9th-order system than it does the 10th-order system. One difference between the 17th and the 9th-order systems is that, over the same period of time ($0 < t < 1000$), we observe two additional ‘peaks’ in the 17th-order system. A

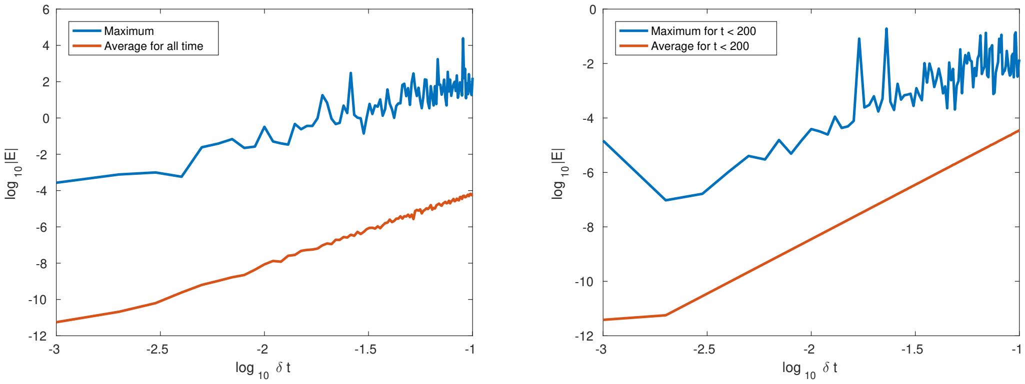

(a) $0 < t < 1000$

(b) $0 < t < 200$

Figure 3.19: Maximum and average error in the 17th-order system, simulated using $\gamma = 0$, $Pr = 7$, $\tau = 0.01$, and $(k, m) = (0.19, 0.09)$. over two different ranges of time t.

discussion of the behaviour of this system is reserved for § 3.6. Here, we focus on the accuracy of the simulations.

The maximum and average relative error, calculated over the range $0 < t < 1000$, in the 17th-order system is plotted against δt in Figure 3.19a. Note that 100 points were used to produce this plot. We see that both the maximum and the average error increase with increasing time step δt, though the average error fluctuates slightly more than in the 9th-order system. The gradient of the average error curve is 3.80, which closely resembles that of the 9th-order system (3.78), suggesting inaccuracies are consistent across both systems.

Figure 3.19b shows a plot of the maximum and the average error calculated over the range $0 < t < 200$, which represents the exponential growth phase. The maximum error in this region is generally lower than over the whole range $0 < t < 1000$. Furthermore, the average error curve is straighter and has a gradient of 3.99, which is much closer to the expected gradient of 4 as calculated on the basis of equation (3.5.2). Hence the 4th/5th-order Runge-Kutta method appears to be highly accurate in the linear phase, and only marginally less accurate when the solution is non-linear.

3.6 Evolution of Modes in Truncated Systems

3.6.1 Ninth-Order System

Choice of Parameters

We are now in a position to study the behaviours of modes in each of the 9th-, 10th- and 17th-order systems in more detail. We start off by simulating the 9th-order system using oceanic parameters of $Pr = 7$ and $\tau = 0.01$. We start by taking a value of $\gamma = 0.9$ ($R_\rho^{-1} = 1.11$) and select wavenumbers (k, m) based on the findings of NN. We later vary these parameters to study the behaviour under different stability characteristics of the individual modes.

The static basic state is unstable to growing $(1, 0)$ elevator modes for a range of R_ρ^{-1} defined by equation (2.52) in Chapter 2, which is dependent on k. Figure 2.4 shows the growth rates of $(1, 0)$ elevator modes (i.e. with $m = 0$) as a function of k and R_ρ^{-1}. When $k = 0$, the system is unstable for:

$$1 \leq R_\rho^{-1} \leq (Pr + 1)/(Pr + \tau) = 1.141. \tag{3.12}$$

This gives a range of γ of $1 \geq \gamma \geq 0.876$. NN studied the system at a marginally supercritical $\gamma = 0.88$ ($R_\rho^{-1} = 1.136$), for which the fastest-growing mode is found to have $(k, m) = (0.187, 0)$. As discussed in § 3.4, the vertical wavelength of the $(0, 2)$ layering mode was found to be almost identical to the horizontal wavelength of the $(0, 1)$ elevator mode. In other words, the authors observed a $(0, 1)$ layering mode (and $(1, 1)$ cellular mode) with $m = k/2$.

We initially take $\gamma = 0.9$ in our simulations to ensure that the basic state is unstable, but we later vary this. For each value of γ, we select wavenumbers (k, m) such that the $(1, 0)$ elevator mode is the fastest-growing elevator mode, and such that $m = k/2$. Thus, for $\gamma = 0.9$, we get $(k, m) = (0.257, 0.129)$.

It is pertinent here to discuss the stability of the static basic state as a function of both k and m. If we take equations (2.42) in Chapter 2 and instead express them as $(\psi, T, S) = (A_\psi, A_T, A_S)e^{i(kx+mz)}e^{\sigma t}$, i.e. including non-zero m, we obtain the following dispersion relation, which should be contrasted with equation (2.44):

$$(\lambda_0 + (k^2+m^2))(\lambda_0 + Pr(k^2+m^2))(\lambda_0 + \tau(k^2+m^2))\left(1 + \frac{m^2}{k^2}\right)$$
$$+ Pr(\mathrm{sgn}(T_z)(\lambda_0 + \tau(k^2+m^2) - \mathrm{sgn}(S_z)R_\rho^{-1}(\lambda_0 + (k^2+m^2))) = 0. \quad (3.13)$$

Figure 3.20 shows the growth rates of (k, m) modes when $\gamma = 0.9$ ($R_\rho^{-1} = 1.11$), $Pr = 7$, and $\tau = 0.01$. Clearly, the fastest-growing modes are $(1, 0)$ elevator modes with $m = 0$, but there still exists growing $(1, 1)$ cellular modes with non-zero m. The region of unstable wavenumbers is limited to a semi-elliptical region that intersects the $m = 0$ axis. It suffices to say that our choice of $(k, m) = (0.257, 0.129)$ leads to a $(1, 1)$ cellular mode that grows exponentially with a growth rate that is roughly 80% of the growth rate of the fastest-growing elevator mode. We later return to this plot when studying the effects of varying k and m on the results.

Results at $\gamma = 0.9$

The absolute magnitudes of the streamfunction ψ', temperature T', salinity S' and density ρ' perturbations are plotted over time for $\gamma = 0.9$ ($R_\rho^{-1} = 1.11$) in Figure 3.21, using the parameters set out above. Figure 3.22 shows the evolution of modes as shown in Figure 3.21 but without logarithmic scaling and without taking the absolute magnitude of the modes.

The density perturbation ρ' was calculated using the following expression derived in Chapter 2:

$$\rho' = -R_T T' + R_S S' = -T' + \frac{S'}{\gamma}.$$

Therefore, the density is representative of the combined effects of the temperature and salinity modes.

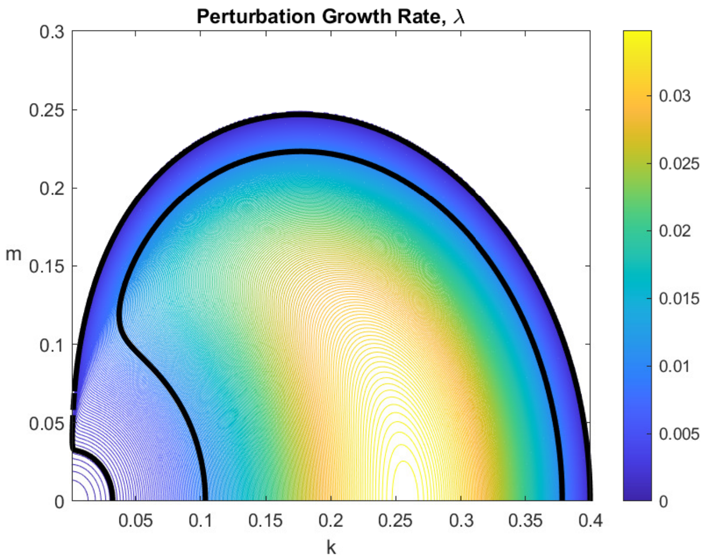

Figure 3.20: Growth rates of perturbations to a static basic state in wavenumber (k, m) space when $\gamma = 0.9$ ($R_\rho^{-1} = 1.11$), $Pr = 7$ and $\tau = 0.01$. The uncontoured white region represents stable wavenumbers (i.e. those with negative growth rates).

The modes are initialised using the same values as in NN. That is, the initial state comprises a dominant $(1, 0)$ elevator mode and a lower-amplitude $(1, 1)$ cellular mode in each variable. The $(0, 1)$ and $(0, 2)$ layering modes are not present in the initial state, having an amplitude of zero. These are generated through non-linear interactions as will be described hereinafter. We note, for completeness, that the choice of initial conditions appears to have little effect on the overall dynamics of the system. Therefore, we do not vary the initial conditions here. We split the evolution of modes into the following phases, for ease of explanation: (1) an exponential growth phase ($0 < t < 130$); (2) an 'accelerated' growth phase ($130 < t < 175$); (3) a 'secondary growth phase' ($175 < t < 275$), and (4) a 'layering' phase ($275 < t < 400$). These are indicated on the streamfunction plot of Figure 3.21. The accelerated growth phase (2) and the secondary growth phase (3) are separated by a 'first peak', while the secondary growth phase (3) and the layering phase (4) are separated by a 'second peak', or 'burst'.

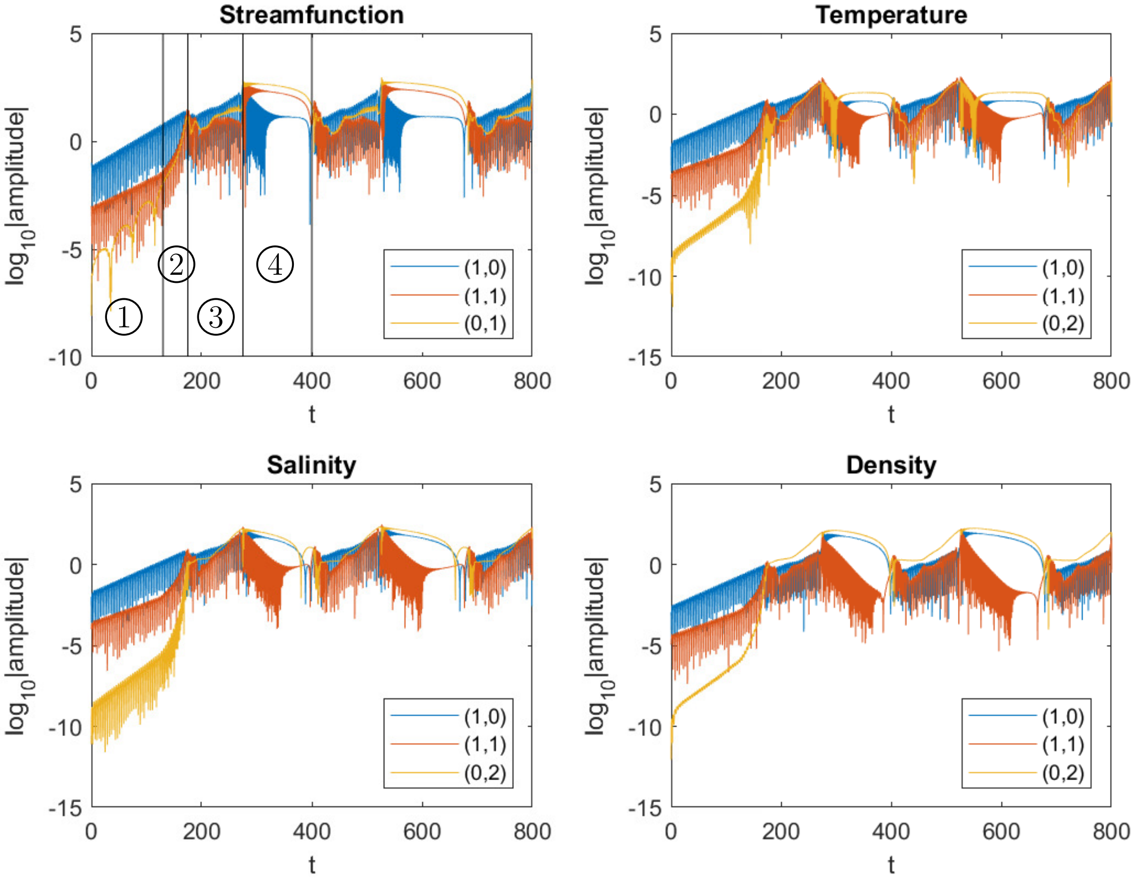

Figure 3.21: Modal decomposition of ψ', T', S' and ρ' perturbations in the 9th-order system, when $\gamma = 0.9$ ($R_\rho^{-1} = 1.11$), $Pr = 7$, $\tau = 0.01$, and $(k, m) = (0.257, 0.129)$.

As noted previously, one of the benefits of employing a low-order model is that we can attempt to study the specific modal interactions that lead to a behaviour of interest. Thus, below, we describe each of the above phases with reference to the relative sizes of each of the terms in equations (3.6). The relative sizes are determined numerically using the results of our simulations and are then plotted over time in each phase. We use the plots to try to explain the behaviour observed in Figures 3.21 and 3.22 in terms of specific modal interactions.

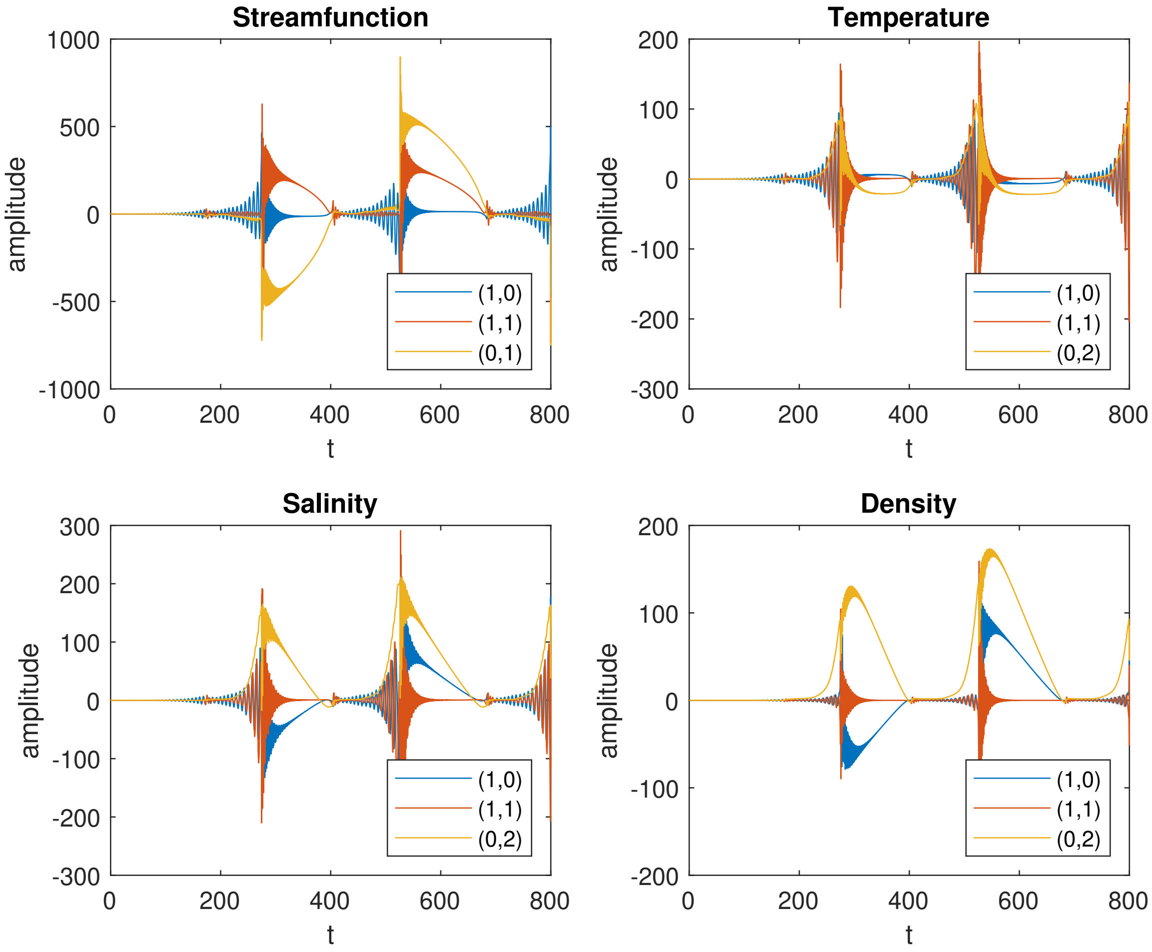

Figure 3.22: Unscaled modal decomposition of ψ', T', S' and ρ' perturbations in the 9th-order system between $t = 0$ and $t = 1000$ when $\gamma = 0.9$ ($R_\rho^{-1} = 1.11$), $Pr = 7$, $\tau = 0.01$, and $(k, m) = (0.257, 0.129)$.

Herein, for brevity and for ease of comparison with equations (3.6), we refer to the modes based on their respective designations in equations (3.6). That is, we indicate with a letter the type of mode ($\psi = a$, $T = b$ and $S = c$), and with a subscript the mode's structure ($1 =$ elevator $(1, 0)$, $2 =$ cellular $(1, 1)$ and $3 =$ layering $(0, 1)$ and $(0, 2)$.). For reference, the 9th-order system of equations is:

$$
\begin{aligned}
a_1' &= -\frac{\sigma}{k}(r_T b_1 - r_S c_1) \; -\frac{1}{2}kma_2a_3 \; -\frac{\sigma}{k}a_1k^3,\\
a_2' &= \frac{1}{p}(\sigma(r_T k b_2 - r_S k c_2) \; +(k^3m - km^3)a_1a_3 \; -\frac{1}{p}p^2a_2,\\
a_3' &= \frac{1}{2}kma_1a_2, \; -\sigma m^2 a_3\\
\\
b_1' &= -ka_1 \; +\frac{1}{2}kma_3b_2 \; -b_1k^2,\\
b_2' &= ka_2 \; +km(a_2b_3 - a_3b_1) \; -pb_2,\\
b_3' &= -\frac{1}{2}kma_2b_2 \; -4b_3m^2,\\
\\
c_1' &= -ka_1 \; +\frac{1}{2}kma_3c_2 \; -\tau c_1k^2,\\
c_2' &= ka_2 + km(a_2c_3 - a_3c_1) \; -\tau pc_2,\\
c_3' &= -\frac{1}{2}kma_2c_2 \; -4\tau c_3m^2,
\end{aligned}
\tag{3.14}
$$

where $p = (k^2 + m^2)$. To aid in our discussions in this section, the terms in equations (3.14) are colour-coded based on their respective roles: the blue terms represent terms that naturally interact to cause a linear growth of the modes; the red terms are terms that are generated through nonlinear interactions; and the orange terms are terms that cause the modes to decay. Note that there are no blue terms in any of the $(0, 1)$ or $(0, 2)$ layering modes, as these are only generated through nonlinear interactions in the red terms.

Furthermore, we herein refer to the terms with the subscripts: L, for the 'linear growth' terms; N, for the 'nonlinear' terms; and D for the 'decaying' terms. For example, the red term in the equation for b_2' is referred to as $b_{2,N}$, as it is what we have called a 'nonlinear' term.

Exponential Growth Phase

The $(1, 0)$ elevator mode (a_1, b_1 and c_1) is the fastest-growing mode arising from a static basic state, and initially grows exponentially in each case. The $(1, 1)$ cellular modes (a_2, b_2 and c_2) similarly grow exponentially, as discussed above, at approximately 80% of the rate of the $(1, 0)$ elevator modes. The a_3 mode is stimulated by the nonlinear term $a_{3,N}$ which is influenced by a_1 and a_2. These are both growing modes, and since $a_3 \ll a_1 a_2$ initially, the nonlinear term $a_{3,N}$ is much larger than the decaying term $a_{3,D}$ and a_3 begins to grow. This leads to an exponential growth rate for the $(0, 1)$ layering mode, a_3, which is faster than that of each of the $(1, 0)$ elevator and $(1, 1)$ cellular modes.

The $(0, 2)$ layering mode in T (that is, b_3') comprises a nonlinear term, $b_{3,N} = -\frac{1}{2} kma_2 b_2$. This is dependent on two $(1, 1)$ cellular modes, and so is also observed in the 5th-order Veronis (1965) system. Since a_2 and b_2 are both growing exponentially, b_3 similarly grows exponentially, and faster than both a_2 and b_2. The $(0, 2)$ layering mode in S (that is, c_3) grows in a similar way, but is instead dependent on a_2 and c_2.

In summary, in this first phase, the exponentially growing $(1, 0)$ elevator modes and $(1, 1)$ cellular modes interact to cause the $(0, 1)$ and $(0, 2)$ layering modes to grow at faster rates than each of the $(1, 0)$ elevator and $(1, 1)$ cellular modes.

Accelerated Growth Phase

The exponential growth phase continues until approximately $t = 140$ in Figure 3.21. At this point, the growth rates of the $(1, 1)$ cellular modes (a_2, b_2, c_2) and the $(0, 1)$ and $(0, 2)$ layering modes (a_3, b_3, c_3) begin to increase. To see why, we first look at the magnitudes of the terms in equations (3.6) for a_3' and b_2' (equivalently, c_2'). These are shown in Figure 3.23. In each case, the colours of the terms match those in equations (3.14) above; however, we note that there are actually two separate nonlinear terms within $b_{2,N} = km(a_2 b_3 - a_3 b_1)$ (and similarly within $c_{2,N}$). We therefore colour one of these terms red and the other purple, for clarity. The resulting growth rate is black.

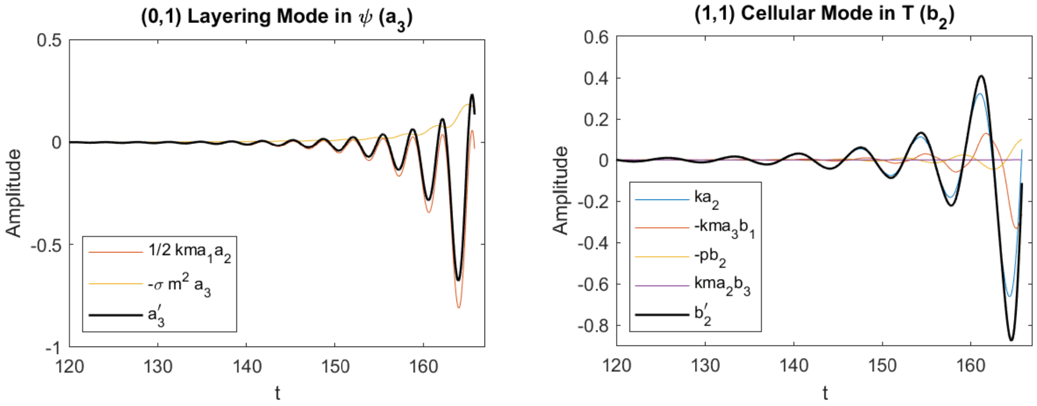

Figure 3.23: Amplitudes of terms in equations (3.6) for the growth rates of the a_3 (layering) and b_2 (cellular) modes in the 9th-order system during the 'accelerated growth' phase. Here, $\gamma = 0.9$ ($R_\rho^{-1} = 1.11$), $Pr = 7$, $\tau = 0.01$, and $(k, m) = (0.257, 0.129)$.

We see that the growth rate, b_2' (shown by the black line in the right-hand plot), is normally driven by the $b_{2,L}$ term (blue line) during the linear phase, as expected. The nonlinear term $b_{2,N}$ (red and purple lines) then eventually becomes sufficiently large to modify this exponential growth. During the accelerated growth phase, we see that a_3 and b_1 are each larger than a_2 and b_3, so the $-kma_3b_1$ term (red line) in $b_{2,N}$ is larger than the kma_2b_3 term (purple line). Indeed, we see from Figure 3.23 that the kma_2b_3 term (purple) has very little influence on the flow at this stage, as b_3 is very small. The growing $b_{2,N}$ term then interacts with the $b_{2,L}$ term in such a way as to increase the growth rate of the b_2 cellular mode. A similar accelerated growth is observed in c_2, due to the $c_{2,N}$ term.

Though not shown here, we see that the growth rate of the a_2 (cellular) mode increases in line with b_2 and c_2 due to the $a_{2,L} = r_Tb_1 - r_Sc_2$ term. Moreover, although k and m are small, a_1 is sufficiently large to cause the nonlinear $a_{2,N} = (k^3m - km^3)a_1a_3$ term to further enhance the growth of the a_2 mode. The increase in a_2' leads to a further increase in the growth rate of the a_3 (layering) mode, and so on. This feedback loop causes an accelerated growth of all modes except for the $(1, 0)$ elevator modes, which are currently large enough in amplitude to continue growing exponentially, unimpeded by the other modes.

Thus, to summarise, as the a_3 (layering) mode grows, it begins to interact with the already-large a_1, b_1 and c_1 (elevator) modes to increase the growth rates of the a_2, b_2 and c_2 (cellular) modes. Subsequently, via a feedback loop, this further increases the growth rate of the a_3 (layering) mode, and we see an overall accelerated growth of these modes.

First Peak

At approximately $t = 175$, the $(1, 1)$ cellular modes and $(0, 1)$ and $(0, 2)$ layering modes have grown to approximately the same order of magnitude as the $(1, 0)$ elevator modes in each case. NN only ran their simulations up to this point. It was unclear from the results presented in the NN study whether either of the $(0, 1)$ and/or $(0, 2)$ layering modes became the largest modes at this point, and if they did, whether they would remain dominant thereafter. Notably, in our simulations, the $(0, 2)$ layering modes are the lowest amplitude modes at this point; however, it may be that the peak observed in NN actually corresponds to the second peak (the ‘burst’ phase) that we discuss below. In any case, even though linear theory begins to break down at such large amplitudes, we consider it is still worth studying the longer-term, non-linear interactions of the modes.

It is important to note that during these ‘peaked’ stages it becomes much more difficult to identify the specific interactions in equations (3.6) that lead to the growth and suppression of specific modes. This is because the modes are all of similar amplitudes and tend to vary quite wildly during a peak in terms of both amplitude and frequency. Furthermore, a change in frequency of certain of the modes can correspond to a change in relative phase of the modes, which heavily influences the behaviour of any related nonlinear terms, as will be shown below.

We see in Figure 3.21 that, once the modes reach a similar amplitude, the elevator and cellular modes reduce in amplitude momentarily before growing once again. Though not shown here, we see that at $t = 170$ the nonlinear $a_{1,N}$ term eventually grows to be comparable in amplitude to the $a_{1,L}$ and $a_{1,D}$ terms. Specifically, at this point, the a_2 cellular and a_3 layering modes are large enough to disrupt the growth rate of the a_1 elevator mode in ψ. The same is true with respect to the b_1' and c_1' elevator modes. The nonlinear terms in the system affect the frequencies of respective modes just enough to cause a relative change in phase (at least momentarily) between the modes. For example, the upper plot of Figure 3.24 shows the modal amplitudes of the a_1, b_1 and c_1 (elevator) modes at this point, while the lower plot shows modal amplitudes of the a_2, b_2, and c_2 (cellular) modes. The b_1 and b_2 modes generally track the c_1 and c_2 modes. We see in the elevator plots, at around $t = 170$, that the a_1 elevator mode changes phase with respect to the corresponding b_1 and c_1 elevator modes. This actually causes a relative shift in phase of the ‘linear growth’ terms (L) in relation to the ‘decaying’ (D) and ‘nonlinear’ (N) terms in each of the elevator modes, thereby resulting in a reduction in amplitude of the elevator modes.

This shift in phase does not immediately propagate through the system, so between $t = 175$ and $t = 185$ we see that the growth rate of the a_3 (layering) mode temporarily changes sign (not shown here) due to a relative shift in phase between the a_1 (elevator) and a_2 (cellular) modes in the $a_{3,N}$ term. In the same interval, the relative phases of the $(1, 1)$ cellular modes in ψ, T and S also change, as shown in the bottom plot in Figure 3.24, thereby causing a temporary suppression of the cellular modes, too.

Following this transitional period, between $t = 170$ and $t = 190$, the elevator modes (a_1, b_1, c_1) begin to grow exponentially once again. This causes the $a_{3,N} = \frac{1}{2}kma_1a_2$ term to remain relatively large, even when the a_2 cellular mode is suppressed. Thus, the size of the $a_{2,N} = (k^3m - km^3)a_1a_3$ term also remains large, as do the correspond-

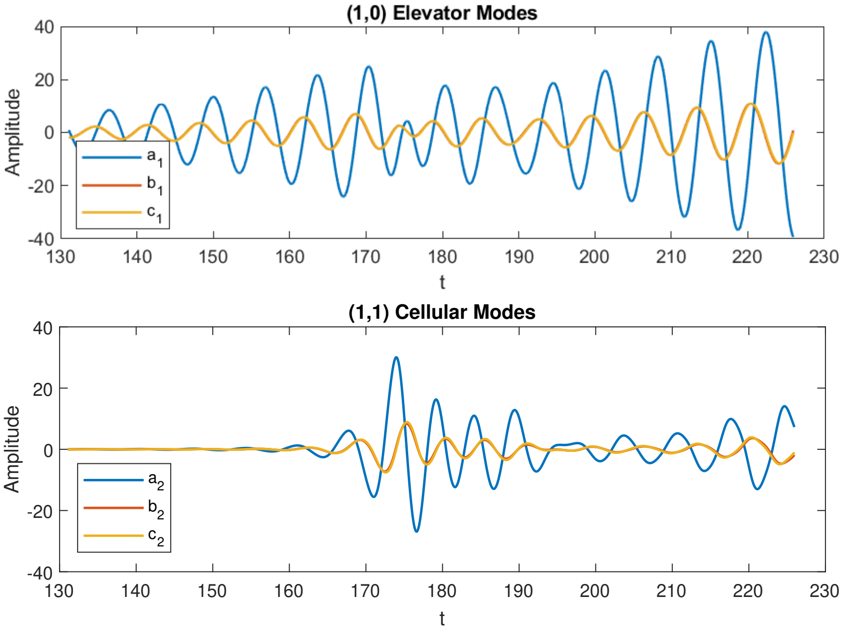

Figure 3.24: Top: Amplitudes of the $(1, 0)$ elevator modes in ψ,T and S; Bottom: Amplitudes of the $(1, 1)$ cellular modes in ψ,T and S. The results are shown around the ‘first peak’, taking $\gamma = 0.9$ ($R_\rho^{-1} = 1.11$), $Pr = 7$, $\tau = 0.01$, and $(k, m) = (0.257, 0.129)$.

ing nonlinear terms $b_{2,N}$ and c_{2_N}. The b_3 and c_3 layering modes have, until now, been relatively small. At this stage, however, the these modes are large enough to start influencing the behaviours of the a_2, b_2 and c_2 cellular modes.

Specifically, we see a subtle change in the shapes of the peaks in the lower plot of Figure 3.24, from $t = 200$. The change is such that the a_2 mode interacts differently with the b_2 and c_2 modes. For example, the nonlinear $b_{3,N} = -\frac{1}{2}kma_2b_2$ term now takes on a positive sign for a majority of the time, as a_2 and b_2 are almost always of opposite sign. This is shown for the b_3 layering mode in Figure 3.25. Prior to the peak, the amplitude of the $b_{3,N}$ term oscillated around the zero axis. The same thing happens with respect to the nonlinear $c_{3,N} = -\frac{1}{2}kma_2c_2$ term. This results in the b_3 and c_3 modes essentially ‘jumping off’ the zero-axis and gradually becoming more and more positive following the first peak.

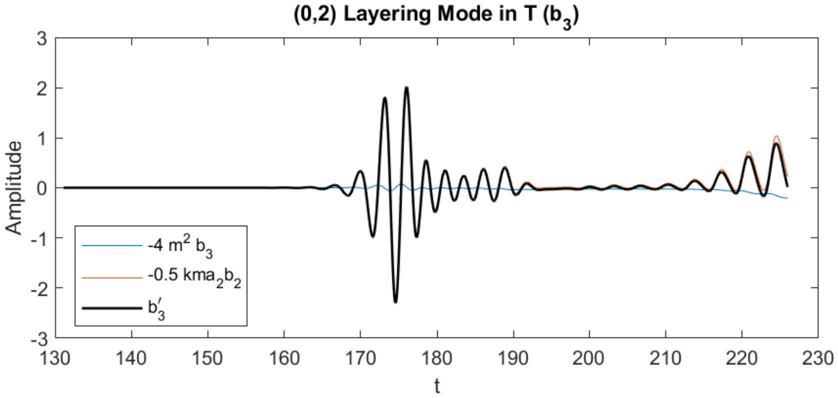

Figure 3.25: Amplitudes of terms in the equation for the growth rate of the b_3 (layering) mode in the 9th-order system (3.6) around the 'first peak'. Here, $\gamma = 0.9$ ($R_\rho^{-1} = 1.11$), $Pr = 7$, $\tau = 0.01$, and $(k, m) = (0.257, 0.129)$

Notably, we still do not see the emergence of a 'dominant' layering mode in either ψ', T', or S' individually during this peak; however, we do see that immediately following the peak, the $(0, 2)$ (layering) mode in the density perturbation, ρ', becomes larger than the other modes in Figure 3.21. As discussed below, this appears to indicate the start of layer formation in the system.

Second Growth Phase

The $(1, 0)$ elevator modes continue to grow exponentially following the peak. Meanwhile, the $(1, 1)$ cellular modes are influenced by the now large $(0, 1)$ and $(0, 2)$ modes. This is perhaps best seen in Figure 3.26, which shows the relative magnitudes of terms in the equations for a_2' and b_2' in (3.14). The terms in c_2' behave in a similar way to those in b_2'.

We see that growth rate of the b_2 cellular mode in T (lower plot) is predominantly driven by the two nonlinear terms in $b_{2,N}$, coloured in red and purple, which depend on the a_3 and b_3 layering modes, respectively. The $b_{2,L}$ term (blue) is relatively small

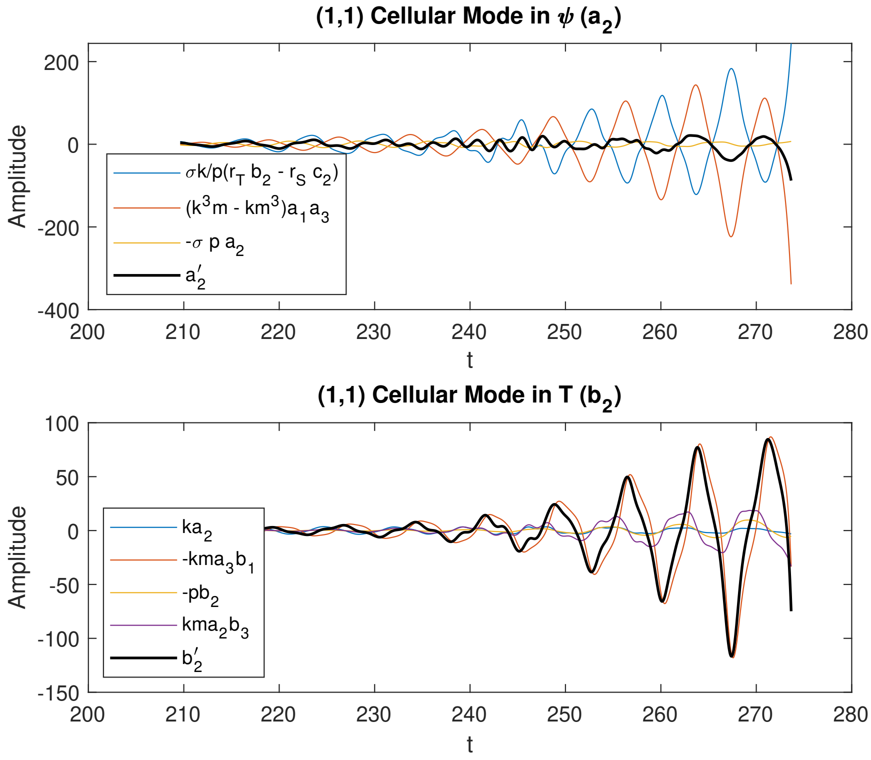

Figure 3.26: Amplitudes of terms in the equations for the growth rates of the a_2 and b_2 (cellular) modes in the 9th-order system (3.6) during the 'second growth' phase. Here, $\gamma = 0.9$ ($R_\rho^{-1} = 1.11$), $Pr = 7$, $\tau = 0.01$, and $(k, m) = (0.257, 0.129)$.

here. In contrast, the $a_{2,L}$ term (blue) in ψ (upper plot) is of a similar amplitude to the nonlinear $a_{2,N}$ term (red), but the terms have opposite signs. The result is that the 'accelerated growth' of a_2 that we saw previously is now suppressed. This is due to the due to the $(0, 1)$ and $(0, 2)$ layering modes now largely driving the growth of the b_2 and c_2 cellular modes, which causes causes a subsequent change in phase of the $a_{2,L}$ mode (blue) relative to the $a_{2,N}$ mode (red).

The $(0, 2)$ layering modes, b_3 and c_3, continue to grow during this phase as the nonlinear terms $b_{3,N} = \frac{1}{2}kma_2b_2$ and $c_{3,N} = \frac{1}{2}kma_2c_2$ continue to be largely positive.

Burst Phase

At approximately $t = 275$ we see a drastic change in the behaviour of modes. Firstly, we see all modes increase in amplitude almost instantaneously. At the same time, the frequencies of the modes change. This is a highly nonlinear process. We have very closely studied the relative amplitudes of the terms in equations (3.14) in an attempt to understand this process; however, it is not clear exactly which modes are responsible for triggering this change. We do see a momentary change in frequency of the b_2 cellular $(1, 1)$ mode shortly prior to the rapid growth. This is caused by a change in the behaviour of the nonlinear $b_{2,N} = km(a_2b_3 - a_3b_1)$ term, which is likely due to having large layering modes (b_3 and a_3). A corresponding change in behaviour is observed in S. It appears that the change in frequency of b_2 acts to shift the relative phases of some of the modes, which subsequently triggers the system to enter the 'layering' phase described below. This suggests the large $(0, 1)$ and/or $(0, 2)$ layering modes are responsible for causing the system to enter the layering phase.

Following the burst phase, the b_3 and c_3 layering modes remain at substantially the same amplitudes as they were before the burst phase. This further supports the idea that the large amplitude $(0, 2)$ layering modes primarily drive this change in behaviour of all of the modes.

Layering Phase

Following the peak in amplitudes, there exists a period of time between $t = 275$ and $t = 400$ during which all modes gradually reduce in amplitude—some faster than others. During this phase, the oscillatory frequencies of all modes are significantly higher than in the previous phases. Furthermore, the ψ modes oscillate at lower frequencies than the corresponding T and S modes. To illustrate this, we plot in Figure 3.27 the magnitudes of terms in the equations for a_1' and b_1' in the 9th-order system (3.14).

We see that the nonlinear terms (red) in each case tend to drive the growth rates

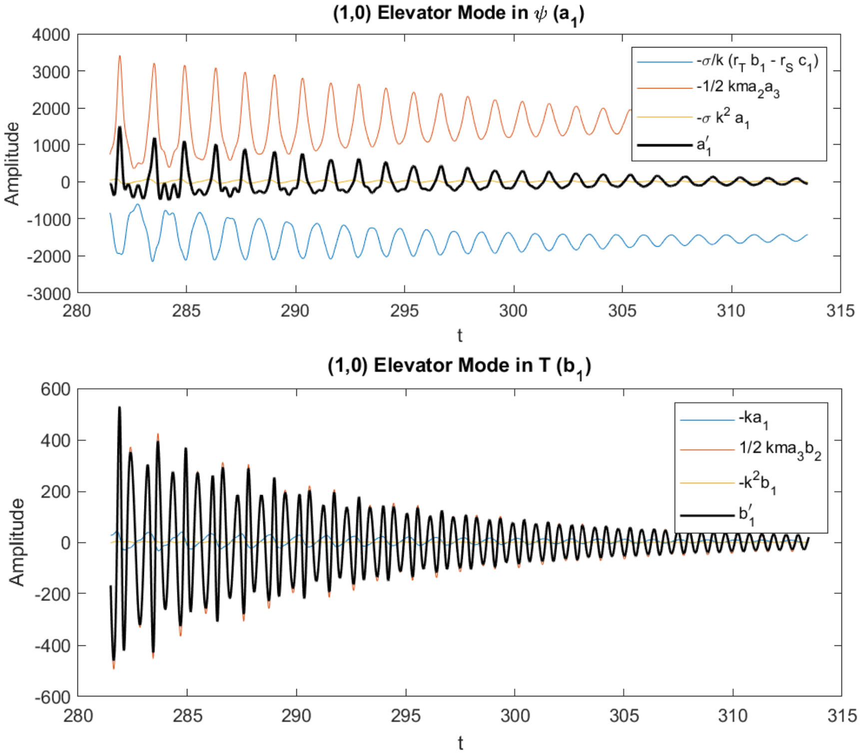

Figure 3.27: Amplitudes of terms in the equations for the growth rates of the a_1 and b_1 (elevator) modes in the 9th-order system (3.6). Here, $\gamma = 0.9$ ($R_\rho^{-1} = 1.11$), $Pr = 7$, $\tau = 0.01$, and $(k, m) = (0.257, 0.129)$.

(black), while the 'linear growth' terms (blue), which previously caused the elevator modes to interact and grow in amplitude, now tend to actively dampen the effects of the nonlinear terms (red), at least in a_1. A similar behaviour is observed in the $(1, 1)$ cellular modes in the system, wherein the modes are largely driven by nonlinear terms (red/purple) and dampened by the linear terms (blue). The nonlinear terms are large here due to the dominant $(0, 1)$ and $(0, 2)$ layering modes in the system.

Again, it is difficult here to identify the specific modal interactions that lead to the behaviour observed. One thing we can conclude is that, as seen in Figures 3.21 and 3.22, the amplitudes of certain modes decay towards fixed values, which appear to be transient fixed points, while others remain elevated. For example, the a_1 elevator mode shown in Figure 3.27 moves towards a value determined by the nonlinear $a_{1,N}$ term (red), and the linear $a_{1,L}$ term (blue), since the decaying term $a_{1,D} = -\sigma k^2 a_1$ (orange) is relatively small at this point. We see that these modes remain at a relatively constant amplitude when the linear terms (blue) balance the nonlinear terms (red) in each case. Another observation is that the b_2 cellular and b_3 layering modes in T change sign before reaching their 'fixed' points. This is why we observe an initial dip in these modes even as the same modes in S remain elevated.

Eventually, by roughly $t = 400$, the amplitudes of all modes have dropped to the levels observed during the 'first peak' and the cycle begins again from this point. Thus, we see intermittent periods of growth and suppression of all modes.

Comparison with Pure Convection

We here make a comparison of our results with those of Howard and Krishnamurti (1986), who extended the Lorenz model of convection to include three extra terms to account for large-scale horizontal motions in the flow. Specifically, in our notation, the system of Howard and Krishnamurti (1986) employs a $(1, 1)$ cellular mode, a $(0, 1)$ 'layering', or 'horizontal shear' mode, and a $(1, 2)$ 'tilting' mode in streamfunction, along with a $(1, 1)$ cellular mode, a $(0, 2)$ 'layering' mode and a $(1, 2)$ tilting mode in temperature. Thus, this system is 6th-order.

The system of Howard and Krishnamurti (1986) is not a subset of our 9th-order or higher systems, as the $(1, 2)$ mode is excluded in our truncation. Nevertheless, we can draw certain parallels between the two models. In the 6th-order system, the convective system becomes unstable to steady 'tilted' cells. Figure 6 of Howard and Krishnamurti (1986), which we import here in Figure 3.28, for reference, shows the formation of a hot plume in the lower part of the region, which rises and tilts from lower left to upper right. Later, a cold plume forms in the upper part of the region and sinks and tilts from upper right to lower left. Meanwhile, a leftward-propagating wave forms near the bottom of the layer, while a rightward-propagating wave forms near the top of the layer.

Interestingly, we find that the left- and right-propagating waves correspond to the $(0, 1)$ streamfunction mode in our system, which is essentially a horizontal shear mode, while tilted plumes form in our system through a combination of the $(1, 0)$ elevator and $(1, 1)$ cellular modes, modified by the $(0, 2)$ layering mode. For example Figure 3.29 shows contours of the temperature perturbation, T, in our system over one oscillatory period during the layering phase, starting from $t = 278$. The parameters have been selected to permit a direct comparison with Figure 3.28.

We note that in our model the waves and tilted cells propagate and tilt in opposite directions to those in Howard and Krishnamurti (1986). This is merely a matter symmetry in the system. Furthermore, in our 9th-order system we do not employ horizontal impermeable boundaries in the vertical direction, so our flow is not distorted in this region as it is in Howard and Krishnamurti (1986). Nevertheless, we see strikingly similar results between the two models. Going from left to right in Figure 3.29, we see the formation of a hot ‘plume’ (yellow) that eventually tilts toward the upper left. We then see the formation of a cold ‘plume’ (blue) that tilts toward the lower right. Though not shown here, we see also see corresponding ‘tilted cells’ in the streamfunction perturbation that are reminiscent of those in Figure 4(a) of Howard and Krishnamurti (1986). In our system, this behaviour arises due to the $(1, 0)$ elevator, $(1, 1)$ cellular and $(0, 2)$ layering modes in T being of a similar amplitude to one another at the start of the layering phase (and, indeed, for part of the ‘second growth’ stage).

This behaviour suggests that, once layered structures have formed, convective motions may occur within each layer, as was observed in the full DNS simulations by NN. In this case, the convective motions appear to correspond to those of Howard and Krishnamurti (1986), comprising tilted cells and horizontal motions at the upper and lower sides of each layer. As discussed above, over time, the $(1, 0)$ elevator modes in T become suppressed relative to the $(1, 1)$ cellular and $(0, 2)$ layering modes, which eventually leads to a mostly vertically banded structure in the domain. That is, the convective motions appear reduce over time as each layer becomes homogenously mixed, as in the full system. It may be that, in the presence of higher-order modes, the layers become more defined and mixing in the cell looks more like that of Howard and Krishnamurti (1986) in the presence of rigid boundaries. It may be interesting to extend our system to include the $(1, 2)$ modes, though this is left for future study.

Modal Structure

In terms of the density perturbation, ρ', as shown in Figure 3.21, we see that the $(0, 2)$ mode is dominant throughout both the 'accelerated growth' phase and the 'layering' phase. This implies the formation of density layers, or staircases, immediately following the first peak. This process can be observed more directly by plotting contours of the ψ', T', S' and ρ' perturbations, calculated by substituting the modal amplitudes from simulations into the truncated equations,

$$\begin{aligned}
\psi' &= a_1 \sin(kx) + a_2 \cos(kx) \sin(mz) + a_3 \cos(mz), \\
T' &= b_1 \cos(kx) + b_2 \sin(kx) \sin(mz) + b_3 \sin(2mz), \\
S' &= c_1 \cos(kx) + c_2 \sin(kx) \sin(mz) + c_3 \sin(2mz).
\end{aligned}$$

It is also useful to present the ρ' perturbation as a 'total density', ρ_T, by adding the density perturbation on to the background basic state using equation (2.37) as derived in Chapter 2. That is, the scaled total density ρ_T is given by,

$$\rho_T = -(\mathrm{sgn}(T_z) - \frac{\mathrm{sgn}(S_z)}{\gamma})z - (T - \frac{S}{\gamma}) + C, \tag{3.15}$$

where C is a constant reference density, $C = (\alpha|T_z|\delta)^{-1}$ and δ is the length scale used to non-dimensionalise the equations.

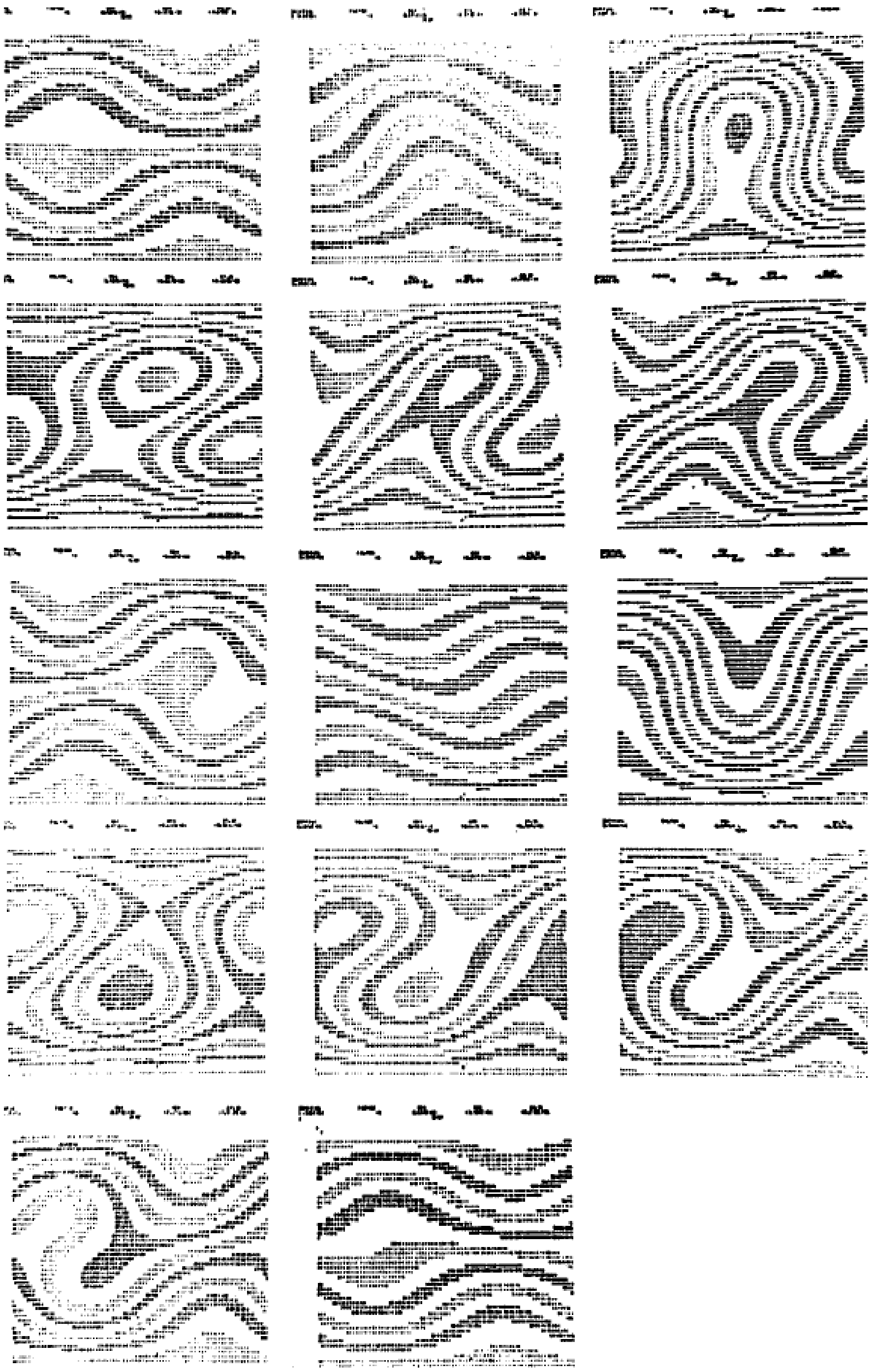

Figure 3.28: Contours of T at successive time intervals within one oscillation period, from Figure 6 of Howard and Krishnamurti (1986).

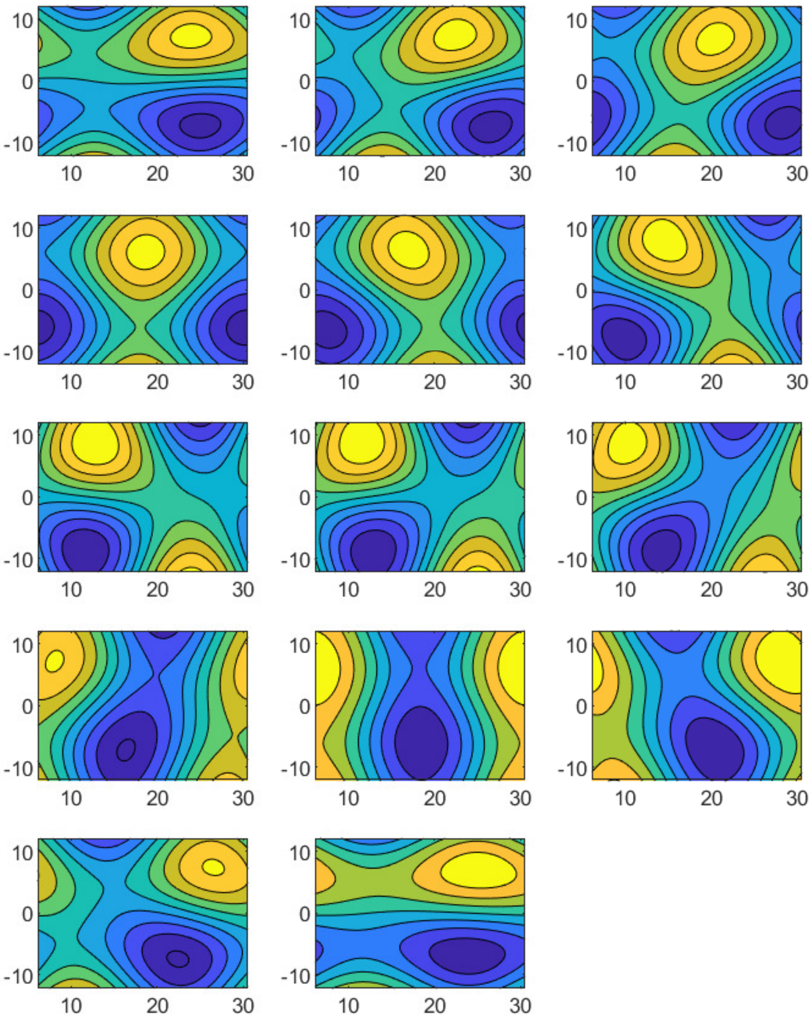

Figure 3.29: Contours of T at successive time intervals within one oscillation period during the ‘layering’ phase, starting from $t = 278$. The abscissa shows a horizontal extent (x) of π/k, while the ordinate shows a vertical extend of πm, to match the plots shown in Figure 6 of Howard and Krishnamurti (1986). Here, $\gamma = 0.9$ ($R_\rho^{-1} = 1.11$), $Pr = 7$, $\tau = 0.01$, and $(k, m) = (0.257, 0.129)$.

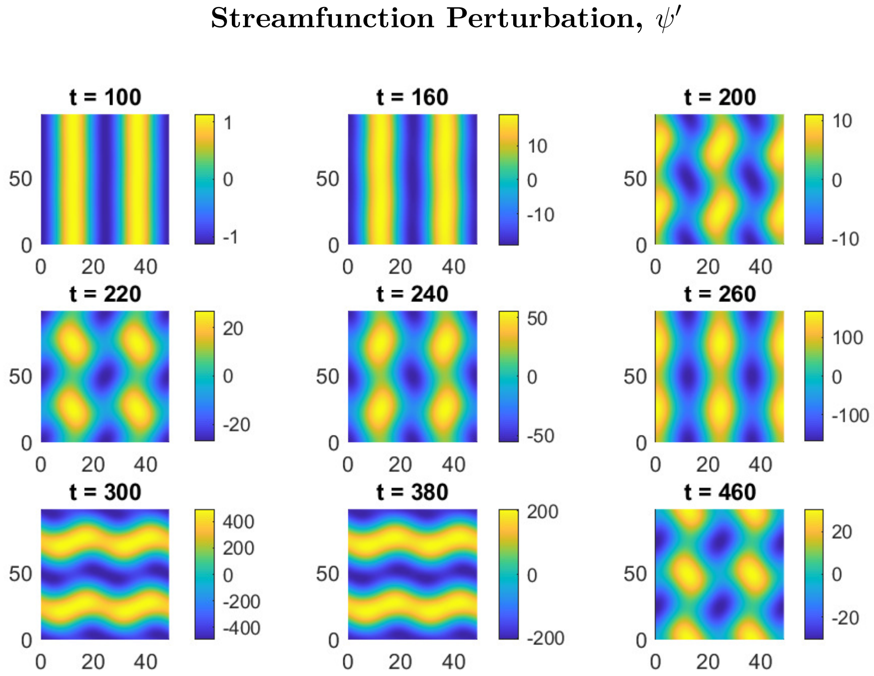

Figure 3.30: Contour plots of the streamfunction perturbation, ψ', at different times in the 9th-order system, using $\gamma = 0.9$ ($R_\rho^{-1} = 1.11$), $Pr = 7$, $\tau = 0.01$, and $(k, m) = (0.257, 0.129)$. The box is two horizontal and vertical wavelengths in size.

Figures 3.30 to 3.33 show contour plots of the ψ', T' and S' perturbations, along with the total density ρ_T, in the 9th-order system at different times. Comparing the contour plots with the modal evolution plots shown in Figure 3.21, we see that, at $t = 100$, the elevator mode dominates in each of the parameters. The elevator mode manifests as vertically-oriented bars in ψ', T' and S' perturbations. The modes are relatively low amplitude in comparison to the basic state at $t = 100$, so the total density ρ_T in Figure 3.33 is largely representative of the constant background gradient. By $t = 200$, the cellular modes in the system reach amplitudes that are approaching those of the respective elevator modes. The result is a disruption of the elevator modes. Indeed, at this point the streamfunction perturbation starts to exhibit 'tilted cell' behaviour, as discussed above in relation to the study by Howard and Krishnamurti (1986). The total density perturbation at this point in time begins to show signs of layering, and in

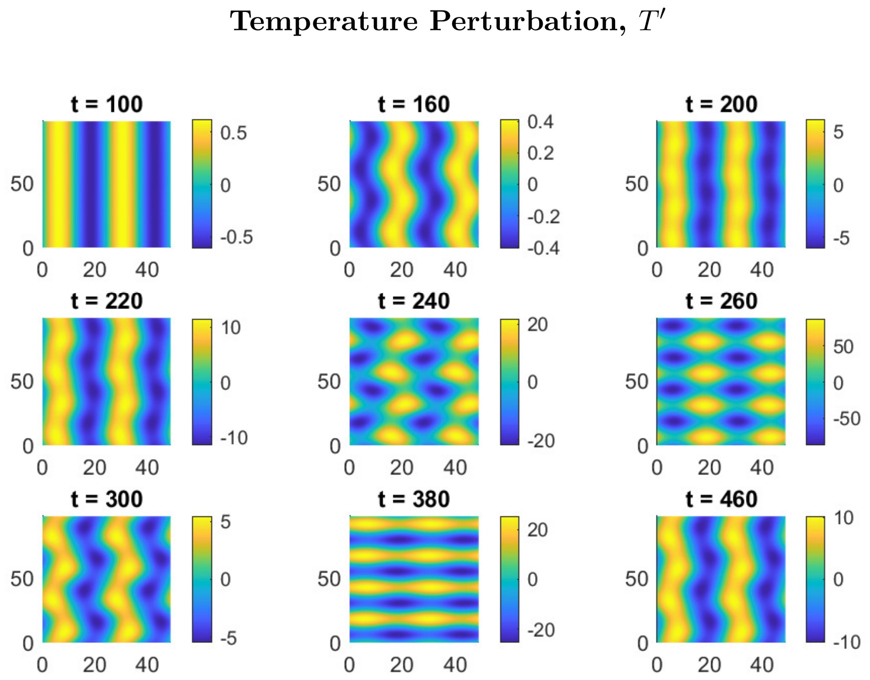

Figure 3.31: Contour plots of the temperature perturbation, T', at different times in the 9th-order system, using $\gamma = 0.9$ ($R_\rho^{-1} = 1.11$), $Pr = 7$, $\tau = 0.01$, and $(k, m) = (0.257, 0.129)$. The box is two horizontal and vertical wavelengths in size.

particular a ‘stepped’ structure. That is, horizontal bands of relatively constant density begin to form.

It is illustrative here to look at the total density, ρ_T, averaged in the x-direction and plotted against the height of the domain, as shown in Figure 3.34. At $t = 100$ we clearly see the background linear density gradient. This begins to give way to a stepped structure, or ‘density staircase’, at $t = 200$ and $t = 220$. Over the period $t = 220$ to $t = 260$, during the ‘accelerated growth phase’, we see the layers become gradually more defined.

At $t = 300$, the system is in the ‘layering’ phase. This corresponds to a very large increase in the amplitudes of all modes, and the layering modes begin to dominate in each case. The total density ρ_T plot of Figure 3.34 appears to show what we here refer

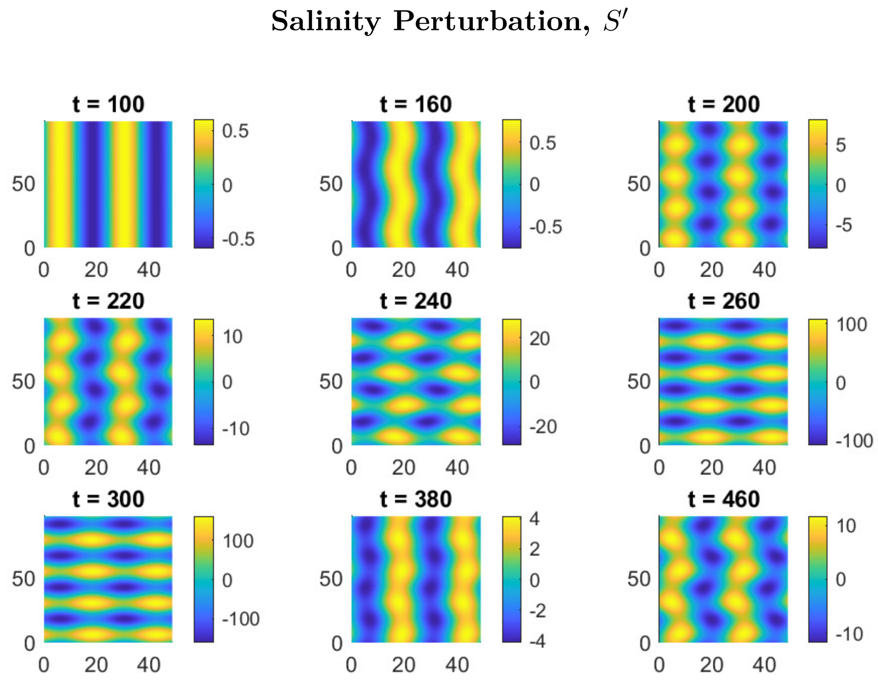

Figure 3.32: Contour plots of the salinity perturbation, S', at different times in the 9th-order system, using $\gamma = 0.9$ ($R_\rho^{-1} = 1.11$), $Pr = 7$, $\tau = 0.01$, and $(k, m) = (0.257, 0.129)$. The box is two horizontal and vertical wavelengths in size.

to here as ‘over-layering’. For example, the effect of the background density gradient is no longer distinguishable at $t = 300$, as the density perturbation at this point is very large compared to the background gradient. This may, at least in part, be due to the scaling used to generate Figures 3.33 and3.34. The density perturbation is normalised with respect to the maximum value of the background density gradient. Specifically, the density perturbation is divided by 10.87 non-dimensional units before being added to the background gradient.

Regardless of the scaling used, these figures provide a visual descriptor of how the growing modes affect the background density gradient. We see that if the density perturbation is sufficiently large, the ‘steps’ may grow in amplitude to the point that the density gradient is, in essence, locally unstable (i.e. heavier fluid overlying a lighter

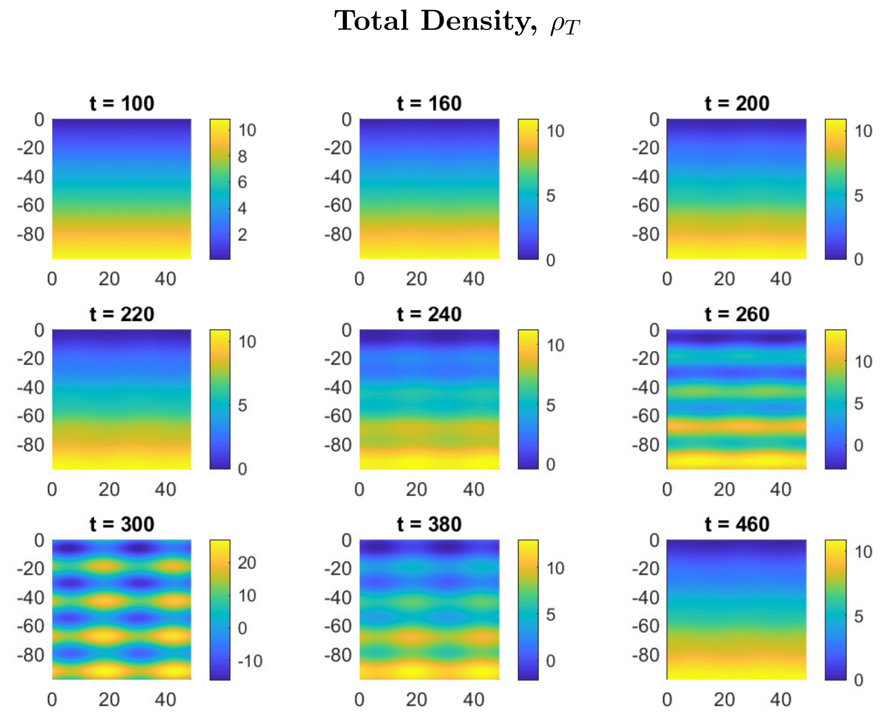

Figure 3.33: Contour plots of the total density, ρ_T, at different times in the 9th-order system, using $\gamma = 0.9$ ($R_\rho^{-1} = 1.11$), $Pr = 7$, $\tau = 0.01$, and $(k, m) = (0.257, 0.129)$. The box is two horizontal and vertical wavelengths in size. The total density is given by adding the density perturbation ρ' to the linear background gradient.

fluid at the boundaries between layers). Higher order modes are likely to be generated before and/or during the layering phase. It is feasible that such higher order modes may attenuate such over-layering, or permit density overturning that leads to layer merger events as observed in previous studies (Noguchi and Niino, 2010b).

It was predicted in Radko (2003) that a horizontally-uniform secondary mode in the form of the γ-instability (as introduced in Chapter 1) may grow and disrupt salt fingers, at least in a fingering state. It was then suggested in Radko (2013), for example on pages 197–198 with reference to Figure 8.17 thereof, that if the growth of the horizontally-uniform secondary mode persists, the fluid may develop ‘density reversals’, comprising

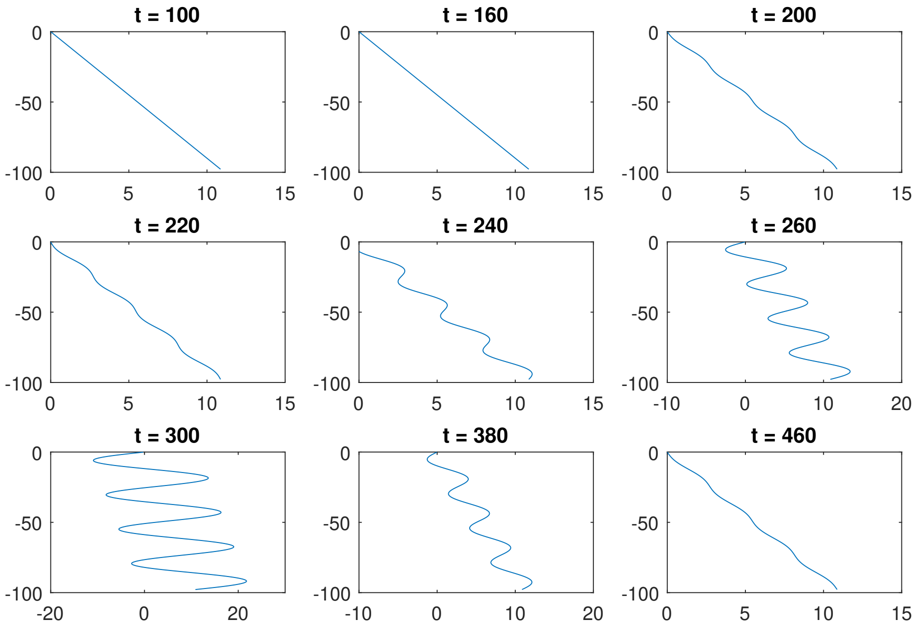

Figure 3.34: The horizontally-averaged total density, ρ_T, plotted on the abscissa as a function of height in the domain. This figure shows the evolution of a density 'staircase'.

top-heavy regions which then overturn to form homogeneous convecting layers. The density pattern we see in Figure 3.34 may, therefore, be indicative of such 'density reversals'.

Finally, we note that the 'layers' observed in our model are not as well-defined as those observed in numerical and physical experiments, nor are they as large-scale. For example, contrast Figures 3.30 to 3.33 with the results from NN shown in Figure 3.2, wherein the layers are separated by well-defined diffusive interfaces. Furthermore, layers observed in the oceans and in experiments tend to be much larger scale (e.g. on the order of tens to hundreds of metres high in the ocean(Johannessen and Lee, 1974, Molcard and Tait, 1977)). In contrast, our layers are on the order of the salt finger width.

Nevertheless, as described above, Noguchi and Niino (2010b) showed using DNS that long-lived density layers may not initially form on a large scale. Rather, the first layers to form in the study were observed to have a height that was comparable to the salt finger width. The these initial layers merged successively to eventually form the larger-scale layers typically associated with double-diffusive convection. Thus, the fine-scale layers observed in our model may be precursors to the larger, longer-lived density layers typically observed in experiments. If sufficiently high-order modes were to be included in our model, we may even be able to observe sharper diffusive interfaces between layers, overturning and homogeneous mixing within layers, or even layer merging events.

Parameter Study

We now briefly study the effect of changing certain parameters on the evolution of modes in the 9th-order system.

Wavenumber

Starting with the wavenumbers, (k, m), we start by noting that, as shown earlier in Figure 3.20, when $\gamma = 0.9$, the system is unstable for all (k, m) in a semi-elliptical region between $k = 0.4$ and $m = 0.25$. The fastest-growing mode here has $k = 0.257$. We previously selected $m = k/2$ based on the results of NN, which showed that the layers intially have a depth on the scale of horizontal wavelength of the $(1, 0)$ elevator modes. The layers are $(0, 2)$ modes, so the $(1, 1)$ cellular modes have a vertical wavelength that is double the horizontal wavelength of the elevator modes, i.e. $k/2$.

We have varied the wavenumbers quite widely and arrived at the following conclusions. For any stable value of k, we never see layering. For any values of (k, m) that give unstable elevator modes and stable cellular modes, we see that the cellular modes initially reduce in amplitude (if initialised at finite amplitude), but are eventually excited through nonlinear interactions with the $(0, 1)$ layering mode that is generated.

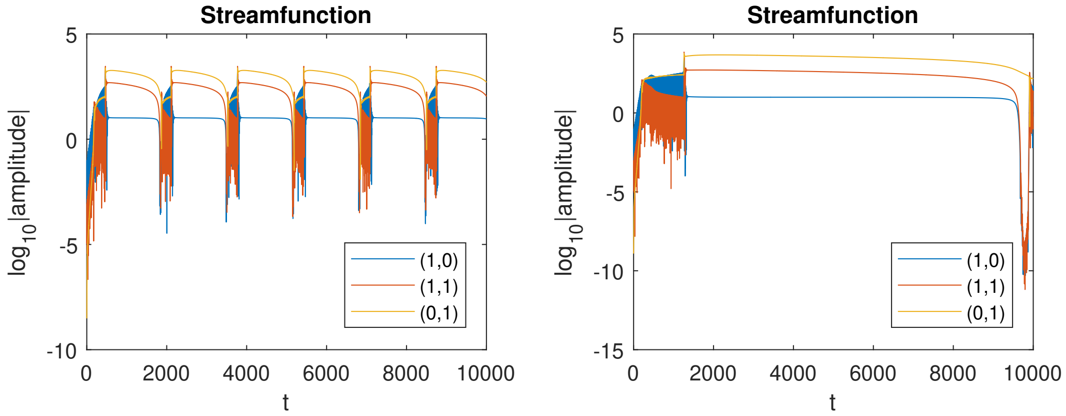

Figure 3.35: Evolution of modes in the streamfunction perturbation for different wavenumbers when $\gamma = 0.9$ ($R_\rho^{-1} = 1.11$), $Pr = 7$ and $\tau = 0.01$. LEFT: $(k, m) = (0.257, 0.05)$. RIGHT: $(k, m) = (0.257, 0.02)$.

Peaks are still observed, but the timescales are much longer since the $(1, 1)$ cellular mode cannot support itself.

If we reduce m towards zero, we observe much wider, longer-lived peaks in the 'layering phase'. This is shown for $(k, m) = (0.257, 0.05)$ and $(k, m) = (0.257, 0.02)$ in Figure 3.35. We only show the streamfunction modes here, for brevity. The other variables exhibit similarly wide peaks. The fact that the amplitudes remain relatively time-independent implies the existence of (unstable) fixed points for small m.

If $k \leq m$, we do not see any large peaks at all, and the modes in all variables appear to oscillate around fixed points. This is shown in Figure 3.36 for $(k, m) = (0.2, 0.205)$. Note that the $(1, 1)$ cellular mode is unstable at these parameters. Increasing m to 0.26, for example, leads to a stable cellular mode, though the system still eventually evolves toward the state shown in Figure 3.36. We do see layering in the S and ρ perturbations in this regime, and this layering is persistent. These values of k and m are unique in that they change the sign of the $a_{2,N} = (k^3 m - k m^3)$ term in the a_2 layering mode shown in equations (3.14). We do not study the effect of this change in detail here.

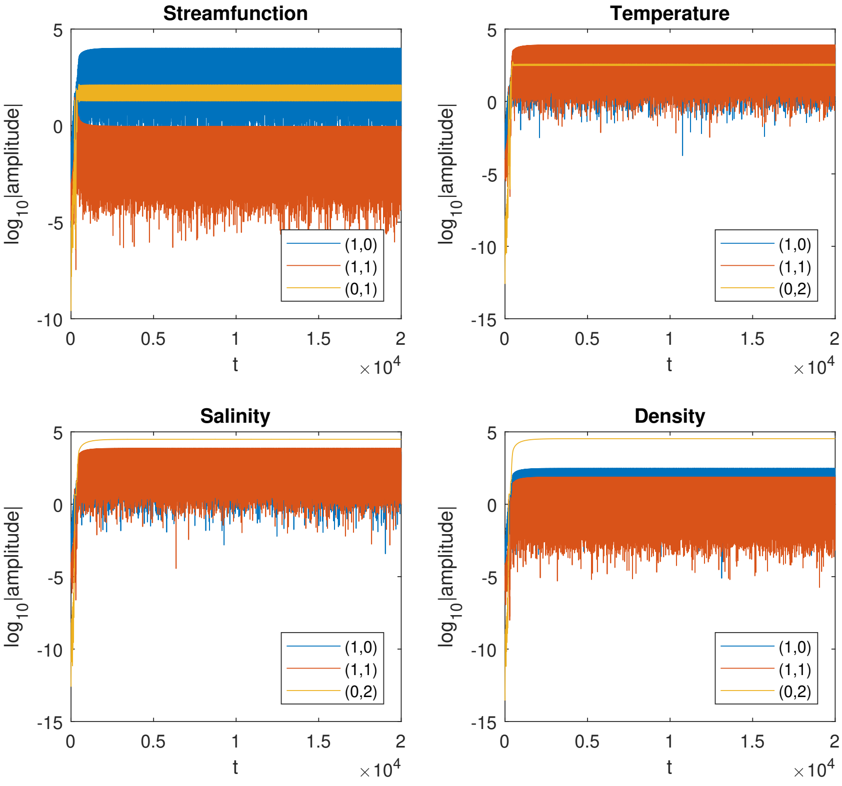

Figure 3.36: Evolution of modes in the streamfunction perturbation when $\gamma = 0.9$ ($R_\rho^{-1} = 1.11$), $Pr = 7$, $\tau = 0.01$ and $(k, m) = (0.2, 0.205)$.

This would be of interest for future study.

Background Stratification

We now vary the strength of the background state, γ, while selecting k to be the fastest-growing elevator mode from linear theory, and m to be equal to $k/2$, as above. We later discuss the reliability of our solutions as the strength of the background state is varied. Figure 3.37 shows the evolution of modes in the ψ', T', S' and ρ' perturbations when $\gamma = 0.88$ ($R_\rho^{-1} = 1.136$), which represents a marginally unstable state close to the critical value of $\gamma = 0.876$ ($R_\rho^{-1} = 1.141$). Here, the fastest-growing mode has

$(k, m) = (0.187, 0.09)$. This regime was studied by NN.

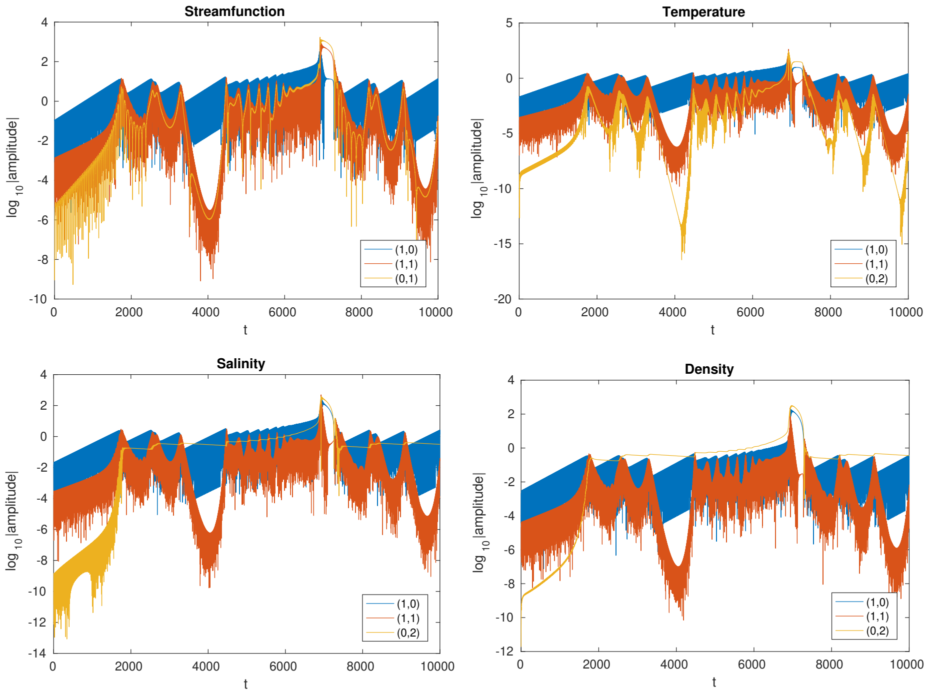

Figure 3.37: Evolution of modes in the 9th-order system when $\gamma = 0.88$ ($R_\rho^{-1} = 1.11$), $Pr = 7$, $\tau = 0.01$, and $(k, m) = (0.187, 0.09)$.

We see that the modes here grow slower than those with $\gamma = 0.9$, and that some of the 'peaks' are larger than others. Specifically, we see a repeating pattern of large peaks (corresponding to the 'layering' phase) interspersed with a number of of smaller peaks (each corresponding to the 'second growth' phase). The $(0, 2)$ layering modes in particular grow more slowly here than when $\gamma = 0.9$, likely because of the reduced growth rates of the $(1, 0)$ elevator and $(1, 1)$ cellular modes. This means that the $(0, 2)$ modes are not large enough during the smaller peaks to cause the system to enter the 'layering' phase. Only when the $(0, 2)$ layering modes are large enough in T and S, relative to the $(1, 1)$ cellular modes specifically, does the system enter the 'layering' phase. This is consistent with our findings when $\gamma = 0.9$. Nevertheless, in this case,

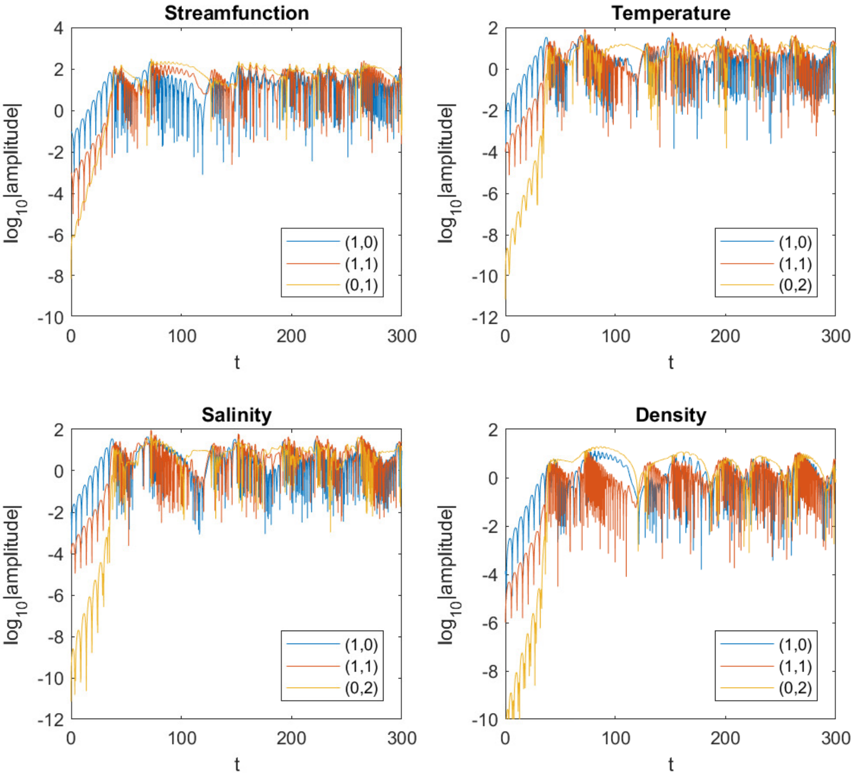

Figure 3.38: Evolution of modes in the 9th-order system when $\gamma = 0.99$, ($R_\rho^{-1} = 1.01$), $Pr = 7$, $\tau = 0.01$, and $(k, m) = (0.232, 0.116)$

intermittent layering is still observed during the smaller peaks, as the $(0, 2)$ layering mode remains elevated in S and ρ).

Figure 3.38 shows the results when $\gamma = 0.99$ ($R_\rho^{-1} = 1.01$) , which is close to the value of $\gamma = R_\rho^{-1} = 1$ at which the basic state becomes unstably stratified. In this case, the initial growth of the modes is more rapid than when $\gamma = 0.9$. The long-term behaviour of the modes is similar to that observed when $\gamma = 0.9$ in that a series of peaks is formed, each peak corresponding to a temporary layered state. The peaks are more frequent in the present example and are much more variable in size, indicating that a stronger basic state may produce more chaotic mixing.

It is informative to note that we see a layered state with all unstable values of γ. We also note here that the long-term behaviour of the modes is somewhat unaffected by the choice of initial conditions. By way of example, Figure A.9 shows the results at $\gamma = 0.9$ when the $(1,1)$ cellular mode is initialised with an amplitude of 10^{-20} in each perturbation. We see that layering modes are still generated in this system, and that once the $(0,2)$ layering modes increase in amplitude to a sufficient extent, modal interactions result in a rapid increase in amplitude of the cellular and layering modes, as observed previously. This growth is arrested when the modes reach the same amplitude as that of the elevator mode. Thereafter, the long-term behaviour is the same as that observed when using the initial conditions of NN. Indeed, regardless of the initial state taken (for instance, taking larger cellular modes than elevator modes), the system tends towards a state exhibiting intermittent layering, as shown and described above.

Summary of the Ninth-Order System Results

The ninth-order system is able to successfully reproduce results obtained by NN, which were obtained using a higher-order system of minimum order 12. We see the $(1,0)$ elevator and $(1,1)$ cellular modes initially grow exponentially and interact to generate, from an initial amplitude of zero, a $(0,1)$ layering mode in ψ' and $(0,2)$ layering modes in T and S. The layering modes are observed to grow until they are of a comparable amplitude to the cellular modes, at which point the cellular and layering modes rapidly increase in amplitude. Following the peak in amplitudes, certain modes are suppressed while the layering modes dominate in each perturbation. This leads to a layered state for a period of time, as indicated by the dominant density perturbation (ρ') modes over the same period of time.

We have shown here that including $(0,2)$ layering modes in ψ' and $(0,1)$ layering modes in T' and S', as in NN, is not vital for initiating layer formation via a growth and eventual dominance of layering modes in the system. It was suggested by NN that layering modes overtake and eventually dominate in the system, though it was unclear from their results whether the layering modes would continue to dominate thereafter. Thus, it was unclear, following the instantaneous layered state, whether the layering mode would be immediately disrupted, continue to grow, or otherwise remain noticeably elevated. Our low-order system not only reproduces the results of NN, but also shows that the layered state may not be so easily disrupted once it is formed, and the layered state persists for a substantial period of time. Once a layered state is disrupted, the layering modes are stimulated once again by interactions between growing elevator and cellular modes, which leads to intermittent layering over time.

Our study has shown how the introduction of exponentially-growing elevator modes to the 5th-order system of Veronis (1965) leads to a generation and growth of other modes in the system. The $(1, 0)$ (elevator) and $(1, 1)$ (cellular) modes in ψ first interact to generate the $(0, 1)$ layering mode, a_3. This is essentially a shear mode. Growth of this mode causes the cellular modes to grow faster. In turn, a growth in all of the cellular modes results in a growth of the $(0, 2)$ mode, which eventually dominates. Thus, it appears that horizontal shear, at least at low amplitudes, has a reinforcing effect on the cellular motions, but eventually disrupts the elevator modes. Indeed, it was shown by Radko (2016) and subsequently by Brown and Radko (2019) that a static, diffusively stable basic state can become unstable to horizontal shear. Thus, the elevator modes here appear to be important merely in that they generate the horizontal shear mode, which then subsequently drives layer formation.

The ninth-order system appears to exhibit a local ‘overturning’ of density at step interfaces during a layered state. This was not observed in the 12-th order system of NN. This overturning may be representative of the initiation of mixing within a layer, or it may be indicative of the start of a layer-merging event. Furthermore, we saw in Figure 3.29 that, during the ‘layering’ phase, ‘tilted cells’ may be formed between regions of horizontal shear. The regions of shear essentially define layer boundaries, and within these layers we observe convective plumes that, in a higher-order system, would act to mix the layers. That is, it may be that the bounded region studied by Howard and Krishnamurti (1986) (and, indeed, by Veronis (1965) and Da Costa et al. (1981)) represents a single, long-lived diffusive layer. In which case, it would not be surprising for our system to behave in a similar way to the Howard and Krishnamurti (1986) system within each layer, once the layers have formed.

The scale of the layers we observe is small compared to that of layers observed in the ocean; however, simulations performed by Noguchi and Niino (2010b) suggest that fine-scale layers do emerge from a seemingly chaotic basic state, and that the layers merge to eventually form larger-scale layers. The presence of the locally unstable density gradients in our simulations is suggestive of further development of the fine-scale density staircase.

Increasing the strength of the linear background density gradient state, γ causes the peaks to occur sooner and more frequently, while as $\gamma \to 1$, the system appears to enter an increasingly chaotic state. It could be that higher-order modes that we have neglected in our truncation become more important at higher values of γ. It is very important to note here that as γ is increased towards 1 (or as R_ρ^{-1} is reduced towards 1), which is the points at which the global density gradient becomes top-heavy, the solutions most likely become increasingly unreliable as a model of double-diffusive convection. The Lorenz (1963) system, for example, fails as a model of convection well before the onset of chaos. However, as γ is reduced (or R_ρ^{-1} is increased) towards the critical point for marginal stability, the results of low-order models appear to be relatively reliable. Noguchi and Niino (2010a), for example, showed that their 12th-order system quite accurately reproduced the results of the full direct numerical simulations, at least until the modes reach large amplitudes. Indeed, at larger modal amplitudes, one might expect a heavily truncated system to be less reliable; however, we have shown here that our low-order model is able to capture convective ‘tilted cell’ motions within individual layers during the 'layering' phase. These motions have been observed in experiments of pure convection within a bounded region (Howard and Krishnamurti, 1986), while convective motions within layers have been observed in numerical experiments of double-diffusive convection (Noguchi and Niino, 2010a, Rosenblum et al., 2011). Thus, our relatively simple model appears surprisingly capable of capturing seemingly more complex behaviours.

The potency of our low-order model is suggestive that only a few modes are responsible for the initial formation of layers. That is, the initial formation of fine-scale layers appears to depend on relatively few modes; once formed, a different mechanism, such as the γ instability, may take over, causing the layers to evolve and eventually form long-lived density staircases.

3.6.2 Tenth-order system

It was noted briefly in § 3.5.3, that the modes in the 'aligned' tenth-order system behave differently to those in the 'misaligned' ninth-order system. Figure 3.39 shows the evolution of modes in the tenth-order system over a period of $t = 1500$.

The evolution comprises an exponential growth phase wherein the elevator and cellular modes grow in amplitude and interact with one another to generate layering modes in the T and S perturbations, as expected and as is consistent with the ninth-order system. We note that there no layering modes are generated in the ψ perturbation, and thus there is no horizontal shear in the system, except in the form of horizontally moving fluid due to the presence of cellular modes.

As the modes reach a similar amplitude to one another, there appears to be a burst of energy as each of the modes rapidly grows in amplitude. Again, this is somewhat consistent with the ninth-order system. This is followed by a sudden drop in amplitude

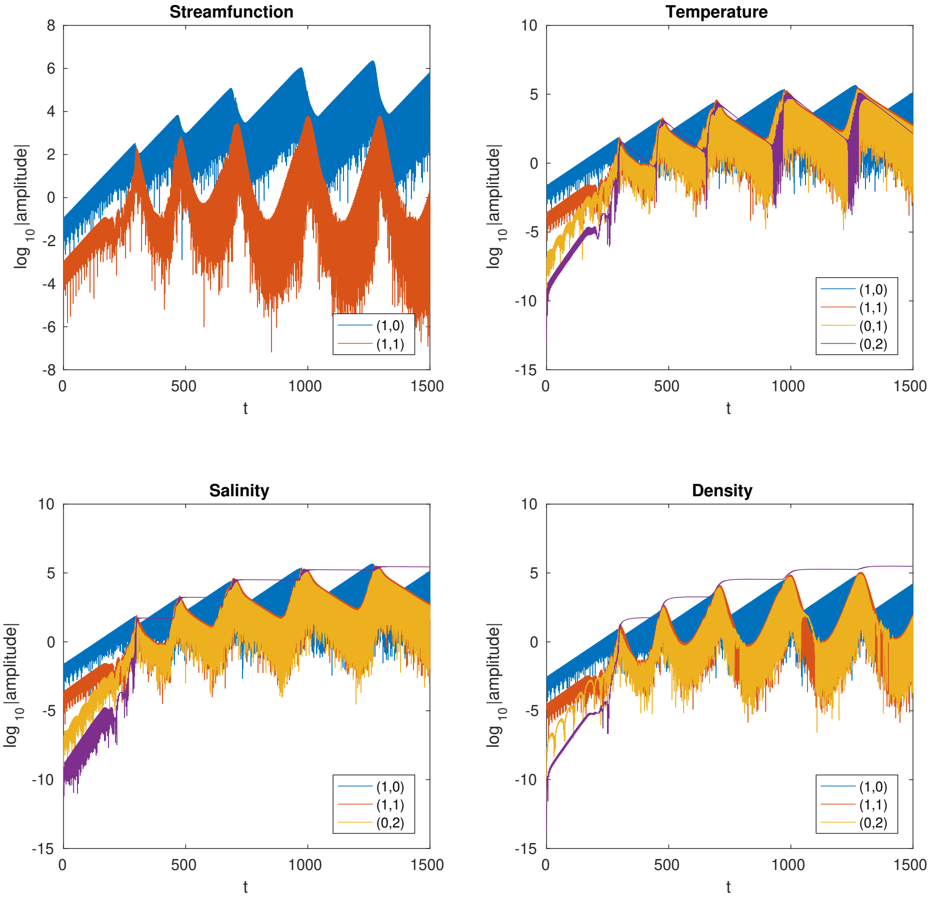

Figure 3.39: Evolution of modes in the 10th-order system with Simulated using $\gamma = 0.9$, $Pr = 7$, $\tau = 0.01$, $(k, m) = (0.187, 0.09)$, $\mathrm{RelTol} = 10^{-6}$ and $\mathrm{AbsTol} = 10^{-9}$.

of all modes except for the $(0, 2)$ layering mode in the salinity perturbation S (and thus in the density perturbation ρ'). The elevator mode then begins to grow exponentially once again in each perturbation, while the cellular and $(0, 1)$ layering modes continue to decay. This may be due to an incompatibility between the aligned elevator $(1, 0)$ and cellular $(1, 1)$ modes in the streamfunction perturbation.

By way of example, Figure 3.40 shows a schematic of modes in the streamfunction perturbation ψ' in the misaligned, 9th-order system (left) and the aligned, 10th-order system (right). The schematic shows coloured contours of streamfunction perturbation, along with arrows indicating the direction of fluid flow between streamlines of constant ψ'. The top row shows the cellular $(1, 1)$ modes alone, in each case, in the absence of elevator modes.

In the second row, low-amplitude elevator modes are introduced. The misaligned elevator modes in the schematic on the left hand side of figure 3.40, i.e. in the 9th-order system, cause fluid to flow in general alignment with rows of cells. The aligned elevator modes in the in the aligned, 10th-order system, result in a fluid flowing generally in-between the rows of cells.

In the third row, we show how the cellular modes begin to influence the elevator modes (and vice-versa). In the misaligned 9th-order system on the left, the elevator modes are able to follow the contours of the cellular modes and become wavy in structure, as we have seen already in § 3.6.1. In the aligned 10th-order system on the right, however, the elevator modes move *with* the flow adjacent to a first set of cells and then *against* flow adjacent to a second set of cells which are located in-between the cells in the first set in the vertical direction. The red arrows each show a direction of local flow which is opposite to that of a respective elevator mode at that point. Thus, the elevator modes tend to reinforce and ‘stretch’ certain cells, and to suppress and ‘compress’ certain other cells.

The fourth row of Figure 3.40 shows the approximate resulting structure When the elevator and cellular modes are of comparable amplitudes. It appears that misaligned elevator and cellular modes, as in the 9th-order system, may readily coexist, and may naturally reinforce one another for a period of time. Indeed, in the 9th-order system, as shown in § 3.6.1, the $(0, 1)$ layering mode in ψ' eventually grows, disrupts, and contributes to the suppression of the ψ' elevator mode. In the 10th-order system, it may

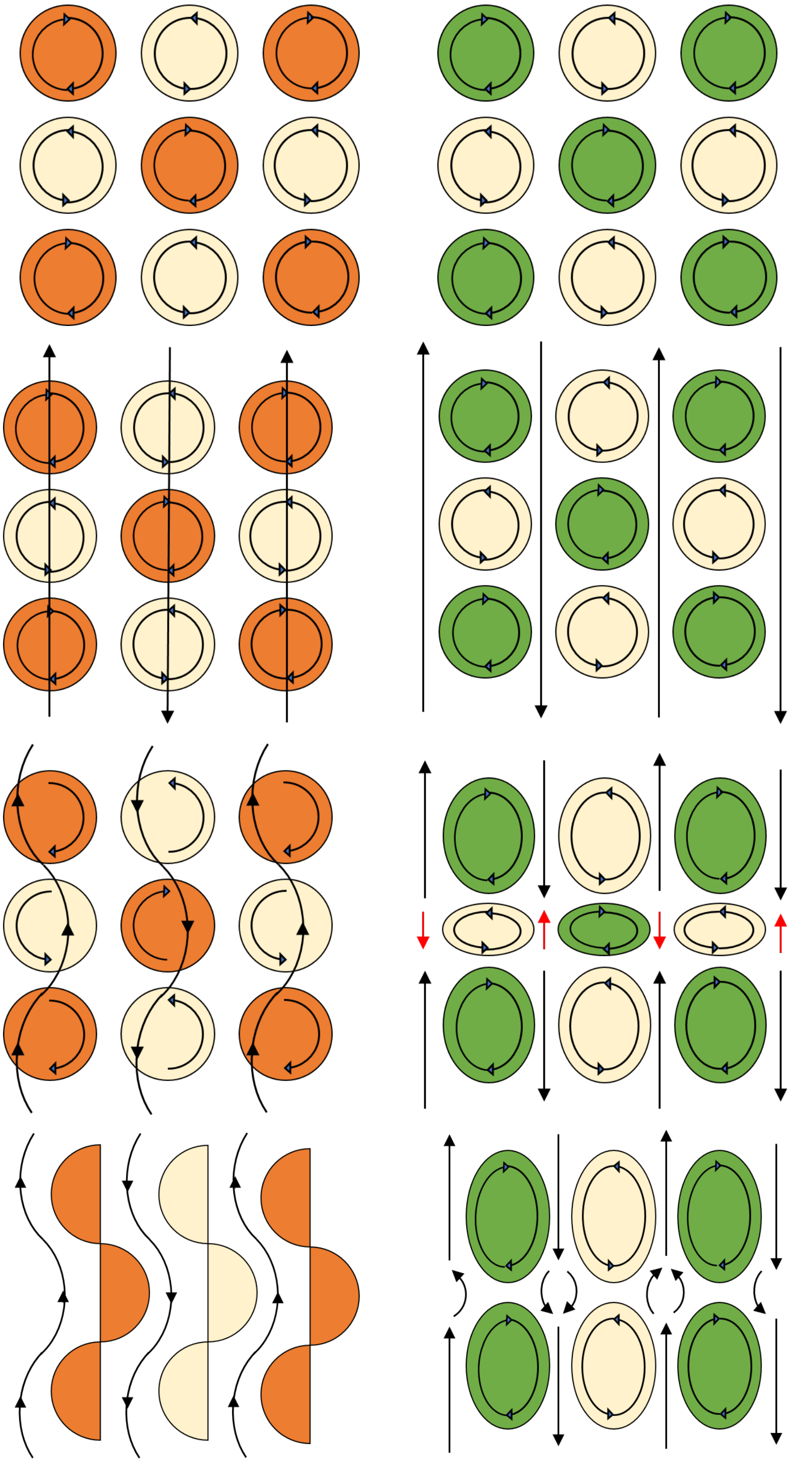

Figure 3.40: Schematic diagrams showing interactions of misaligned (left) and aligned (right) elevator and cellular modes in the streamfunction perturbation ψ'. The arrows show the direction of fluid flow along streamlines of constant ψ'. The aligned modes correspond to those in the 9th-order system, while the misaligned modes correspond to those in the 10th-order system.

be that the aligned cellular and elevator modes are incompatible with one another. That is, it may be that the cellular modes grow to disrupt the structure of the elevator modes, and vice-versa, due to locally opposing flows in certain regions.

As we see later when studying the 17th-order system—which includes both aligned and misaligned modes—such a configuration of elevator and cellular modes may not naturally arise. That is, it may be that forcing the elevator and cellular modes to be aligned, as in the 10th-order system, may produce interactions which are not representative of those that would naturally occur in double-diffusive convection. Regardless, we find it insightful to study the modal interactions and layering phenomena in the 10th-order system.

Returning to Figure 3.39, it appears that, following the first ‘peak’ of modes, all modes except for the $(0, 2)$ salinity rapidly drop in amplitude. The ψ' elevator mode is the first mode to begin growing once again. This is likely because there is no $(0, 1)$ layering mode in ψ', and so the elevator may grow relatively unimpeded. In contrast, in the 9th-order system, the elevator mode appears to be suppressed by the layering and cellular modes, and is unable to grow. The growth of the ψ' elevator mode in the 10th-order system corresponds to a decay of the cellular mode in each of the ψ', T', and S' perturbations. The $(0, 1)$ layering modes in T' and S' almost directly track the respective cellular modes, indicating that these modes are closely linked. Eventually, the $(0, 1)$ layering modes and cellular modes begin to grow once again, and the growth is faster than the linear growth rate of the cellular modes. This implies that certain interactions lead to the re-excitement of the cellular and layering modes and lead to another rapid-growth phase. The rapid growth phase is followed by a peak and the cycle repeats, as in the 9th-order system.

In-between the peaked states, the $(0, 2)$ layering mode in salinity remains dominant, appearing to gradually decrease in amplitude. This leads to the $(0, 2)$ layering mode remaining dominant in the density ρ' perturbation. Hence, even though the configuration of aligned cellular and elevator modes may not be a natural state of the system, the configuration still leads to intermittent ‘layering’ phenomena.

Stability of Simulations of the Tenth-order System

Investigations of the 10th-order system highlighted a number of issues with the solver. Firstly, the variable-time-step solver persistently selected a small time step throughout the simulation, meaning simulations would take much longer than those of the 9th- and 17th-order systems. Furthermore, simulations would regularly crash at large modal amplitudes, likely because the solver could not find a solution without reducing the time step below the specified tolerance.

In an attempt to gain a deeper understanding of these issues, we studied the behaviour of individual modes both during the exponential growth phase, and during peaks. Figure 3.41 shows the evolution of modes in the 10th-order system without a logarithmic scaling, and without taking an absolute magnitude of the modes. The initial exponential growth of elevator modes is clearly visible, as is the eventual dominance of the $(0, 2)$ layering mode in S' and ρ' (and, indeed, to some extent in T'). Each subsequent peak is larger in amplitude than the previous peak, though as seen in Figure 3.39 the peaks eventually appear to reach an upper limit.

Figure 3.42 shows a close-up view of a section of the streamfunction perturbation ψ' plot between around $t = 435$ to $t = 470$. In this region, the amplitudes of the $(1, 0)$ elevator modes actually reach (non-dimensional) amplitudes of approximately 5000; hence, the vertical blue lines in Figure 3.42 show the elevator modes only as they pass through zero. Strikingly, we see here that the cellular $(1, 1)$ mode is highly oscillatory compared to the elevator mode, and that both the amplitude of and frequency of the oscillations is related to the amplitude of the elevator mode.

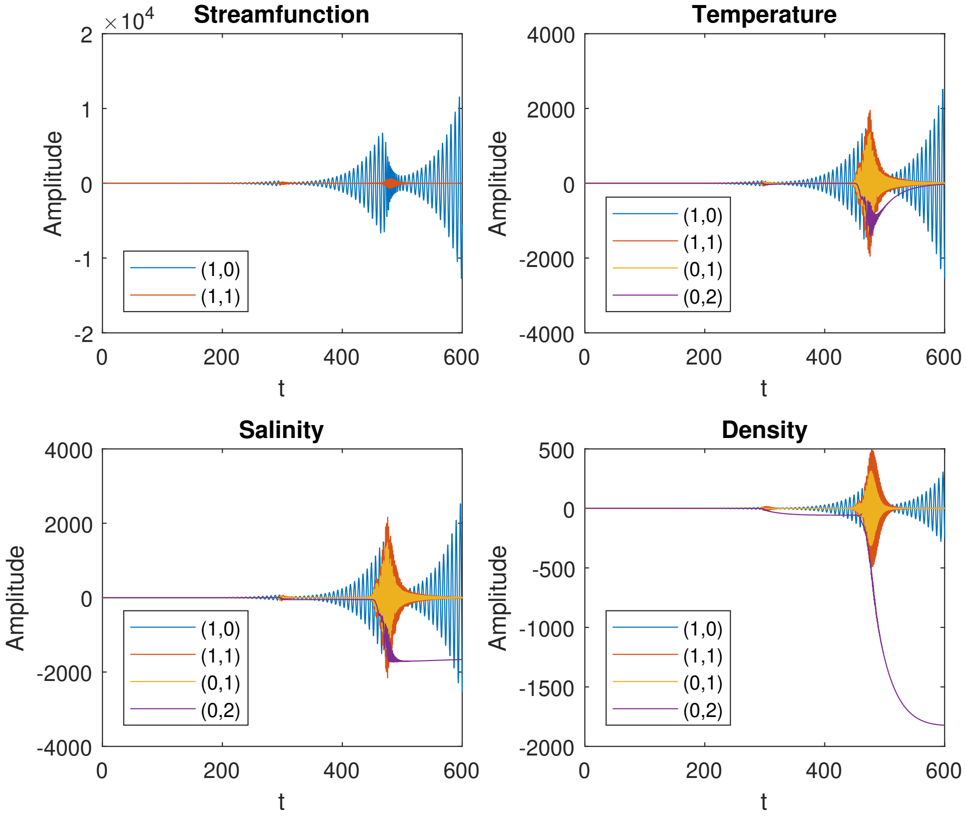

Figure 3.41: Evolution of modes in the tenth-order system with $\gamma = 0.9$, $Pr = 7$, $\tau = 0.01$, $(k, m) = (0.187, 0.09)$, $\mathrm{RelTol} = 10^{-6}$ and $\mathrm{AbsTol} = 10^{-9}$.

We see that as the elevator modes reach maximum amplitude (i.e. in between the vertical lines of Figure 3.42), the frequency of the cellular mode increases and the amplitude decreases. The amplitudes of the cellular modes tend to increase again when the elevator mode is close to zero, while the frequency decreases. The opposite is observed in the Temperature T' and Salinity S perturbations. Figure 3.43 shows the temperature perturbation in a similar region in which we see that, as well as the cellular $(1, 1)$ and $(0, 1)$ layering modes tracking one another, the frequency of the modes increases as the elevator mode passes through zero. This may be because the b_1 elevator mode is out-of-phase with the a_1 elevator mode, and the high-frequency motions that we observe are influenced more by the amplitude of the a_1 elevator mode.

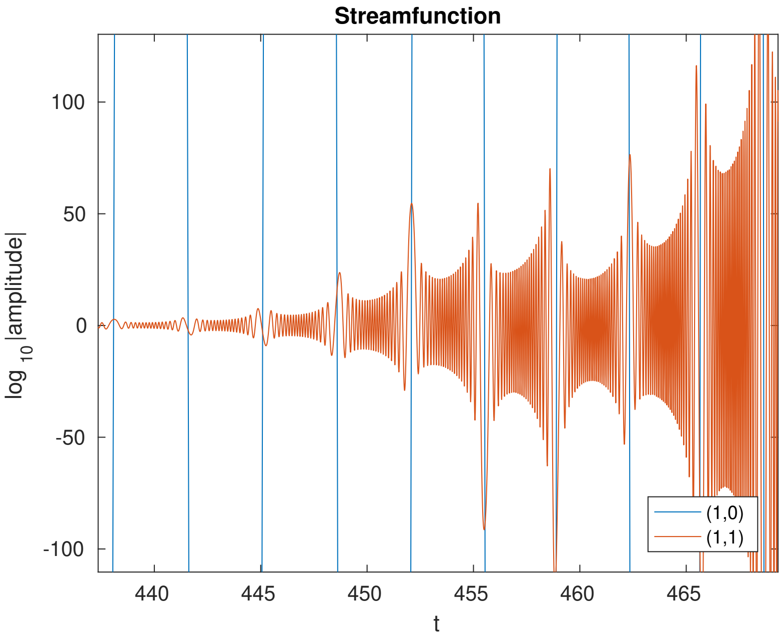

Figure 3.42: Evolution of modes in the streamfunction ψ' perturbation in the 10th-order system between $t = 435$ and $t = 470$, showing highly oscillatory cellular modes. Simulated using $\gamma = 0.9$, $Pr = 7$, $\tau = 0.01$, $(k, m) = (0.187, 0.09)$, $\text{RelTol} = 10^{-6}$ and $\text{AbsTol} = 10^{-9}$.

In order to further study the link between the amplitude of the elevator mode and and the frequency of the cellular mode, we here look at the number of times the cellular mode in ψ passes through zero in-between each ‘cycle’ of the elevator mode. By way of example, Figure 3.44 shows the x-axis intersects (corresponding to zero-crossings) of the elevator mode (top) and the cellular mode (bottom), extracted from our results.

For each sequential pair of zero-crossings in the elevator mode, we obtain the number of zero-crossings of the cellular mode between the pair of crossings, and the average value of t between the pair of crossings. This allows us to plot the number of crossings of the cellular mode against a respective value of t, thereby producing a representation of the change in frequency of the cellular mode over time. Figure 3.45 shows such a plot between $t = 0$ and $t = 700$ (top), along with a plot of the maximum value of the elevator mode at the same points in time (bottom), for comparison.

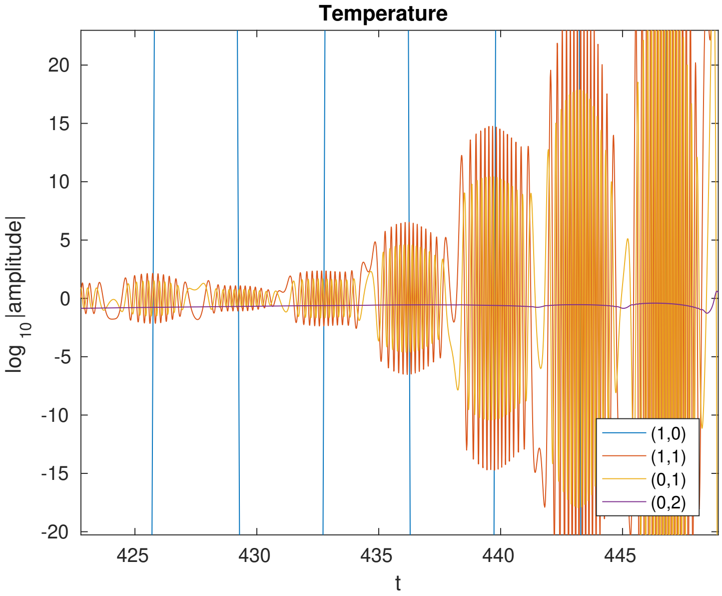

Figure 3.43: Evolution of modes in the temperature T' perturbation in the 10th-order system between $t = 424$ and $t = 450$, showing highly oscillatory cellular and layering modes. Simulated using $\gamma = 0.9$, $Pr = 7$, $\tau = 0.01$, $(k, m) = (0.187, 0.09)$, RelTol $= 10^{-6}$ and AbsTol $= 10^{-9}$.

Qualitatively, it is clear that the frequency (represented by a number of zero-crossings) of the $(1, 1)$ cellular mode in ψ' is directly proportional to the amplitude of the $(1, 1)$ elevator mode in ψ'. This behaviour is not observed in either the 9th- or 17th-order system, and so this phenomenon appears to be a symptom of forcing the elevator and cellular modes to be aligned in the x-direction.

We conclude by noting that the highest frequencies were observed when the amplitudes of modes became large, such as during peaks. When simulating the system using `ode45`, time to simulate is large due to the small time steps required to resolve the high-frequency oscillations. The simulations regularly crash when the modes reach a significant amplitude, regardless of the value of γ chosen. It is therefore difficult to simulate the 10th-order system over large periods of t.

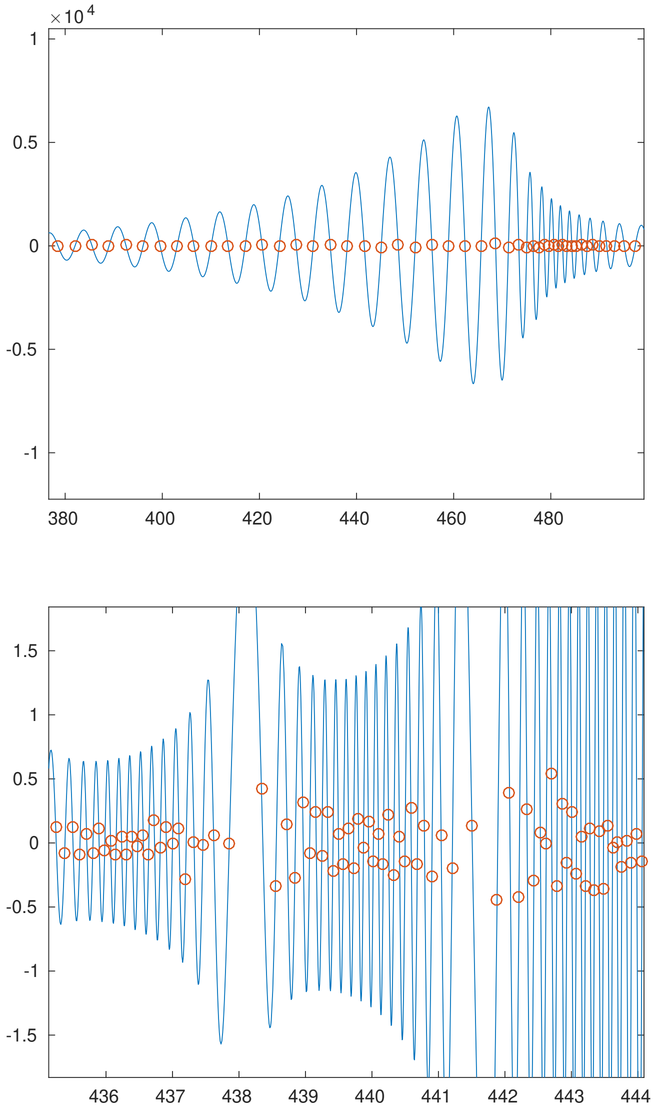

Figure 3.44: Evolution of modes in the streamfunction ψ' perturbation in the 10th-order system, highlighting points where the elevator (top) and cellular modes (bottom) pass through zero. Simulated using $\gamma = 0.9$, $\mathrm{RelTol} = 10^{-6}$, $\mathrm{AbsTol} = 10^{-9}$.

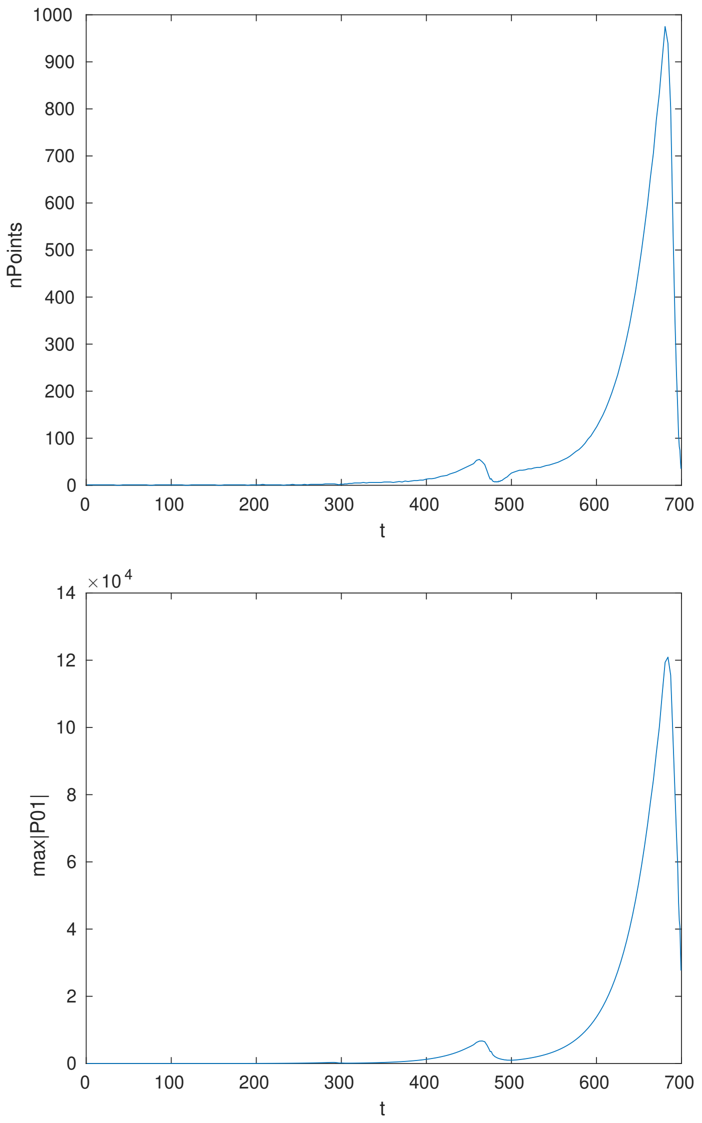

Figure 3.45: **Top:** Number of zero-crossings ('nPoints') of the cellular mode between a pair of zero-crossings of an elevator mode in the 10th-order system as a function of time, t. **Bottom:** Maxmimum value of the ψ' elevator mode in the 10th-order system over time. Results shown between $t = 0$ and $t = 700$, and simulated using $\gamma = 0.9$, $\mathrm{RelTol} = 10^{-6}$, $\mathrm{AbsTol} = 10^{-9}$.

We instead simulate the system using a different solver, `ode113`, which is a variable time-step *and* variable order solver. The solver uses an Adams-Bashforth-Moulton PECE solver of orders 1 to 13, meaning that the system is solved using up to a 13th-order scheme, depending on the error at each time step. The `ode113` solver is thought to be more efficient than the `ode45` solver at stringent tolerances or if the ODE function is particularly expensive to evaluate, as is the case here due to the high-frequency $(1, 1)$ cellular modes (Shampine and Gordon, 1975, Shampine and Reichelt, 1997). We see that `ode113` is readily able to solve the 10th-order system, even when the amplitudes are large and frequencies are high. This allows us to study the evolution of modes over larger periods of time, for instance to see whether the sequentially larger 'peaks' eventually reach an upper limit. Using `ode45`, only two or three peaks may be observed. The results presented in this section were all obtained using `ode113`, due to the unsuitability of the `ode45` solver.

Summary of the Tenth-order System Results

The particular alignment of elevator and cellular modes that leads to the 10th-order system appears to result in a unique evolution of modes over time. The cellular mode is observed to oscillate with a frequency that is linked to the instantaneous amplitude of the elevator modes. This leads to simulations which are particularly difficult to solve using low-order schemes when modal amplitudes are large. As shown in the schematic of Figure 3.40, the elevator modes, particularly when strong, tend to cause localised flow reversals in cells of the cellular mode, thereby disrupting the cellular mode. The cellular mode may then regrow with cells rotating in the opposite direction. The repeated suppression of cellular modes may lead to the high frequency oscillations of cellular modes observed in the 10th-order system.

We see in the following section that no such high-frequency mode is observed in the 17th-order system, and that the 17th-order system behaves more like the 9th-order system than the 10th-order system. This is suggestive that it is not a preferred configuration of the system to have elevator and cellular modes which are ‘aligned’. The dependency of the frequency of the cellular mode on the amplitude of the elevator mode raises questions with regard to the stability of the elevator modes themselves. In Chapter 5, we study the secondary modes arising from a basic state consisting entirely of oscillatory elevator modes. We ask whether the secondary modes generated are oscillatory, and whether the frequency of the oscillations are dependent on the amplitude of the elevator mode. In summary, we find that the frequency of the secondary modes are not dependent on the amplitude of the elevator mode. This further reinforces the idea that the alignment of modes in the 10th-order system is not a preferred state.

3.6.3 Seventeenth-order system

Including both aligned and misaligned elevator and cellular modes in the truncated model leads to a 17th-order system. The 17th-order system comprises a $(0,2)$ layering mode in T' and S', as is the case in each of the 9th- and 10th-order systems. The 17th-order system further comprises a $(0,1)$ layering mode in ψ', generated from the misaligned sets of modes, and a $(0,1)$ layering mode in T' and S', generated from the aligned sets of modes.

Figure 3.46 shows the evolution of modes in the 17th-order system when $\gamma = 0.9$, for ease of comparison with the results from the lower-order systems discussed hereinbefore. The amplitudes of the elevator modes are represented as a sum of squares of the individual elevator modes, and similarly for the cellular modes. For example, the amplitudes of the elevator and cellular modes in the streamfunction perturbation, ψ'_e and ψ'_c say, are taken to be

$$\psi'_e = \sqrt{a_1^2 + a_2^2} \qquad \text{and} \qquad \psi'_c = \sqrt{a_3^2 + a_4^2}. \tag{3.16}$$

The modes in Figure 3.46 are therefore representative of the combined effect of aligned and misaligned modes. We see that, as with the lower-order models, the elevator and cellular modes interact in the 17th-order system to generate layering modes from zero

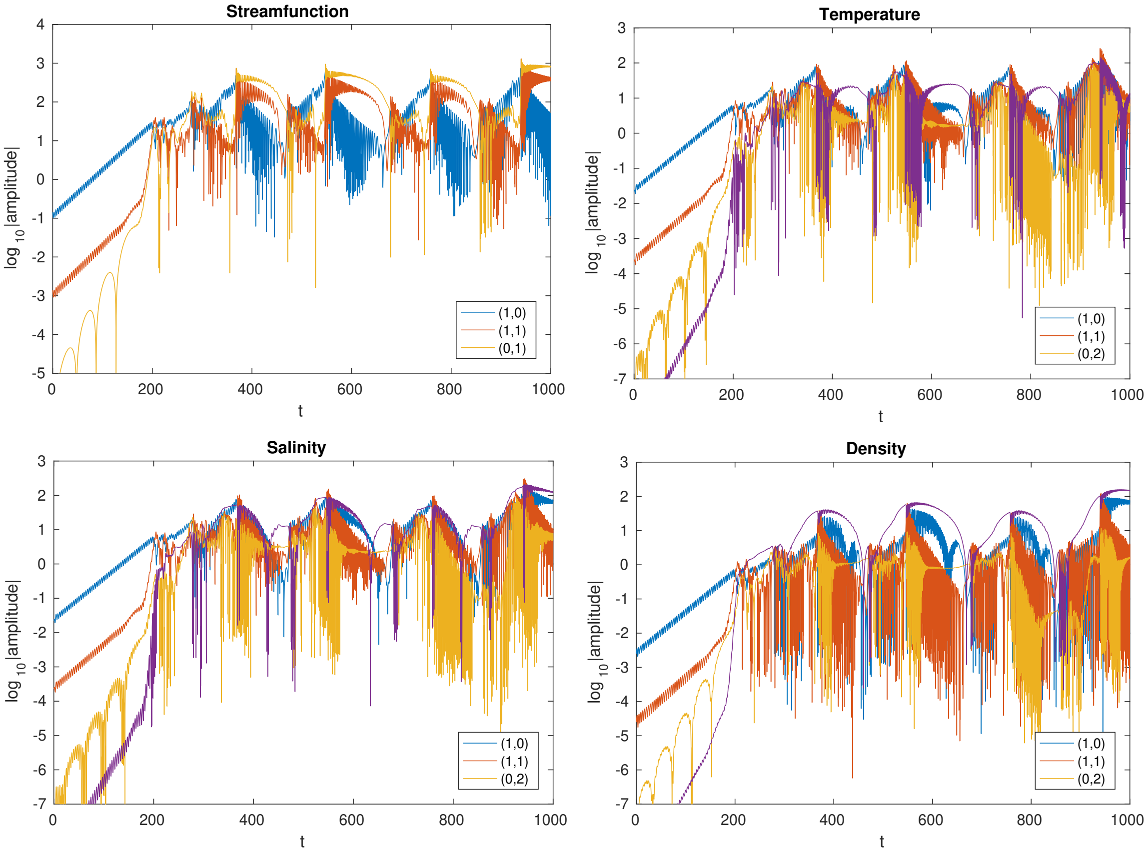

Figure 3.46: Evolution of modes in the ψ', T', S' and ρ' perturbations in the 17th-order system when $\gamma = 0.9$.

amplitude. These modes grow faster than the elevator and cellular modes and eventually overtake, leading to ‘peaks’ and intermittent layering reminiscent of the behaviour of modes in the 9th-order system.

The behaviour of modes differs between the two systems in that the peaks in the 17th-order system are more frequent. It appears that the layering modes decay more quickly in the layered states in the 17th-order system than in the 9th-order system. Furthermore, in-between the peaks in the ψ' perturbation, there is a period during which the elevator mode grows in amplitude and the cellular mode decreases in amplitude.

This is also seen in the 9th-order system to some extent during the accelerated growth phase. 0th-order system and is not observed in the 9th-order system. Thus, it appears that the 'aligned' sets of modes, although seemingly incompatible, still interact with one another during the simulation to generate and influence the $(0, 1)$ layering modes in T and S.

Thus, it appears that the modes in the 17th-order system behave most similarly to those in the 'misaligned' 9th-order system, and the 'aligned' modes merely influence the periodicity of the layered state. Furthermore, we do not observe a high-frequency cellular mode whose frequency is dependent on the amplitude of an elevator mode, as in the 10th-order system. We conclude that the modes in the 10th-order system alone are unrepresentative of those arising in the early stages of double-diffusive convection. The modes in the 9th-order system, on the other hand, appear to be most influential in the initial formation of a layered state.

Reducing the 17th-order System

The 17th-order system reduces exactly to 9th and 10th order system when appropriate modes are set to zero, both in the system of ODEs and in the simulations. That is, initialising only the 'misaligned' elevator and cellular modes in the 17th-order system at non-zero amplitude, and initialising the 'aligned' modes at zero amplitude, the misaligned modes never grow. In this way, the associated layering modes never grow, and the system behaves exactly as in the aligned 9th-order system.

If we take such a reduced seventeenth-order system and perturb, at low amplitude, a single elevator mode that is horizontally aligned with the existing cellular mode, then the elevator mode grows and eventually generates, through nonlinear interactions, the remaining modes which are present in the 17th-order system. Figures 3.47 and 3.48 show, over different time periods, the evolution of modes when the 17th-order system is

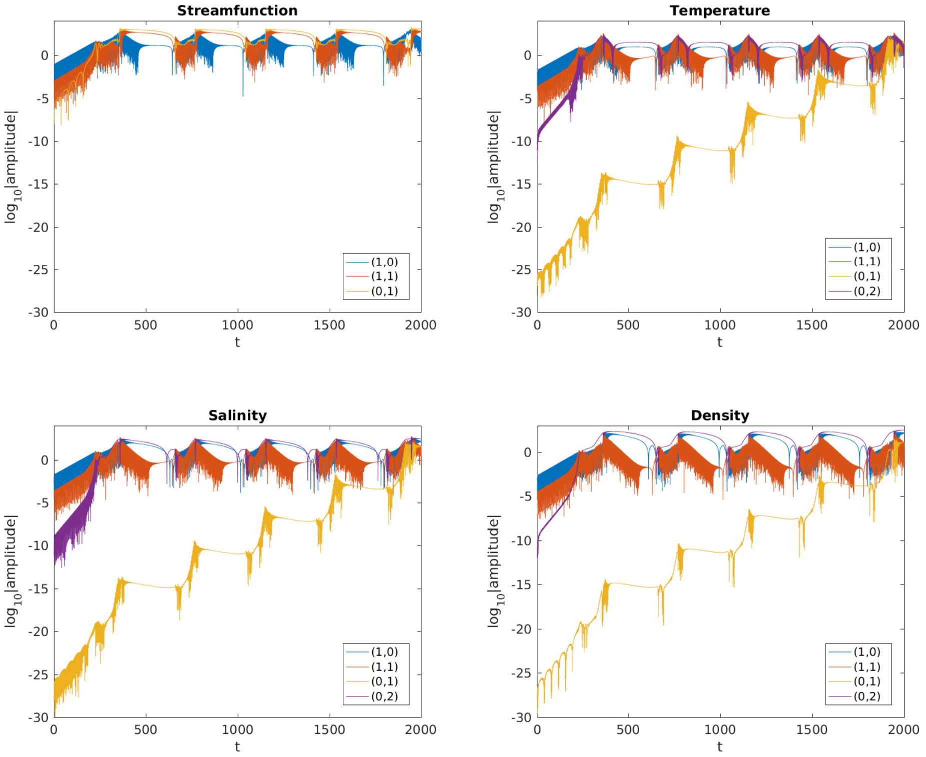

Figure 3.47: Evolution of modes between $t = 0$ and $t = 2000$ in the 17th-order system which has been reduced to a 9th-order system by appropriate initialisation of modes, when $\gamma = 0.9$. An ‘aligned’ elevator mode in ψ' has been initialised as a small-amplitude perturbation.

reduced to 9th-order, and wherein one of the aligned elevator modes in ψ' is initialised as a small-amplitude perturbation, i.e. $a_1 \ll 1$.

Initially, we see that the modes evolve as in the 9th-order system, except that a low-amplitude $(0, 1)$ cellular mode exists and is growing over time. The other low-order modes which are generated are not visible in these Figures, as the total amplitudes of cellular and elevator modes are shown as the root sums of squares of respective modal amplitudes, for clarity.

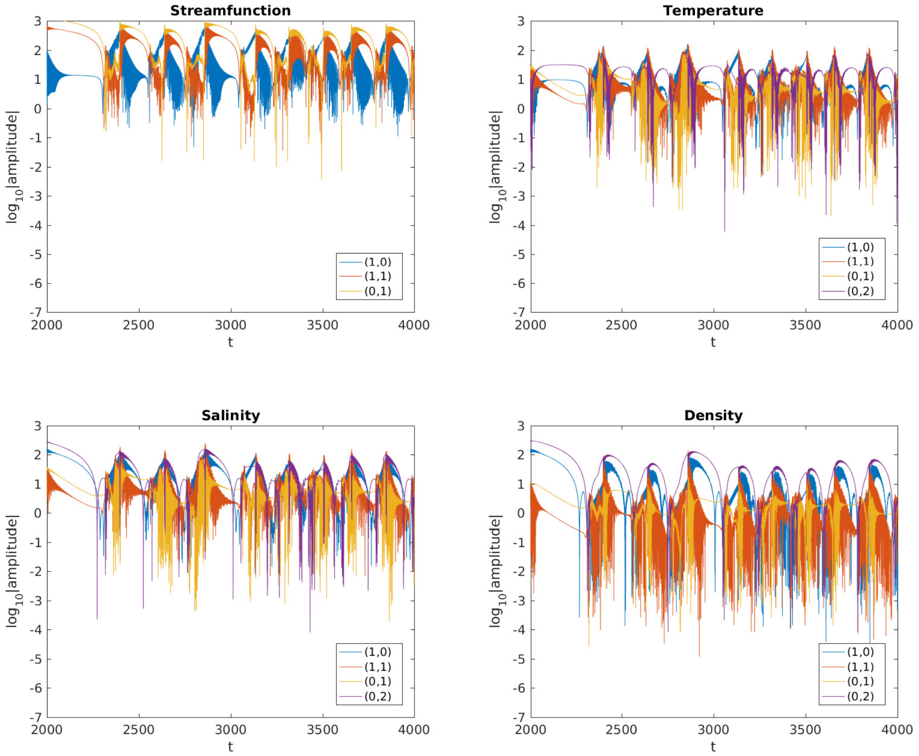

Figure 3.48: Evolution of modes between $t = 2000$ and $t = 4000$ in the 17th-order system which has been reduced to a 9th-order system by appropriate initialisation of modes, when $\gamma = 0.9$. An 'aligned' elevator mode in ψ' was initialised as a small-amplitude perturbation, and has generated other modes which have grown to eventually constitute the 17th-order system.

The $(0, 1)$ layering mode in T' and S' is excited from zero-amplitude by interactions between the low-amplitude elevator mode a_1 and a corresponding *horizontally-aligned* cellular mode, which already exists, to generate a $(0, 1)$ layering mode in T and S. This layering mode was observed to form in the aligned 10th-order system. The layering mode grows over time until it reaches the same amplitude as the other modes at around $t = 2000$. Following the peak at $t = 2000$, all modes which were generated via the perturbed elevator mode reach a similar amplitude, and the system thereafter behaves as in the full 17th-order system. This shows that, although the 9th-order system is able to reproduce layering phenomena on its own, the system is sensitive to small perturbations towards the 17th-order system. Regardless, the 17th-order system only marginally differs from the 9th-order system in terms of long-term behaviour, and so the former serves as a suitable, lower-order approximation to the full system, unlike the 10th-order system.

3.7 Equilibrium Points

The system studied by Veronis (1965) (and subsequently by Da Costa et al. (1981)) was found to have time-independent solutions. The 9th-, 10th- and 17th-order systems each reduce to the 5th-order Veronis system in the absence of elevator modes (i.e. $a1, b1, c1 = 0$); therefore, we would expect the equilibrium points of the Veronis system to be present in each of our models. We here determine the equilibrium points in the Veronis system, before working out the stabilities of these points in the 9th-order system.

3.7.1 Veronis System

If we take zero-amplitude elevator modes, i.e. $a_1 = b_1 = c_1 = 0$ in the 9th-order system (3.6), we see that $a_3 = -\sigma m^2 a_3$, which is a decaying mode, and

$$\begin{aligned} a_2' &= \frac{\sigma}{p}(r_T k b_2 - r_S k c_2 - p^2 a_2) \\ b_2' &= k m a_2 b_3 - p b_2 + k a_2, \\ b_3' &= -4 b_3 m^2 - \frac{1}{2} k m a_2 b_2, \\ c_2' &= k m a_2 c_3 - \tau p c_2 + k a_2, \\ c_3' &= -4 \tau c_3 m^2 - \frac{1}{2} k m a_2 c_2. \end{aligned} \tag{3.17}$$

This 5th-order system of equations is equivalent to that studied by Veronis (1965) under the transformation $a_2 \to -a_2$, with $k = \pi\alpha$ and $m = \pi$ (cf. equations (31) of Veronis (1965)). The transformation $a_2 \to -a_2$ arises due to the convention adopted by Veronis (1965) in equation (10), which leads to $\psi = -\psi$ in our notation.

Equations (3.17) similarly match equations (11) of Da Costa et al. (1981) under the following transformations:

$$\begin{aligned} a_2(t) &= \frac{2}{k}(2p^{\frac{1}{2}})a(t*), \\ b_2(t) &= 2\left(\frac{2}{p}\right)^{\frac{1}{2}} b(t*), \qquad & b_3(t) &= -\frac{1}{m}c(t*), \\ c_2(t) &= 2\left(\frac{2}{p}\right)^{\frac{1}{2}} d(t*), \qquad & c_3(t) &= -\frac{1}{m}e(t*), \end{aligned} \tag{3.18}$$

with $k = \frac{\pi}{\lambda}$, $m = \pi$ and $t* = pt$. See equations (8)–(10) of Da Costa et al. (1981).

We determine steady-state solutions to equations (3.17) by first setting the time derivatives equal to zero, i.e. $a_2' = b_2' = b_3' = c_2' = c_3' = 0$. We then rearrange the equations to find

$$\begin{aligned} b_2 &= \frac{ka_2}{p + \frac{k^2}{8}a_2^2}, \qquad & b_3 &= -\frac{k}{8m}a_2 b_2, \\ c_2 &= \frac{ka_2}{\tau p + \frac{k^2}{8\tau}a_2^2}, \qquad & c_3 &= -\frac{k}{8\tau m}a_2 c_2, \end{aligned} \tag{3.19}$$

and hence,

$$\begin{aligned} (a_2^2)^2 + 8a_2^2\left(\frac{p}{k^2}(\tau^2+1) + \frac{1}{p}(\tau r_S - r_T)\right) \\ + 64\left(\frac{\tau^2 p^2}{k^4} + \frac{1}{pk^2}(\tau r_S - \tau^2 r_T)\right) = 0, \end{aligned} \tag{3.20}$$

which is a quadratic equation in a_2^2. This is equivalent to equation (35) in Veronis (1965) and equation (21) in Da Costa et al. (1981) under the transformations set out above. Thus, for given values of r_T, r_S, k and m, we can find equilibrium values of a_2 from equation (3.20), and thereby also equilibrium values of b_2, b_3, c_2 and c_3 from equations (3.19). In this way, we are able to identify the equilibrium points of the Veronis (1965) system that exist in our higher-order systems, and also determine their respective stabilities.

3.7.2 Stability of Equilibrium Points

To determine the stability of the equilibrium points, we determine the (complex) eigenvalues of the matrix $M = \frac{\partial \mathbf{x}'}{\partial \mathbf{x}}$, where $\mathbf{x} = \{a_2, b_2, b_3, c_2, c_3\}$, i.e.:

$$M = \begin{bmatrix} -\sigma p & \frac{\sigma k r_T}{p} & 0 & \frac{-\sigma k r_S}{p} & 0 \\ kmb_3 + k & -p & kma_2 & 0 & 0 \\ -\frac{kmb_2}{2} & -\frac{kma_2}{2} & -4m^2 & 0 & 0 \\ kmc_3 + k & 0 & 0 & -\tau p & kma_2 \\ -\frac{kmc_2}{2} & 0 & 0 & -\frac{kma_2}{2} & -4\tau m^2 \end{bmatrix}. \tag{3.21}$$

If any one of the eigenvalues has a positive real part, then the equilibrium point is unstable; otherwise, the equilibrium point is stable. We substitute the equilibrium values of a_2, b_2, b_3, c_2 and c_3, determined using equations (3.19) and (3.20), into the matrix M and calculate the eigenvalues numerically using the MATLAB function `eig`.

Since equation (3.20) is quadratic in a_2^2, we find two 'sets' of equilibrium values of a_2^2, each set having positive and negative values of a_2. We find that the sign of a_2 in each set does not change the respective growth rates of the equilibrium points. This is to be expected, as the 5th-order system of equations (3.17) is invariant under the transformation that reverses the signs of a_2, b_2 and c_2, while leaving b_3 and c_3 unchanged (Da Costa et al., 1981). Therefore, we here only take positive values of a_2. The Veronis (1965) system is fifth-order, so substituting the equilibrium points into the matrix M in equation (3.21) and calculating the determinant of the matrix results in two sets of five complex eigenvalues.

We determine the stability of the Veronis equilibrium points in the 9th-order system by calculating the eigenvalues of a corresponding 9×9 matrix, M, initialised at the Veronis equilibrium points. We are interested to know whether there are any stable (unstable) equilibrium points in the 5th-order system that are unstable (stable) in the 9th-order system. To do this, for a given choice of parameters, R_ρ^{-1}, Pr, τ, k and m, we determine the Veronis equilibrium points and associated eigenvalues in both the 5th- and 9th-order systems. We then take the maximum real part of each set of eigenvalues. If this is positive, the solution is unstable; if this is negative, the solution is stable. In this way, we can compare the growth rates of the eigenvalues in the 5th order with those in the 9th- order system over a range of different parameters.

Figure 3.49, for example, shows such a comparison over a range of wavenumbers, k and m, when $\gamma = 0.9$ ($R_\rho^{-1} = 1.11$), $Pr = 7$, and $\tau = 0.01$, which correspond to values used in simulations of the 9th-order system in § 3.6. The upper and lower rows of Figure 3.49 show the results for first and second 'sets' of equilibrium points, respectively. In each case, the figures on the left show the growth rates of the equilibrium points in the 5th-order system, while those on the right show the corresponding growth rates in the 9th-order system. The white areas of the plots highlight parameter ranges in which there are either no real (i.e. no non-complex) equilibrium points, or the equilibrium points are stable.

In each of the first and second sets, the only equilibrium points having real values are located in a semi-elliptical region between $0 < m < 1$ and $0 < k < 0.62$. Outside of this region, the eigenvalues are stable. Interestingly, although not shown here, the extent of this region changes vary little as R_ρ^{-1} and Pr are varied in a combination that results in an unstable static basic state for a given value of k (that is, when Rrm satisfies equation (2.52). We have also observed that the equilibrium values in the second set have identical stability characteristics in both the 5th- and 9th-order systems for every combination of parameters that we have tried in this study. That is, the growth rates of equilibrium points in the second set appear unaffected by the additional modes and interactions present in the 9th-order system. Therefore, in the following figures, we only show results obtained using the first set.

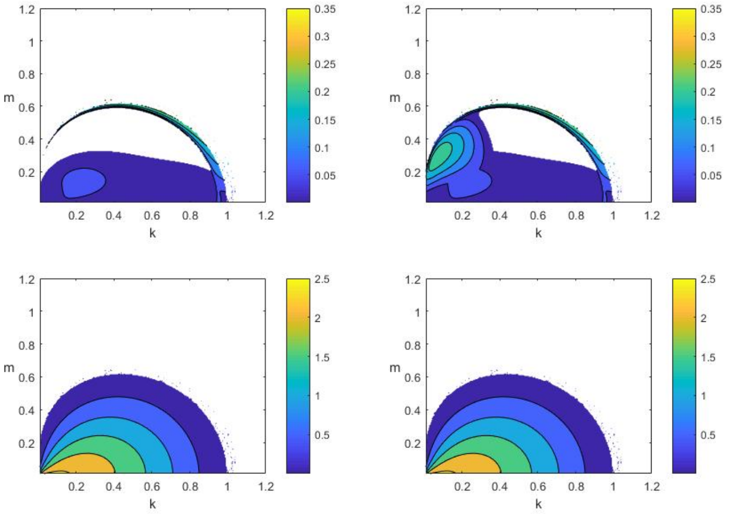

Figure 3.49: rates of Veronis equilibrium points as a function of k and m in LEFT: the 5th-order system and RIGHT: the 9th-order system. The top and bottom rows show the results at first and second ‘sets’ of equilibrium points. The results were obtained using $R_\rho^{-1} = 1.11$, $Pr = 7$, and $\tau = 0.01$, which correspond to the values used in our simulations of the 9th-order system.

In the first set, we do see that some of the equilibrium points that are stable in the 5th-order system are unstable in the 9th-order system. One such value is at $(k, m) = (0.2, 0.4)$. In the upper plots of Figure 3.50, we show the growth rates of equilibrium points at different values of R_ρ^{-1} and Pr using these wavenumbers (keeping $\tau = 0.01$). In the lower plots of Figure 3.50, we show the results using, instead, values of $(k, m) = (0.2, 0.1)$, which were shown in Figure 3.49 to give unstable equilibrium points in both the 5th- and 9th-order systems.

The black lines show the curves of marginal stability of the basic state for constant k, given by equation 2.52 in Chapter 2. When $(k, m) = (0.2, 0.4)$ there does not appear to be any clear change at either side of the marginal stability curve; however, at lower values of m, we do begin to see two distinct regions separated by the marginal stability curve. Specifically, in the lower plots of Figure 3.50, the behaviour in the 9th-order

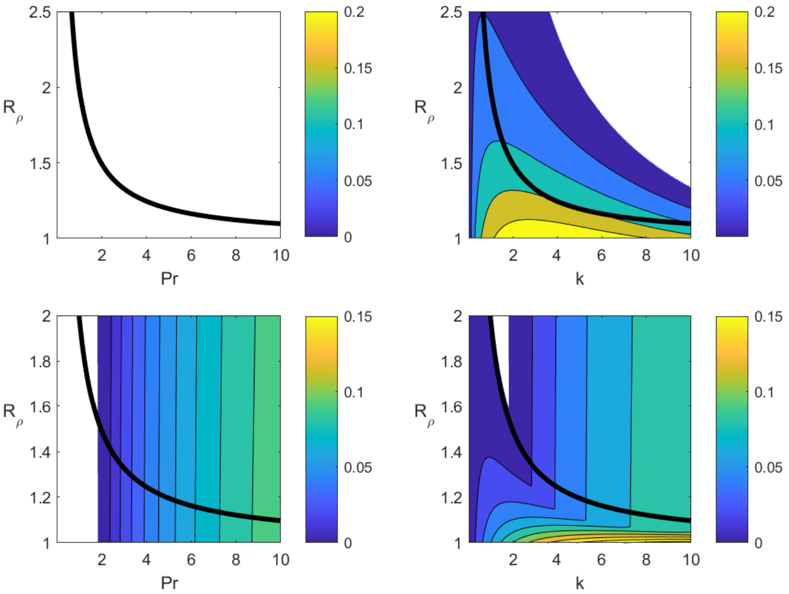

Figure 3.50: Growth rates of Veronis equilibrium points as a function of R_ρ^{-1} and Pr in LEFT: the 5th-order system and RIGHT: the 9th-order system. The top and bottom rows show the results at $(k, m = 0.2, 0.4)$ and $(k, m) = (0.2, 0.1)$, respectively.

system outside (above) the curve is the same as that in the 5th-order system, while the growth rates within (beneath) the curve differ in each case. The growth rates are larger in the 9th-order system within the marginal stability curve. This is likely because in the 9th-order system, the static basic state is most unstable to elevator modes within the curve, i.e. modes with $m = 0$. As $m \to 0$, the modes within the marginal stability curve take on larger growth rates, while outside the boundary, where the elevator modes are not growing, the equilibrium points behave in the same way as they would in the 5th-order system. Thus, we see that the equilibrium points in the 9th-order system are always unstable in the presence of growing elevator modes, while in the 5th-order system, *sans* elevator modes, these equilibrium points may be stable.

The same behaviour is observed, perhaps to a greater extent, when looking at the growth rates of the equilibrium points in the 9th-order system while varying both R_ρ^{-1} and k_x when $m << 1$. Figure 3.51, for example, shows results with $m = 0.001$ when

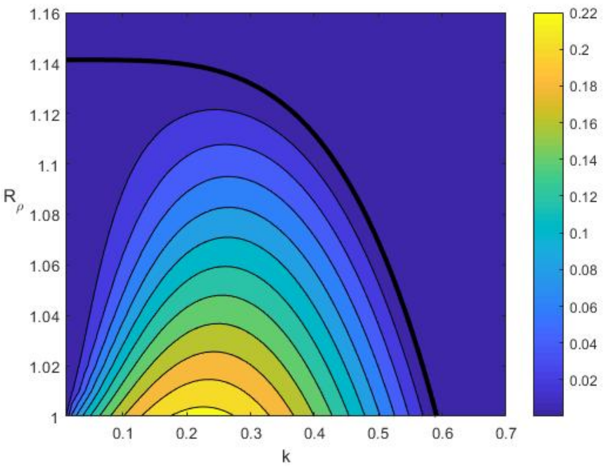

Figure 3.51: Growth rates of Veronis equilibrium points as a function of R_ρ^{-1} and Pr in the 9th-order system. Values of $m = 0.001$, $Pr = 7$ and $\tau = 0.01$ were employed in this case.

$Pr = 7$ and $\tau = 0.01$. This should be contrasted with Figure 2.4 of Chapter 2 which shows the stability of the static basic state to elevator modes under the same conditions. Clearly, the growth rates within the boundary at low values of m correspond to the growth rates of the primary elevator mode instabilities of the basic state, which are not present in the 5th-order system.

It would be interesting to study the behaviour of these equilibrium points further, for example in the 10th- and 17th-order systems, though such an in-depth study lies outside the scope of this thesis. We here conclude that, as might be expected, under certain conditions—particularly, but not exclusively as $m \to 0$—the Veronis equilibrium points that are ordinarily stable in the 5th-order system can be destabilised in the 9th-order system. This appears to be, at least in part, due to the effects of growing elevator modes in the 9th-order (and higher) system(s).

3.8 Discussion

In this Chapter, we have shown that seemingly complex phenomena, such as the formation of layers from a chaotic state, may be reproduced by relatively low-order models. We have observed the formation of layers using models as low as 9th and 10th-order, where previous models such as that described by Noguchi and Niino (2010a) used up to 32 modes (decomposing into 12 modes at minimum). We see that the fastest-growing mode from linear theory—an elevator mode $(1, 0)$—interacts nonlinearly with a cellular mode $(1, 1)$ to generate a number of layering modes $(0, 1)$ and $(0, 2)$. The layering modes generated depend on the particular alignment of elevator and cellular modes. In each case, the layering modes grow faster than the cellular and elevator modes and eventually overtake, leading to a 'layered' state comprising a dominant layering mode in the density perturbation.

Our models readily reproduce the results of Noguchi and Niino (2010a) using fewer modes. Our models differ from those of Noguchi and Niino (2010a) in that a different approach was taken to obtain the ODE system to be solved. In the latter study, the modes were identified from a direct numerical simulation of the governing equations. In contrast, we extended the work of Da Costa et al. (1981) and Veronis (1965) who studied a minimal representation of double-diffusive convection using a fifth-order model, but who did not observe layering. The addition of elevator modes to this system resulted in the generation of layering modes, indicating that elevator modes are an essential component of layer formation in double-diffusive systems. Elevator modes are the fastest-growing modes in double-diffusive convection, and have long been speculated as essential components in the formation of layers. Our study supports this speculation, and shows that very few additional modes may be required to form layering or vertical staircase structures in diffusive systems.

Additionally, our models extend the work of Noguchi and Niino (2010a) to look at the behaviour of modes once an initial layered state has been reached. We see that once all modes in the system reach the same amplitude, the $(0, 2)$ layering mode overtakes and dominates for a period of time, particularly in the 9th- and 17th-order models. This corresponds with a suppression of certain other modes. The layering mode eventually decays, leading to a growth of the other modes in the system. Eventually, all modes reach a similar amplitude and grow together to once again form a layered state. This process repeats indefinitely.

Such intermittent layering suggests that the $(0, 2)$ layering mode is relatively persistent once it has grown to a sufficient amplitude. Indeed, the direct numerical simulations of Noguchi and Niino (2010a) show that the $(0, 2)$ layering mode continues to grow in amplitude once it has overtaken the other modes. The lack of higher-order modes in our system means that we do not see this continued growth and evolution; however, our models do show that the system is always trying to evolve to a layered state, even in the presence of very few low-order modes.

It is informative to note that the elevator modes do not continue to grow indefinitely, and appear to be disrupted by the other modes in the system, particularly during a first ‘peak’ preceding the layered state. This appears to support the findings of Radko and Smith (2012) who showed, using direct numerical simulations, that an amplitude of salt-fingers (corresponding to elevator modes) is equilibrated following a rapid growth in energy in a diffusive system.

We have shown that, during the layered state, the modes appear to exhibit ‘tilted cell’ behaviour reminiscent of that in pure convection studied by Howard and Krishnamurti (1986). This suggests that our low order model is able to pick up certain convective motions within the layers once they have formed. Furthermore, we have shown that certain stable equilibrium points of the 5th-order Veronis (1965) system are unstable in the 9th-order system. Some of our simulations suggest the existence of fixed points in the 9th-order system, particularly when m is small. It would be of interest for future study to determine the equilibrium points of the 9th-order system (if there are any) and work our their stability.

We conclude by noting that this study assumes cellular modes having the same horizontal wavenumber as the elevator modes exist at the same time as elevator modes. This is indeed suggested by the simulations of Noguchi and Niino (2010a). However, since the fastest growing modes in a double-diffusive system are elevator modes, and since the elevator modes would grow indefinitely in the absence of other modes according to linear theory, we ask whether the cellular modes would be generated directly by the elevator modes, or whether they arise due to other interactions. Indeed, the link between the frequency of the cellular modes and the amplitude of the elevator modes in the 10th-order system may be indicative that the cellular modes are generated as secondary instabilities of the elevator modes. On the other hand, Radko (2016) shows that layers may form in the presence of horizontal (i.e. vertically-dependent) shear modes, and in the initial absence of elevator modes. It may be that such layering modes, for example the $(0, 1)$ layering mode in ψ', are generated as secondary instabilities of elevator modes and therein cause the system to become more unstable.

In light of the above questions, in the following Chapters we shift our focus from the evolution of modes in different systems instead to the stability of elevator modes themselves. In Chapter 4 we begin by studying the stability of elevator modes in the salt-finger regime, rather than in the diffusive regime as has been studied in this Chapter. This is partly because the elevator modes in the salt-finger regime are non-oscillatory, thereby providing a simpler context in which to develop our methods, and partly because we discovered gaps in the literature surrounding the use of such methods in the study of salt-fingering convection. We extend this work in Chapter 5 to study the secondary modes arising from oscillatory elevator modes, and link the results back to the findings of the present chapter.

CHAPTER 4

Instabilities of Non-Oscillatory Elevator Modes

4.1 Introduction

The linear stability of a static basic state was discussed in §2.3.6. The elevator mode is the fastest growing mode in a doubly-periodic domain in both the salt-finger and the oscillatory regimes. The Jacobian terms in the governing equations—for instance the term $J(\psi, \nabla^2\psi) = (\partial_x\psi\partial_z\nabla^2\psi - \partial_z\partial\nabla^2\psi)$—are all zero, because ∂z is zero for any elevator mode. Therefore, no additional modes are generated through nonlinear interactions and the elevator mode represents a full solution to the governing non-linear equations. Mathematically, the elevator modes may grow indefinitely and exponentially. The linear stability model does not account for secondary instabilities generated by the primary elevator mode. It is informative to take a basic state consisting of fully developed elevator modes and to study the growth of any secondary perturbations to this state. Such a study seeks to identify the form of the fastest growing secondary modes, which grow in amplitude and eventually disrupt the primary elevator modes. Stern and Simeonov (2005) studied the fastest growing secondary modes arising from a salt-finger basic state. The authors computed a vertical wavelength of the fastest growing secondary instability by integrating a system of linear partial differential equations (PDEs) with time-dependent and horizontally periodic coefficients. It was suggested that the fastest growing secondary instability limits the amplitude of the primary mode. It is this philosophy that is applied in the present chapter.

Taking a basic state consisting of the primary instability in the form of a sinusoidal (in x) elevator mode introduces spatially periodic coefficients into a set of ODEs governing the behaviour of secondary modes. Solutions to such equations may be sought using Floquet theory, in which perturbed variables are expanded in an infinite sum of harmonics, leading to an infinite set of equations for the growth rates of different modes. Approximate solutions may obtained by truncating the system and solving numerically for the growth rate. The fastest-growing secondary mode may then be identified as that having the largest real growth rate. Floquet theory and similar methods have been employed in numerous studies to solve ODEs having periodic coefficients. Examples include: the solution of the Matthieu equation in Stoker (1950), page 201; the solution of the generalised Orr-Sommerfeld equation governing viscous plane parallel flows (Orszag, 1971); plane Couette and Poiseuille flows (Davey, 1973, George and Hellums, 1972); flat Stokes Layers (Blennerhasset and Bassom, 2002); and Kolmogorov flow (Beaumont, 1981).

The theory was applied to double-diffusive convection by Holyer (1984). Holyer used Floquet theory to study the stability of elevator modes in the salt-finger regime. The basic state was taken to comprise steady elevator modes, i.e. modes having zero growth rate. A later study by Veronis (1987) looked at a similar problem taking instead the fastest-growing elevator mode as the basic state, while Kerr (1992) applied Floquet theory to study instabilities in steady double-diffusive interleaving. The collective instability described in Chapter 1 was the primary focus of the Holyer (1984) study. It was found that at relatively low Prandtl numbers of $Pr = 10$—as encountered in the ocean—the collective instability, i.e. a mode having horizontal and vertical values of wavenumber (k and m in Holyer's notation) of order $\mathcal{O}\left(10^{-3}\right)$, was never the fastest growing secondary mode (FGSM). Rather, the fastest growing secondary mode at $Pr = 10$ was found to have a horizontal wavenumber of zero, and a vertical wavenumber of $m = 0.3$. At large Prandtl number (e.g. $Pr = 10^4$), Holyer found that the collective instability was the dominant mode. The Holyer study, although informative, was limited in that only a small selection of secondary instabilities were investigate over a narrow range of governing parameters. This was most likely due to limitations in computational ability at the time.

We here extend Holyer's results in several ways. First, we examine the other secondary instabilities that arise from a steady elevator basic state—including those that are not fastest growing—using the parameters employed by Holyer. We then vary the strength of the background T and S gradients (in the form of R_ρ^{-1}), the Prandtl number

Pr, and the amplitude of the elevators A_ψ, thereby deriving a more complete picture of the relationship between governing parameters and secondary modes. We contrast the results with those arising from a system in which the basic state is the *fastest-growing* elevator mode, rather than a steady elevator mode. This also permits a comparison of our results with those obtained by Veronis (1987) for fastest-growing elevators.

Finally, we look at the importance of heat and salt in such systems by contrasting the fastest-growing secondary mode arising from a double-diffusive elevator basic state with that arising instead from a purely hydrodynamic shear mode. The basic state in the hydrodynamic system is prescribed in the same way, by taking a horizontally-dependent, sinusoidal shear flow; however, we no longer consider the influence of heat and salt. This type of flow is known as Kolmogorov flow (Beaumont, 1981, Meshalkin and Sinai, 1961, Thess, 1992). In Kolmogorov flow, a single equation describes the evolution of the streamfunction perturbation in terms of a Reynolds number Re. As we shall see, the Reynolds number here is analagous to the Prandtl number in diffusive convection. We find that Kolmogorov flows generate secondary modes which are similar to those arising from double-diffusive elevator modes, albeit less unstable.

Further instances of Floquet theory as applied to double-diffusive convection are found in, for example: Radko and Stern (2011) and Radko (2016), in which studies the authors investigate the instabilities arising when a vertically dependent shear mode is applied to a double-diffusive domain; Radko and Smith (2012), in which the authors study the saturation of the linear growth of salt fingers, and whose results we reproduce in this chapter; and Xie et al. (2017) and Xie et al. (2019) in which reduced models are obtained and studied in the salt-finger regime. We refer to these studies throughout the present chapter.

4.2 Secondary Instabilities

In Chapter 2 we looked at the stability of a static basic state, showing that the fastest growing mode—an elevator mode—grows indefinitely. In other words, elevator modes represent fully non-linear solutions to the perturbation equations (4.24)–(4.26). This means that the perturbation may instead be represented as a linear combination of an elevator mode ($A\cos(k_x x)$), and a secondary perturbation. Thus, we have

$$\begin{aligned} \psi &= \bar{A_\psi}\cos(k_x x) + \psi', \\ T &= \bar{A_T}\sin(k_x x) + T', \\ S &= \bar{A_S}\sin(k_x x) + S', \end{aligned} \tag{4.1}$$

where $\bar{A_\xi} = A_\xi e^{\lambda_0 t}$ for $\xi = \{\psi, T, S\}$, and λ_0 is the growth rate of the primary, elevator instability. In this chapter, we are interested in non-oscillatory convection in the salt-finger regime, meaning that λ_0 is real. Furthermore, we are interested in secondary instabilities that grow faster than the primary elevators; in other words, if we take $\lambda_0 = 0$ and we find that the growth rates of secondary perturbations are large in comparison to the growth rate of elevator modes from linear theory, then the fingers will be 'quasi-steady' for the time it takes perturbations to grow (Holyer, 1984). Hence, substituting perturbations in the form of (4.1) into the perturbation equations (4.24)–(4.26) and linearising, under the assumption of a quasi-steady basic state ($\lambda_0 = 0$), yields

$$\begin{gathered} \left(\frac{\partial}{\partial t} - Pr\nabla^2\right)\nabla^2\psi' = k_x A_\psi \sin(k_x x)\frac{\partial}{\partial z}\nabla^2\psi' + k_x^3 A_\psi \sin(k_x x)\frac{\partial \psi'}{\partial z} + Pr\left(\frac{\partial T'}{\partial x} - \frac{\partial S'}{\partial x}\right), \\ \left(\frac{\partial}{\partial t} - \nabla^2\right)T' + \mathrm{sgn}(T_z)\frac{\partial \psi'}{\partial x} = k_x A_\psi \sin(k_x x)\frac{\partial T'}{\partial z} + k_x A_T \cos(k_x x)\frac{\partial \psi'}{\partial z}, \\ \left(\frac{\partial}{\partial t} - \tau\nabla^2\right)S' + \mathrm{sgn}(S_z)\frac{\partial \psi'}{\partial x}R_\rho^{-1} = k_x A_\psi \sin(k_x x)\frac{\partial S'}{\partial z} + k_x A_S \cos(k_x x)\frac{\partial \psi'}{\partial z}. \end{gathered} \tag{4.2}$$

4.2.1 Floquet Theory

Floquet theory is employed to solve PDEs with periodic coefficients—a form consistent with (4.2) above. The coefficients in (4.2) are independent of z and t, so we can seek solutions with ψ, T, and S proportional to $\exp(ik_z z + \lambda t)$, where k_z and λ are the vertical wavenumber and the growth rate of the secondary perturbation, respectively.

The periodicity of the coefficients lies in the x-direction, with a period of $2\pi/k_x$. It has been shown by Coddington and Levinson (1955) that for a linear homogeneous system system with periodic coefficients, e.g.

$$\dot{x} = A(t)x \qquad (-\infty < t < +\infty), \tag{4.3}$$

where A is a matrix of complex continuous functions, and

$$A(t+T) = A(t), \tag{4.4}$$

where T is the period, then if $\phi(t)$ is the fundamental matrix for (4.3), so is $\phi(t+T)$. The matrix $\phi(t)$ is a fundamental matrix of (4.3) if $\dot{\phi}(t) = A(t)\phi(t)$, so that $x = \phi(t)c$ for some constant vector c. Corresponding to every such ϕ there exists a periodic non-singular matrix P with period T, and a constant matrix μ such that

$$\phi(t) = e^{\mu t} P(t). \tag{4.5}$$

The system studied in this Chapter is periodic in x, and so our solutions $\xi' = (\psi', T', S')$ will be of the form

$$\xi' = e^{\mu x} P(x), \tag{4.6}$$

where μ is called a 'Floquet coefficient', and P is periodic in x with period $X = 2\pi/k_x$. Such a P is obtained through the expansion

$$P(x) = \sum_{n=-\infty}^{\infty} \xi_n \exp(ink_x x), \tag{4.7}$$

where $n \in \mathbb{Z}$. In this way, if μ is replaced by $\mu + 2\pi i/X$, then we get

$$\xi(x)' = e^{\mu t} P(x) \exp(2\pi i t/X), \tag{4.8}$$

where $P(x)\exp(2\pi i t/X)$ is still periodic with period X, and the fact that μ is not unique does not alter our results.

Instead of defining μ in the range $0 < \mu < ik_x$ (as above), we find it convenient to take $\mu = ifk_x$ and instead vary f between 0 and 1. The Floquet coefficient then becomes f, rather than μ. Combining this solution with that of $\xi' \propto \exp(ik_z z + \lambda t)$ as previously defined, we find that solutions to (4.2) may be written in the Floquet form

$$\begin{pmatrix} \psi' \\ T' \\ S' \end{pmatrix} = \exp(ifk_x x + ik_z z + \lambda t) \sum_{n=-\infty}^{\infty} \begin{pmatrix} \psi_n \\ T_n \\ S_n \end{pmatrix} \exp(ink_x x), \tag{4.9}$$

4.2.2 Application to the Quasi-Steady Equations

On substitution of (4.9) into equations (4.2), the periodic coefficients—which represent a single elevator mode in x—are, in a sense, absorbed into the infinite sum. By way of example, the $\sin(k_x x)$ term in the coefficient $k_x^3 A_\psi \sin(k_x x)$ interacts with $\frac{\partial \psi'}{\partial z}$ as follows:

$$\begin{aligned} \sin(k_x x)\frac{\partial \psi'}{\partial z} &= \sin(k_x x)\frac{\partial}{\partial z}\left(\exp(ifk_x x + ik_z z + \lambda t) \sum_{n=-\infty}^{\infty} \psi_n \exp(ink_x x)\right), \\ &= ik_z \exp(ifk_x x + ik_z z + \lambda t) \cdot \sin(k_x x) \sum_{n=-\infty}^{\infty} \psi_n \exp(ink_x x). \end{aligned}$$

For clarity, we can define $B = k_z \exp(ifk_x x + ik_z z + \lambda t)$, giving

$$\begin{aligned} iB\sin(k_x x) \sum_{n=-\infty}^{\infty} \psi_n e^{ink_x x} &= \frac{B}{2}\left(e^{ik_x x} - e^{-ik_x x}\right) \sum_{n=-\infty}^{\infty} \psi_n e^{ink_x x}, \\ &= \frac{B}{2} \sum_{n=-\infty}^{\infty} \left(\psi_n e^{i(n+1)k_x x} - \psi_n e^{i(n-1)k_x x}\right). \end{aligned}$$

Summation indices may be shifted to recover a factor of $\exp(ik_x x)$ in each term, i.e.

$$\sum_{n=-\infty}^{\infty} \psi_n e^{i(n+1)k_x x} \equiv \sum_{n=-\infty}^{\infty} \psi_{n-1} e^{ink_x x} \quad \text{and} \quad \sum_{n=-\infty}^{\infty} \psi_n e^{i(n-1)k_x x} \equiv \sum_{n=-\infty}^{\infty} \psi_{n+1} e^{ink_x x}.$$

Thus, the $\sin(k_x x)$ term and the $\frac{\partial \psi'}{\partial z}$ term combine to be written instead in terms of modal amplitudes. That is,

$$\sin(k_x x)\frac{\partial \psi'}{\partial z} = \frac{B}{2}\sum_{n=-\infty}^{\infty}\left[\psi_{n-1} - \psi_{n+1}\right] e^{ink_x x}. \tag{4.10}$$

In other words, the growth rate of any particular secondary mode (ψ_n, say) is a function of the amplitudes of neighbouring modes (ψ_{n-1} and ψ_{n+1}). Similar expressions may be obtained for each of the periodic coefficients in (4.2). With this in mind, substituting the perturbations expressed in Floquet form (4.9) into the governing PDEs (4.2)—noting that $\mathrm{sgn}(T_z) = \mathrm{sgn}(S_z) = 1$ in the salt fingering regime—we obtain the following infinite set of equations for the growth rate of secondary perturbations λ, in terms of the modal amplitudes ψ_n, T_n and S_n:

$$\begin{aligned} -\lambda\psi_n = Pr K_n^2 \psi_n - \frac{k_x k_z A_\psi}{2K_n^2}\left[K_{n-1}^2\psi_{n-1} - K_{n+1}^2\psi_{n+1}\right] \\ + \frac{k_x^3 k_z A_\psi}{2K_n^2}\left[\psi_{n-1} - \psi_{n+1}\right] + iPr\frac{(f+n)k_x}{K_n^2}(T_n - S_n), \end{aligned} \tag{4.11}$$

$$\begin{aligned} \lambda T_n = -K_n^2 T_n + \frac{k_x k_z A_\psi}{2}\left[T_{n-1} - T_{n+1}\right] \\ + \frac{ik_x k_z A_T}{2}\left[\psi_{n-1} + \psi_{n+1}\right] - i\ \mathrm{sgn}(T_z)(f+n)k_x\psi_n, \end{aligned} \tag{4.12}$$

$$\begin{aligned} \lambda S_n = -\tau K_n^2 S_n + \frac{k_x k_z A_\psi}{2}\left[S_{n-1} - S_{n+1}\right] \\ + \frac{ik_x k_z A_S}{2}\left[\psi_{n-1} + \psi_{n+1}\right] - i\ \mathrm{sgn}(S_z)R_\rho^{-1}(f+n)k_x\psi_n, \end{aligned} \tag{4.13}$$

where $K_n^2 = [(f+n)k_x]^2 + k_z^2$. The equations are solved with numerical techniques described in §4.3. λ may be real or complex. If the real part of any of the calculated growth rates $\Re(\lambda) > 0$, then the system will be unstable and secondary perturbations will grow. The (f, k_z) mode with the largest positive value of λ will be the fastest growing secondary mode under the given conditions. Note that f need only be varied between 0 and 0.5.

Equations (4.11)–(4.13) are the same as those solved by Holyer (1984) under the following notational changes: $R_\rho^{-1} \to \gamma^{-1}$, $k_x \to 1$, $k_z \to m$, $f \to k$, and $A_\psi \to W$. Holyer solved these equations along the $f = 0$ and $k_z = 0$ axes to determine the fastest growing mode in: the heat-salt system with $Pr = 10$ and $\tau = 0.01$; in the salt-sugar system with $Pr = 1000$, $\tau = 1/3$; and in a high-Pr system with $Pr = 10^4$ and $\tau = 0.01$. Holyer showed results in each of these systems for single values of R_ρ^{-1} and A_ψ, and only along the $f = 0$ and $k_z = 0$ axes. Here we extend this work by studying the effects of varying R_ρ^{-1} and A_ψ on the form of the secondary instabilities over a full range of wavenumbers and for different Prandtl numbers.

Holyer also scaled the governing equations such that the basic state was marginally stable (meaning that the basic state elevator modes have zero growth rate) when $k_x = 1$. Here, our system is marginally stable for a different value of k_x that is dependent on the value of R_ρ^{-1}, due to the way we have scaled our equations. Furthermore, it is unnecessary to assume that the basic state is marginally stable, so we extend the work to obtain solutions to the equations when k_x is chosen to give the *fastest-growing* basic state for a given R_ρ^{-1} (under a quasi-steady approximation). The methods by which we achieve extensions to the work of Holyer are described hereinafter.

4.3 Numerical Implementation and Convergence

To solve our infinite set of equations numerically, we first truncate the expansion (4.9) at a level of truncation, N, where $n \in \{-N, N\}$. Collecting individual Fourier components, we then express these equations in the matrix form

$$\lambda\eta = \boldsymbol{A}\eta, \tag{4.14}$$

where

$$\eta = (\psi_{-N}, ..., \psi_{n-1}, T_{n-1}, S_{n-1}, \psi_n, T_n, S_n, ..., S_N)^T$$

and $\boldsymbol{A}$ is the square matrix of size $3(2N+1)$ obtained from (4.11) - (4.13), and is a function of (k_x, k_z, f, R_ρ, τ, Pr, N, A_ψ, A_T, A_S).

4.3.1 Solver

The truncated matrix form (5.9) lends itself well to implementation in MATLAB using in-built eigenvalue solvers. In particular, MATLAB offers two functions for obtaining eigenvalues and eigenvectors. The first, `eig`, computes all eigenvalues of the non-symmetric matrix A using QZ-factorisation, normalising the eigenvectors to Euclidian length 1. The function `eigs` instead uses an iterative method to return only a subset of eigenvalues. This was first thought to be useful in that we could request, say, only the 5 largest positive eigenvalues and thereby reduce computational demand; however, `eigs` was later found to be either slower or negligibly faster than `eig`. For this reason, we herein obtain results using the function `eig`.

The code for the MATLAB program is written such that a user specifies the driving parameters, including R_ρ^{-1} and the amplitude of the basic state elevator mode A_ψ. The values of A_T and A_S are calculated from A_ψ using equations (2.43). The values of τ and Pr default to oceanic parameters of 0.01 and 10 respectively; however, we later study the effect of varying these parameters. The ranges of f and k_z to be studied are specified by the user, along with a desired resolution. Owing to the symmetry of the system, f need only be varied between 0 and 0.5. However, in verifying the code we may at times take $0 \leq f \leq 1$ to ensure that the results are symmetrical about $f = 0.5$.

The MATLAB program calculates eigenvalues for each specified (f, k_z) mode. This is achieved by iterating over f and k_z at the chosen resolution, calculating the matrix A at each point, and calculating the determinant of the matrix A using either `eig` or `eigs`. As discussed hereinbefore, `eig` was found to be the most appropriate in the present study. The matrix A is initially truncated at a relatively low, user-selectable value of N. On calculating the eigenvalue for a single (f, k_z) mode, N is incremented by 1 and the eigenvalue is calculated again. This process is repeated until the difference between successive eigenvalues drops below a given tolerance, as discussed in section §4.3.2. The calculated eigenvalues are stored, and the program then moves on to the next (f, k_z) mode. This continues until all required eigenvalues have been calculated.

4.3.2 Convergence

In this section we demonstrate that the results we obtain are accurate and that the program is working correctly. We develop a range of techniques to achieve such confidence. Firstly, we compare preliminary results to those obtained by Holyer (1984) and Radko and Smith (2012), thereby showing a general agreement. We also ensure that the method is able to reproduce an exact, linear solution.

We then proceed to study the convergence of eigenvalues as N is increased. A pragmatic, largely qualitative approach is taken initially, whereby calculated growth rates are shown to be symmetrical about $f = 0.5$ for large enough N. A more quantitative method is then employed to pin-point the value of N at which eigenvalues change only negligibly with any further increase in N. We also highlight the structure of the eigenvectors as a way to gain a deeper understanding of the convergence, paying particular attention to modal magnitudes at extreme values of N.

Verification

As an initial check on the accuracy of our code, we compare our results with those of Holyer (1984) at different values of N. Results are compared for a single set of parameters only—we take oceanic conditions of $Pr = 10$ and $\tau = 0.01$, as used by Holyer, along with $R_\rho^{-1} = 0.02$ and $A_\psi = 4$, which correspond respectively to $\gamma = 0.5$ and $W = 4$ in Holyer's notation. We determine growth rates along the $f = 0$ and $k_z = 0$ axes, with $0 \leq k_z \leq 0.5$ and $0 \leq f \leq 0.5$, respectively. The results are shown in Figure 4.1, and corresponding plots from Holyer (1984) are displayed in Figure 4.2.

Our results are in good agreement with those of Holyer, particularly at higher values of N. The growth rates presented in Figure 4.1b overlap when $N = 9$ and $N = 12$. This suggests that $N \geq 9$ is sufficient to ensure convergence when $f = 0$. For context,

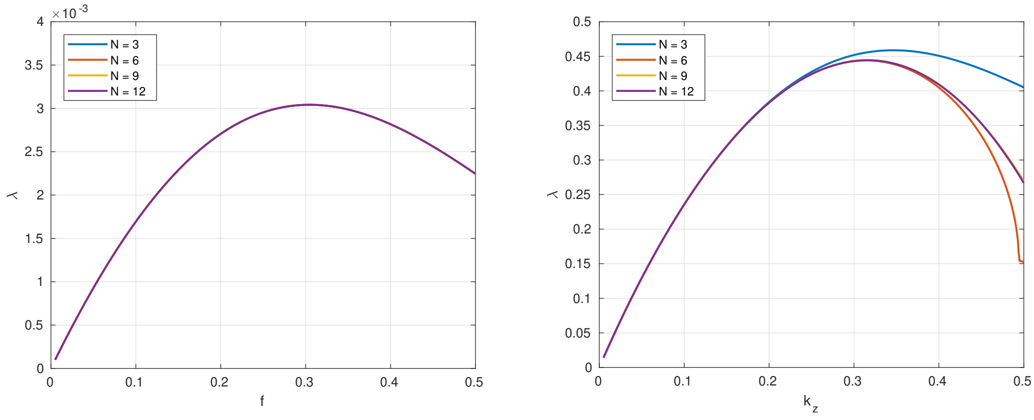

(a) (b)

Figure 4.1: Growth rate of secondary modes along (a) the $k_z = 0$ axis, and (b) the $f = 0$ axis with $Pr = 10$, $\tau = 0.01$, $R_\rho^{-1} = 0.02$ and $A_\psi = 4$. The value of N has little effect on the calculated growth rates when $k_z = 0$; however, N does impact the growth rates calculated when $f = 0$.

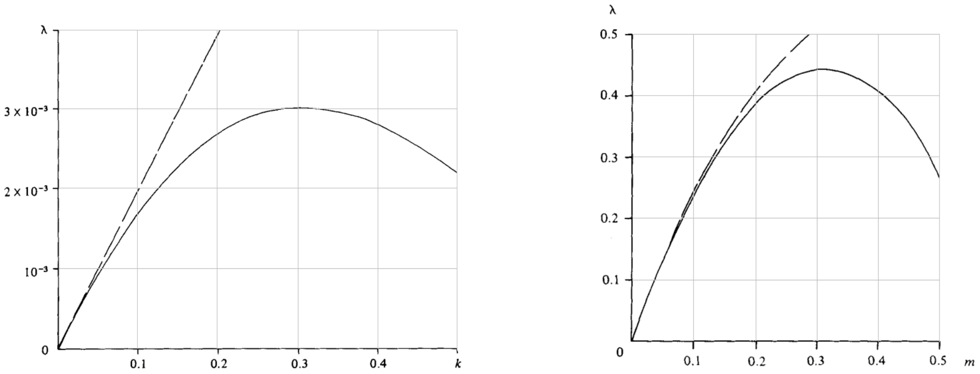

(a) (b)

Figure 4.2: Results from Holyer (1984) showing the growth rate of secondary modes along (a) the $k_z = 0$ axis, and (b) the $f = 0$ axis with $Pr = 10$, $\tau = 0.01$, $R_\rho^{-1} = 0.02$ and $A_\psi = 4$. The dashed lines are approximate solutions described in the paper. Note the transformation of coordinates from (f, k_z) in our notation to (k, m) in Holyer's notation.

$N = 9$ gives a fundamental matrix $\mathbf{A}$ of size 57×57, so obtaining the determinant of $\mathbf{A}$ requires relatively little in the way of modern day computational power.

The results obtained with $k_z = 0$ (Figure 4.1a) are independent of $N > 0$. This is because $k_z = 0$ modes exhibit no vertical variation and so they do not interact with the salt fingers. Indeed, when $k_z = 0$ we can solve equations (4.11)–(4.13) exactly, obtaining for each n the equation

$$(\lambda + K_n^2)(\lambda + PrK_n^2)(\lambda + \tau K_n^2) + Pr\left((\lambda + \tau K_n^2) - R_\rho^{-1}(\lambda + K_n^2)\right) = 0, \tag{4.15}$$

where $K_n^2 = ((f + n)k_x)^2$. This is the standard equation for the growth rate of salt fingers, and is equivalent to that derived in Chapter 2 under the transformation $K_n^2 \to k_x^2$. This provides an additional opportunity to verify our results: the growth rates observed when $k_z = 0$ (Figure 4.1a), obtained by solving equations (4.11)–(4.13), should match those obtained from the exact equation for the growth rates of salt fingers (4.15). Figure 4.3 shows a comparison of the linear solution computed using (4.11)–(4.13) with $k_z = 0$, and the independent contributions of equation (4.15) at three different values of n.

The solutions match, and it is perhaps now clear to see what range of values of n is required to obtain a complete picture of the behaviour of growth rates. In particular, only by including the contribution of the $n = -1$ term do we observe a maximum value of λ, i.e. the fastest growing mode.

A Comparison with Radko (2012)

In order to further verify our code and methodology, we are also able to reproduce results obtained by Radko and Smith (2012) in the salt-finger regime. Their model looks at a competition between linear growth mechanisms and investigates the disruptive action of secondary instabilities. In other words, the study aims to quantify at what amplitude the linear growth of salt fingers is arrested in a double-diffusive system. This is to predict the equilibrium fluxes of heat and salt. A 'growth rate balance' is assumed,

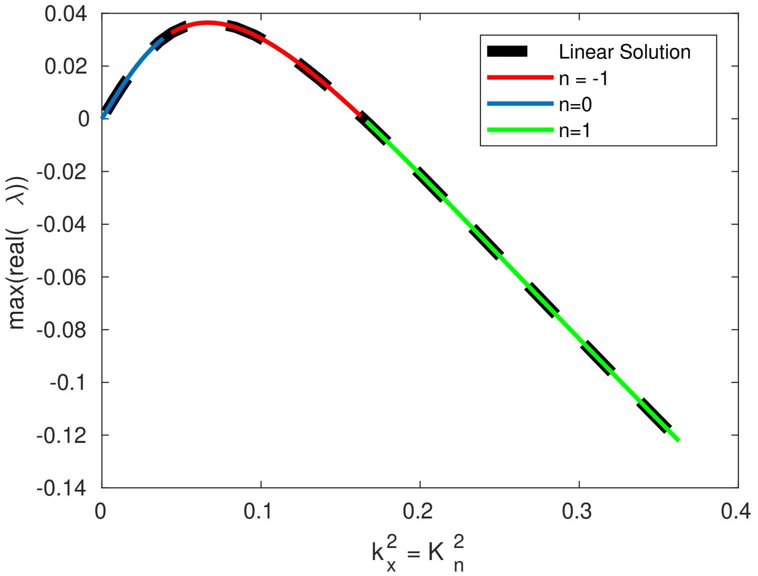

Figure 4.3: Comparison of the growth rate of the linear solution (computed using equations (4.11)–(4.13) with $k_z = 0$) with the contributions from solutions of (4.15) at $n = -1$, $n = 0$, and $n = 1$.

of the form

$$\lambda_2 = C\lambda_1 \tag{4.16}$$

where λ_1 is the linear growth rate of salt fingers, λ_2 is the growth rate of secondary instabilities, and C is a dimensionless $\mathcal{O}(1)$ quantity. λ_1 is determined from background gradients and dimensionless parameters using (2.44). λ_2 is determined using Floquet theory, as in Holyer (1984), and is dependent on the amplitude of primary salt fingers. The primary salt fingers are taken to be those with the largest growth rate, which we define here as having a horizontal wavenumber of k_x^*. The value of C is calibrated by computing equilibrium temperature and salinity fluxes as

$$F_T = \overline{wT} = \frac{1}{2}A_T^2(\lambda_1 + k^{*2}), \quad \text{and} \quad F_S = \overline{wS} = \frac{1}{2}R_\rho^{-1}A_T^2\frac{(\lambda_1 + k^{*2})^2}{(\lambda_1 + \tau k^{*2})}, \tag{4.17}$$

and comparing these against those obtained from direct numerical simulations. This is repeated for different values of R_ρ, to determine a relationship between the equilibrium temperature flux, and R_ρ.

We may re-purpose our existing code to reproduce the results of Radko by first taking λ_1 from linear theory (2.44) and calculating λ_2 for a series of values of A_T. Note that A_ψ and A_S can be determined from A_T using (2.43). The value of A_T is incrementally adjusted until the growth rate balance (4.16) is satisfied for a particular value of $C > 1$. Note that if $C < 1$ the primary modes grow faster than the secondary instabilities and continue to grow without being disrupted. The equilibrium eddy fluxes of heat and salt are then calculated using equation (4.17). This process is repeated for the different values of C and R_ρ that were used by Radko.

Figure 4.4 shows the results obtained from our simulations, while Figure 4.5 shows an annotated version of Figure 5 of Radko and Smith (2012), for ease of comparison. The red lines in the annotated figure show the values of F_T when $R_\rho = 1.3$, which can be seen to correspond closely to those obtained from our simulations. Indeed, we see that the equilibrium eddy fluxes from our simulations and those of Radko and Smith (2012) are in generally good agreement for each value of C and R_ρ, indicating that our code is working as intended.

Accuracy

We are now in a position to study how the accuracy of our results depends on the level of truncation N. This provides a check on the convergence of the results and ensures our conclusions are reliable. Ideally, we would like the program to be able to select a value of N for each (f, k_z) mode for which the eigenvalue changes negligibly with any further increase in N. Knowledge of which modes require larger values of N to converge (and so are more error-prone) will help in achieving this goal. We have already seen from Figure 4.1 that when $k_z = 0$ the choice of N is unimportant, but when $f = 0$ we require some $N > 9$ for convergence. We here investigate, qualitatively, what value of N may be required when both f and k_z are greater than zero.

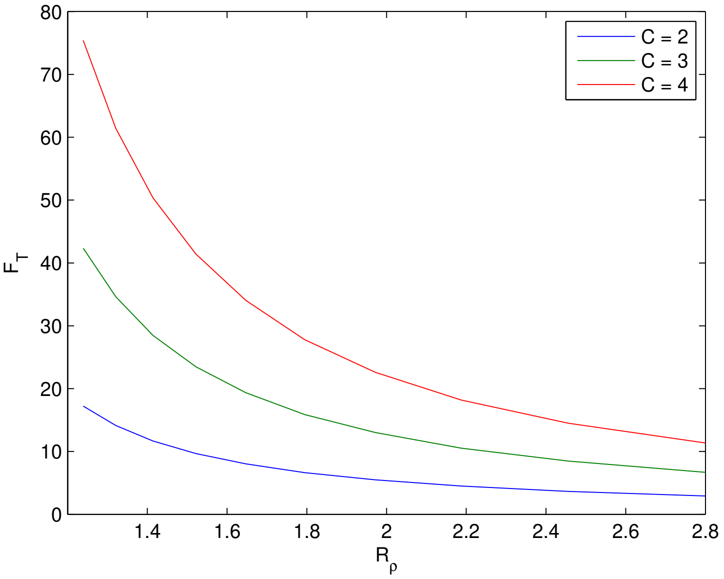

Figure 4.4: Heat flux vs. R_ρ for various values of C obtained from our simulations.

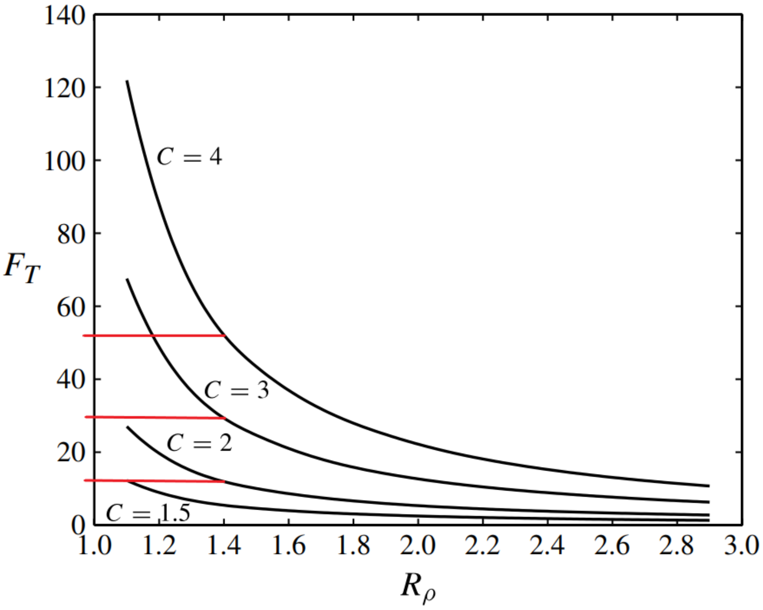

Figure 4.5: Heat flux vs. R_ρ for various values of C from Radko and Smith (2012), Figure 5.

It is known that solutions should be symmetrical about $f = 0.5$ due to the inherent symmetry of the system. Therefore, we may qualitatively check our results by calculating eigenvalues for $0 \leq f \leq 1$ and $0 \leq k_z \leq 0.5$ at progressively increasing values of N until such symmetry is achieved. Figures 4.6, 4.7 and 4.8 show the eigenvalues at $N = 3$, $N = 6$, and $N = 9$ respectively, along with a plot of the absolute difference between corresponding results to the left and right of $f = 0.5$. For reference, the figures show results at 500 wavenumbers in both the f and k_z directions.

We see that in all cases the errors are greatest as $f \to 0$, while seemingly accurate results are obtained along both the $f = 0$ and $k_z = 0$ axes. The error is given by $E = |\lambda_+ - \lambda_-|$, where λ_+ represents growth rates for values of $f > 0.5$, and λ_- represents corresponding growth rates when $f < 0.5$. When $N = 9$, the absolute error over a majority of the domain is less than 10^{-6}, with the exception of a region surrounding $(f, k_z) = (0.1, 0.4)$. The eigenvalues of different secondary modes have different convergence properties, so it important to assess the convergence of each eigenvalue individually. An accurate result for the fastest growing secondary mode is desirable, but we must also ensure that the growth rates and frequencies of the other secondary modes are accurate in order to permit any meaningful conclusions regarding those modes to be drawn.

In analysing the symmetry of the system it is clear that, for the most part, results are accurate above $N = 9$, as seen in Figure 4.8; however, the results at low values of k_z are accurate even at $N = 3$, as shown in Figure 4.6. In certain regions of (k_x, k_z) space, such as around (0.1,0.5), the errors are large, as shown in Figure 4.8b. It may be that $N = 12$ or higher is required in such regions, which would considerably increase computation time if such a value of N was used at every point in wavenumber space. We therefore wish to take relatively small values of N over the majority of the domain, while reserving larger values of N for only those points at which the errors are greatest. To achieve this, we first study the behaviour of individual eigenmodes as N is increased.

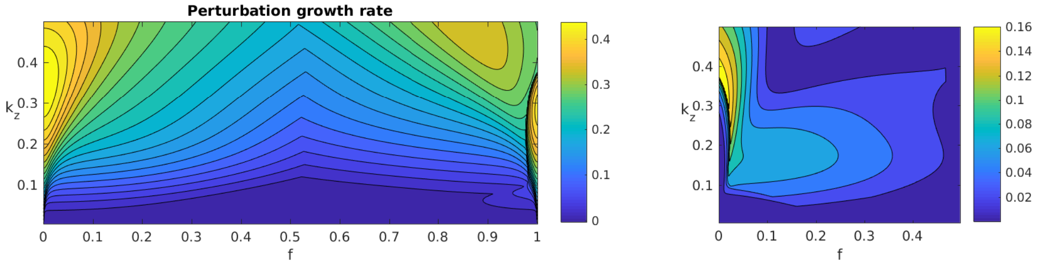

(a) (b)

Figure 4.6: (a) Growth rate, λ, and (b) Absolute error, E, for $N = 3$, when $R_\rho^{-1} = 0.02$, $\tau = 0.01$ and $Pr = 10$.

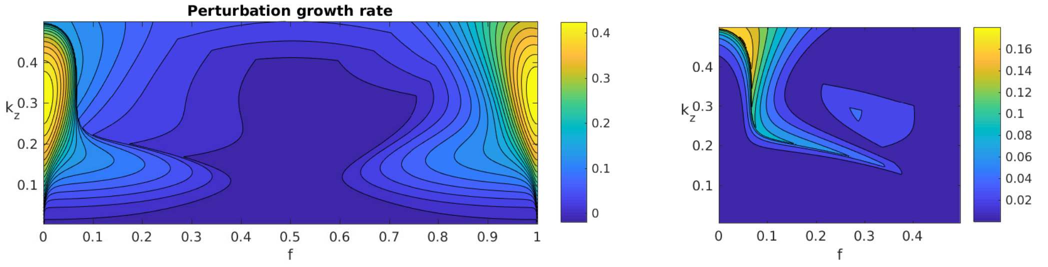

(a) (b)

Figure 4.7: (a) Growth rate, λ, and (b) Absolute error, E, for $N = 6$, when $R_\rho^{-1} = 0.02$, $\tau = 0.01$ and $Pr = 10$.

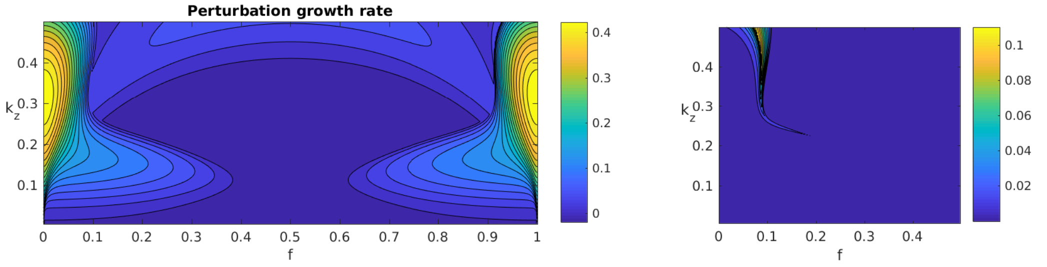

(a) (b)

Figure 4.8: (a) Growth rate, λ and (b) Absolute error, E, for $N = 9$, when $R_\rho^{-1} = 0.02$, $\tau = 0.01$ and $Pr = 10$.

We expect eigenvalues to change only negligibly at large values of N. The rate at which an eigenvalue reaches such a state is dependent on f and k_z, as highlighted in our symmetry analysis—some eigenvalues reach a fixed value at $N = 3$, others at $N > 12$. A method for ensuring eigenvalues have converged for a particular mode may be as follows: take a minimum value of N, as low as 1; calculate the eigenvalue λ_N; increment N; calculate the eigenvalue λ_{N+1}; and take the difference between the current and previous eigenvalues to obtain the error, $E = \lambda_{N+1} - \lambda_N$. This process may be repeated with successively larger values of N. A solution may be said to have converged when the error E drops below a threshold value.

Figure 4.9 shows the real part of the eigenvalue $\Re(\lambda)$ and the error E for the fastest growing mode $(f, k_z) = (0, 0.32)$ under the same conditions as in the symmetry analysis, i.e. $(R_\rho^{-1}, A_\psi, Pr, \tau) = (0.02, 4, 10, 0.01)$. The eigenvalue in this case converges relatively quickly to a fixed value of $\lambda = 0.444$, exhibiting an incremental absolute error of $E = 10^{-3}$ at $N = 7$, dropping below a tighter tolerance of $E = 10^{-5}$ at $N = 10$. The results should be contrasted with similar plots shown in Figure 4.10 for the wavenumber $(0.1, 0.45)$, which was shown in the symmetry analysis to be a particularly tricky eigenvalue to calculate.

The eigenvalue of the mode $(0.1, 0.45)$ varies significantly in that the predicted growth rate at low N is of the same order as the growth rate of the fastest growing secondary mode (FGSM) $(0, 0.33)$, whereas at large N the growth rate is closer to zero. Futhermore, the value of N required for convergence is much larger for the 'tricky' mode than for the FGSM. In the former case, the eigenvalue reaches a fixed value of 0.0237 at approximately $N = 12$ or 13; however, the error does not drop below a tight tolerance of $E = 10^{-5}$ until $N = 16$.

Although it takes relatively little computational time to execute a single calculation

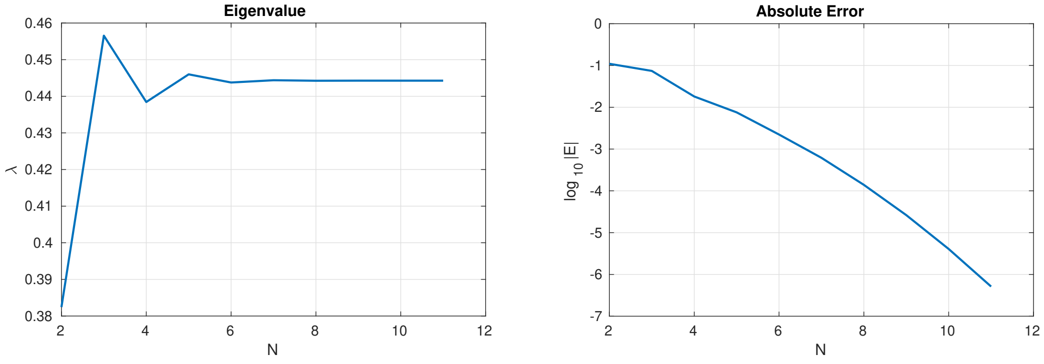

(a) (b)

Figure 4.9: (a) Variation of the growth rate λ with level of truncation N, and (b) the associated error E as a function of N, for the fastest growing secondary mode $(f, k_z) = (0, 0.32)$. Here, $(R_\rho^{-1}, A_\psi, Pr, \tau) = (0.02, 4, 10, 0.01)$

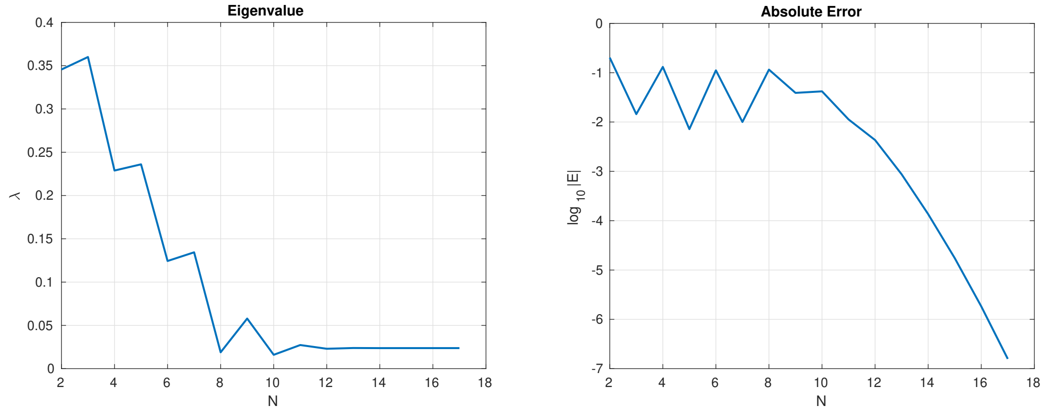

(a) (b)

Figure 4.10: (a) Variation of the growth rate λ with level of truncation N, and (b) the associated error E as a function of N, for the mode $(f, k_z) = (0.1, 0.45)$. Here, $(R_\rho^{-1}, A_\psi, Pr, \tau) = (0.02, 4, 10, 0.01)$

with $N = 16$ (on the order of milliseconds), the computational time can become significant when producing high-resolution contour plots such as those in Figures 4.6, 4.7 and 4.8, which each have a resolution of 500 × 500 modes. Therefore, the MATLAB code is written such that, for each mode, a calculation is first performed with $N = 3$.

The calculation is repeated with successively higher values of N until the error E drops below a set threshold. Typically we employ a threshold of 10^{-5}, though Holyer (1984) used a stricter value of 10^{-6}. As discussed hereinbefore, the parameter range studied in Holyer (1984) was limited, and so a tighter tolerance was reasonable. Here, we find a threshold of $E = 10^{-5}$ provides sufficiently accurate results and permits a broad parameter regime to be explored.

Eigenmode Spectra

The frequency spectra of the eigenmodes ψ_n, T_n and S_n (corresponding to the eigenvalues with largest real parts) provide additional insight into the convergence of results. Through a spectral decomposition of the eigenfunctions, we see that modes for which a larger value of N is required to achieve convergence tend also to have large-amplitude eigenmodes at extreme values of n. In other words, if we find modes with large ψ_n, T_n or S_n for values of n close to N or $-N$, then it is likely that N needs to be increased in order to adequately capture the contributions of such harmonics. To illustrate this, we plot in Figure 4.11 a spectral decomposition of the two modes $(f, k_z) = (0, 0.32)$ and $(f, k_z) = (0.1, 0.44)$ which we considered earlier.

In both cases we see peaks at $n = 1$ and $n = -1$, indicating that contributions from these harmonics are significant. Eigenfunction magnitudes decrease with increasing $|n|$, meaning that modes having high values of n are not as influential, and may ultimately be disregarded. A value of n at which a given mode ψ_n exerts a negligible contribution is the point at which the truncation should be made. We know that the eigenvalue of the FGSM reaches convergence at a lower value of n than the $(0.1, 0.44)$ mode. The reason for this is now clear from the spectra plots: contributions of modes in the eigenfunction for the FGSM all drop below 10^{-4} at $n = 11$, while those in the eigenfunction for the $(0.1, 0.44)$ mode do not drop below this value until $n = 15$.

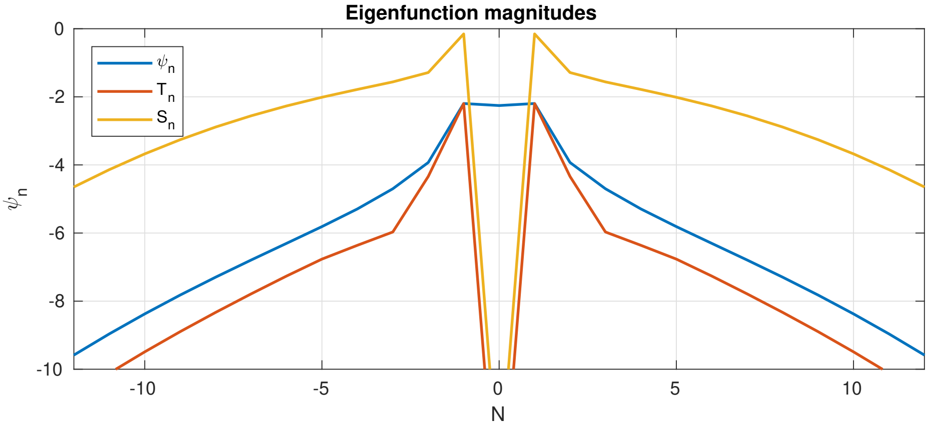

(a)

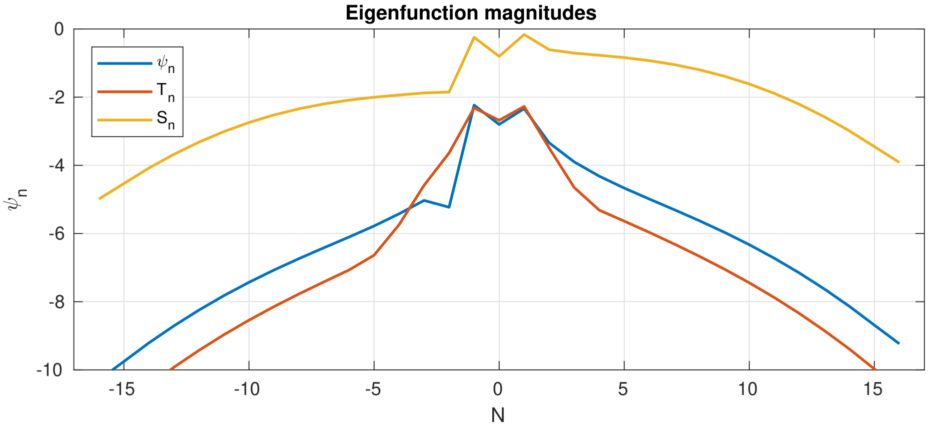

(b)

Figure 4.11: Spectral decompositions of eigenfunctions with the largest growth rate in: (a) the fastest growing mode, $(f, k_z) = (0, 0.33)$; and (b) the mode $(0.1, 0.45)$. The y-axis is scaled as $\log_{10}|\psi_n|$.

4.4 Parametric Study

We now turn to solving equations (4.11)–(4.13) using the numerical techniques outlined in §4.3. We first explore the effect of varying R_ρ^{-1} and A_ψ in the Heat-Salt system, which has $Pr = 10$ and $\tau = 0.01$. We then do the same for the Salt-Sugar system, with $Pr = 1000$ and $\tau = 1/3$; a high-Pr system with $Pr = 10^4$ and $\tau = 0.01$; and finally a low-Pr system with $\mathrm{Pr} = 0.01$ and $\tau = 0.01$. The results are contrasted with those presented in Holyer (1984). We find that the dominant secondary mode predicted by Holyer (i.e. that having $f = 0$) is not the fastest-growing mode at lower values of A_ψ, and that at large Prandtl numbers it appears that this mode never dominates.

We then proceed to investigate the influence of heat and salt by comparing our results with those obtained for a hydrodynamic (i.e. heat- and salt-free) sinusoidal shear flow. We find that the $f = 0$ mode observed at low Pr and/or large A_ψ is similar to that observed in purely hydrodynamic shear flow. Furthermore, we observe a new mode in the diffusive system that does not dominate in hydrodynamic shear, indicating that heat and salt do critically influence the dynamics.

We also look at the secondary instabilities of fastest-growing elevators (as opposed to marginal elevators). Varying R_ρ^{-1}, A_ψ and Pr has a similar effect in the fastest-growing system as in the marginal system, though the growth rates of secondary instabilities are larger and they possess slightly different structure.

A Note on Scaling

If we wish to recover results in the dimensions of Holyer (1984) then we must scale our solutions in accordance with the length-scale set out in §4.2. That is, we scale k_z and λ as

$$(k_z)_H = k_z \left(\frac{l_H}{l}\right), \qquad \lambda_H = \left(\frac{l_H}{l}\right)^2 \lambda, \tag{4.18}$$

where subscript H denotes the scaling adopted by Holyer, and

$$\left(\frac{l}{l_H}\right)^4 = \frac{1}{\frac{R_\rho^{-1}}{\tau} - 1}. \tag{4.19}$$

There is an exception for which we do not need to scale. Holyer studied the heat-salt system at a value of $\gamma = 0.5$, which corresponds to $R_\rho^{-1} = 0.02$. In this case, with $\tau = 0.01$, we find that $l/l_H = 1$.

4.4.1 Heat-Salt System

Basic State Stability

The Heat-Salt system as studied by Holyer (1984) is defined by $Pr = 10$ and $\tau = 0.01$. It was shown in Chapter 2 that the basic state is unstable to elevator modes in the range $1 \leq R_\rho^{-1} \leq \tau$, which corresponds to a range of $\tau \geq \gamma \geq 1$ in Holyer's notation under the transformation $R_\rho^{-1} = \tau/\gamma$.

We first study a quasi-steady basic state in which the elevator modes are assumed to have not grown appreciably in the time taken for secondary instabilities to grow. Holyer achieves this by taking a horizontal wavenumber of $k_x = 1$ and changing the length scale (as a function of Rayleigh numbers R_T and R_S) to produce a state with zero growth. However we specify a length on the scale of the 'buoyancy-layer' (Howard and Veronis, 1987) which gives a thermal Rayleigh number of $R_T = 1$, so we instead vary k_x to give zero growth rate for a given R_ρ^{-1}. The growth rates of primary elevator modes as functions of R_ρ^{-1} and k_x are displayed in Figure 4.12, which is the same as Figure 2.3.

We may select a value of R_ρ^{-1} and determine the value of k_x to give either marginal stability or fastest growth ($k_x = k_x^*$). The curve $\lambda_0 = 0$ in Figure 4.12 represents the marginal solution—anything within and above this line is unstable, whilst anything on the line is marginally stable and will not grow.

Comparison with Holyer

We begin with an extension of the results presented by Holyer (1984) for the heat-salt system with $\gamma = 0.5$ and $W = 4$, which corresponds in our notation to $R_\rho^{-1} = 0.02$, $A_\psi = 4$ and $k_x = 1$. Our contribution includes a study of the growth rates of *all* secondary modes in the region $0 \leq f \leq 0.5$ and $0 \leq k_z \leq 0.6$. We also study the effect of changing the amplitude of the elevator mode A_ψ on the observed fastest growing

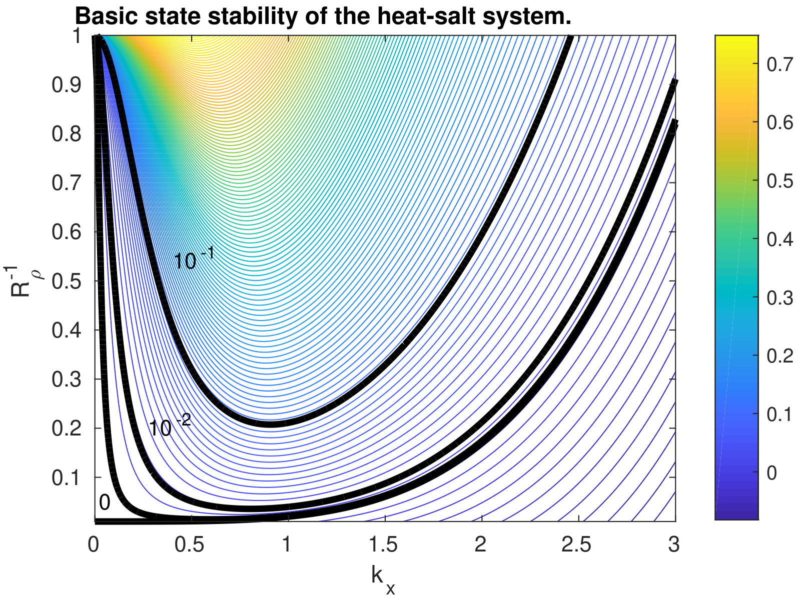

Figure 4.12: Growth rate of the primary elevator mode λ_0 as a function of the background density gradient ratio R_ρ^{-1} and the basic-state wavenumber k_x for the heat-salt system ($Pr = 10$, $\tau = 0.01$). The black lines are contours of $\lambda_0 = [0, 10^{-3}, 10^{-2}, 10^{-1}]$.

secondary mode. As previously noted, in the heat-salt system with $\gamma = 0.5$ we do not need to scale our results to compare them with Holyer's, as $l/l_H = 1$.

Figure 4.13 shows the real and imaginary parts of the growth rates of secondary instabilities when $R_\rho^{-1} = 0.02$ and $A_\psi = [10^{-2}, 10^{-1}, 1, 10]$. The form of the secondary instability is dependent on the value of A_ψ. At low A_ψ, as in Figure 4.13 (a), we see that the instability takes the form of an elevator mode ($k_z = 0$), which has the same growth rate as the fastest-growing elevator mode from linear theory. Thus, at low A_ψ the problem reduces to that given by the cubic dispersion relation (4.15). This secondary elevator arises because the growth rate of the dominant primary instability is larger than that of any mode driven by low-amplitude, marginal fingers. However, it should be noted that there exists an oscillatory mode with positive growth rate when $f = 0.5$. This means that, although other modes are generated by and interact with the elevator modes, they do not do so to the extent that they disrupt the growth of the

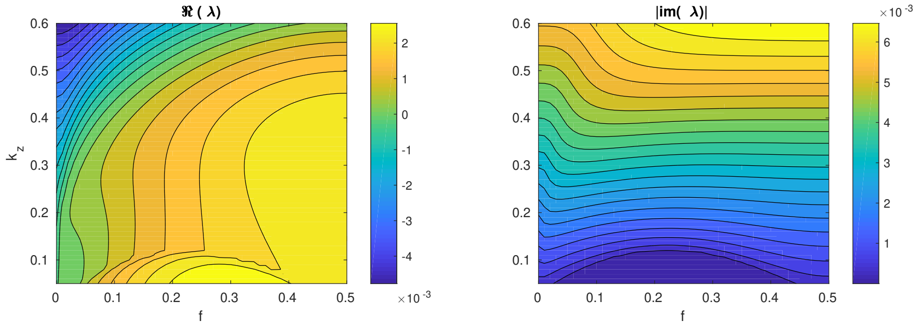

(a) $A_\psi = 10^{-2}$

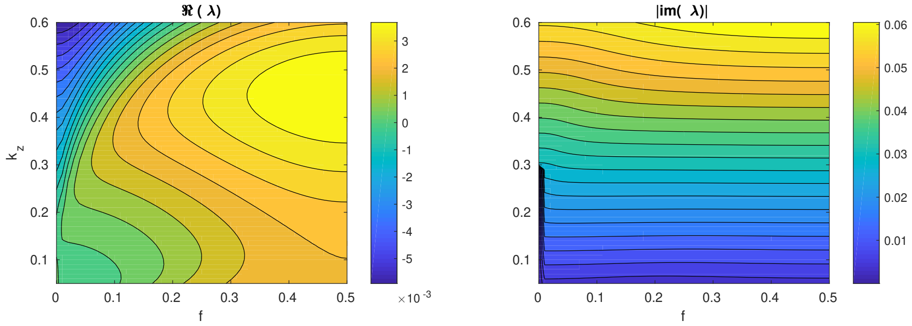

(b) $A_\psi = 10^{-1}$

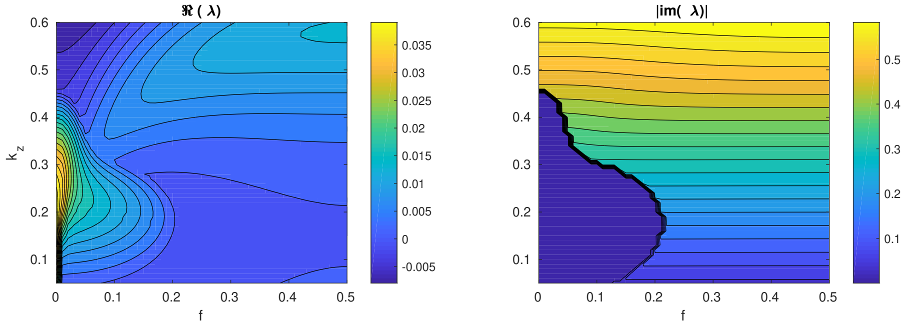

(c) $A_\psi = 1$

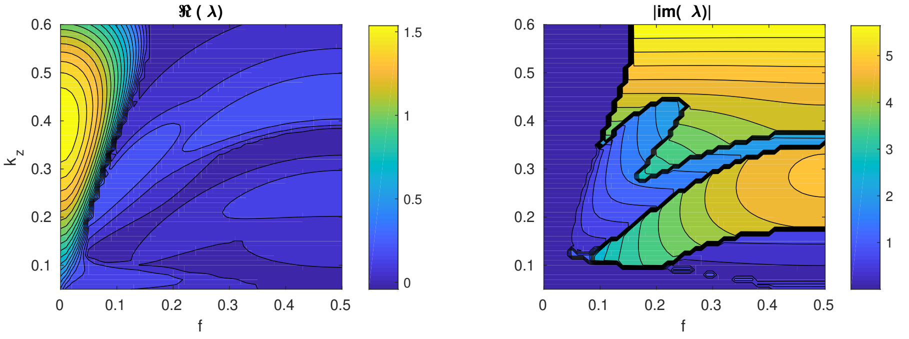

(d) $A_\psi = 10$

Figure 4.13: Real and imaginary part of the growth rates of secondary instabilities λ in the heat-salt system with $R_\rho^{-1} = 0.02$, $Pr = 10$, $\tau = 0.01$ and $A_\psi = [10^{-2}, 10^{-1}, 1, 10]$.

fastest-growing elevator modes.

Figure 4.13b shows growth rates at $A_\psi = 10^{-1}$. Here we see that the (oscillatory) $f = 0.5$ mode is now dominant and it has assumed a larger value of k_z. The presence of this mode is interesting as it was not captured in the study by Holyer, who concluded that the dominant secondary instability in the heat-salt system was a non-oscillatory mode with $f = 0$.

We do see a dominant, non-oscillatory $f = 0$ mode at $A_\psi = 1$, as shown in Figure 4.13 (c). This value of A_ψ is closer to the value of $A_\psi = 4$ chosen by Holyer, so similar results are to be expected. This mode remains dominant (and non-oscillatory) as A_ψ is increased to 10 as shown in Figure 4.13 (d), though its vertical wavenumber k_z also increases. There are still oscillatory modes present at $f = 0.5$; however, these are no longer the fastest growing modes.

It is clear that the wavenumber of the fastest growing mode is dependent on the strength of the basic state. Figure 4.14 shows the values of f and k_z of the FGSM as A_ψ is increased. As already described, the FGSM at low A_ψ is an elevator mode with $k_z = 0$. Increasing A_ψ leads to an FGSM with $f = 0.5$ and a finite value of k_z which increases with A_ψ until around $A_\psi = 0.4$. At this point, the FGSM takes on a value of $f = 0$ and has finite k_z. A further increase in A_ψ leads to larger k_z. The fastest growing modes with $f = 0.5$ are oscillatory in time, while all modes with $f = 0$ are non-oscillatory. This suggests that there exists two different regimes depending on the strength of the basic state. These are numbered 1 and 2 on Figure 4.14, and the modes in each regime are referred to herein as ‘R1’ and ‘R2’ modes.

We now look at the eigenfunctions corresponding to the two different regimes. Figure 4.15 shows contours of streamfunction ψ and density ρ perturbations for a mode in R1, along with the total streamfunction ψ_T and total density ρ_T; Figure 4.16 shows the

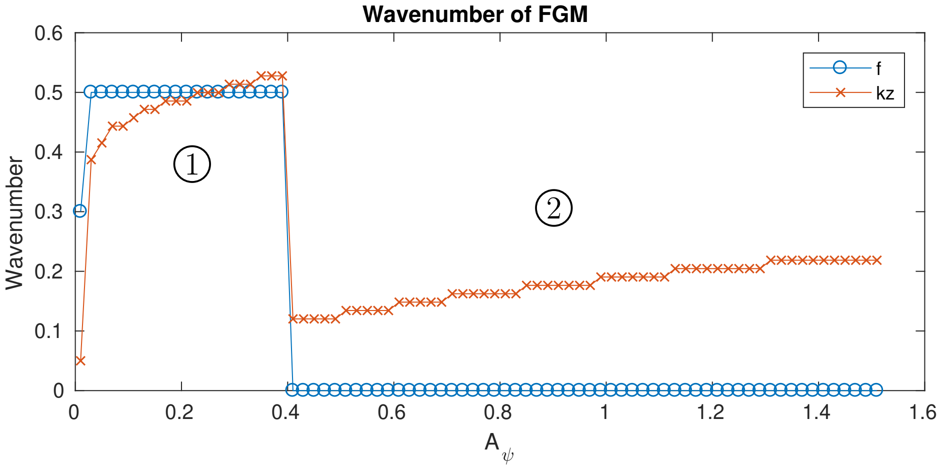

Figure 4.14: Wavenumbers f and k_z of the fastest growing secondary mode vs. A_ψ for the heat-salt system with $R_\rho^{-1} = 0.02$.

same for an R2 mode. The 'total' values are obtained by superposing perturbations of amplitude A_ψ with background elevator modes. The amplitudes of the ψ, T and S perturbations are normalised to the amplitude of the basic state, A_ψ. The horizontal scale of plots is set to show four basic-state wavelengths ($x = \{0, 8\pi/k_x\}$), while the vertical scale permits two secondary z-wavelengths ($z = \{0, 4\pi/k_z\}$).

The R1 perturbations take the form of cells with a horizontal wavelength that is twice as wide as the basic state elevators, and a vertical wavelength of a similar order. These perturbations are oscillatory in time in the sense that the mode is a travelling wave moving upwards—there also exists an equivalent downwardly-propagating mode. Notably, the total streamfunction takes on a form similar to that of the 10th-order system in Chapter 3. The results of the present study are not directly comparable with those of Chapter 3, as the elevator modes in Chapter 3 were both fastest-growing and oscillatory; however, it is promising that we should see similar behaviour here. Indeed, we see in Chapter 5 that the secondary modes arising in oscillatory double-diffusive convection are similar to those arising from steady elevators. We have not studied here whether the frequency of the oscillations is dependent on the amplitude of the elevator

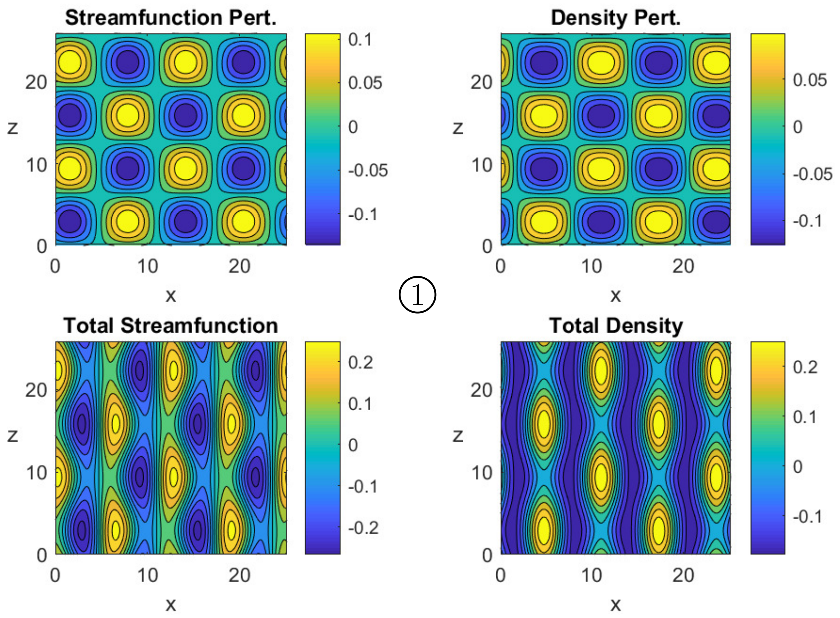

Figure 4.15: Perturbations and total values of streamfunction and density for the fastest growing mode $(f, k_z) = (0.5, 0.486)$ in the heat-salt system with $R_\rho^{-1} = 0.02$ and $A_\psi = 0.17$. This corresponds to an R1 mode of Figure 4.14. The amplitudes are normalised w.r.t. A_ψ.

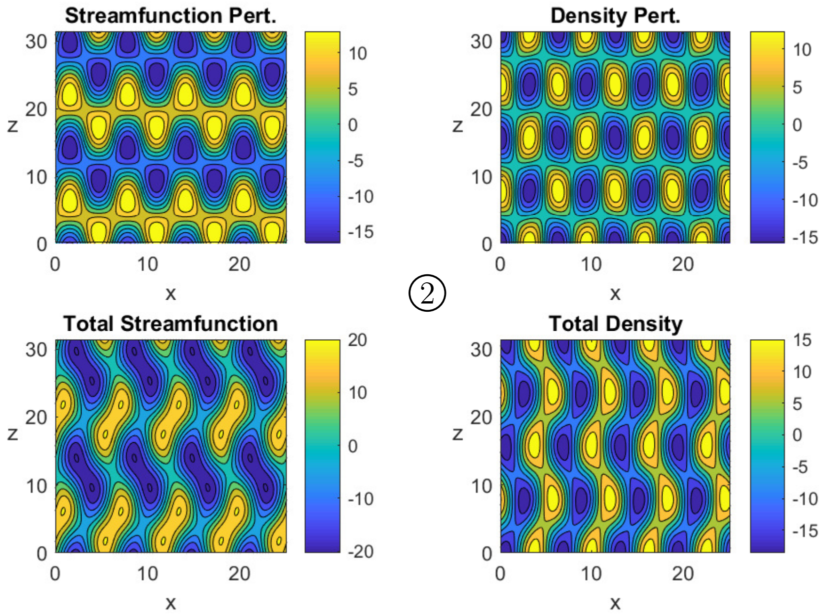

Figure 4.16: Perturbations and total values of streamfunction and density for the fastest growing mode $(f, k_z) = (0, 0.4)$ in the heat-salt system with $R_\rho^{-1} = 0.02$ and $A_\psi = 10$. This corresponds to an R2 mode of Figure 4.14. The amplitudes are are normalised w.r.t. A_ψ.

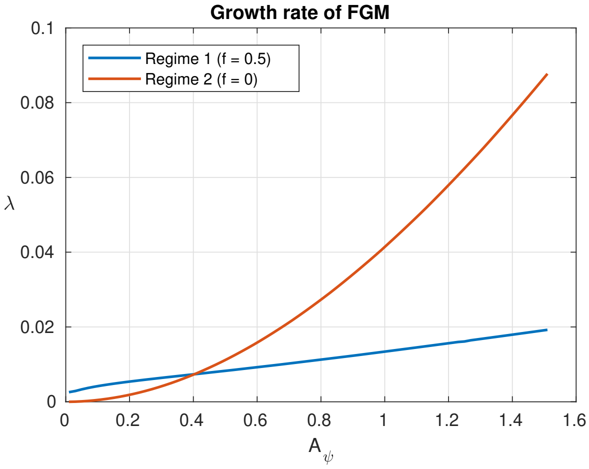

Figure 4.17: Growth rate λ of the fastest growing secondary modes as a function of A_ψ for the heat-salt system with $R_\rho^{-1} = 0.02$. Regimes 1 and 2 correspond to those shown in Figure 4.14.

modes, as in the 10th-order system. This would be of interest to future studies. The R2 perturbations are non-oscillatory, and take on a slightly elongate, cellular form. The secondary modes cause the elevator modes take on a wavey structure, and forms recirculating regions between the elevator modes, as shown by the total streamfunction in Figure 4.16. This is similar to the behaviour observed in the 9th-order system in Chapter 3, which suggests that perhaps the cellular modes observed here are the same as those observed to cause layering in the truncated models.

Figure 4.17 shows the growth rate of the FGSM as a function of A_ψ. The growth rate increases monotonically with the strength of the basic state. Here we have shown that the marginal system first becomes unstable to an oscillatory mode with $f = 0.5$, albeit with a relatively small amplitude compared to the FGSM from linear theory. This is somewhat contrary to Holyer's conclusion that the fastest growing secondary mode is non-oscillatory with $f = 0$; however, the $f = 0$ mode does dominate at larger values of A_ψ.

Finally, it is worth noting at this point how A_ψ affects the accuracy of simulations.

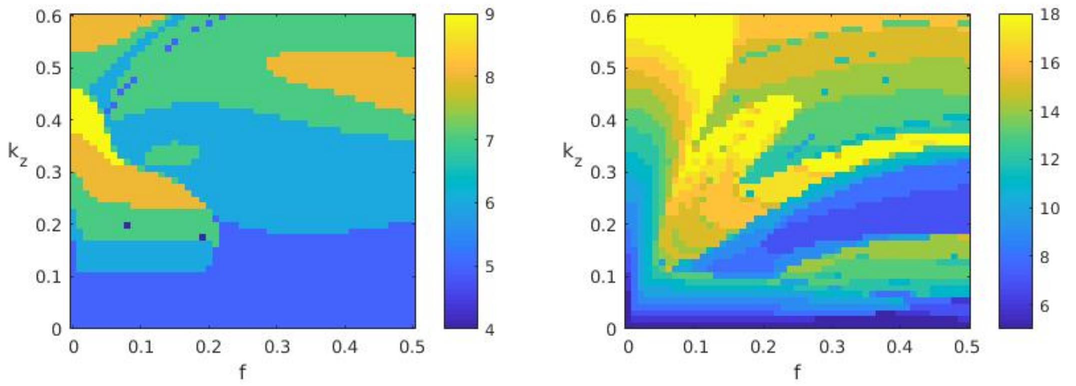

(a) $A_\psi = 1$

(b) $A_\psi = 10$

Figure 4.18: Value of N required to achieve convergence at each point in (f, k_z)-space for two different values of A_ψ.

Figure 4.18 shows the ultimate value of N taken to achieve convergence at each simulation point for $A_\psi = 1$ and $A_\psi = 10$. For clarity, we reduced the number of points in f and k_z to 50 in either direction (down from 100). We see that if $A_\psi \leq 0.1$ then $N = 5$ is sufficient to ensure that growth rates converge to a tolerance of 10^{-5}. However as we increase A_ψ the solution requires ever higher values of N. When $A_\psi = 1$ certain points require $N = 9$, while at $A_\psi = 10$ the majority of points require $N \geq 14$, with some even taking $N = 18$. Hence simulations at increasingly high values of A_ψ require increasingly more computational time.

Sweep over R_ρ^{-1} and A_ψ

The system studied by Holyer was limited in the sense that it was restricted to a single, very small inverse density gradient ratio $R_\rho^{-1} = 0.02$ ($R_\rho = 50$). This is much smaller (greater) than the typical oceanic value of $R_\rho^{-1} = 0.5$ ($R_\rho \simeq 2$) (Stern and Simeonov, 2005). With this in mind, we proceed to investigate the influence of R_ρ^{-1} and A_ψ on the form of the secondary instabilities in a heat-salt system. Unlike Stern and Simeonov (2005) who studied the behaviour of fastest-growing elevator modes (with $k_x = k_x^*$), we restrict our attention (for now) to that of a system with a marginal basic state ($\lambda_0 = 0$).

Figures 4.19 to 4.21 show plots of the wavenumber of the fastest growing mode along with plots of the growth rates of R1 and R2 modes at different values of R_ρ^{-1}. When $R_\rho^{-1} = 0.17$, as shown in Figure 4.19, there appears initially to be two different R1 and two different R2 modes. These are actually the same mode, whose vertical wavenumber reduces with increasing A_ψ. The reason this appears twice is because the growth rate of the R2 mode overtakes that of the R1 mode for a short period of time at around $A_\psi = 1.6$. This implies that, as the elevator mode grows, the form of the secondary instability may flip between an R1 mode and an R2 mode.

Figure 4.20 shows the results at $R_\rho^{-1} = 0.5$, which corresponds to typical oceanic conditions. Here we see that the R1 mode first dominates at a larger value of A_ψ than when $R_\rho^{-1} = 0.17$. That is, the fastest growing elevator mode remains dominant until larger values of A_ψ as the strength of the background state is increased. This implies that, for a given, low value of A_ψ, the growth rate of the fastest growing elevator mode increases faster than the growth rate of the R1 mode, as R_ρ^{-1} is increased.

The system eventually gives way to an R2 mode, whose vertical wavenumber grows as A_ψ is increased. When $R = 0.5$, we see that the R2 mode becomes the dominant secondary mode at a larger value of A_ψ than when $R_\rho^{-1} = 0.17$. We later show that the R2 mode may be generated predominantly by shear effects in the system. If this is the case, it appears that a more unstable background state may reduce the effects of shear-driven secondary modes, or enhance the effects of diffusively-driven secondary modes.

Figure 4.21 shows the results when $R_\rho^{-1} = 0.9$. This represents the most unstable background state. We see little difference in results between $R_\rho^{-1} = 0.5$ and $R_\rho^{-1} = 0.9$, except that the fastest-growing elevator mode has a larger growth rate, and so the R1 mode once again becomes dominant at a larger value of A_ψ. Similarly, the R2 mode

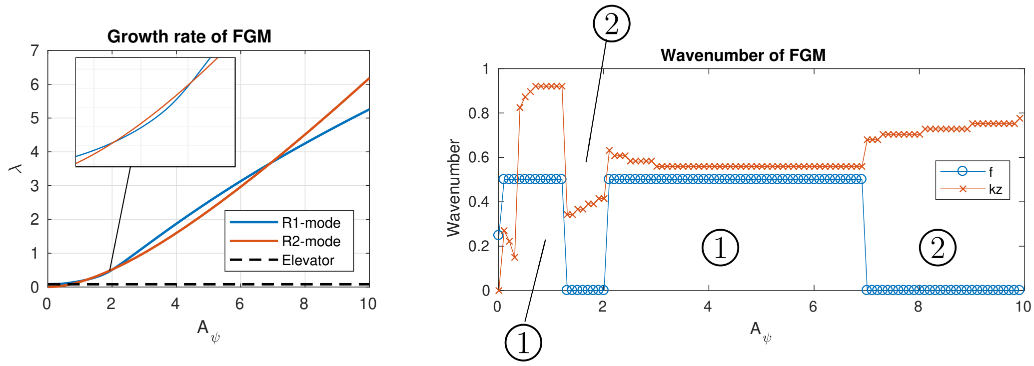

Figure 4.19: Relative growth rate and wavenumber of the fastest-growing secondary mode for $R_\rho^{-1} = 0.17$, $Pr = 10$ and $\tau = 0.01$.

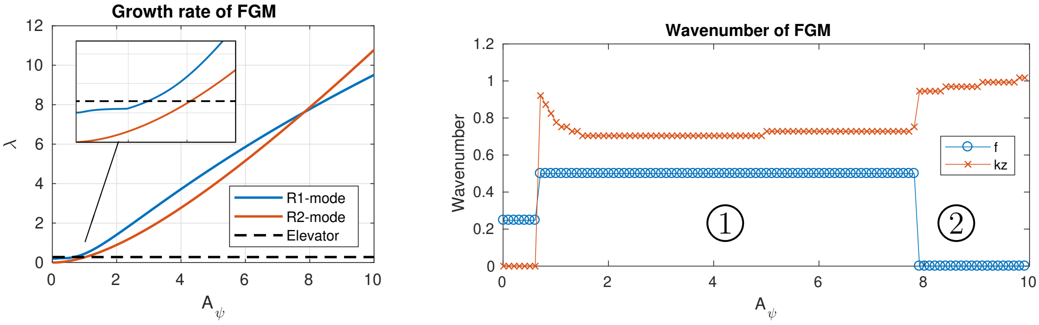

Figure 4.20: Relative growth rate and wavenumber of the fastest-growing secondary mode for $R_\rho^{-1} = 0.5$, $Pr = 10$ and $\tau = 0.01$.

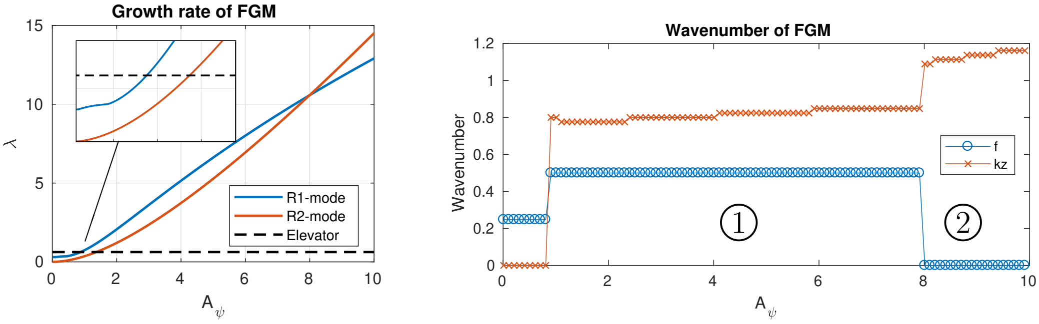

Figure 4.21: Relative growth rate and wavenumber of the fastest growing mode for $R_\rho^{-1} = 0.9$, $Pr = 10$ and $\tau = 0.01$.

becomes dominant at a larger value of A_ψ, in keeping with the observed pattern.

Overall, the behaviour is consistent across all values of R_ρ^{-1} in that the initial FGSM is an elevator mode, followed by a mode with $f = 0.5$ (R1), and finally a mode with $f = 0$ (R2). What differs is the value of A_ψ required to enter R1 and R2, and the growth rates of the corresponding secondary modes. It follows that in the Oceanic case ($R_\rho^{-1} = 0.5$), as shown in Figure 4.20, the behaviour is similar to that observed by Holyer (1984) for $R = 0.02$, as shown in Figure 4.14. The fact Holyer restricted her search to a low value of R_ρ^{-1} is relatively inconsequential—there is no collective instability observed, and the $f = 0$ mode dominates when A_ψ is large enough. The difference here is that Holyer did not observe the $R1$ mode which first becomes unstable.

It is informative to plot the values of A_ψ at which the secondary mode transitions into R1 and R2 modes as R_ρ^{-1} is varied. Looking at such 'critical' values of A_ψ allows us to better understand the behaviour at different R_ρ^{-1}. We call the critical values at which the R1 and R2 modes become dominant $A_{\psi,R1}$ and $A_{\psi,R2}$ respectively. Figure 4.22 shows the values of $A_{\psi,R1}$ and $A_{\psi,R2}$ as a function of R_ρ^{-1} for the heat-salt system.

The dashed lines represent the critical values at which the system transitions into an R1 mode (and subsequently an R2 mode) for a second time as A_ψ is increased. These second critical values are denoted with a dash, i.e. $A_{\psi,R1'}$. It is clear that there exists a region of R_ρ^{-1} in which we see behaviour similar to that in Figure 4.19; namely that the growth rate of the R2 mode overtakes that of the R1 mode for a brief period as A_ψ is increased, before yielding again to the R1 mode. At $R_\rho^{-1} = 0.2$ we see that the R1 mode no longer emerges for a second time, and we just have a single value for $A_{\psi,R1}$ and $A_{\psi,R2}$.

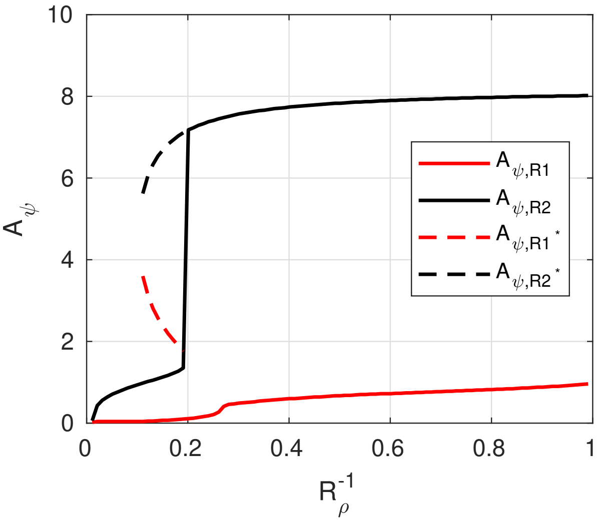

Figure 4.22: Critical values of A_ψ as a function of R_ρ^{-1} for the heat-salt system, which has $Pr = 10$ and $\tau = 0.01$.

4.4.2 Fastest growing elevators with $k_x = k_x*$

The foregoing investigations focused on the stability of a steady basic state, in which k_x was selected to give zero growth rate. However, there exists a fastest growing primary elevator mode with positive growth rate, the wavenumber of which we define as k_x^*. Radko and Smith (2012) used Floquet theory to analyse the equilibrium amplitude of salt-fingers and found that predictions using k_x^* were more in line with results of DNS than those with a marginal basic state. Veronis (1987) also showed that the width of the initial salt-fingers affects fluxes between the fingers, and thus affects the form of the secondary instability. Therefore, we here study the secondary instabilities arising in a heat-salt system from a basic state with $k_x = k_x^*$, but assuming the basic state is not growing. That is, since the basic state would be growing, we must make a quasi-steady approximation and assume that $\lambda_0 = 0$. If we find secondary instabilities with growth rates much larger than that of the fastest-growing elevator modes (i.e. $\lambda/\lambda_e > 1$) then this approximation is reasonable.

Figure 4.23 shows the growth rate and wavenumber of the fastest growing mode as a function of A_ψ for the system studied by Holyer (1984), with $Pr = 10$, $\tau = 0.01$ and $R_\rho^{-1} = 0.02$. Note that the growth rate is displayed as a fraction of the basic-state growth rate; secondary instabilities are meaningful when $\lambda/\lambda_0 > 1$. Herein we call this the growth rate ratio (GRR).

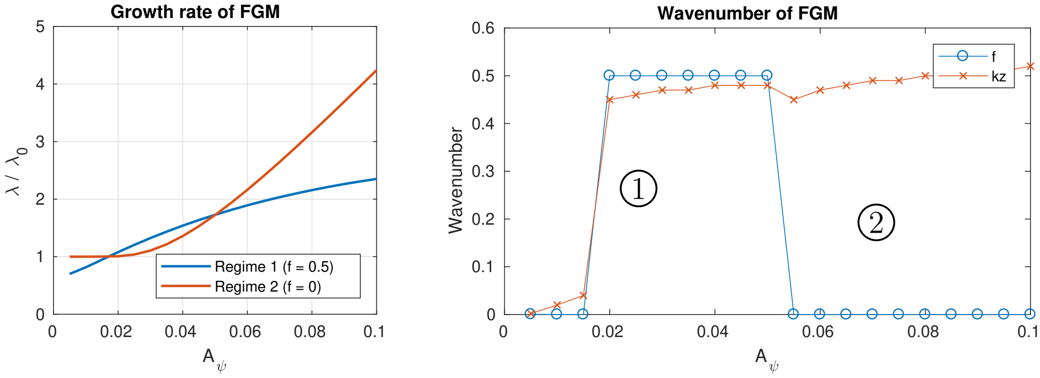

Figure 4.23: Relative growth rate and wavenumber of the FGSM for $R_\rho^{-1} = 0.02$, $Pr = 10$ and $\tau = 0.01$.

The most unstable mode at low A_ψ is no longer an elevator ($k_z = 0$) mode. This is because the basic state was taken to be the fastest growing elevator mode. The system instead first becomes unstable to a mode with $f = 0$, which we have previously categorised as a ‘regime 2’ (R2) mode. This then yields to an R1 mode with $f = 0.5$, before returning again to an R2 mode at larger A_ψ. This is reflected in the plot of the growth rate ratio, in which the R1 mode (red line) initially dominates with a GRR greater than one. The GRR of the R2 mode (blue line) then overtakes for a short period before yielding again to the R1 mode.

The behaviour is qualitatively similar to that observed for the heat-salt system with a marginal basic state (c.f. Figure 4.17); however, the instabilities here occur at values of A_ψ that are 10 times smaller than in the marginal case. This implies that those basic states with a longer wavelengths in the x-direction (smaller k_x) are more readily destabilised.

Differences are also observed in the eigenfunctions. Figures 4.24 and 4.25 show contours of the perturbations and total values of the streamfunction and density for the FGSM in the heat-salt system in the two different regimes. The patterns are similar to those observed in the marginal case (cf. Figures 4.15 and 4.16); however, the recirculating regions in both regimes are either slightly elongate (regime 1) or angled (regime 2). Again, the combinations of primary and secondary modes are similar to those observed in Chapter 3 for the truncated systems. That is, the regime 1 eigenfunctions resemble those observed in the 10th-order system, while the regime two eigenfunctions resemble those in the 9th- and 17th-order systems.

Furthermore, the results are similar to those obtained by Veronis (1987), who employed a similar analysis to show that the fastest growing elevator modes, with optimal horizontal width, can be unstable to modes which cause upward and downward penetrations into adjacent elevators. Indeed, the total density shown in 4.25 comprises such alternately penetrating regions. This feature is, as noted by Veronis, unsurprising, as it efficiently transports the stabilising property across the finger boundary from a finger where it hinders instability towards a finger where it assists the instability. Radko (2016) also notes that such horizontal transport, for instance initiated by purely horizontal shear, assists in the development of the instability. We note that the results of Veronis (1987) were obtained in the salt-sugar system, so this may be why the horizontal intrusions are more prevalent in that study. Furthermore, Veronis (1987) did not observe the oscillatory R1 mode which occurs at lower value of A_ψ, at least in the heat-salt system.

Sweep over R_ρ^{-1} and A_ψ

Figures 4.26, 4.27 and 4.28 show the wavenumbers and growth rates of the fastest growing modes when $R_\rho^{-1} = 0.2, 0.5$ and 0.991 respectively. Indicated on the plots

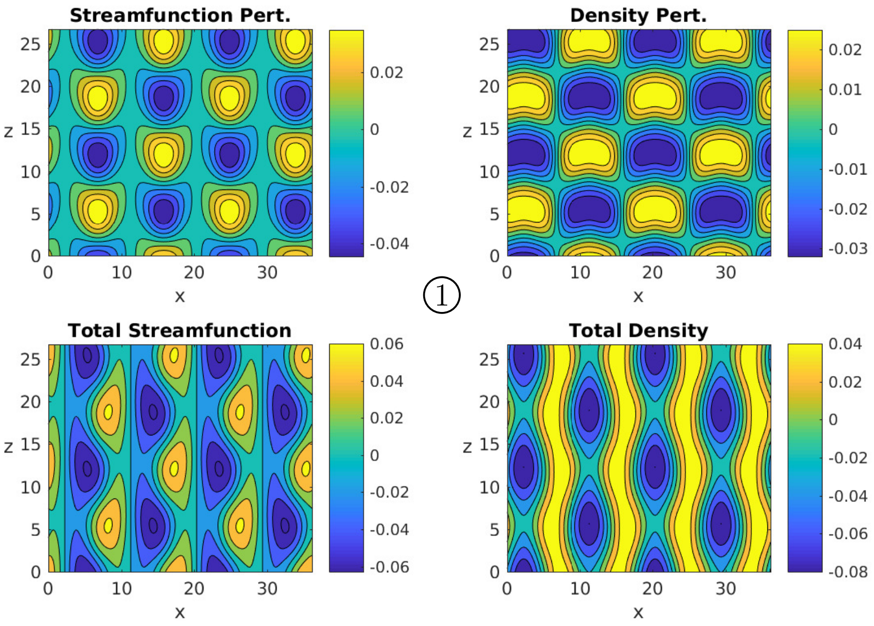

Figure 4.24: Perturbations and total values of streamfunction and density for the fastest growing mode $(f, k_z) = (0.5, 0.47)$ in the heat-salt system with $R_\rho^{-1} = 0.02$, $A_\psi = 0.035$ and $k_x = k_x^*$. This corresponds to a point in R1 in Figure 4.23.

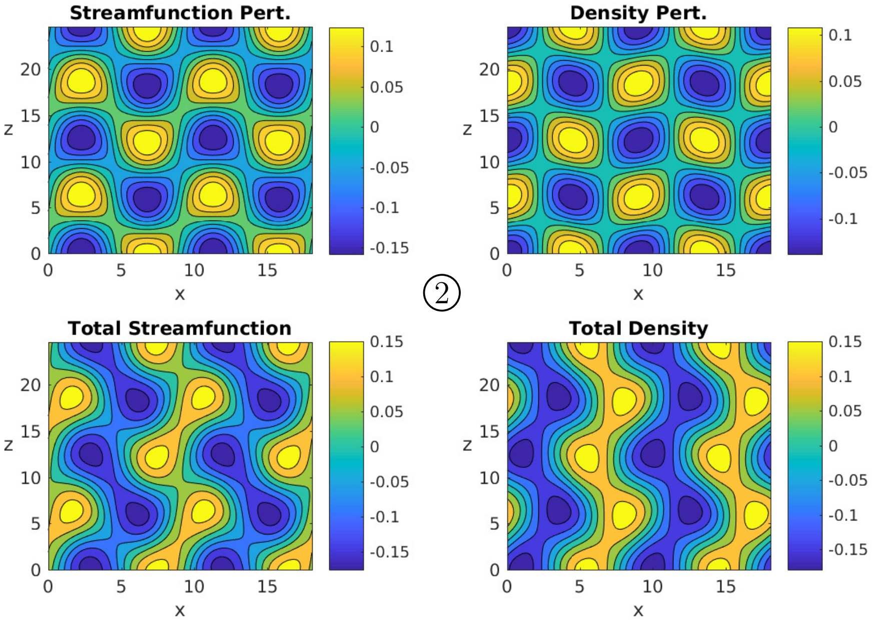

Figure 4.25: Perturbations and total values of streamfunction and density for the fastest growing mode $(f, k_z) = (0.0, 0.511)$ in the heat-salt system with $R_\rho^{-1} = 0.02$, $A_\psi = 0.08$ and $k_x = k_x^*$. This corresponds to a point in R1 in Figure 4.23.

are regimes 1 and 2, corresponding to secondary instabilities with $f = 0.5$ and $f = 0$ respectively. We see that the GRR for any particular A_ψ decreases as $R_\rho^{-1} \to 1$, despite the magnitude of the growth rate actually increasing over this range. This is because the growth rate of the basic state also increases as $R_\rho^{-1} \to 1$. We note that in each case, as in the marginally stable case, the fastest growing mode (that is not an elevator mode) has a horizontal floquet factor of $f = 0$, or $f = 0.5$, but never inbetween.

The way in which the system first becomes unstable is relatively unchanged by R_ρ^{-1}, in that we first observe a regime 1 mode which subsequently yields to a regime 2 mode. This corresponds to the crossing of red and blue lines in the growth rate vs. A_ψ plots as A_ψ is increased. One quite striking observation is that as $R_\rho^{-1} \to 1$ the red and blue lines approach each other until they almost overlap. However, even at $R_\rho^{-1} = 0.991$ (Figure 4.28) the lines do not reach such a point, with a regime 1 mode (blue) still dominating at low A_ψ and a regime 2 mode (red) dominating at large A_ψ. Hence the two regimes grow at almost the same rate at all values of A_ψ as R_ρ^{-1} approaches unity, implying that when the background T and S gradients are most unstable (large R_ρ^{-1}) both secondary modes could influence the basic state elevator modes.

It appears that in all cases, the system first becomes unstable to modes with $f = 0.5$. The growth rates of such modes are $\mathcal{O}(10) - \mathcal{O}(100)$ times larger than that of the basic elevator modes before we even see the $f = 0$ modes, which implies that as A_ψ increases from a low-amplitude perturbation, the system will first become unstable to a fast-growing mode with $f = 0.5$.

However it must be noted that at low values of A_ψ and high values of R_ρ^{-1}, the collective instability can be the fastest growing mode. As discussed in Chapter 1, the collective instability is characterised by very long internal gravity waves, and are thus represented here by very small values of f and k_z. Figure 4.29 shows the growth rate and wavenumber when $R_\rho^{-1} = 0.991$, detailing a smaller region of A_ψ. Here the growth

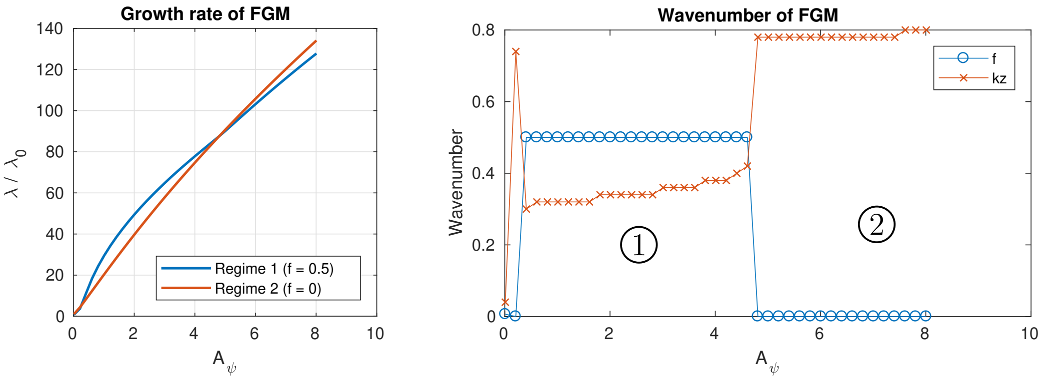

Figure 4.26: Relative growth rate and wavenumber of the FGSM for $R_\rho^{-1} = 0.2$, $Pr = 10$ and $\tau = 0.01$.

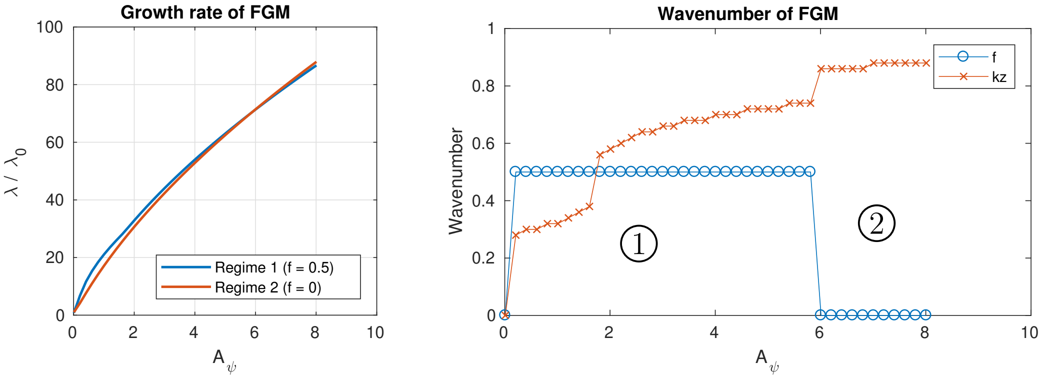

Figure 4.27: Relative growth rate and wavenumber of the FGSM for $R_\rho^{-1} = 0.5$, $Pr = 10$ and $\tau = 0.01$.

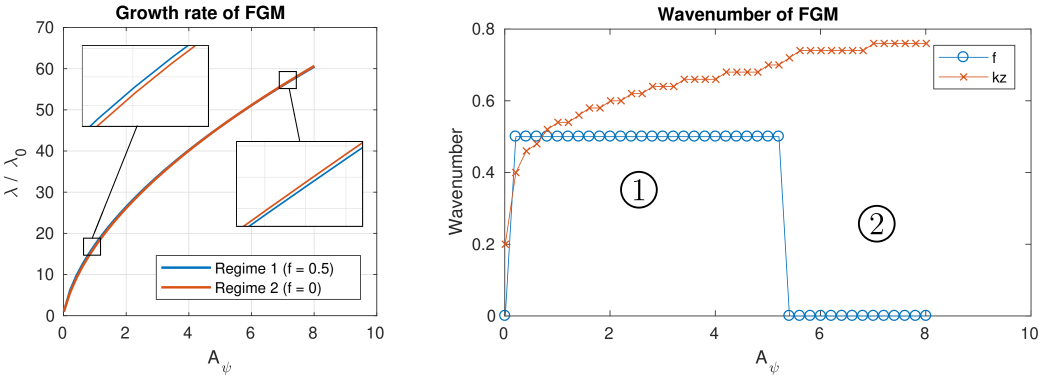

Figure 4.28: Relative growth rate and wavenumber of the fastest growing mode for $R_\rho^{-1} = 0.991$, $Pr = 10$ and $\tau = 0.01$.

rate plot shows the growth rate of the regime 1 mode, along with the growth rate of the fastest growing mode with any wavenumber. Here, the FGSM initially has non-zero (but very small) values of f and k_z, indicating the presence of the collective instability. This subsequently gives way to an R2 mode at $A_\psi = 0.08$ and then an R1 mode at $A_\psi = 0.017$.

Figure 4.30 shows the growth rate and wavenumber of the FGSM at even lower values of A_ψ. It is clear that f and k_z are both non-zero and take on very small values, indicating the presence of the collective instability. Although this is the FGSM at this point, the growth rate is only marginally larger than that of the basic state elevator mode and so the quasi-steady approximation may not be accurate. Nevertheless, it indicates that—perhaps contrary to Holyer's findings—the collective instability may indeed be the fastest growing mode under certain conditions in the heat-salt system.

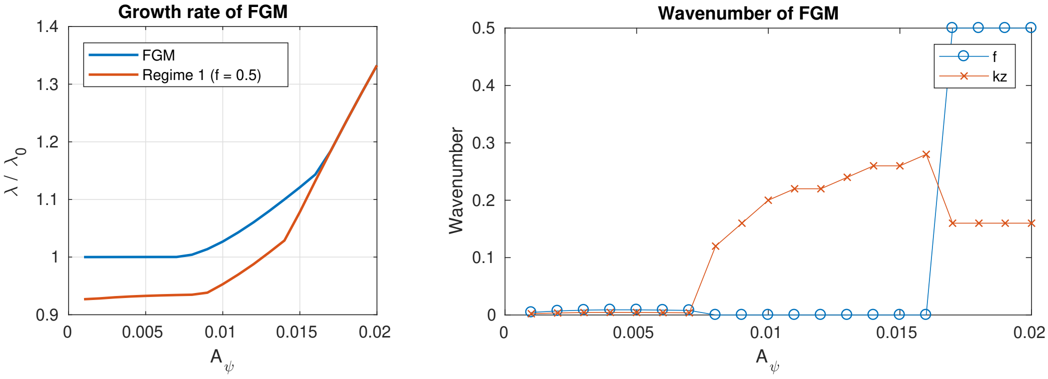

Figure 4.29: Relative growth rate and wavenumber of the fastest growing mode for $R_\rho^{-1} = 0.991$, $Pr = 10$ and $\tau = 0.01$, presented at low A_ψ to capture the collective instability

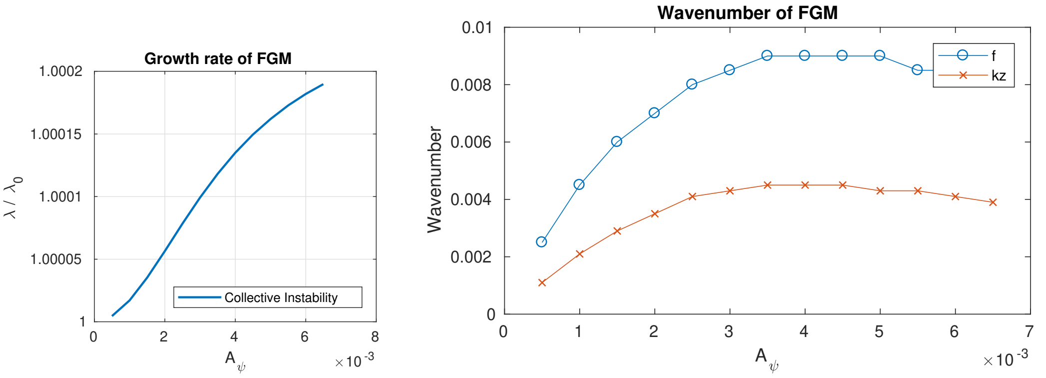

Figure 4.30: Relative growth rate and wavenumber of the fastest growing mode for $R_\rho^{-1} = 0.991$, $Pr = 10$ and $\tau = 0.01$, presented at low A_ψ to capture the collective instability

4.4.3 Effect of the Prandtl Number

We have shown that the form of the secondary mode is dependent on the horizontal scale and amplitude of the basic state A_ψ, along with the strength of the background thermal and compositional gradients R_ρ^{-1}. We now investigate the influence of the Prandtl number $Pr = \nu/\kappa_T$. The Prandtl number may be thought of as akin to the strength of inertial terms in the system—an infinite Prandtl number represents an effectively inertia-free system, and vice-versa. For reference, low-Pr double-diffusive convection is typically observed in the Sun, while a salt-sugar system typically has $Pr = 10^3$ (though τ is also different in each case).

Here we briefly investigate the influence of Pr on the form of the secondary instabilities. Whilst the wavenumber plots presented in the previous section were useful for describing the interplay between modes, it may not be so easy to spot patterns when reproducing such plots for a wide range of Prandtl numbers. Therefore, we instead look at the 'critical' values of A_ψ at which the dominant mode switches between an R1 mode and an R2 mode. Using Figure 4.26 as an example, $A_{\psi,1}$ will be the value of A_ψ at which the R1 mode becomes dominant—here, $A_{\psi,1} = 0.2$—while $A_{\psi,2}$ will be the value at which the R2 mode becomes dominant—here, $A_{\psi,2} = 4.7$.

In Figure 4.31 we plot $A_{\psi,1}$ and $A_{\psi,2}$ as a function of R_ρ^{-1} for $Pr = [0.1, 10, 100]$ when $k_x = k_x^*$. At higher values of Pr, a larger A_ψ is required for the R2 mode (black line) to dominate. This implies that for infinite Pr, we may never see the R2 mode. A larger value of A_ψ leads to larger velocities within the elevators and correspondingly high levels of shear between the elevators. Thus, a larger Pr implies that a larger shear would be required to see a shear-driven flow. Owing to the fact that the R2 mode is observed at larger values of A_ψ, and that the R2 mode is less prominent at higher values of Pr, we hypothesise that the R2 mode is, at least in part, shear-driven. The shear instability is perhaps reinforced by diffusive effects—that is, the instability leads to the passing of diffusive components into adjacent elevators, as described above.

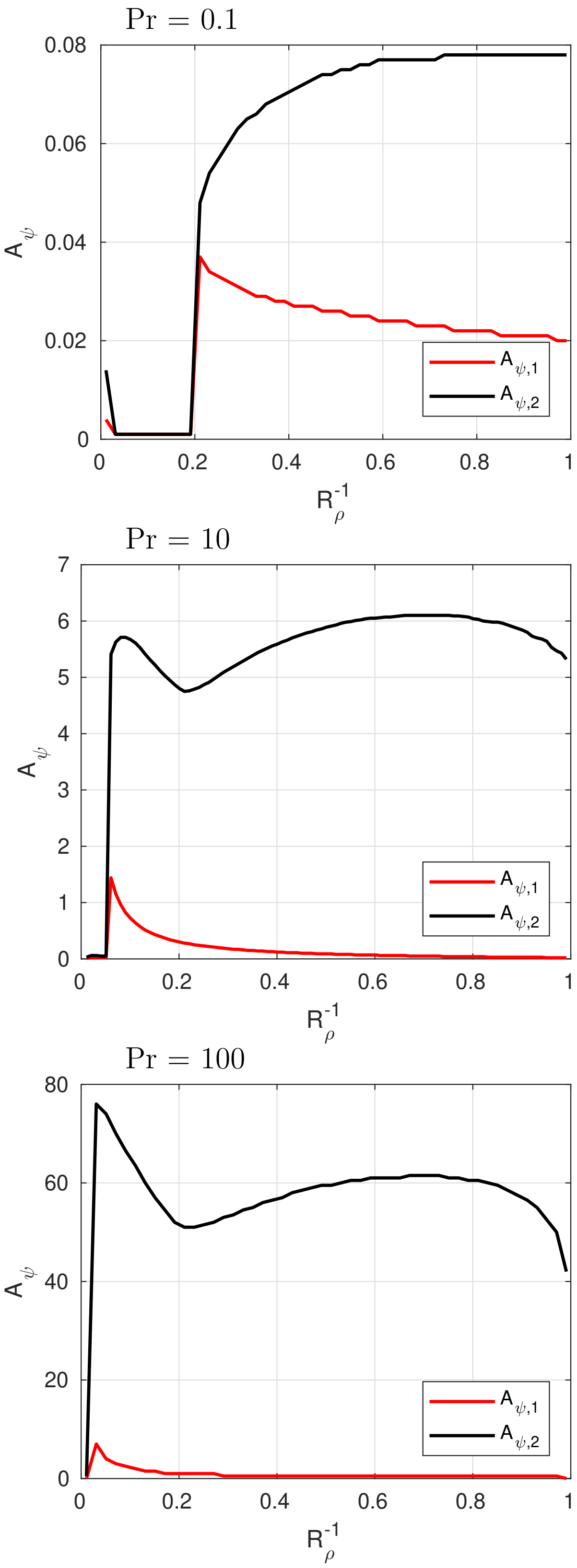

Figure 4.31: Critical values of A_ψ as a function of R_ρ^{-1} for $Pr = [0.1, 10, 100]$ and $\tau = 0.01$.

We investigate this hypothesis further in section 4.5. We here conclude that a large value of Pr corresponds to relatively low inertial effects, suggesting that the R1 instability predominantly observed at high Pr is driven entirely by diffusive, rather than shear effects.

4.4.4 Salt-Sugar System

It can be difficult to generate meaningful results from experiments using the heat-salt system, because the system evolves over long time-scales (Merryfield, 2000). For this reason, researchers may resort to either field data (Molcard and Tait, 1977), or experiments with two other different diffusive components—-most commonly salt and sugar (Stern and Turner, 1969). In this configuration, salt plays the role of the faster-diffusing component, while sugar plays the role of the slower-diffusing component. Mathematically, this results in a change of the Prandtl and Lewis numbers to $Pr = 1000$ and $\tau = 1/3$ respectively. Holyer (1984) studied the salt-sugar system and concluded that the fastest growing secondary mode in such a system was oscillatory with $f = 0.5$— much like the R1-modes we observed in the heat-salt system at low A_ψ. Veronis (1987), on the other hand, found a fastest growing secondary mode with $f = 0$ which corresponds to an R2 mode. We once again expand on the work of Holyer to study the salt-sugar system over a much larger range of wavenumbers (f, k_z) and amplitudes A_ψ.

Figure 4.32 shows the growth rate of elevator modes as a function of R_ρ^{-1} and k_x. In line with Holyer (1984), we first take $R_\rho^{-1} = 0.91$ and choose k_x to give marginal stability. Hence, in this case, $k_x = 1.18$. Figure 4.33 shows the growth rate of secondary modes (left) along with the when $R_\rho^{-1} = 0.91$, $Pr = 1000$, $\tau = 0.01$ and $A_\psi = 100$. Here, the results are scaled using $l_H = \left(\frac{1}{((R/\tau)-1)}\right)^{-4}$) as described in the scaling section to allow a direct comparison to be made with the results of Holyer (1984). Holyer identifies the fastest-growing secondary mode under these parameters as that having a wavenumber $f = k_z = 0.5$, and growth rate $\lambda = 5.8+39.8i$. This matches the results we

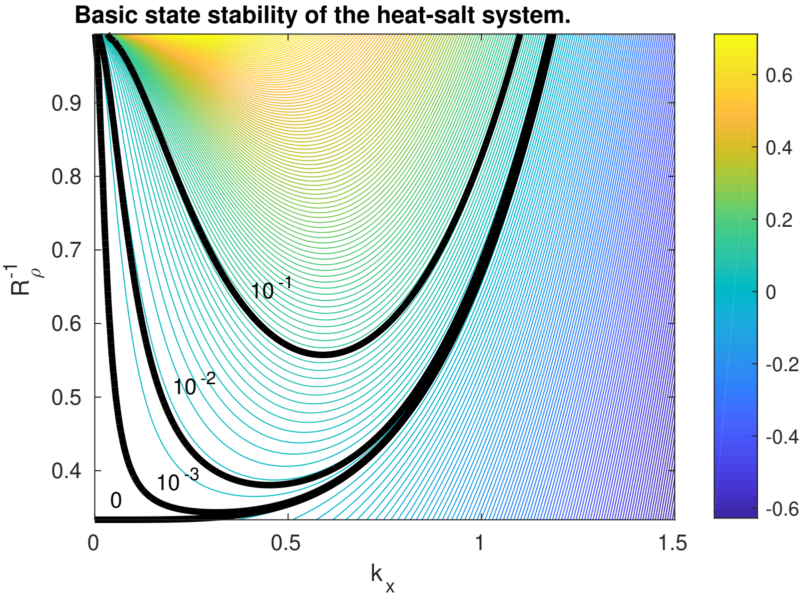

Figure 4.32: Growth rate of the primary elevator mode λ_0 as a function of the background density gradient ratio R_ρ^{-1} and the basic-state wavenumber k_x for the salt-sugar system ($Pr = 1000$, $\tau = 1/3$). The black lines are contours of $\lambda_0 = [0, 10^{-3}, 10^{-2}, 10^{-1}]$.

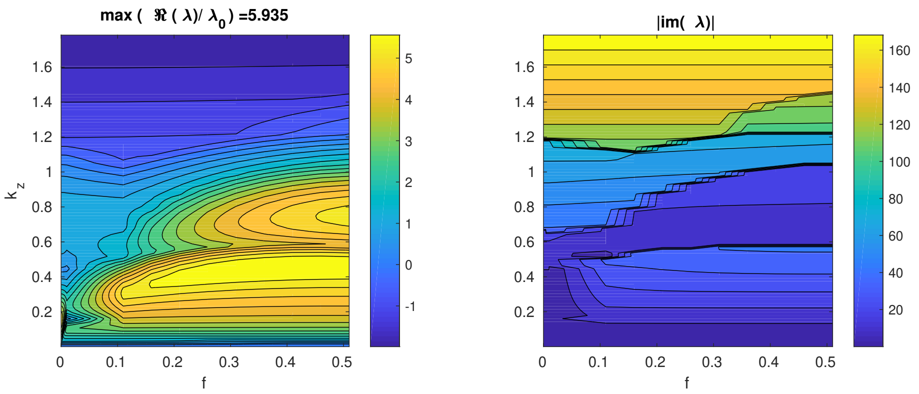

Figure 4.33: Real and imaginary parts of the growth rate of secondary modes in the salt-sugar system when $R_\rho^{-1} = 0.91$, $Pr = 1000$, $\tau = 0.01$ and $A_\psi = 100$.

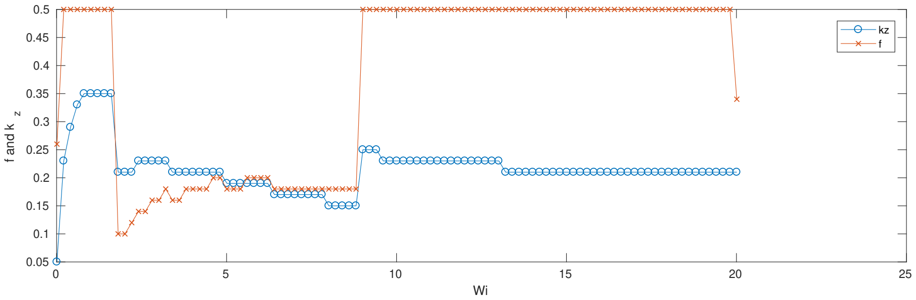

Figure 4.34: Wavenumber of the FGSM vs. A_ψ in the salt-sugar system, when $R_\rho^{-1} = 0.91$

see in Figure 4.33, indicating that our model is working as expected. Furthermore, we see from our model that the fastest growing non-oscillatory mode has $f = 0$, $k_z = 0.15$, and a growth rate of $\lambda = 3.89$, which is also in agreement with Holyer.

We now proceed to vary the strength of the elevator modes by varying A_ψ. Figure 4.34 shows the wavenumber of the fastest growing mode for $0 < A_\psi < 20$. We see that the fastest-growing mode initially occurs at low A_ψ as an R1 mode, with $f = 0.5$; however, between $A_\psi = 2$ and $A_\psi = 9$, we see an additional mode with finite f and k_z emerges as the fastest growing mode. This 'intermediate' mode eventually gives way to the R1 mode, before emerging again at $A_\psi = 20$. Although not shown here, the R1 mode eventually dominates once again, and remains the FGSM until approximately $A_\psi = 600$, at which point an R2 mode takes over as the FGSM. Thus, we see here that the modes observed by Holyer (1984) are the fastest growing modes at low A_ψ, while those observed by Veronis (1987) are observed at large A_ψ. We further see the emergence of an 'intermediate' mode which has not prveiously been documented.

The behaviour observed is generally consistent with that in the heat-salt system, so we do not investigate this system further at this time. It may be of interest to further study the 'intermediate' mode, for example to determine whether this mode is more prominent in different parameter regimes. For now, we move on to studing the role of heat and salt in the system, before looking at the stability of oscillatory elevator modes.

4.5 Role of Heat and Salt

Previous studies have investigated the stability of purely hydrodynamic, sinusoidal shear flows, generally referred to as Kolmogorov flows. Beaumont (1981) studied the stability of a vertical sinusoidal velocity profile (i.e. $\mathbf{U} = U(z)\mathbf{i}$) using Floquet theory applied to the so-called Orr-Sommerfeld equation. The Orr-Sommerfeld equation, derived as in Lin (1966), describes the growth of perturbations to a viscous fluid subject to a spatially periodic velocity profile. For ease of comparison with Beaumont (1981), we here derive the Orr-Sommerfeld equation using a slightly different notational convention than has been used so far in this thesis. The equations are later transformed to be consistent with our usual notation.

The viscous momentum equation describing perturbations to a static basic state, non-dimensionalised using the thermal diffusivity κ_T, but in the absence of stratification, becomes

$$\left(\frac{\partial}{\partial t} - Pr\nabla^2\right)\nabla^2\psi = -J(\psi, \nabla^2\psi). \tag{4.20}$$

where $Pr = \nu/\kappa_t$ is here an inverse Reynolds number, as discussed below. We note that $Re = \rho U d/\nu$ could instead be obtained by non-dimensionalising using the viscosity, ν, as opposed to κ_T. We take the perturbation ψ to be the sum of a spatially periodic basic state and a secondary perturbation, i.e. $\psi = \bar{\psi} + \psi'$, with $\bar{\psi}(x) = \bar{\psi}(x+T)$ for some period T and all x. We then assume a secondary perturbation of the form,

$$\psi' = \phi(z)e^{i\alpha(z-ct)}, \tag{4.21}$$

where $c = c_R + ic_I$ is a complex wave velocity and α is a positive wavenumber. The sign of c_I then determines the stability of the basic flow to this perturbation (Beaumont, 1981). Noting that $\bar{\psi}' = U(z)$ and $\phi = -\phi''$, where prime denotes differentiation with respect to z, we obtain the viscous Orr-Sommerfeld equation,

$$(U-c)(\phi'' - \alpha^2\phi) - U''\phi = \frac{Pr}{i\alpha}(\phi^{\text{iv}} - 2\alpha^2\phi'' + \alpha^4\phi). \tag{4.22}$$

To retrieve the equations in the form of Beaumont, we require $Pr = 1/Re$. Hence Pr is, in this case, an inverse Reynolds number. This system is identical to that of Beaumont, except that Beaumont employed a z-dependent basic state ($U = \cos z$), in contrast to our x-dependent basic state. Since we are not interested here in gravitational terms we may assume, without loss of generality, that Beaumont used an x-dependent basic state. Thereby, $U = \cos x$ is consistent with an elevator mode of the form $\bar{\psi} = A_\psi \sin(k_x x)$ when $A_\psi = k_x = 1$. The vertical wavenumber is transformed by $\alpha \to k_z$, and the growth rate is transformed by $-i\alpha c \to \lambda$, hence $\lambda_R = \alpha c_I$.

Beaumont expanded the function $\phi(x)$ in Floquet form as,

$$\phi(x) = e^{\gamma x} \sum_{n=-\infty}^{\infty} a_n e^{\frac{2\pi i n x}{T}}, \tag{4.23}$$

where $n \in \mathbb{Z}$, and T is the period of the basic state ($T = 2\pi$). To obtain the equations in our usual notation, we employ the following transformations: Floquet factor $\gamma \to f$; eigenmode $a_n \to \psi_n$; and horizontal wavenumber $2\pi/T \to k_x = 1$. We assume a basic state streamfunction of the form $\bar{\psi} = A_\psi \cos(k_x x)$, giving $U = \bar{\psi}' = -A_\psi k_x \sin(k_x x)$, and $\bar{U}'' = A_\psi k_x^3 \sin(k_x x)$. Note that we could equally take $\bar{\psi} = A_\psi \sin(k_x x)$ as our initial state. Furthermore, introducing the amplitude $A\psi$ affects the Reynolds number; to retreive the equations in the form of Beaumont, we require $Pr/A_\psi = Re$. This makes sense intuitively—for a given Pr, a larger basic state streamfunction (and thus, velocity) will give a larger Reynolds number. Increasing A_ψ increases the strength of the shear.

4.5.1 Beaumont Results

Beaumont showed that steady Kolmogorov flow is unstable for $Re > \sqrt{2}$. The author derived an infinite system of equations, not dissimilar to ours, and determined the growth rates of secondary modes. In Figures 1 and 2 we present results obtained using our code, taking parameters consistent with Beaumont. That is, we take $A_\psi = k_x = 1$, and $Re = 1/Pr = [10, 20]$.

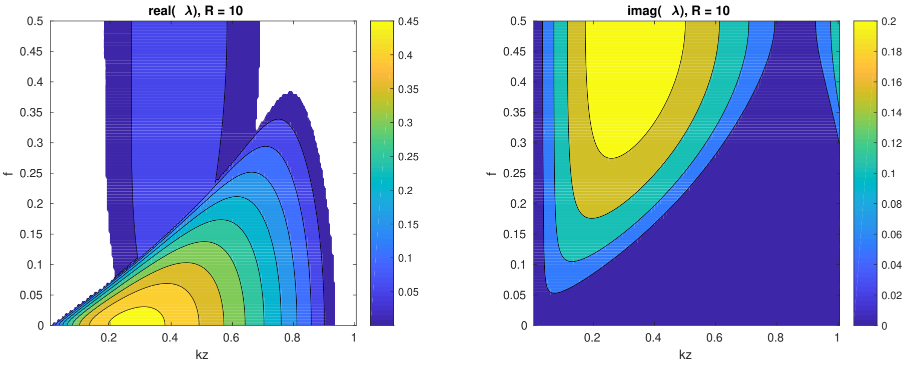

Figure 4.35: Growth rate of secondary instabilities in steady Kolmogorov flow with $Re = 10$.

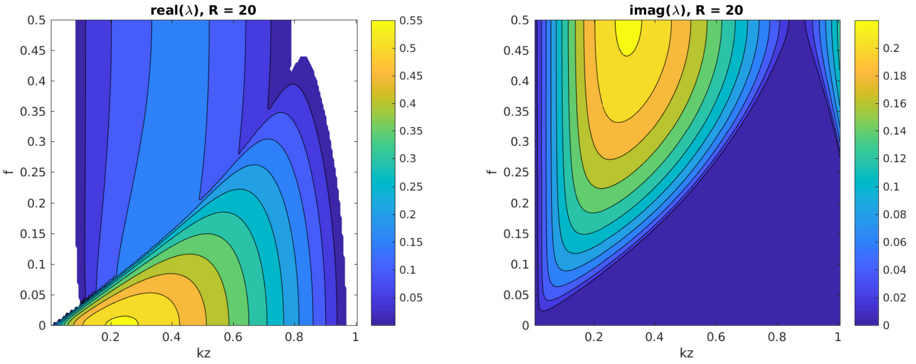

Figure 4.36: Growth rate of secondary instabilities in steady Kolmogorov flow with $Re = 20$.

Note that f is now on the vertical axis and k_z is on the horizontal axis to permit a direct comparison with the results of Beaumont. We see that the results are identical to those of Beaumont (1981), with the fastest-growing secondary mode having a floquet factor $f = 0$ and a finite vertical wavenumber k_z. The FGSM is non-oscillatory, though growing modes do exist having finite λ_i. Increasing Re from 10 to 20 for the same value of $A_\psi = 1$ (which is equivalent to reducing the Prandtl number Pr) reveals a FGSM having a larger growth rate and a lower value of k_z than that observed when $Re = 10$. Increasing Re (reducing Pr) may be thought of as strengthening the inertial terms (i.e. $\rho U \delta$) or weakening any viscous effects. This suggests that in fixed-amplitude sinusoidal hydrodynamic shear, the fastest growing secondary mode has a larger growth rate, and a longer wavelength in the z-direction, when basic state inertial effects are stronger.

Figure 4.37 shows the growth rate of fastest-growing secondary modes having positive growth rates when $Pr = 10$ ($Re = 1/10$), which corresponds to that in the heat-salt system. The results are shown at $A_\psi = 10$, $A_\psi = 12$, and $A_\psi = 15$. The white regions here are stable. We see that, initially, there are no secondary modes with positive growth rates; i.e. we do not see a mode with $f = 0.5$. At $A_\psi = 12$, the FGSM has $f = 0$ and $k_z = 0.125$. Increasing A_ψ further, to 15, leads to the vertical wavenumber of the $FGSM$ increasing to 0.175. This behaviour is similar to that observed for the R2 mode in the heat-salt system. Indeed, the plot of the growth rate as a function of f and k_z for this system appears to resemble that of Figure 4.13 for the heat-salt system, wherein the R2 mode has comparable vertical wavenumbers of $k_z = 0.2$ at $A_\psi = 1$, and $k_z = 0.38$ when $A_\psi = 10$.

Relating this back to double-diffusive convection, one might expect that increasing the strength of inertial terms (reducing Pr or increasing A_ψ) could lead to a faster-growing, underlying secondary mode arising due to hydrodynamic shear. If the inertial effects are strong enough, this underlying instability may eventually dominate over a 'diffusive' instability. To the contrary, removing intertial effects from the system, for instance by increasing the Prandtl number towards infinity, may ensure that secondary modes indicative of hydrodynamic shear never appear. Indeed, it was observed from Figure 4.31 that as Pr is increased, we require an increasingly larger value of A_ψ to observe a dominant mode having $f = 0$.

Furthermore, as shown in Figure 4.37, increasing A_ψ in the Kolmogorov system results in the vertical wavenumber of the FGSM increasing, as with the $f = 0$ mode in the double-diffusive system. Furthermore, the $f = 0$ mode emerges at lower values of A_ψ in the double-diffusive system, when compared to the Kolmogorov system. This leads us to conclude that the $f = 0$ mode observed at large A_ψ in the double-diffusive system is largely a shear-induced instability that is perhaps reinforced by double-diffusive effects.

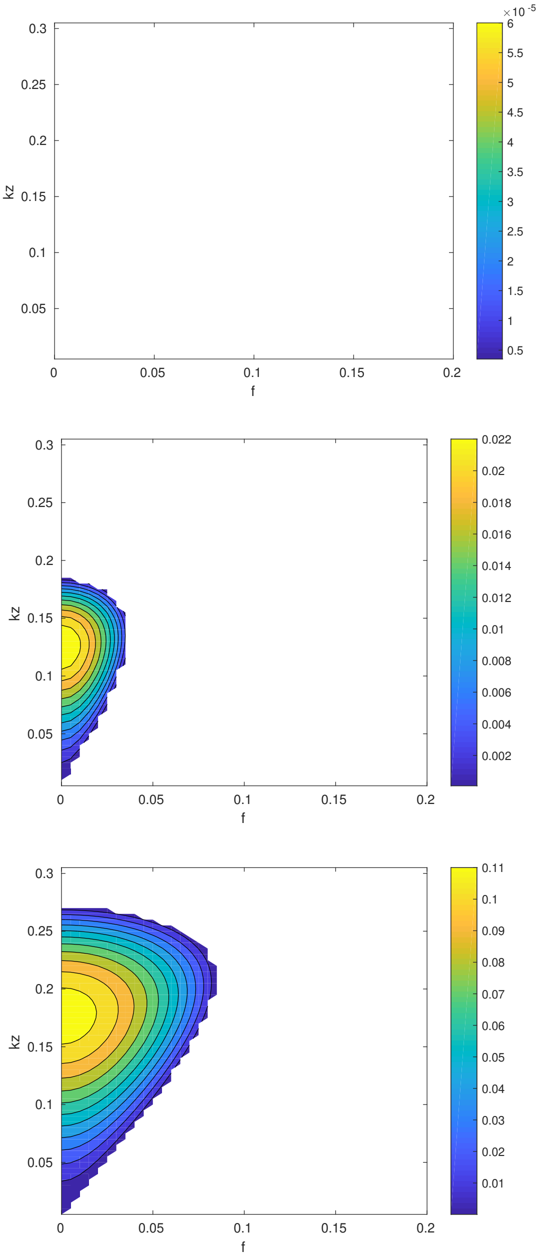

Figure 4.37: Growth rate of secondary modes in the Kolmogorov system when $Pr = 10$ and, **Top:** $A_\psi = 10$; **Middle:** $A_\psi = 12$; and **Bottom:** $A_\psi = 15$.

4.6 Shear-free System

Kerr and Tang (1999) studied a double-diffusive system enclosed between two vertical boundaries and stratified by a vertical salinity gradient. The boundaries were heated to create a horizontal temperature difference. Under certain conditions, the resulting instability was found to be destabilised by an increased horizontal salinity gradient and stabilised by a background shear flow. Indeed, it is not unusual to see shear flows providing a stabilising effect in double-diffusive systems. Linden (1974), for example, showed that convection can be suppressed by shear in a salt fingering system.

Therefore, in order to further understand the influence of hydrodynamic shear on the secondary instabilities in our system, we now study the secondary instabilities that arise in the absence of any shear term in the momentum equation. Specifically, rather setting $T = S = 0$ as we did in § 4.5, we now delete the Jacobian shear term in the momentum equation of (4.24)–(4.26). This gives,

$$\left(\frac{\partial}{\partial t} - Pr\nabla^2\right)\nabla^2\psi = Pr\left(\frac{\partial T}{\partial x} - \frac{\partial S}{\partial x}\right), \tag{4.24}$$

$$\left(\frac{\partial}{\partial t} - \nabla^2\right)T + \operatorname{sgn}(T_z)\frac{\partial \psi}{\partial x} = -J(\psi, T), \tag{4.25}$$

$$\left(\frac{\partial}{\partial t} - \tau\nabla^2\right)S + \operatorname{sgn}(S_z)R_\rho^{-1}\frac{\partial \psi}{\partial x} = -J(\psi, S), \tag{4.26}$$

Substituting for perturbations in the form given by equation (4.1), linearising, and seeking solutions in Floquet form, we get,

$$-\lambda\psi_n = PrK_n^2\psi_n + \frac{k_x^3 k_z A_\psi}{2K_n^2}\left[\psi_{n-1} - \psi_{n+1}\right] + iPr\frac{(f+n)k_x}{K_n^2}(T_n - S_n n),$$

$$\lambda T_n = -K_n^2 T_n + \frac{k_x k_z A_\psi}{2}\left[T_{n-1} - T_{n+1}\right] + \frac{ik_x k_z A_T}{2}\left[\psi_{n-1} + \psi_{n+1}\right] - i\operatorname{sgn}(T_z)(f+n)k_x\psi_n,$$

$$\lambda S_n = -\tau K_n^2 S_n + \frac{k_x k_z A_\psi}{2}\left[S_{n-1} - S_{n+1}\right] + \frac{ik_x k_z A_S}{2}\left[\psi_{n-1} + \psi_{n+1}\right] - i\operatorname{sgn}(S_z)R_\rho^{-1}(f+n)k_x\psi_n,$$

We first determine the secondary instabilities arising when $R_\rho^{-1} = 0.02$ and when $k_x = 1$ (corresponding to marginal growth. These parameters correspond to those used to generate Figures 4.13, so we can make direct comparisons of the results in each case. Figure 4.38 shows contours of the growth rate of secondary modes as a function of f and k_z at specific values of A_ψ from 0.01 to 10.

We see that, initially, as A_ψ is increased from 0.01 to 0.1, the fastest growing mode 'jumps' from the $k_z = 0$ axis to the $f = 0.5$ axis. This behaviour was observed in our previous simulations of the full system, but notably was not observed in the Kolmogorov system. Unlike in the full system, however, where a further increase in A_ψ to 1 resulted in an $f = 0$ mode becoming the dominant mode, we here see that the fastest growing mode remains an $f = 0.5$ mode. Further increasing A_ψ to 10 leads only to changes in k_z. That is, we see that the fastest growing mode remains on the $f = 0.5$ axis. We have even studied the system up to $A_\psi = 10000$, and we find the dominant mode is always an $f = 0.5$ mode, though it is not always oscillatory.

The behaviour at low A_ψ is consistent with that of the full system, as low A_ψ implies low shear. At larger values of A_ψ, i.e. when shear terms are larger in the full system, the dominant mode is always an $f = 0$ mode. In the purely hydrodynamic Kolmogorov system, in contrast, we never see an $f = 0$ mode. Rather, the secondary instabilities in the Kolmogorov system more closely resemble those at large A_ψ (large hydrodynamic shear) in the full system. This further supports the our hypothesis that the $f = 0$ modes are largely shear-driven instabilities, while the $f = 0.5$ modes are largely diffusively-driven.

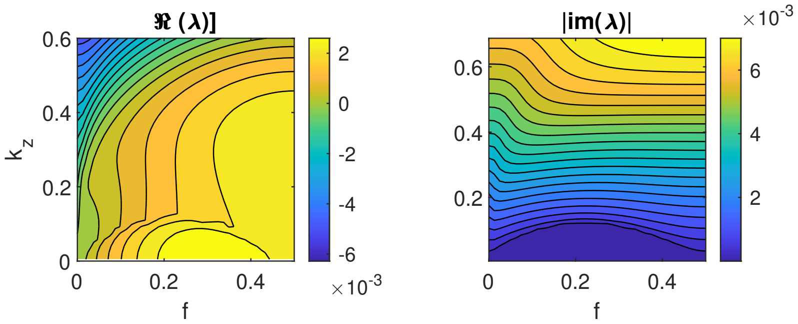

(a) $A_\psi = 10^{-2}$

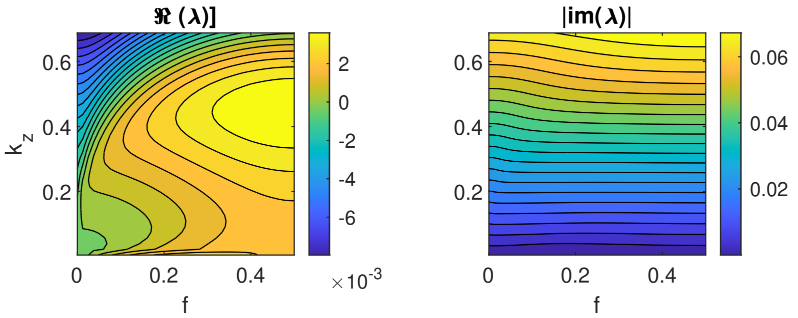

(b) $A_\psi = 10^{-1}$

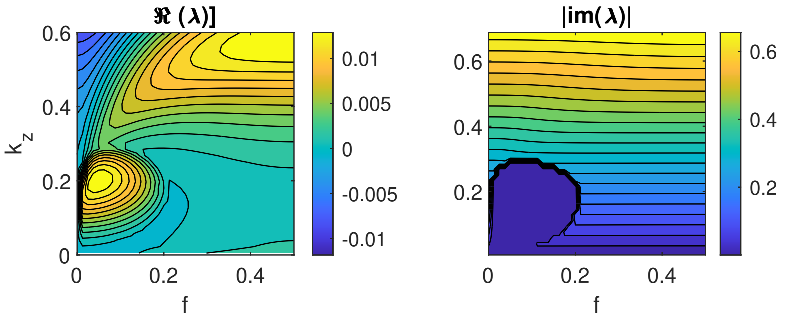

(c) $A_\psi = 1$

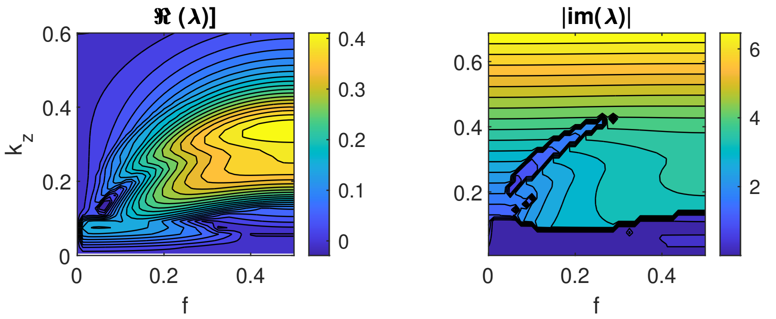

(d) $A_\psi = 10$

Figure 4.38: Real and imaginary part of the growth rates of secondary instabilities λ in the shear-free heat-salt system with $R_\rho^{-1} = 0.02$, $Pr = 10$, $\tau = 0.01$ and $A_\psi = [10^{-2}, 10^{-1}, 1, 10]$.

4.7 Conclusions

We have seen that the form of the secondary modes arising from steady (in time) elevator modes is highly dependent in the amplitude of the elevator modes. At low amplitudes, we see an oscillatory mode with $f = 0.5$ as identified in the study by Holyer (1984), while at larger amplitudes, we see a non-oscillatory mode with $f = 0$, as identified in the study by Veronis (1987). We have thus developed a more complete picture of the stability properties of steady elevator modes, which shows that the different modes observed by previous authors are each present in the system, but that different values of A_ψ are required to observe them.

In particular, we see that the $f = 0$ modes, driven by higher-amplitude elevator modes, are likely symptomatic of a shear instability. Indeed, the effect of increasing the Prandtl number on the results is that a higher value of A_ψ is required to observe a mode with $f = 0$. This is because larger Prandtl number corresponds to lower intertial terms, and so the viscious shear effects become less effective. Our hypothesis is supported by a model of hydrodynamic shear which was developed using similar Floquet methods. The modes observed in such systems always have $f = 0$. Furthermore, the vertical wavenumber of the secondary mode increases with increasing A_ψ, as in the heat-salt system.

Finally, we conclude here by noting that the structure of the $f = 0$ mode corresponds closely to that of the cellular mode used in the truncated models of Chapter 3. This is particularly interesting, as the truncated models are oscillatory in nature, while we are here looking at a steady, salt-fingering system. This similarity is discussed further in Chapter 5, when we look at the stability of fully oscillatory elevator modes.

CHAPTER 5

Instabilities of Oscillatory Elevator Modes

5.1 Introduction

In this Chapter, we investigate the instabilities arising from oscillatory elevator modes, which are the fastest-growing modes in double-diffusive convection when the temperature gradient is destabilising. We extend the Floquet methods developed in Chapter 4 to study the stability of steady elevator modes, and develop a new model which takes into account the time-dependency of the basic state. The findings of previous studies, such as those of Holyer (1984), Veronis (1968), and Radko and Smith (2012) in combination with the results presented in Chapter 4, provide a broad picture of the behaviour of steady elevator modes. We here apply these methods to investigate whether, in combination with the upended basic state temperature and salinity gradients, the oscillatory nature of the primary modes affects the structure of the known secondary modes. We also study whether oscillating elevator modes give rise to any different secondary modes, and we begin to compare the results with a fully hydrodynamic system to determine the influence of inertia on the secondary modes.

We find that the observed secondary modes exhibit structures similar to those of secondary modes arising from a steady basic state, except that the structures oscillate in time. Additional secondary modes are discovered, and it is found that the system responds to changes in the width of the basic state, or varying fluid parameters, in the same way as a system comprising steady elevator modes—that is, an increase in the Reynolds number drives a shear instability comparable to that arising in a purely hydrodynamic, oscillatory shear flow.

Despite the interest in Floquet analysis as applied to (infinitely long) salt-fingers, little attention has been paid to its applications in the diffusive regime. Perhaps the only notable example is found in a recent paper by Radko (2016) in which Floquet analysis was used to show that a system consisting of both a dynamically stable shear flow and a diffusively stable stratification could become unstable. The results are relevant to ocean dynamics, wherein phenomena associated with instabilities (such as layering) are observed in regions with linearly stable temperature and salt gradients. Radko showed that a dynamically stable shear flow can cause a statically stable double-diffusive system to become unstable. We are interested in cases in which a static diffusive state is in itself unstable, i.e. in the absence of any external shear.

The time-dependency of the basic state makes it trickier to model than its steady counterpart. In other applications of Floquet theory, including that of Radko (2016) discussed above, the basic state is assumed to be quasi-steady in time; however, in the presence of an inherently time-dependent basic state, this assumption no longer makes sense. Instead we formulate our Floquet expansion in such a way that accounts for the oscillatory nature of the basic state, but maintains the assumption that the basic state amplitude does not grow (significantly) in the time that it takes for secondary perturbations to grow.

This Chapter begins in §5.2.1 with an introduction to time-dependent Floquet analysis, followed by a derivation of the equations governing the growth rates of secondary instabilities arising from time-dependent elevator modes. In §5.3 we discuss methods for solving the resulting eigenvalue problem, while in §5.3.2 we look at ensuring the solutions are accurate. §5.4 comprises a parametric study, in which we sweep over different parameters and compare our results with those of Chapter 4.

We then outline the potential for future studies on the basis of our model, including studying an associated purely hydrodynamic oscillatory shear flow and a simplified set of equations for studying a high Prandtl number system. We conclude by comparing how the fastest growing secondary modes in the oscillatory system relate to those modes included in the truncated models of Chapter 3.

5.2 Secondary Instabilities

The stability of a static basic state was explored in Chapter 2, showing that the system is unstable to infinitely long, oscillatory, x-dependent elevator modes. Elevator modes are full solutions to the governing nonlinear equations, hence they do not interact with themselves to produce other modes. This means that we can take such a solution as a basic state and look at *secondary* perturbations to that state. In the diffusive case, the growing elevator solutions are oscillatory, so perturbations may be written as

$$\begin{aligned}\psi &= \bar{A_\psi}\cos(k_x x) + \psi',\\ T &= \bar{A_T}\sin(k_x x) + T',\\ S &= \bar{A_S}\sin(k_x x) + S',\end{aligned} \tag{5.1}$$

where $\bar{A_\xi} = A_\xi e^{\lambda_0 t}$ for $\xi = \{\psi, T, S\}$, and λ_0 is the growth rate of the primary instability. In the oscillatory regime the growth rate is complex, i.e. $\lambda_0 = \sigma + i\omega$, where ω is the basic state frequency. The fastest growing elevator modes are defined to be those with $k_x = k_x^*$. In order to find secondary modes that grow much faster than these elevator modes, we may make the assumption that the basic state is quasi-steady with $\sigma = 0$ and $\omega \neq 0$. Alternatively we may take a marginal basic state with k_x chosen to give zero growth rate (but non-zero ω), resulting in a purely oscillatory basic state which satisfies the same conditions.

Substituting perturbations of the form of (5.1) into the governing nonlinear perturbation equations (4.24)- (4.26) and linearising, under the assumption of a quasi-steady basic state with $\lambda_0 = i\omega$, yields

$$\begin{aligned}\left(\frac{\partial}{\partial t} - Pr\nabla^2\right)\nabla^2\psi' &= k_x\bar{A_\psi}\sin(k_x x)\frac{\partial}{\partial z}\nabla^2\psi' + k_x^3\bar{A_\psi}\sin(k_x x)\frac{\partial\psi'}{\partial z} + Pr\left(\frac{\partial T'}{\partial x} - \frac{\partial S'}{\partial x}\right),\\ \left(\frac{\partial}{\partial t} - \nabla^2\right)T' + \mathrm{sgn}(T_z)\frac{\partial\psi'}{\partial x} &= k_x\bar{A_\psi}\sin(k_x x)\frac{\partial T'}{\partial z} + k_x\bar{A_T}\cos(k_x x)\frac{\partial\psi'}{\partial z},\\ \left(\frac{\partial}{\partial t} - \tau\nabla^2\right)S' + \mathrm{sgn}(S_z)\frac{\partial\psi'}{\partial x}R_\rho^{-1} &= k_x\bar{A_\psi}\sin(k_x x)\frac{\partial S'}{\partial z} + k_x\bar{A_S}\cos(k_x x)\frac{\partial\psi'}{\partial z}.\end{aligned} \tag{5.2}$$

where ω is real and non-zero, and $\bar{A}_\xi = A_\xi e^{i\omega t} + A_\xi^* e^{-i\omega t}$ where $\xi = \{\psi, T, S\}$ and A_ξ^* is the complex conjugate of A_ξ.

5.2.1 Floquet Theory

The basis of Floquet theory was discussed in Chapter 4 in relation to a system with a steady basic state. It was shown that a set of PDEs with periodic coefficients may be reduced to an infinite eigenvalue problem by expanding the variables (in this case, the secondary perturbations) in an infinite sum of integer multiples of wavenumbers in the direction of periodicity. This method may be applied to systems which are periodic in multiple directions. Indeed, Radko and Smith (2012) studied 3D salt fingers using a so-called 'double-Floquet expansion' in two spatial directions. In this Chapter, we use a double-Floquet expansion in space and time to model 2D oscillatory elevator modes which are periodic in both space and time.

The coefficients in equations (5.2) are independent of z, periodic in x with period $2\pi/k_x$ and periodic in t with period $2\pi/\omega$; hence, solutions may be written in the double-Floquet form

$$\begin{pmatrix} \psi' \\ T' \\ S' \end{pmatrix} = \exp(ifk_x x + ik_z z + \lambda t) \sum_{n=-\infty}^{\infty} \sum_{m=-\infty}^{\infty} \begin{pmatrix} \psi_{n,m} \\ T_{n,m} \\ S_{n,m} \end{pmatrix} \exp(ink_x x + im\omega t), \tag{5.3}$$

where n and m are integers and f is the 'Floquet coefficient' governing the fundamental wavelength in x. Instead of defining the value of k_x, we here employ the spatial Floquet coefficient f to limit the parameter space to be explored to a range of $0 < f < 0.5$. This is explained further in the section on Floquet theory in Chapter 4. In contrast, since the value of the growth rate, λ, is to be calculated, and may take any (complex) value, we do not require a temporal Floquet coefficient that can varied to limit a parameter range to be studied.

It is, however, important to limit the values of λ that we take in some way (Blennerhasset and Bassom, 2002). We note that λ is a complex growth rate defined by $\lambda = \lambda_R + i\lambda_I$. In the same way that the *total* horizontal wavenumber of a perturbation is given by $k_{x,T} = (f+n)k_x$ with $0 < f < 0.5$ and $n \in \mathbb{Z}$, the *total* temporal wavenumber of such a variable is given by $\lambda_{i,T} = \lambda_I + m\omega$ with $m \in \mathbb{Z}$. We may limit λ_I to the range $0 \leq \lambda_I \leq \omega$ whilst still capturing any value of $\lambda_{i,t}$ through the infinite sum over m.

It may at first appear unnecessary to restrict λ in this way, since λ_I is a calculated value. However, for any particular λ_I, only one value of m will correspond to the largest growth rate λ_R. We observe in simulations that the modes with the largest values of λ_R typically have large positive or negative values of λ_I with correspondingly large values of m with the opposite sign. In other words, if λ_I is large and positive, the modes with maximum growth rate have large negative values of m (and vice versa). This means that the total wavenumber $(\lambda_I, T) = \lambda_I + m\omega$, which is representative of the form of the perturbation, is actually not large. The value of m taken is typically the maximum value possible, $m = M$. Such large values of m are misleading, as they imply that the solution is not converged. We return to this issue again in § 5.3.3.

Floquet Equations

We are now in a position to obtain the infinite set of equations governing the growth rates of secondary instabilities. We substitute the Floquet form of perturbations (5.3) into the governing PDEs (5.2) to deal with the periodic coefficients. Here, we demonstrate how the equations are obtained by looking at just one term in the momentum equation. For example, the coefficient $k_x^3 \bar{A}_\psi \sin(k_x x)$ interacts with $\frac{\partial \psi'}{\partial z}$ as follows:

$$
\begin{aligned}
&k_x^3 \bar{A}_\psi \sin(k_x x) \frac{\partial \psi'}{\partial z} \\
&= k_x^3 \bar{A}_\psi \sin(k_x x) \frac{\partial}{\partial z} \left(\exp(ifk_x x + ik_z z + \lambda t) \sum_{n=-\infty}^{\infty} \sum_{m=-\infty}^{\infty} \psi_{n,m} \exp(ink_x x + im\omega t) \right) \\
&= ik_x^3 k_z \bar{A}_\psi \exp(ifk_x x + ik_z z + \lambda t) \cdot \sin(k_x x) \sum_{n=-\infty}^{\infty} \sum_{m=-\infty}^{\infty} \psi_{n,m} \exp(ink_x x + im\omega t).
\end{aligned}
$$

For clarity we set $B = k_x^3 k_z \bar{A_\psi} \exp(ifk_x x + ik_z z + \lambda t)$, giving

$$\begin{aligned}
iB\sin(k_x x) &\sum_{n=-\infty}^{\infty}\sum_{m=-\infty}^{\infty}\psi_{n,m}e^{i(nk_x x+m\omega t)} \\
&= \frac{B}{2}\left(e^{ik_x x}-e^{-ik_x x}\right)\sum_{n=-\infty}^{\infty}\sum_{m=-\infty}^{\infty}\psi_{n,m}e^{i(nk_x x+m\omega t)} \\
&= \frac{B}{2}\sum_{n=-\infty}^{\infty}\sum_{m=-\infty}^{\infty}\left(\psi_{n,m}e^{i(n+1)k_x x}-\psi_{n,m}e^{i(n-1)k_x x}\right)e^{im\omega t}.
\end{aligned}$$

Summation indices may be shifted to recover a factor of $\exp(ik_x x)$ in each term, i.e.

$$\sum_{n=-\infty}^{\infty}\psi_{n,m}e^{i(n+1)k_x x} \equiv \sum_{n=-\infty}^{\infty}\psi_{n-1,m}e^{ink_x x},$$

$$\sum_{n=-\infty}^{\infty}\psi_{n,m}e^{i(n-1)k_x x} \equiv \sum_{n=-\infty}^{\infty}\psi_{n+1,m}e^{ink_x x}.$$

Hence, the periodic coefficients and partial derivatives are replaced with modal amplitudes as

$$k_x^3\bar{A_\psi}\sin(k_x x)\frac{\partial\psi'}{\partial z} = \frac{B}{2}\sum_{n=-\infty}^{\infty}\sum_{m=-\infty}^{\infty}\left[\psi_{n-1,m}-\psi_{n+1,m}\right]e^{i(nk_x x+m\omega t)}. \tag{5.4}$$

The periodicity in t is handled in the same way. Taking a factor of $\bar{A_\psi}$ out of B (and redefining B appropriately), equation (5.4) becomes

$$\begin{aligned}
&\frac{B}{2}(A_\psi e^{i\omega t}+A_\psi^* e^{-i\omega t})\sum_{n=-\infty}^{\infty}\sum_{m=-\infty}^{\infty}\left[\psi_{n-1,m}-\psi_{n+1,m}\right]e^{i(nk_x x+m\omega t)} \\
&= \frac{B}{2}\sum_{n=-\infty}^{\infty}\sum_{m=-\infty}^{\infty}\Big(A_\psi\left[\psi_{n-1,m-1}-\psi_{n+1,m-1}\right]+A_\psi^*\left[\psi_{n-1,m+1}-\psi_{n+1,m+1}\right]\Big)e^{i(nk_x x+m\omega t)}.
\end{aligned}$$

Similar expressions may be obtained for each set of periodic coefficients in (5.2). The inclusion of the time-periodicity doubles the number of modes in each of the three perturbation variables (ψ, T, S). Expanding as above, and noting that in the oscillatory regime $\mathrm{sgn}(T_z) = \mathrm{sgn}(S_z) = -1$, we obtain the following infinite set of equations for the growth rate of secondary perturbations λ in terms of the modal amplitudes:

$$\begin{aligned}\lambda\psi_{n,m} = -im\omega\psi_{n,m} - PrK_n^2\psi_{n,m} - i\,\mathrm{Pr}\,\frac{(f+n)k_x}{K_n^2}(T_{n,m} - S_{n,m})& \\ +\frac{k_xk_z}{2K_n^2}[(K_{n-1}^2 - k_x^2)(A_\psi\psi_{n-1,m-1} + A_\psi^*\psi_{n-1,m+1})& \\ -(K_{n+1}^2 - k_x^2)(A_\psi\psi_{n+1,m-1} + A_\psi^*\psi_{n+1,m+1})]&\end{aligned} \qquad (5.5)$$

$$\begin{aligned}\lambda T_{n,m} = -im\omega T_{n,m} - K_n^2 T_{n,m} - i\mathrm{sgn}(T_z)(f+n)k_x\psi_{n,m}& \\ +\frac{k_xk_z}{2}[A_\psi(T_{n-1,m-1} - T_{n+1,m-1}) + A_\psi^*(T_{n-1,m+1} - T_{n+1,m+1})]& \\ +\frac{ik_xk_z}{2}[A_T(\psi_{n-1,m-1} + \psi_{n+1,m-1}) + A_T^*(\psi_{n-1,m+1} + \psi_{n+1,m+1})]&\end{aligned} \qquad (5.6)$$

$$\begin{aligned}\lambda S_{n,m} = -im\omega S_{n,m} - \tau K_n^2 S_{n,m} - i\mathrm{sgn}(S_z)R_\rho^{-1}(f+n)k_x\psi_{n,m}& \\ +\frac{k_xk_z}{2}[A_\psi(S_{n-1,m-1} - S_{n+1,m-1}) + A_\psi^*(S_{n-1,m+1} - S_{n+1,m+1})]& \\ +\frac{ik_xk_z}{2}[A_S(\psi_{n-1,m-1} + \psi_{n+1,m-1}) + A_S^*(\psi_{n-1,m+1} + \psi_{n+1,m+1})]&\end{aligned} \qquad (5.7)$$

Since we have obtained these equations under the assumption that ω is non-zero, we cannot reduce them to steady form by simply setting $\omega = 0$. Truncating the system at N and M, we can express equations (5.5) - (5.7) in the matrix form,

$$\lambda\eta = \boldsymbol{A}\eta \qquad (5.8)$$

where

$$\eta = (...\psi_{n-1,m}, T_{n-1,m}, S_{n-1,m}, \psi_{n,m}, T_{n,m}, S_{n,m}...)^T,$$

and A is a square matrix of size $3(2N+1)(2M+1)$.

The equations decompose into two systems—one with $(n{+}m)$ even, and one with $(n{+}m)$ odd. This is because each $\xi_{n,m}$ is a function of $\xi_{n\pm1,m\pm1}$ only, where $\xi = (\psi, T, S)$. If $n+m$ is even (odd), then $(n\pm1)+(m\pm1)$ is also even (odd). Hence, only even terms or odd terms interact with one other. Only one of the two systems gives the largest value of λ_R—the other is ignored. This is observed in the eigenmode spectra of § 5.3.3

We may make use of this feature to speed up simulation times. In hindsight, solving the full eigenvalue problem requires significant computational resources, with simulations running for days to weeks depending on the desired resolution, level of truncation and parameter range. Splitting the system in half reduces the order of the problem by a factor of four—the full system is of the order $3(2N+1)(2M+1) = \mathcal{O}(12N^2)$ (assuming $N = M$), while the reduced systems are each of order $3(N+1)(M+1) = \mathcal{O}(3N^2)$.

It is unknown beforehand which system (even or odd) will provide the largest growth rate, so we calculate λ for both systems separately and then select that with the largest growth rate. Solving two systems of order $\mathcal{O}(3N^2)$ separately is still faster than solving the full system at $\mathcal{O}(12N^2)$. Note that we obtain the two systems by first calculating the full matrix A and then splitting it into two. The building of the matrix takes a significant amount of computational time in itself; however, it would be difficult to make this process any quicker.

5.3 Numerical Implementation and Convergence

To solve our set of ODEs numerically, we first truncate the expansion (5.3) at a value N and M, such that $n \in \{-N, N\}$ and $m \in \{-M, M\}$. Collecting individual Fourier components, we then express these equations in the matrix form

$$\lambda\eta = \boldsymbol{A}\eta, \tag{5.9}$$

where

$$\eta = (...\psi_{n-1,m}, T_{n-1,m}, S_{n-1,m}, \psi_{n,m}, T_{n,m}, S_{n,m}...)^T,$$

and $\boldsymbol{A}$ is the square matrix of size $3(2N+1)(2M+1)$ obtained from (5.5) - (5.7), and is a function of (k_x, k_z, f, R_ρ, τ, Pr, N, M, A_ψ, A_T, A_S).

5.3.1 Solver

The eigenvalue problem (5.8) is solved using the in-built MATLAB function `eig`, which computes all eigenvalues of the non-symmetric matrix A using QZ-factorisation, normalising the eigenvectors to Euclidian length 1. We contrasted this solver with a second MATLAB function `eigs`, which instead uses an iterative method to return only a subset of eigenvalues.

This study was performed as simulations of the unsteady system were found to require significant computational resources and take a long time to run—it was thought that finding only the largest real solutions would improve the speed of simulations. It was discovered that this was not the case and that, in some cases `eigs` either struggled to converge or was not significantly faster. for this reason, all simulations in this chapter were performed using `eig`.

The program was built in a similar way to that in Chapter 4, in that the user specifies the parameters to be investigated (i.e. R_ρ^{-1}, Pr, τ and A_ψ) and the program then calculates two different values of k_x and ω: one for the marginal state with $\lambda_R = 0$, and one for the fastest growing mode with $k_x = k_x^*$. The program then loops over a defined range of wavenumbers (f, k_z), calculating the growth rate with the largest real part at each point.

It is important to note at this stage that we restrict the range of λ_I from which we obtain modes. It is clear from the form of the double-Floquet expansion (4.9) that the frequency of each eigenmode is made up of two parts, i.e. $\text{Im}(\lambda) = \lambda_I + m\omega$. Since m is an integer, we need restrict our attention only to values of $\lambda_I \in [0, 1)$. It is not only desirable to restrict our results as such, but also necessary to ensure the results are accuratey. This will be expanded on in the following section as we study the convergence of our results.

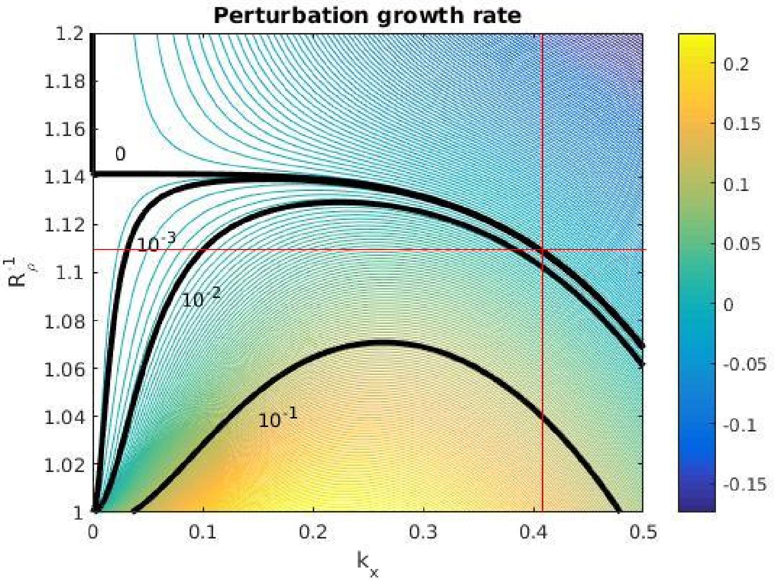

Figure 5.1: Growth rate of elevator modes, highlighting the values chosen in our test-case.

5.3.2 Convergence

This section details a number of tests that were performed to ensure the results are accurate. We discuss how the simulations were improved to obtain reliable results from which to draw conclusions, while reducing the computational cost. All tests are performed under the same conditions of $R_\rho^{-1} = 1.11$, $Pr = 10$, $\tau = 0.01$ and $A_\psi = 10$. We take a value of $A_\psi = 10$, as this was shown to give a secondary mode which changes little with small variations in A_ψ. We also choose $k_x = 0.417$ which corresponds to a marginal elevator mode as determined by equation (2.52) in § 2.3.8. These parameters correspond to a heat-salt system which is herein referred to as our test case.

The growth rates of elevator modes as instabilities to the static basic state in our test-case are shown in Figure 5.1. The red lines correspond to the chosen value of R_ρ^{-1} and the corresponding value of k_x giving marginal stability. Figure 5.2 shows a converged contour plot of the growth rates of secondary instabilities for our test case, which will serve as a reference throughout this section.

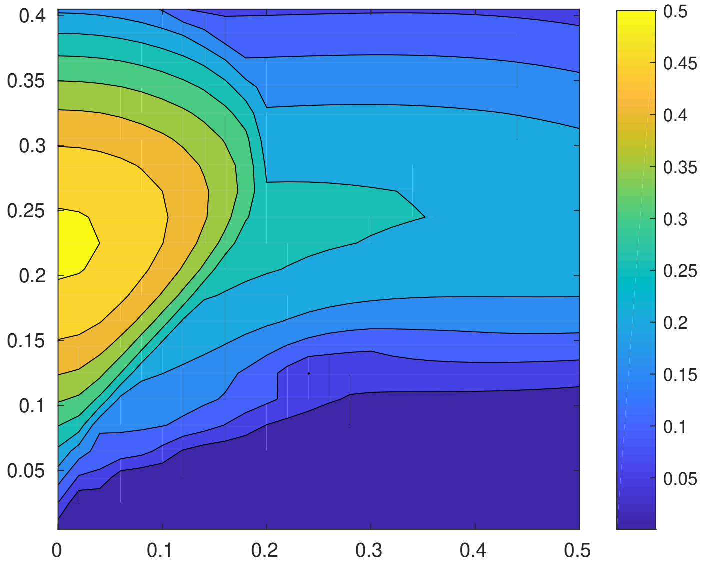

Figure 5.2: Growth rate of secondary modes in the test case, where $R_\rho^{-1} = 1.11$, $Pr = 10$, $\tau = 0.01$ and $A_\psi = 10$.

5.3.3 Accuracy

It is important to investigate how the results are affected by increasing N and M. If the truncation level is too low, then we could be missing out important information and obtaining inaccurate results. On the other hand, if the truncation is unnecessarily large, the simulations may take a long time to run for very little gain. In this study we simulate the system at the previously defined test parameters of $(R_\rho^{-1}, A_\psi) = (1.11, 10)$, and increase N and M until the solution 'converges'.

There are a number of ways to look at convergence, one of which is largely qualitative and involves varying f between 0 and 1, and comparing the growth rates at either side of $f = 0.5$ for a range of k_z. As the equations possess a symmetry about $f = 0.5$, so too should the solutions. This analysis was performed in Chapter 4 for the steady system, and need not be repeated here; it suffices to say that increasing N and M leads to better symmetry.

A more quantitative way to evaluate convergence is to increase N and M at a particular value of (f, k_z) and calculate the eigenvalue at each increment. Evaluating the difference between subsequent values of λ gives a measure of error, which should decrease to an acceptable level (defined by the user) with an increasing level of truncation.

A third method, and the one we first explore here, is to look at the spectrum of eigenvalues. This was performed for the steady system (Chapter 4, §4.3.2) and showed that the amplitudes of eigenmodes decrease towards the extremes of n. This implies that the most influential modes are clustered around $n = 0$ and they become less important at large n. If we instead found large amplitude modes at the extremes of n then the level of truncation would be too low, and important information may be omitted. We follow the same reasoning here, but instead look at the eigenmode spectra over a range of n and m.

Eigenmode Spectra

Initial testing showed that there was no particular advantage to varying N and M separately; thus, for this study we set $N = M$ at all times. Figure 5.3 shows the spectrum of eigenmodes $(\psi_{n,m})$ at $(f, k_z) = (0, 0.225)$ and for $N = 3$. This is the mode with the largest growth rate from the initial test case shown in Figure 5.2.

In this case, the largest amplitude eigenmodes are clustered around $n = 0$ and $m = 0$, however there are still large values at the edges. This implies that we are missing important information and the truncation should be increased. Figure 5.4 shows the same plot for $N = 7$.

The solutions become more accurate in both the n and m directions with increasing N and M. For example, we see that the amplitudes at $n = 7$ drop below 10^{-5}, indicating that these eigenmodes do not significantly effect the solution. Furthermore, we see

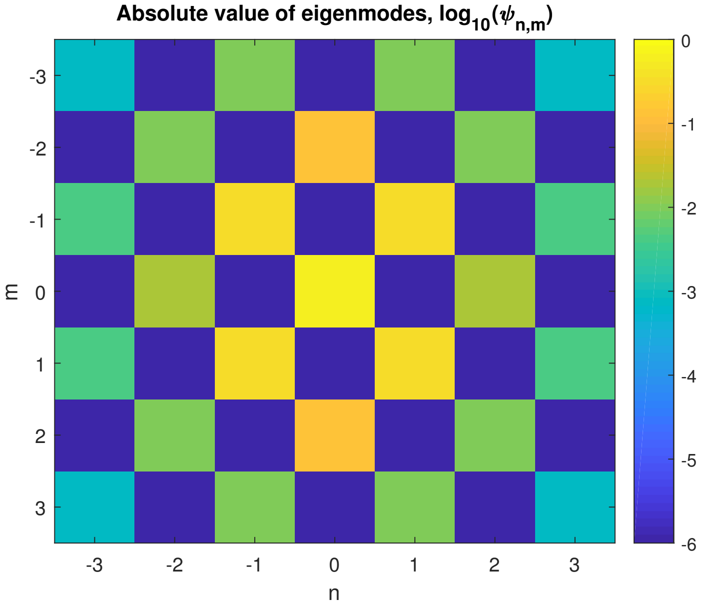

Figure 5.3: Spectrum of $\psi_{n,m}$ with $(f, k_z) = (0, 0.225)$ when N = M = 3.

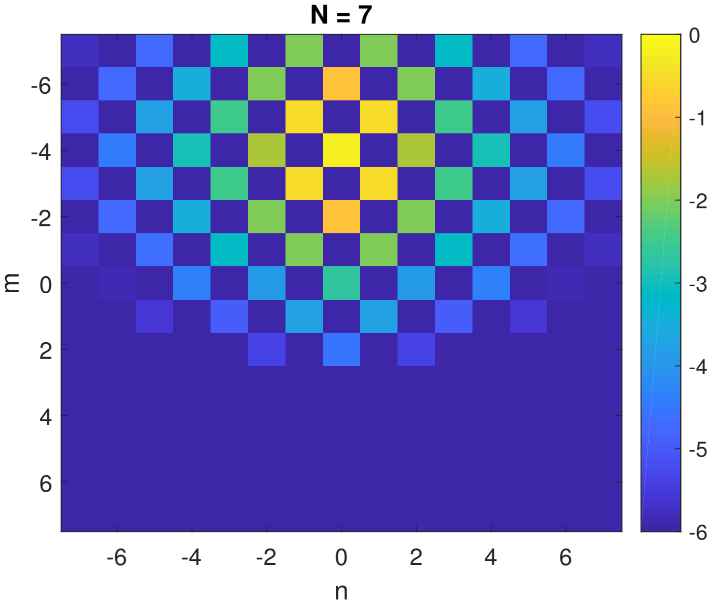

Figure 5.4: Spectrum of $\psi_{n,m}$ with $(f, k_z) = (0, 0.225)$ when $N = M = 7$.

that when $N = 3$, the dominant eigenvalue has contributions from only the eigenmodes with $(n + m)$ even, whereas when $N = 7$, the contributions are from eigenmodes with $(n + m)$ odd.

We also see that when N = 7, the largest eigenmodes are now offset in the m-direction from $M = 0$. In § 5.2 we noted that the growth rate is given by $\lambda = \lambda_{+} i\lambda_i$, and that the total temporal wavenumber is given by $\lambda_{i,T} = \lambda_I + m\omega$. Although the largest eigenvalue has a dominant eigenmode at $m = 4$, as shown in Figure 5.4, the value of λ_I is approximately -4ω. That is, the total value of $\lambda_{i,T}$ is in the range $0 < \lambda_{i,T} < \omega$.

We see that this is the case at all large values of $N = M$. The eigenvalues having dominant eigenmodes with large m are only marginally faster-growing than those having dominant eigenmodes with m closer to zero. Therefore, we herein take only those eigenvalues with $0 \leq \lambda_I \leq \omega$, which gives dominant eigenvalues centered around $m = n = 0$, and therefore more accurate solutions.

5.3.4 Comparison with Holyer

It is informative to compare the results from the time-dependent system with those of the Holyer system, in order to ensure the program is working correctly. Hence, we here momentarily take the gradients T_z and S_z to be positive, in order to emulate the salt-finger regime. Furthermore, all parameters are set to those used in the Holyer simulations. Note that the values of the complex conjugate pairs, (A_ψ, A_ψ^*), etc. are set to be equal to one other, i.e. $A_\psi = A_\psi^* = W/2$. We first simulate the $m = 0$ case, and compare the sparsity of the matrices (taking $N = M = 1$).

The steady system contains three rows of three columns of entries since there are three variables (ψ, T, S) and three N terms ($N = -1, 1, 0$) for each variable. The addition of three M terms ($M = -1, 0, 1$) in the unsteady system means that the entire steady pattern is repeated three times, as might be expected.

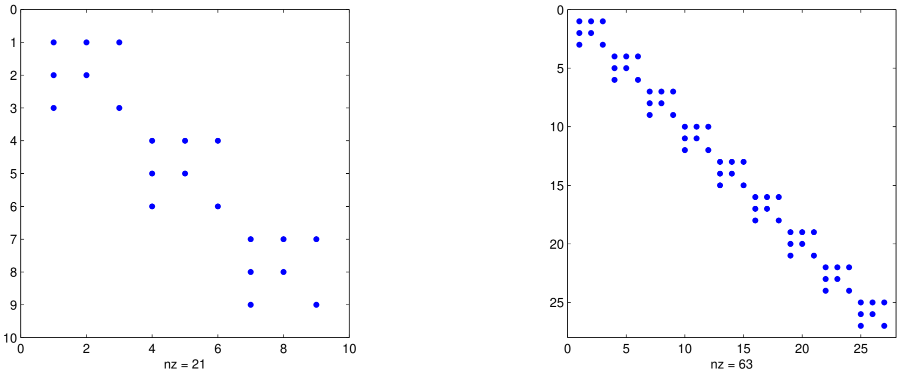

Figure 5.5: Sparsity of the matrix A in the salt-finger regime using **Left:** the steady system, and **Right:** the unsteady system.

We now attempt to reproduce the plot shown in Figure 4.1 of Chapter 4 (§ 4.3.2), showing the growth rate vs. k. Figure (5.6) shows a comparison of λ vs. k using both the steady system and the unsteady system.

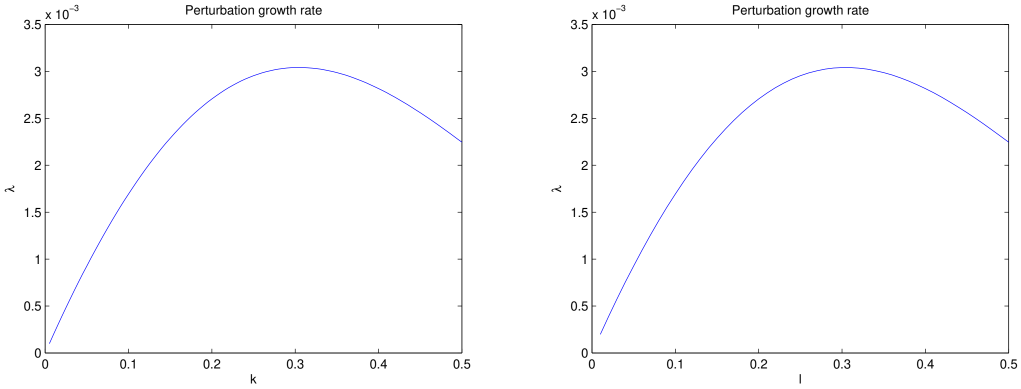

Figure 5.6: Reproducing the results of Holyer (1984) using **Left:** the steady system, and **Right:** the unsteady system.

The plots are identical to one another—-subtracting one from the other gives errors of $\mathcal{O}(10^{-17})$. This provides initial confidence that both the system of equations, and the numerical implementation, are readily able to reproduce well-documented results.

5.4 Parametric Study

We now investigate the behaviour of the system over a range of parameters, starting with the case of a marginal basic state. In such a case we first choose a value of R_ρ^{-1} and then define k_x such that the system has zero growth rate before calculating the corresponding basic state frequency ω. We take oceanic conditions of $Pr = 10$ and $\tau = 0.01$ for the initial parametric study. We also take a value of $R_\rho^{-1} = 1.06$, which gives $k_x = 0.4056$ and $\omega = 0.9806$ for marginal stability. This value of R_ρ^{-1} is chosen as our parameters lie sensibly within the ranges $R_\rho^{-1} \in [1, 1.14]$ and $k_x \in [0, 0.5]$, as seen in Figure 5.1, which is the same as Figure 2.4.

A basic state salt finger amplitude A_ψ is prescribed and A_T and A_S are defined by

$$\begin{aligned} &A_T(\lambda_0 + k_x^2) = \operatorname{sgn}(T_z) k_x A_\psi, \\ &A_S(\lambda_0 + \tau k_x^2) = \operatorname{sgn}(S_z) k_x R_\rho^{-1} A_\psi, \\ &\frac{A_\psi k_x}{Pr}(\lambda_0 + Pr k_x^2) = -(A_T - A_S), \end{aligned} \tag{5.10}$$

where $\lambda_0 = i\omega$, and ω is as previously calculated. Note that A_ψ is chosen to be real, so $A_\psi^* = A_\psi$, and A_T and A_S are complex.

5.4.1 Sweep over A_ψ

We begin by sweeping over A_ψ and plotting the growth rates of secondary instabilities in (f, k_z)-space. Figure 5.7 shows the real and imaginary parts of λ with increasing A_ψ.

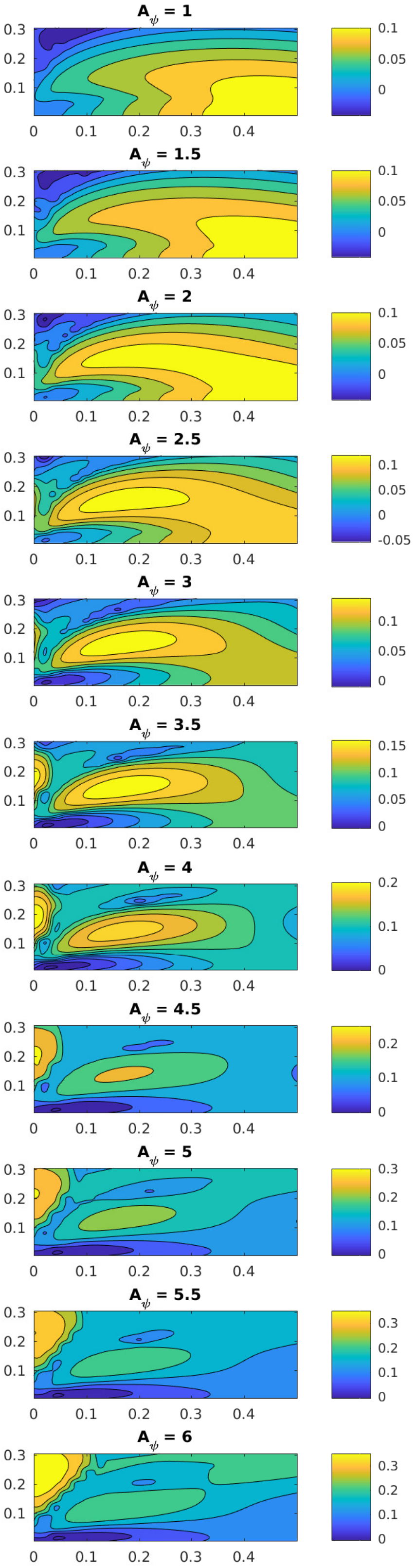

Figure 5.7: Growth rate of modes in wavenumber space for increasing A_ψ, when $R_\rho^{-1} = 1.106$

The first instability to be observed at low A_ψ has $k_z = 0$. This is an elevator mode, and it arises because we have taken a marginal basic state with $\lambda_R = 0$; there exists other possible basic state elevators with $\lambda_R > 0$ from linear theory, and the one observed here is that with the largest λ_R. This is easily verified by comparing the horizontal wavenumber observed here (i.e. fk_x, where $f = 0.66$ and $k_x = 0.4056$) with the horizontal wavenumber of the FGM from linear theory (i.e. $kx^* = 0.27$). If we were to take the FGM as the basic state, then we would no longer observe this elevator mode at low values of A_ψ.

Increasing A_ψ leads to the appearance of a new fastest growing mode with f and k_z both non-zero. We call this an 'intermediate mode'. The growth rate of this mode remains dominant as A_ψ is increased further, before eventually subsiding and giving way to a third FGM with $f = 0$. Further increases in A_ψ serve only to increase the vertical wavenumber k_z of this mode, along with its growth rate.

It is useful to identify the wavenumbers of the fastest growing modes and plot them as a function of A_ψ. This provides a clearer picture of the behaviour of secondary modes and better facilitates a comparison of results as we vary R_ρ^{-1}. Figure 5.11 shows such a plot, along with a plot of the growth rates of each mode. It can be seen that the system is first dominated by the basic state elevator which has the same growth rate at all values of A_ψ. The growth rate of the intermediate mode eventually takes over and this becomes dominant; however, we later see the growth rate of the $f = 0$ mode overtake and continue to increase.

Eigenmodes

The fastest growing mode when $R_\rho^{-1} = 1.06$, $Pr = 10$, $\tau = 0.01$ and $A_\psi = 10$ has a wavenumber of $(f, k_z) = 0.225$. By way of example, the eigenmodes of this mode in ψ and ρ are shown in figure 5.9. Note that the modes in this case are time dependent. We thus initialise the modes at an arbitrary amplitude of 0.001 and allow them to

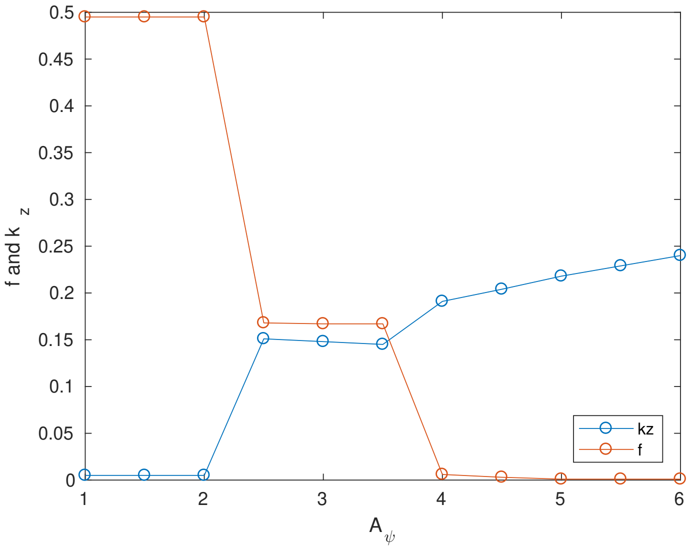

Figure 5.8: Wavenumber of the fastest growing mode when $R_\rho^{-1} = 1.06$ between $A_\psi = 1$ and $A_\psi = 6$.

grow. Figure 5.9 shows the fully-developed eigenmodes of the fastest-growing mode when $t = 8.2 \cdot 2\pi/\omega$, which represents 8.2 oscillations of the basic state.

Figure 5.10 shows the effect of the perturbations on the growing elevator modes in ψ and ρ, at $t = 5.2 \cdot \pi/\omega$, which represents 5.2 oscillations of the elevator modes. The secondary modes are very similar in structure to those observed in the steady system. We see that the cells in the density perturbation are elongate, and extend at an angle to the horizontal.

This causes the total density (i.e. including the effects of the elevator modes) to resemble fingers which with interleaving protrusions into neighbouring fingers. This was observed in our simulations in Chapter 4, and was described in detail by Veronis (1987). Furthermore, the streamfunction secondary mode is ‘aligned’ with the elevator mode, causing the elevator modes to become wavy in structure, as observed in the 9th-order system in Chapter 3.

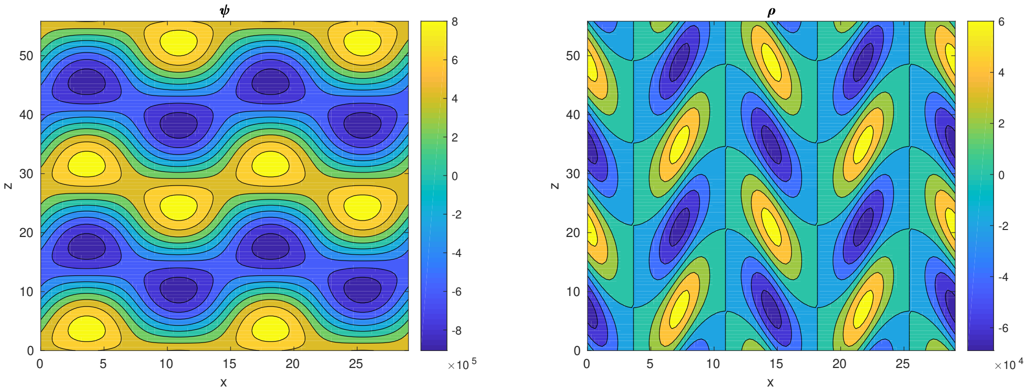

Figure 5.9: Contours of ψ and ρ of the fastest-growing secondary mode having $(f, k_z = 0.225)$ when $R_\rho^{-1} = 1.06$ and $A_\psi = 10$ in the heat-salt system.

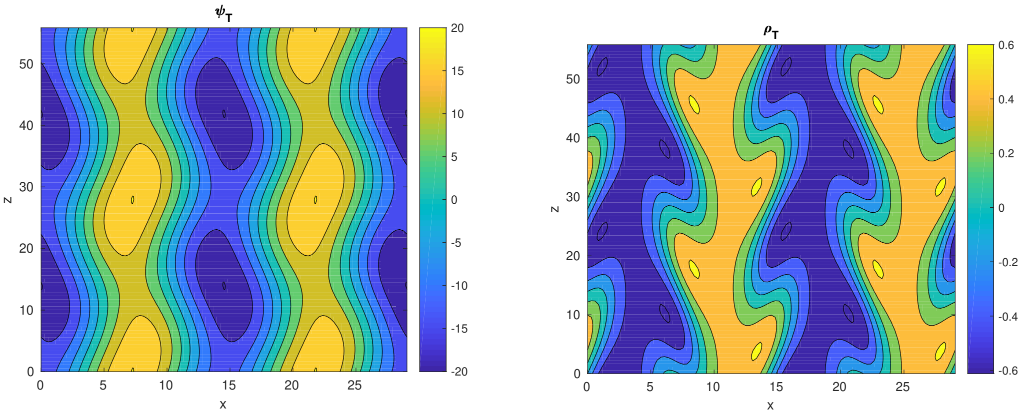

Figure 5.10: Contours of ψ and ρ of the fastest-growing secondary mode having $(f, k_z = 0.225)$ when $R_\rho^{-1} = 1.06$ and $A_\psi = 10$ in the heat-salt system.

Although not shown here, we see that the eigenmodes oscillate with the same frequency as the basic state. As the basic state changes direction, so too do the angle of the cells in the density perturbation of the secondary mode. This suggests that, at least for large A_ψ, the fastest growing secondary modes in the unsteady system are largely the same as those which emerge in the steady system, except that they oscillate with the basic state frequency.

5.4.2 Sweep over R_ρ^{-1}

We now wish to observe the effect that the value of the density gradient ratio R_ρ^{-1} has on the growth rate of secondary modes. We simulated a large range of parameters and produced contour plots of the growth rate as a function of f and k_z over many different values of R_ρ^{-1} and A_ψ. For brevity, we here find it most appropriate to instead plot the wavenumber of the fastest growing modes in each case as a function of A_ψ. We also plot the growth rates of the three distinct modes observed—no other modes arise as we change R_ρ^{-1}. From equation (2.52), the unstable range of R_ρ^{-1} is defined by

$$1 \leq R_\rho^{-1} \leq \frac{(Pr+1)}{(Pr+\tau)}\left(1 - k_x^4(1+\tau)(1+\frac{\tau}{Pr})\right). \tag{5.11}$$

When $Pr = 10$, the range of values of R_ρ^{-1} prescribing an unstable basic state is $1 \leq R_\rho^{-1} \leq 1.141$. Figures 5.11 and 5.12 show the results at values of $R_\rho^{-1} = [1.06, 1.07, 1.08, 1.09, 1.10, 1.11]$, covering almost the full range. The behaviour is similar in all cases except that the range of A_ψ for which the intermediate mode dominates becomes smaller as R_ρ^{-1} is increased, until eventually the intermediate mode no longer dominates at any A_ψ. At large R_ρ^{-1} the basic state elevator mode becomes unstable to a mode with $f = 0$ and nothing else. Further increasing A_ψ serves to increase the vertical wavenumber of the mode. This is similar to the behaviour observed for the secondary modes arising from steady elevator modes, as shown in Chapter 4.

As R_ρ^{-1} is increased, the growth rate of the fastest growing elevator mode reduces as the strength of the background state is weakened, but the curve showing the growth rate of the $f = 0$ mode appears relatively unchanged. Thus, the $f = 0$ mode dominates sooner as R_ρ^{-1} is increased. This causes the intermediate mode to disappear, and the system jumps directly from an elevator mode to an R2 mode, using notation introduced in Chapter 4.

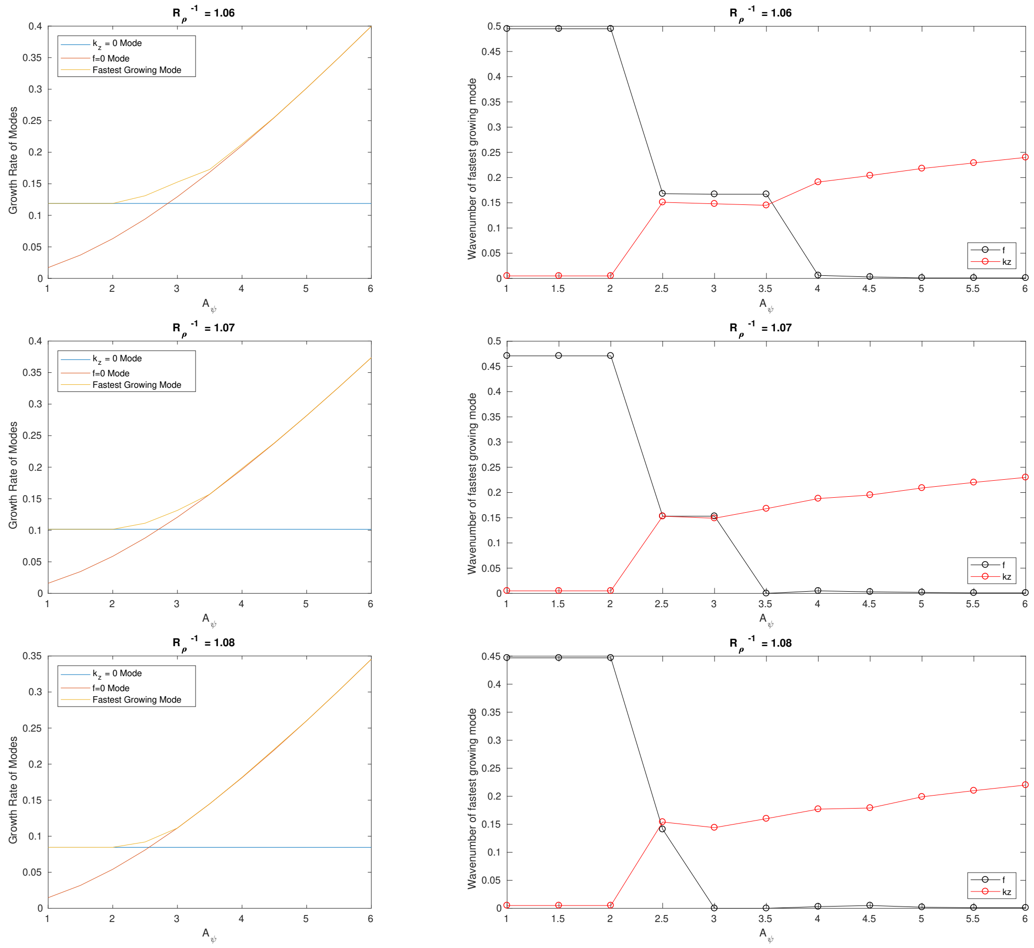

Figure 5.11: Wavenumber of the fastest growing mode with increasing A_ψ for $R_\rho^{-1} = [1.06, 1.07, 1.08]$ in the heat-salt system.

5.4.3 Sweep over Pr

We now study the effect of the Prandtl number on the growth rates at different values of R_ρ^{-1} and A_ψ. We have seen so far that increasing A_ψ leads to a transition between different fastest-growing-modes, with the largest values of A_ψ driving a mode with $f = 0$ in all cases. We see the same behaviour at different values of Pr, though the value of A_ψ required to drive this mode changes. Note that changing Pr modifies the unstable range of R_ρ^{-1} as in equation (5.11).

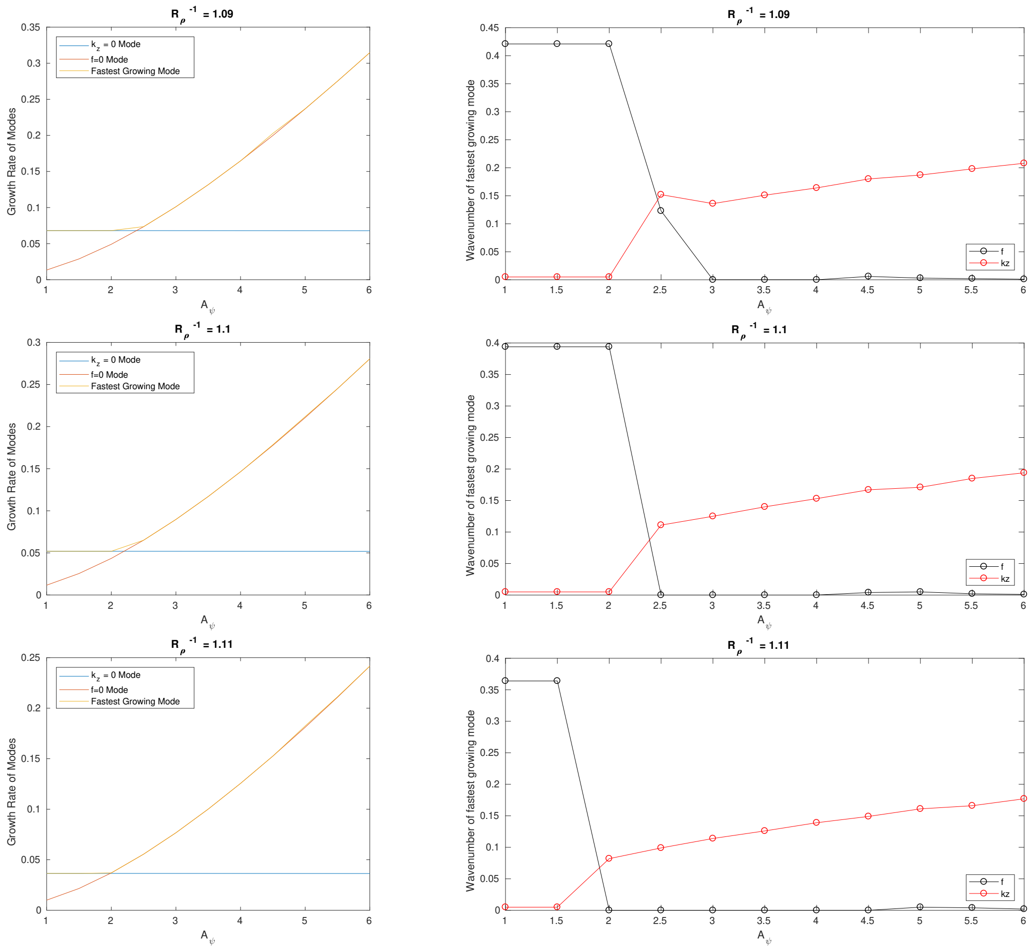

Figure 5.12: Wavenumber of the fastest growing mode with increasing A_ψ for $R_\rho^{-1} = [1.09, 1.10, 1.11]$ in the heat-salt system.

We first reduce Pr to 0.1, for which the range of unstable values of R_ρ^{-1} reduces to $1 \leq R_\rho^{-1} \leq 9.9$. The wavenumbers of the fastest growing modes and the growth rates of the three distinct modes that we observed are plotted in Figure 5.13 for $Pr = 0.1$ and $R_\rho^{-1} = [1, 1.004, 1.006, 1.008]$. The intermediate mode that was observed at $Pr = 10$ (which has non-zero f and k_z) is no longer present when R_ρ^{-1} is small, and the elevator mode instead becomes unstable to a mode with $f = 0$.

To verify the absence of the intermediate mode at low R_ρ^{-1}, we run the simulation at

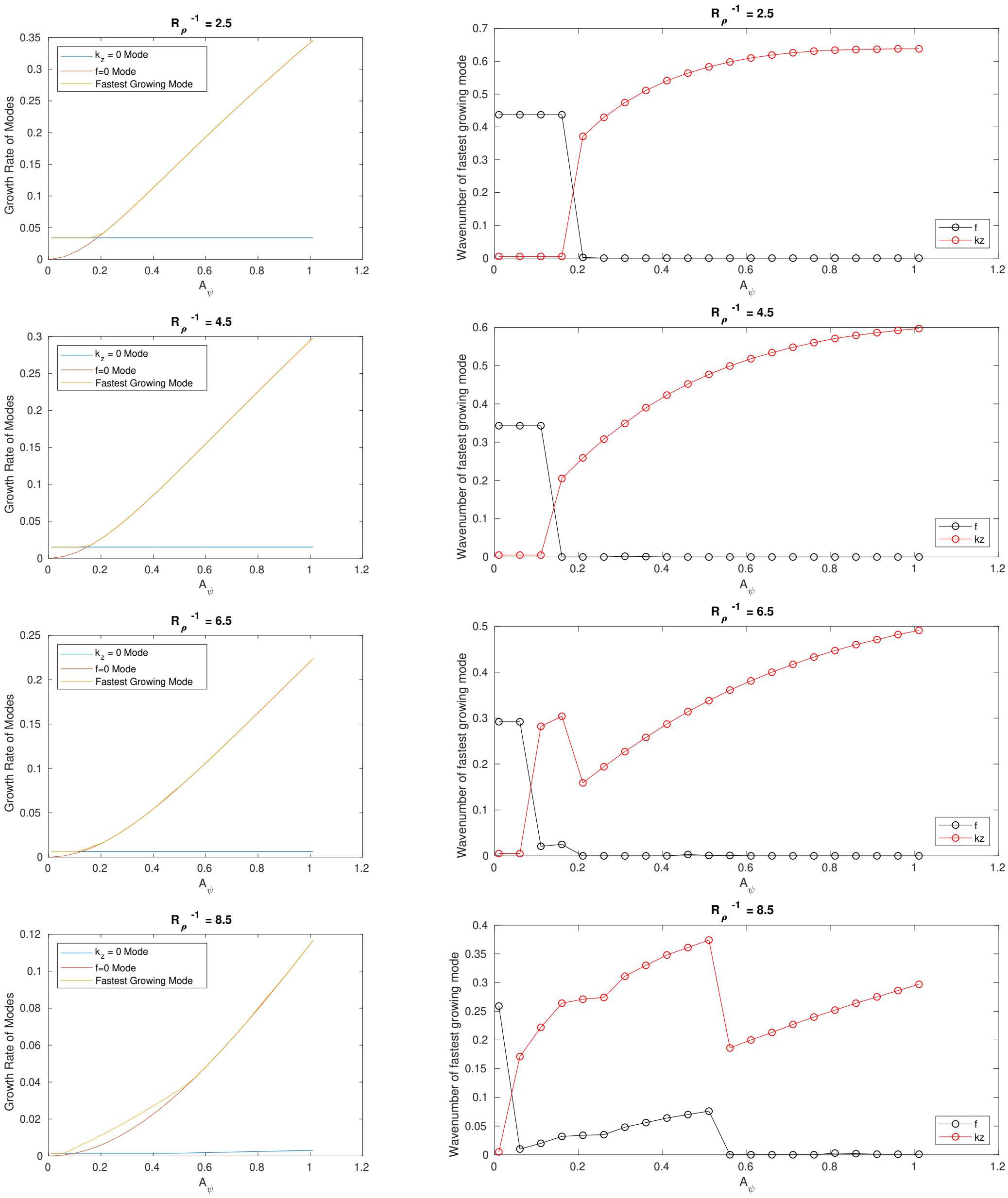

Figure 5.13: Wavenumber of the fastest growing mode with increasing A_ψ for $R_\rho^{-1} = [2.5, 4.5, 6.5, 8.5]$, when $Pr = 0.1$.

$R_\rho^{-1} = 4.5$ once more but with a greater number of points in A_ψ, particularly around the region $A_\psi \in [0.1, 0.2]$. The results are displayed in Figure (5.14). Again, it is quite clear from the growth rate plot that, initially, the $k_z = 0$ elevator mode is fastest-growing,

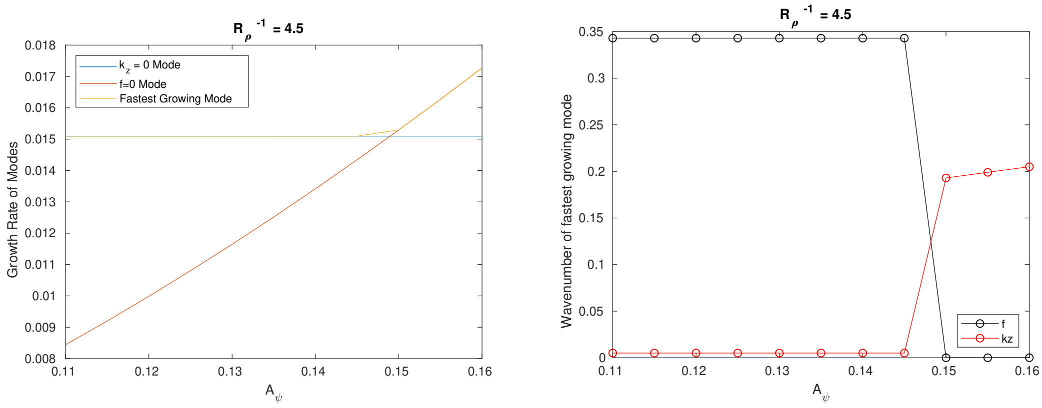

Figure 5.14: Caption

whilst the growth rate of the $f = 0$ mode is still increasing from low amplitude. As A_ψ is increased, the growth rate of the $f = 0$ (R2) mode increases until eventually, at around $A_\psi = 0.148$, the growth rate of the $f = 0$ mode exceeds the growth rate of the $k_z = 0$ mode. No intermediate mode is observed. The slightly raised section of the 'Fastest Growing Mode' at the intersection of the $f = 0$ curve and the $k_z = 0$ curve is a result of the interpolation used to produce the Figure, and is not indicative of an intermediate mode. Indeed, the wavenumber plot shows no such intermediate mode.

Thus, we conclude that the dominant secondary instability of a marginal basic state when Pr and R_ρ^{-1} are both small has a horizontal wavenumber that fits within the basic state (i.e. $f = 0$) in all cases except when A_ψ is sufficiently small—in this case we see the fastest-growing elevator mode. The disappearance of the intermediate mode suggests that when $\mathrm{Pr} = 0.1$, inertial effects are sufficiently large relative to diffusive effects such that an inertial ($f = 0$) instability dominates for all value of R_ρ^{-1}. This is consistent with results in the steady system.

Increasing Pr to 100 has the opposite effect. The unstable range of R_ρ^{-1} at this value of Pr is much smaller than when $Pr = 0.01$ or $Pr = 10$. In this case, $1 \leq R_\rho^{-1} \leq 1.01$. Figure 5.15 shows the wavenumbers and growth rates of the fastest growing modes at

$R_\rho^{-1} = [1.002, 1.004, 1.006, 1.008]$, covering almost the full range. We see that the value of A_ψ required to obtain a mode with $f = 0$ is much larger than at lower Pr. This is likely because, as observed in Chapter 4, a large Pr corresponds to a low Reynolds number—diffusive terms are more dominant here than inertial terms. If the $f = 0$ mode is indeed a shear flow, as predicted, then we would need a much larger value of A_ψ to overcome the diffusion and inject enough momentum to drive the instability.

An intermediate mode dominates at most values of A_ψ, until the $f = 0$ mode takes over. The wavenumber of the intermediate mode also changes over time, and the behaviour for each value of R_ρ^{-1} appears unpredictable. Furthermore, we never see a mode with $f = 0.5$ in the unsteady system. This shows that there are significant differences in the secondary modes generated from steady and oscillatory elevators; however, in each case, as A_ψ becomes large enough, a mode with $f = 0$ always dominates. This, along with the Pr dependency of the $f = 0$ mode, suggests that the intermediate mode and the $f = 0.5$ (R1) modes observed in the steady and unsteady systems, respectfully, are largely driven by diffusive effects, while the $f = 0$ modes are driven by inertial effects.

We see that larger values of A_ψ take longer to simulate as the growth rates become large, thereby requiring larger values of N and M. For this reason, it is impractical to produce a plethora of plots with Pr any larger than 100. Though not shown here, we have obtained results at a single value of R_ρ^{-1} with $Pr = 1000$. The same trends are observed, in that even higher A_ψ is required for a secondary mode with $f = 0$ to dominate, and the intermediate modes dominate for a majority of values of A_ψ.

5.4.4 $k_x = k_x^*$

The foregoing analyses have focused on a system in which the static basic state becomes unstable to marginal elevator modes, i.e. $\Re(\lambda_0) = 0$. In a physical system, however, the static basic state would instead be destabilised by the fastest-growing elevator modes. Indeed, studies have shown that simulations taking the fastest growing elevator as the

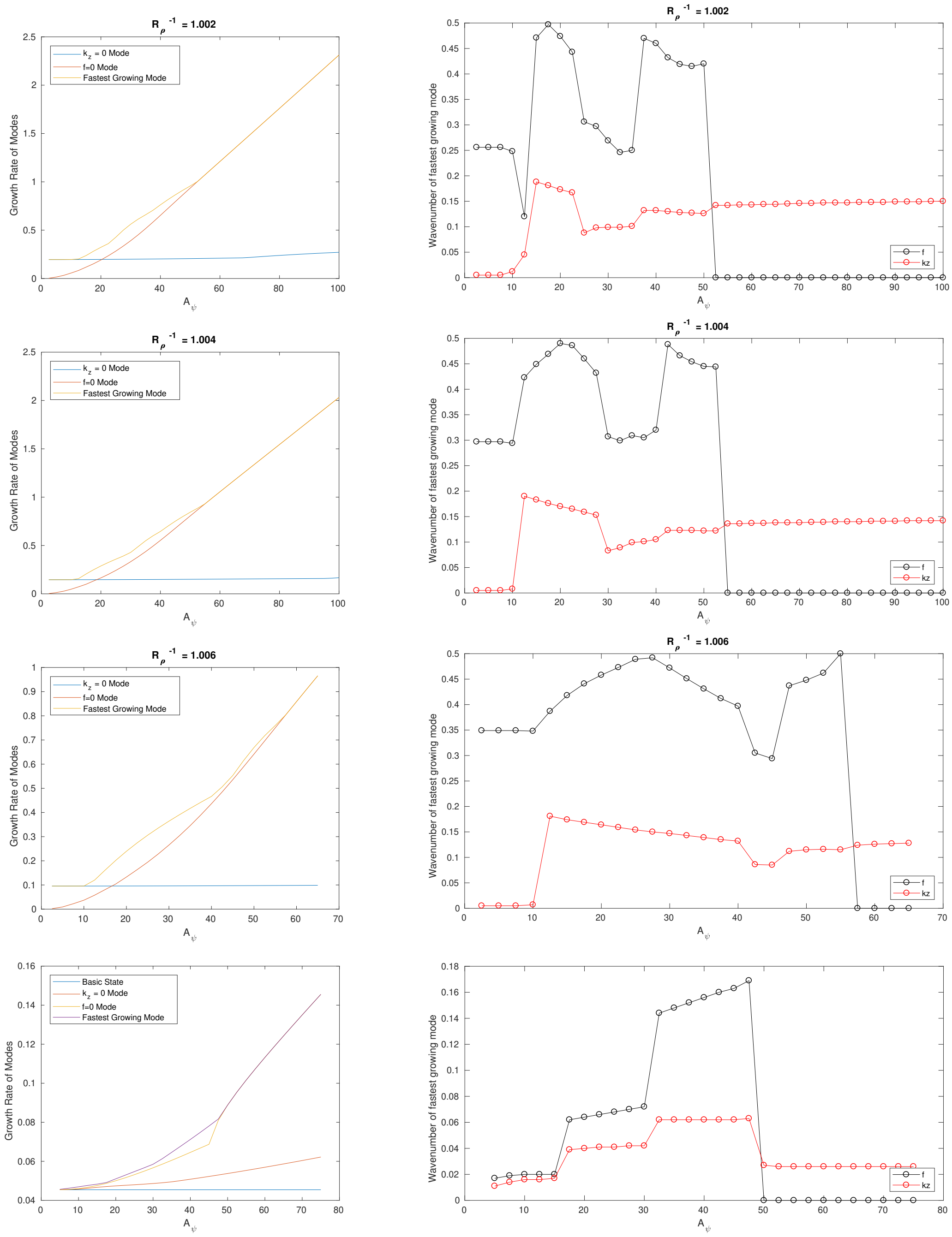

Figure 5.15: Wavenumber of the fastest growing mode with increasing A_ψ for $R_\rho^{-1} = [1.002, 1.004, 1.006, 1.008]$, when $Pr = 10$.

basic state more accurately predict the resulting dynamics, e.g. (Veronis, 1968). Hence, it is desirable to study the secondary instabilities arising from such fastest-growing elevator modes using the elements of Floquet theory developed thus far. We note, for completeness, that although we here study the fastest-growing elevator modes, we assume in our analysis that they are quasi-steady, as discussed in Chapter 4.

In the marginal case, the value of k_x giving marginal stability was calculated using equation 2.52. To determine the value of k_x^* we first calculate the growth rate and frequency of the primary instability over a range of k_x values for a prescribed R_ρ^{-1} using equation (2.44), i.e.

$$(\lambda_0 + k_x^2)(\lambda_0 + Prk_x^2)(\lambda_0 + \tau k_x^2) + Pr(\mathrm{sgn}(T_z)(\lambda_0 + \tau k_x^2) - \mathrm{sgn}(S_z)R_\rho^{-1}(\lambda_0 + k_x^2)) = 0. \tag{5.12}$$

The value of k_x giving the fastest-growing mode is then readily extracted. The analyses of preceding sections may then be repeated using the new values of R_ρ^{-1} and k_x and ω; however, in order to apply the method of Floquet theory, we require that the growth rate of the primary instability is zero. This assumption works as long as the growth rates of secondary instabilities discovered through the analysis are greater than that of the primary instability, in which case we may say that the primary modes do not grow in the time that it takes for secondary instabilities to grow. The larger the growth rates of secondary modes, the more appropriate this assumption will be.

Sweep over R_ρ^{-1} and A_ψ

Before presenting the results at $k_x = k_x^*$, we first present a short aside on simulation time. Simulations of unsteady elevator modes are considerably more computationally expensive than simulations of steady elevator modes, due to the larger matrices involved, as discussed above. The three sets of results presented in the present section were simulated continuously over $3\frac{1}{2}$ days on a desktop PC—this covered three values of R_ρ^{-1}, a single value of Pr, and a low 'resolution' (here meaning number of points) in f, k_z and A_ψ. Furthermore, each simulation was performed by truncating the system with $N = M = 8$, which is relatively low. Increasing the truncation to $N = M = 12$ would increase simulation time considerably (at least two-fold). We find that with $N = M = 8$, the results presented here are slightly inaccurate at large A_ψ; however, they show quite well the qualitative behaviour of the system as the parameters are varied. Although the growth rates had not converged to a value from which they would vary minimally with any change in N or M, the behaviour of the system was consistent with the findings of our previous studies of the steady and unsteady systems. This speaks positively to one of the goals of this method: to provide a lightweight, low-order model able to predict the behaviour of secondary modes over a wide range of parameters, even at relatively low tolerances.

The studies of non-oscillatory elevator modes presented in Chapter 4 highlighted that the secondary modes obtained when $k_x = k_x^*$ were similar in form to those obtained with marginal elevator modes, except that when $k_x = k_x^*$, a lower value of A_ψ was required to observe fastest-growing secondary modes with $f = 0$. Hence it was concluded that, at all values of Pr and R_ρ^{-1}, increasing the width of the basic state elevator modes (i.e. taking the fastest-growing elevator modes) made them more susceptible to inertial, as opposed to diffusive, instabilities.

As the growth rates of secondary modes need to be larger than that of the primary elevator mode to be significant, we plot a relative amplitude, $\lambda_R = \lambda/\lambda_0$. In this way, values of $\lambda_R > 1$ represent secondary modes which grow faster than the primary basic state. Large values of L_R will lend more credence to the zero-growth assumption. Figure 5.16 shows contours of $\lambda_R = \lambda/\lambda_0$ and $|\mathrm{Im}\{\lambda\}|$ for $A_\psi = \{1, 11, 21, 31, 41\}$ when $R_\rho^{-1} = 1.01$. Only the growth rates with $\lambda_R > 1$ are shown, i.e. only those secondary modes which grow faster than the primary basic state.

At low value of A_ψ, the secondary mode grows at about the same rate, or only slightly faster, than the basic state. This is most clearly seen when $A_\psi = 5$, wherein the fastest

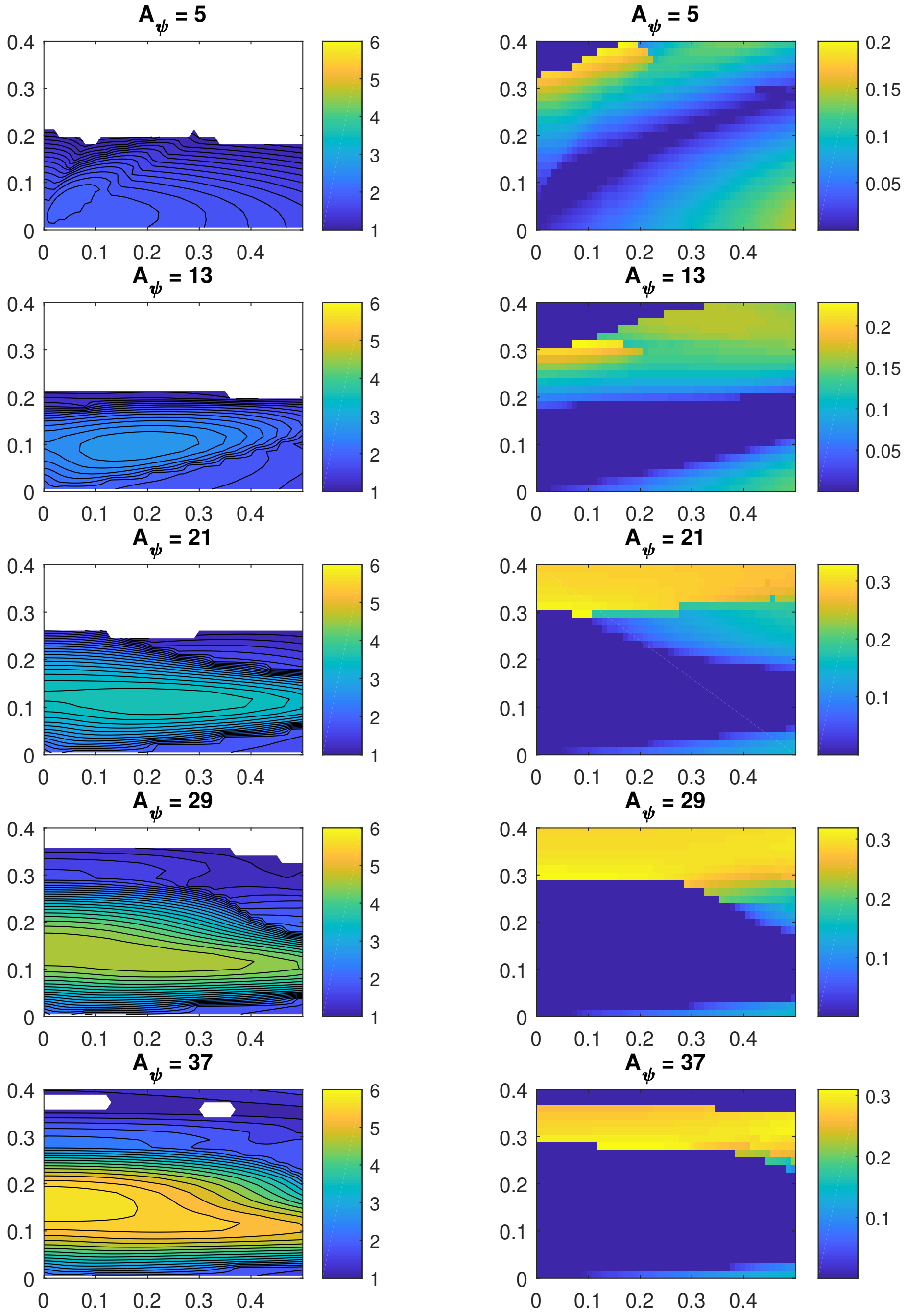

Figure 5.16: **Left:** Relative growth rates, and **Right:** frequencies of secondary modes arising from the fastest-growing elevator mode in the heat-salt system when $R_\rho^{-1} = 1.01$, and $A_\psi = \{1, 11, 21, 31, 41\}$.

growing mode (FGM) has small, non-zero values of f and k_z, and a relative growth rate of $\lambda_R < 2$. The quasi-steady assumption that the primary modes do not grow significantly in the time that it takes for secondary modes to grow may not hold true at this value of A_ψ.

Increasing A_ψ to 13 results in a fastest-growing mode with non-zero wavenumbers and a relative growth rate of $\lambda_R = 3$. Hence, this mode grows three times faster than the primary mode, and our approximation could reasonably be assumed to hold. This mode is similar to the 'intermediate' mode which was observed in the marginal oscillatory case, and notably not observed in the steady system in Chapter 4.

Further increases in A_ψ lead to the now well-documented behaviour of the fastest growing mode jumping from the 'intermediate' mode to an 'inertial' mode with $f = 0$, before increasing in k_z. When $A_\psi = 37$, the relative growth rate of the FGM $\lambda_R = 6$. This makes the quasi-steady assumption more than reasonable at this point. It is notable that the value of A_ψ at which the $f = 0$ mode dominates is lower than in the marginal case. This suggests that, to a certain extent, wider fingers with $k_x = k_x^*$ possess either a lower propensity for diffusion, higher levels of intertia, or both.
In each of the cases presented in Figure 5.16, the imaginary part of the growth rate, i.e. $|\mathrm{Im}\{\lambda\}|$ is zero for the fastest growing mode. Figure 5.16 shows that the bands of largest growth rate tend to correspond to bands of lowest frequency. However, having zero imaginary part does not mean that the frequency of the secondary mode is zero—on the contrary, it could mean that the secondary mode oscillates faster than the primary mode. This would only become clear by studying the frequency spectrum of the fastest growing modes, and perhaps plotting the eigenfunctions over time.

Figure 5.17 shows the wavenumber of the fastest growing mode as a function of A_ψ, along with the growth rates of the following four modes: the 'fastest growing mode', which represents the mode with largest growth rate anywhere inside the (f, k_z) domain;

the '$f = 0$' mode, which represents the mode observed at large A_ψ in our simulations with a marginal basic state (the inertial instability); the '$k_z = 0$' mode, which represents the fastest growing elevator mode; and the primary elevator mode, whose relative growth rate is necessarily unity.

The 'Basic State' and '$k_z = 0$' modes should have identical growth rates, as the basic state should not drive a second elevator mode which grows faster than itself; however, as shown in Figure 5.17, these growth rates deviate as A_ψ is increased. This effect was also observed in the simulations with a marginal basic state, and it arises because simulations with larger values of A_ψ require larger values of N and M to converge. In the present simulations, we take $N = M = 8$, so the accuracy of the results reduces with increasing A_ψ, which may require up to $N = M = 12$.

One way to improve the accuracy would be to use larger upper limits of N and M, but this may be prohibitively expensive in terms of computational demand (as it is here). Furthermore, it is unlikely that doing so would improve the descriptive power of the results. Indeed, it was seen in simulations of the marginal elevator modes that increasing A_ψ above a certain level only serves to increase the value of k_z of the fastest growing secondary instability—a behaviour that is well captured even at low levels of truncation, as shown above.

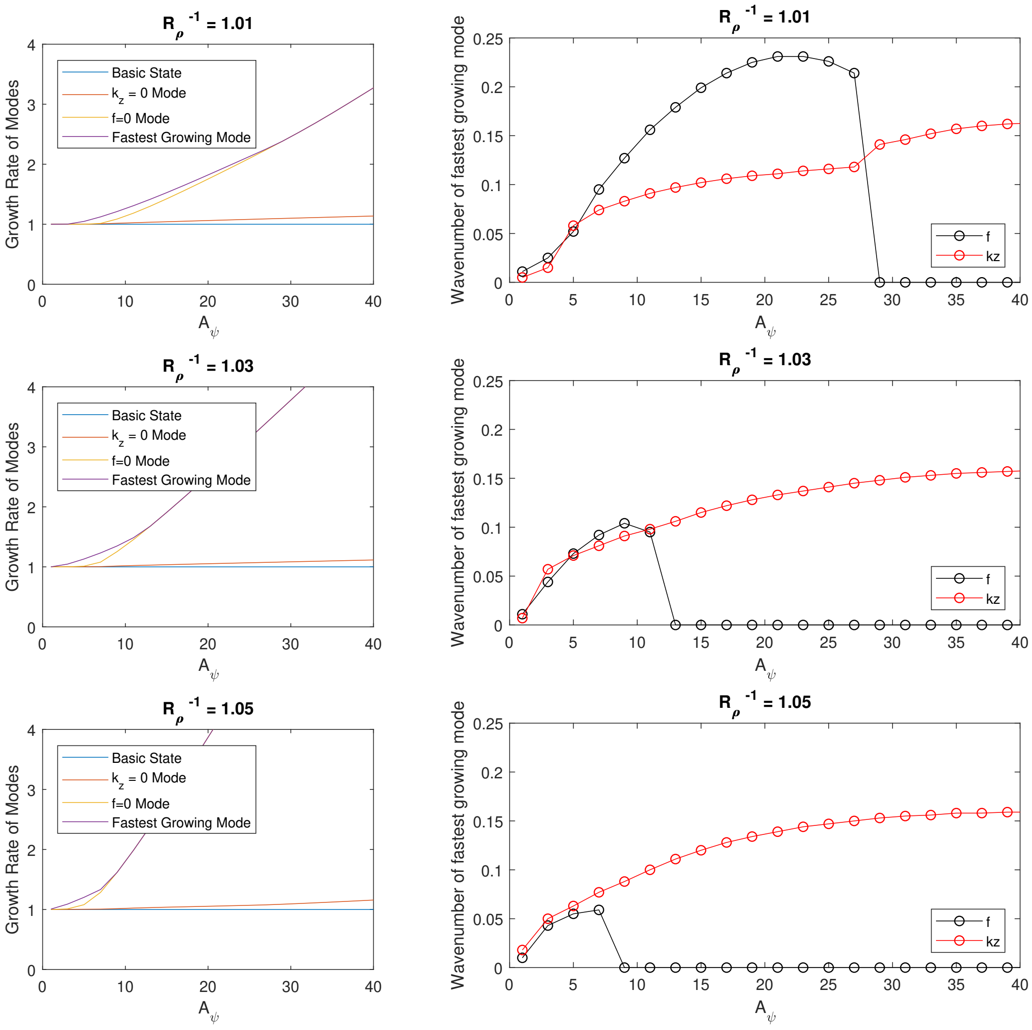

Figure 5.17: Growth rates and wavenumbers of fastest growing modes secondary modes arising from fastest-growing, oscillatory elevator modes with $R_\rho^{-1} = 1.01 - 1.05$, $Pr = 10$ and $\tau = 0.01$.

5.5 The Role of Heat and Salt

We consider the dominant instability observed at large A_ψ to be a shear-driven instability, rather than a diffusive instability. Larger values of A_ψ correspond to large peak velocities, and thus an increased rate of shear between individual elevators. In this section, we modify our double-diffusive system to remove the influence of heat and salt and produce a system of equations representing oscillatory hydrodynamic shear. Beaumont (1981) studied a corresponding steady hydrodynamic shear system, and we extended this work in Chapter 4. We confirmed that the fastest-growing modes arising from such a steady hydrodynamic shear had a similar form to those arising from a steady double-diffusive instability with a strong basic state (a large A_ψ). We expect to observe a similar relationship between oscillatory elevator modes and oscillatory hydrodynamic shear.

Unsteady hydrodynamic shear has been studied in a number of ways (Frenkel, 1991, Frenkel and Xiaojing, 1998) and is typically referred to as unsteady Kolmogorov flow. Secondary instabilities arising from unsteady Kolmogorov flow have yet to be studied using Floquet theory. Hence, this section serves as both a contribution to the literature and a tool for analysing our double-diffusive system. It is expected, based on the double-diffusive results at high A_ψ, that secondary modes in unsteady Kolmogorov flow will exhibit the same structure as in the steady case, albeit oscillating with the same period as that of the basic state.

We derive the viscous Orr-Sommerfeld equation (Lin, 1966) by assuming the perturbations T and S, along with the background gradients T_z and S_z, are zero. The equation governing streamfunction perturbations is,

$$\left(\frac{\partial}{\partial t} - Pr\nabla^2\right)\nabla^2\psi = -J(\psi, \nabla^2\psi). \tag{5.13}$$

Taking a shear flow basic state, plus a secondary perturbation, of the form

$$\psi = \bar{A_\psi}\cos(k_x x) + \psi' \tag{5.14}$$

where $\bar{A_\psi} = A_\psi e^{\lambda_0 t}$, A_ψ is the strength of the shear flow, and $\lambda_0 = \sigma + i\omega$, gives,

$$\left(\frac{\partial}{\partial t} - Pr\nabla^2\right)\nabla^2\psi' = k_x\bar{A_\psi}\sin(k_x x)\frac{\partial}{\partial z}\nabla^2\psi' + k_x^3\bar{A_\psi}\sin(k_x x)\frac{\partial\psi'}{\partial z} \tag{5.15}$$

As in the double-diffusive case, the periodic coefficients are dealt with by expressing the secondary perturbation in Floquet form:

$$\psi' = \exp(ifk_x x + ik_z z + \lambda t)\sum_{n=-\infty}^{\infty}\sum_{m=-\infty}^{\infty}\psi_{n,m}\exp(ink_x x + im\omega t), \tag{5.16}$$

where $\{n, m\} \in \mathbb{Z}$, λ is the growth rate of the secondary instabilities, and f is the Floquet coefficient. If the basic state shear flow is steady ($\lambda_0 = 0$), we may disregard the λ_0 terms and need no longer sum over m. In this case, we obtain the infinite set of equations governing the growth rate of ψ',

$$\lambda\psi_n = -PrK_n^2\psi_n + \frac{A_\psi k_x k_z}{2K_n^2}\left[\left(K_{n-1}^2 - k_x^2\right)\psi_{n-1} + \left(k_x^2 - K_{n+1}^2\right)\psi_{n+1}\right]. \tag{5.17}$$

If the basic state shear flow is purely oscillatory, i.e. $\lambda_0 = i\omega$, and $\bar{A_\psi} = A_\psi e^{i\omega t} + A_\psi^* e^{-i\omega t}$, then we instead obtain the infinite set of equations,

$$\begin{aligned}\lambda\psi_{n,m} = -(PrK_n^2 + im\omega)\psi_{n,m} + \frac{k_x k_z}{2K_n^2}[&\left(K_{n-1}^2 - k_x^2\right)\left(A_\psi\psi_{n-1,m-1} + A_\psi^*\psi_{n-1,m+1}\right)\\ &+ \left(k_x^2 - K_{n+1}^2\right)\left(A_\psi\psi_{n+1,m-1} + A_\psi^*\psi_{n+1,m+1}\right)].\end{aligned} \tag{5.18}$$

If A_ψ is real, then $A_\psi^* = A_\psi$, and,

$$\begin{aligned}\lambda\psi_{n,m} = -(PrK_n^2 + im\omega)\psi_{n,m} + \frac{A_\psi k_x k_z}{2K_n^2}[&\left(K_{n-1}^2 - k_x^2\right)(\psi_{n-1,m-1} + \psi_{n-1,m+1})\\ &+ \left(k_x^2 - K_{n+1}^2\right)(\psi_{n+1,m-1} + \psi_{n+1,m+1})].\end{aligned} \tag{5.19}$$

As before, the equations may be truncated at $n = N$ and $m = M$ and solved for the growth rate λ.

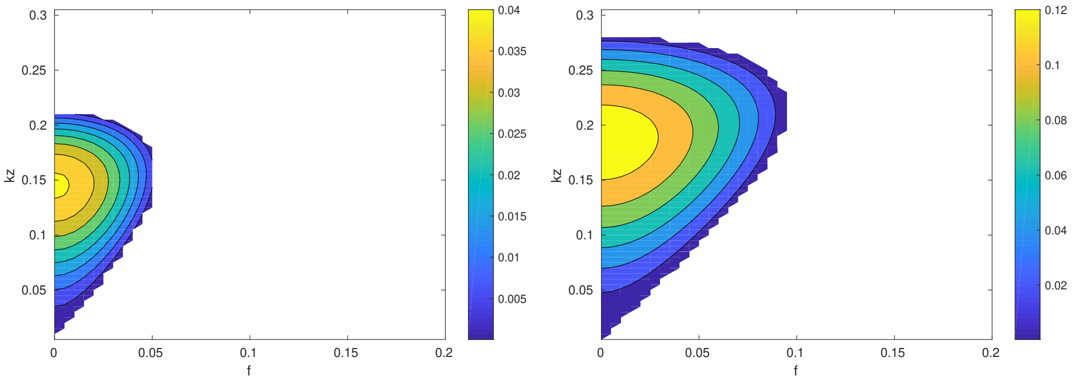

Figure 5.18: Growth rate of secondary modes in unsteady Kolmogorov flow, taking $k_x = 0.515$ and $\omega = 0.$. These correspond to a value of $R_\rho^{-1} = 1.06$ in the heat-salt system.

5.5.1 Unsteady Kolmogorov Results

The double-diffusive heat-salt system showed interesting behaviour for $R_\rho^{-1} = 1.06$ in the range $A_\psi \in \{1, 10\}$. This value of R_ρ^{-1} gives a basic state horizontal wavenumber, $k_x = 0.515$, and frequency, $\omega = 0.9582$. We thus use these values in a preliminary study of the unsteady Kolmogorov system. Figure 5.18 shows the modes with positive growth rates when $A_\psi = 10$ and $A_\psi = 12$.

These preliminary results show that, as in the steady Kolmogorov system studied in Chapter 4, the fastest growing modes have $f = 0$ and a value of k_z that increases with increasing A_ψ. Figure 5.19 shows the imaginary part of the growth rate, λ_I indicating that the modes with $f = 0$ are oscillating modes, as would be expected. The initial results are promising, and support the idea that the $f = 0$ mode observed in the double-diffusive system is indeed a shear mode. It would be of interest to study this system in greater detail in a future study, at least because there does not appear to be evidence of the use of such a Floquet method in the study of oscillatory Kolmogorov flow, as yet.

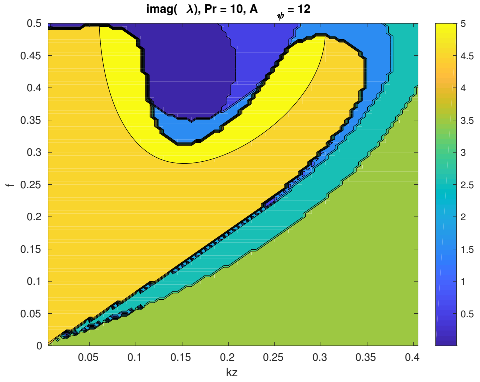

Figure 5.19: Imaginary part of the growth rate λ_I in unsteady Kolmogorov flow, taking $k_x = 0.515$ and $\omega = 0.$. These correspond to a value of $R_\rho^{-1} = 1.06$ in the heat-salt system.

5.5.2 High-Pr System

We have discussed the effect of large Prandtl number on the resulting dynamics—large Prandtl numbers lead to low Reynolds numbers and the resulting flow is highly diffusive. In such a case, we need much larger values of A_ψ to observe modes with $f = 0$, which subsequently increases simulation time. We here consider a simplified case in the limit $Pr \to \infty$. The simplified case is intended to be quicker to simulate, and so would allow higher values of A_ψ to be studied. An infinite Prandtl number corresponds to an inertia-free system, so if our hypothesis holds that the $f = 0$ mode is a shear-driven instability, then in a system with infinite Prandtl number we would likely never see this mode.

We have not yet tested this system to determine its efficacy, but we nevertheless provide a derivation of the system to facilitate any future study. We start with the governing nonlinear perturbation equations in streamfunction form:

$$\left(\frac{\partial}{\partial t} - Pr\nabla^2\right)\nabla^2\psi = -J(\psi, \nabla^2\psi) + Pr\left(\frac{\partial T}{\partial x} - \frac{\partial S}{\partial x}\right) \tag{5.20}$$

$$\left(\frac{\partial}{\partial t} - \nabla^2\right)T + \operatorname{sgn}(T_z)\frac{\partial \psi}{\partial x} = -J(\psi, T), \tag{5.21}$$

$$\left(\frac{\partial}{\partial t} - \tau\nabla^2\right)S + \operatorname{sgn}(S_z)R_\rho^{-1}\frac{\partial \psi}{\partial x} = -J(\psi, S), \tag{5.22}$$

When $Pr >> 1$, the momentum equation reduces to:

$$\nabla^4 \psi = \frac{\partial T}{\partial x} - \frac{\partial S}{\partial x}. \tag{5.23}$$

If we take an elevator basic state, perturb it, and express the perturbations in Floquet form (as described hereinbefore), we are able recover an equation for $\psi_{n,m}$ in terms of $T_{n,m}$ and $S_{n,m}$:

$$\psi_{n,m} = \frac{-i(f+n)k_x}{K_n^4}\left(T_{n,m} - S_{n,m}\right). \tag{5.24}$$

By substituting (5.24) into the equations for $T_{n,m}$ and $S_{n,m}$, we no longer need to solve for $\psi_{n,m}$, thus reducing the size of the matrix $\mathbf{A}$ in our eigenvalue formulation. The $T_{n,m}$ and $S_{n,m}$ equations become:

$$\begin{aligned}\lambda T_{n,m} = {} & \left(\frac{(f+n)^2 k_x^2}{K_n^4} - im\omega - K_n^2\right) T_{n,m} - \frac{(f+n)^2 kx^2}{K_n^4} S_{n,m} \\ & + \frac{k_x k_z}{2}[A_\psi(T_{n-1,m-1} - T_{n+1,m-1}) + A_\psi^*(T_{n-1,m+1} - T_{n+1,m+1})] \\ & + \frac{k_x^2 k_z (f+n-1)}{2K_{n-1}^4}[A_T(T_{n-1,m-1} - S_{n-1,m-1}) + A_T^*(T_{n-1,m+1} - S_{n-1,m+1})] \\ & + \frac{k_x^2 k_z (f+n+1)}{2K_{n+1}^4}[A_T(T_{n+1,m-1} - S_{n+1,m-1}) + A_T^*(T_{n+1,m+1} - S_{n+1,m+1})]\end{aligned} \tag{5.25}$$

$$\begin{aligned}\lambda S_{n,m} = {} & \left(\frac{-R_\rho^{-1}(f+n)^2 k_x^2}{K_n^4} - im\omega - \tau K_n^2\right) S_{n,m} + \frac{R_\rho^{-1}(f+n)^2 kx^2}{K_n^4} T_{n,m} \\ & + \frac{k_x k_z}{2}[A_\psi(S_{n-1,m-1} - S_{n+1,m-1}) + A_\psi^*(S_{n-1,m+1} - S_{n+1,m+1})] \\ & + \frac{k_x^2 k_z (f+n-1)}{2K_{n-1}^4}[A_S(T_{n-1,m-1} - S_{n-1,m-1}) + A_S^*(T_{n-1,m+1} - S_{n-1,m+1})] \\ & + \frac{k_x^2 k_z (f+n+1)}{2K_{n+1}^4}[A_S(T_{n+1,m-1} - S_{n+1,m-1}) + A_S^*(T_{n+1,m+1} - S_{n+1,m+1})]\end{aligned} \tag{5.26}$$

The range of R_ρ^{-1} required for instability of the elevator mode reduces as Pr is increased, as shown by

$$1 \leq R_\rho^{-1} \leq \frac{(Pr+1)}{(Pr+\tau)}\left(1 - k_x^4(1+\tau)(1+\frac{\tau}{Pr})\right). \tag{5.27}$$

Indeed, if $Pr \gg 1$ and $\tau \ll 1$, then $\tau/\mathrm{Pr} \ll 1$, and

$$1 \leq R_\rho^{-1} \leq \frac{(1+\frac{1}{Pr})}{(1+\frac{\tau}{Pr})}\left(1 - k_x^4(1+\tau)(1+\frac{\tau}{Pr})\right), \tag{5.28}$$

$$\implies 1 \leq R_\rho^{-1} \leq 1 + \frac{1}{Pr}\left(1 - k_x^4(1+\tau)\right). \tag{5.29}$$

This gives

$$1 \leq R_\rho^{-1} \leq 1 + \epsilon\left(1 - k_x^4(1+\tau)\right), \tag{5.30}$$

where $\epsilon = 1/Pr$, and hence $R_\rho^{-1} \to 1$ as $Pr \to \infty$. In the High-Pr model, we can take $R_\rho^{-1} = 1$, in which case the wavenumber of the basic state elevator mode for marginal stability is

$$k_x^4 = \left(1 - \frac{R_\rho^{-1} - 1}{\epsilon}\right)(1+\tau)^{-1} \tag{5.31}$$

$$\implies k_x = \frac{1}{(1+\tau)^{1/4}} \tag{5.32}$$

Alternatively, we can assume that R_ρ^{-1} and k_x are the same as those used in the full simulations, allowing for a direct comparison of results.

5.6 Conclusions

The secondary modes arising from oscillatory elevator modes are in some ways very similar to those which arise from steady elevator modes. The difference is that, in the unsteady system, we do not see a mode with $f = 0.5$; however, we instead see an 'intermediate' mode with finite f and k_z. The intermediate mode dominates at lower values of A_ψ, while a mode with $f = 0$ dominates at larger A_ψ.

The structure of the $f = 0$ mode is generally the same in the unsteady system as that in the steady system, except that in the formar case it oscillates with the same frequency as the primary instability. That is, the modes take the form of cells which distort the elevator modes into wave-like patterns in the streamfunction, and which cause density interleaving between adjacent elevator modes. These instabilities are thought to be largely shear-driven, as they occur at large values of A_ψ, while the intermediate modes are thought to be more diffusive in nature.

The $f = 0$ modes are also observed to be similar to those used in the truncated models of Chapter 3. That is, the cellular modes have a vertical scale on the order of the horizontal scale of the fastest-growing elevator modes, and appear to be aligned with the elevator modes. This is reminiscent of the cellular modes in the 9th-order system, which interact with the elevator modes to generate layering modes. The layering modes then grow to form a layered structure. The secondary modes observed in the present study may therefore play a key role in the formation of layers in oscillatory double-diffusive systems.

We have developed a Floquet system for studying purely hydrodynamic, oscillatory shear flow. Previous instances of Floquet theory used to study Kolmogorov flow have been limited to the steady case Beaumont (1981), Xie et al. (2017). The methods we developed in this chapter to study the secondary modes arising from spatially and temporally oscillating systems are readily applied to unsteady Kolmogorov flow, and it would be interesting to perform further study to this effect.

Furthermore, we have developed a simplified, high Prandtl number system which may be used to study the secondary instabilities at larger values of A_ψ than would otherwise be feasible. Though we have not yet applied this model to study the secondary modes at large Pr, we consider that the model may be used to shed light on a number of issues, such as whether $f = 0$ modes are observed at very large Prandtl numbers.

CHAPTER 6

Conclusions

6.1 Discussion

We have demonstrated throughout the thesis that elevator modes, which initially form as primary instabilities of double-diffusive systems, are extremely influential in the subsequent evolution of such systems, particularly in relation to the formation of layers. It was demonstrated in Chapter 3, using highly truncated models, that nonlinear interactions between elevator modes and cellular modes are responsible for the generation and growth of layering modes. That is, when elevator modes are not included in such systems, as in Veronis (1965) and Da Costa et al. (1981), layers are not observed (though the vertically bounded regions in those studies may be considered to constitute a single layer).

The layering modes are observed to grow, and dominate, in systems as low as ninth-order. Taking language introduced in Chapter 3, we find that no $(0, 2)$ mode is required in the streamfunction perturbation to form layers. The vertical scale of the layers is found to be half that of the horizontal scale of the elevator mode, which is supported by direct numerical simulations (Noguchi and Niino, 2010a). This implies that the layering actually occurs on much smaller scale than that predicted by the γ-instability theory, which predicts layer scales on the order of 10 to 20 times that of the elevator modes (Radko, 2013).

We have performed a thorough investigation of the stability of both steady and oscillatory elevator modes. We find that, in both cases, the elevator modes become unstable to secondary modes with a Floquet factor, $f = 0.5$ at low elevator amplitudes, and to secondary modes with $f = 0$ at large elevator amplitudes. Furthermore, the oscillatory system becomes unstable to an 'intermediate' mode at moderate elevator amplitudes. This behaviour has not been observed in previous studies.

Studying the effect of increasing the Prandtl number, Pr, on the fastest growing secondary modes revealed that, in each case, the mode with $f = 0$ requires larger elevator amplitudes, A_ψ to occur when Pr is large. A large Prandtl number implies a reduction in inertial terms, and therefore a reduction in shear in the system. Thus, we hypothesise that the $f = 0$ mode observed in our systems, and by Holyer (1984), is a largely shear-driven instability.

This is supported by a comparison of our results with those of purely hydrodynamic shear in both the steady and oscillatory cases. We see that, in such shear flows (referred to as Kolmogorov flows), the fastest growing mode always takes a value of $f = 0$, and that as A_ψ is increased, the vertical wavenumber of the fastest-growing mode also increases. This behaviour is observed in the double-diffusive system. Furthermore, as the Prandtl number is increased in the Kolmogorov system, a larger A_ψ is required to destabilise the basic state. This is due to the limited influence of inertial terms at high Pr. This behaviour is consistent with that observed in the double-diffusive system, further supporting the hypothesis that the $f = 0$ modes are largely inertia-driven instabilities.

The fastest growing secondary modes arising from oscillatory elevator modes are similar in structure to those arising from steady elevator modes, except that in the former case they are oscillatory. Furthermore, an additional mode is observed in the oscillatory case which is not observed in the steady case (except in the heat-salt system at low elevator amplitudes). The additional mode has nonzero Floquet factor f and nonzero vertical wavenumber k_z. The presence of these modes warrants further study of the oscillatory elevator modes, for instance to determine why such modes do not appear to be fastest-growing the absence of oscillatory motions, and to investigate whether such modes are important in layering.

The secondary modes arising from oscillatory instabilities at larger values of A_ψ interact with the elevator modes to resemble structures observed in the 9th-order truncated model. That is, the secondary modes appear to be cellular in nature, and generally 90 degrees out-of-phase (i.e. 'misaligned') with the elevator modes. Furthermore, the secondary modes have $f = 0$, meaning that they are likely shear-driven instabilities. This suggests that, perhaps, as the amplitudes of elevator modes increase, secondary cellular modes are generated through shear instabilities, reinforced by diffusive effects. The secondary cellular modes may then subsequently interact with the primary elevator modes to generate one or more layering modes. The layering modes, as seen in Chapter 3, then grow and eventually form layered structures in the system. This is a relatively simple mechanism for the formation of layers, but is one which appears to be supported by the results set out in this thesis.

6.2 Development and future work

It would be interesting to repeat the truncated model studies of Chapter 3, instead taking modes with wavenumbers and amplitudes derived from the stability analyses in Chapters 3 and 4. This would further highlight any link between the secondary modes arising from the elevator modes and those leading to layer formation in the truncated models. Furthermore, in the simulations of Chapter 3, the wavenumbers of the modes are constant, even as the background gradients are varied via. the value of γ. Taking instead wavenumbers obtained from the stability analyses of Chapter 3 would remove a requirement to obtain such wavenumbers from DNS, as was done by Noguchi and Niino (2010a).

Our study on the stability of oscillatory elevator modes in Chapter 5 may be developed further. Specifically, it would be interesting to further study the role of heat and salt in such systems, as we did in Chapter 4 for steady elevator modes. The methods we have developed to study both spatially and temporally oscillating flows may readily be applied to purely hydrodynamic systems. Indeed, there appears to be a lack of literature surrounding the use of such methods to study stability of *oscillatory* Kolmogorov shear flows. Thus, this would make an interesting and perhaps relatively straightforward application of our methods, though it is outside the scope of the present study. Furthermore, it would be of interest to study the stability of elevator modes at large Prandtl numbers in more depth, using the simplified high-Pr system we developed in Chapter 5.

The systems and methods developed throughout the thesis may equally be applied to magnetoconvective systems, as introduced in Chapter 1. Further study may look at applying the methods we have developed for studying spatially and temporally oscillating flows to such systems.

We conclude by noting that there a universally accepted model for the formation of layers remains elusive. By studying the basic modes and instabilities arising in such systems, we are able to make progress in understanding the nature of layer formation, and the interactions that lead to it. For example, we see in Chapter 3 that layers may form at scales as small as the wavelength of the primary elevator mode, which is in contrast to, for example, the γ-instability theory, which suggests that layers form on larger scales on the order of at least 10 to 20 times the wavenumber of the primary instability.

We acknowledge that studies such as those presented in this thesis are limited in that, as modal amplitudes become large, further nonlinear effects arise which remain unaccounted for; however, the simplicity of the models makes them powerful for identifying the mechanisms by which double-diffusive systems become unstable, and to develop a deeper understanding of the interactions which may lead to such seemingly complex phenomena as layer formation.

REFERENCES

Baines, P. G. and Gill, A. E. (1969). On thermohaline convection with linear gradients. *Journal of Fluid Mechanics*, 37:289–306.

Beaumont, D. N. (1981). The stability of spatially periodic flows. *Journal of Fluid Mechanics*, 108:461–474.

Blennerhasset, P. J. and Bassom, A. P. (2002). The linear stability of flat stokes layers. *Journal of Fluid Mechanics*, 464:393–410.

Bretherton, C. S. (1981). Double diffusion in a long box. *Woods Hole Geophysical Fluid Dynamics Course Lectures*, WHOI-810-102.

Brown, J. and Radko, T. (2019). Initiation of diffusive layering by time-dependent shear. *Journal of Fluid Mechanics*, 858:588–608.

Chandrasekhar, S. (1961). *Hydrodynamic and Hydromagnetic Stability.* Dover Publications Inc.

Coddington, E. A. and Levinson, N. (1955). *Theory of Ordinary Differential Equations.* McGraw-Hill Book Company Inc.

Cooper, J. W. and Stommel, H. (1968). Regularly spaced steps in the main thermohaline near bermuda. *Journal of Geophysical Research*, 73:5849–5854.

Da Costa, L. N., Knobloch, E., and Weiss, N. O. (1981). Oscillations in double-diffusive convection. *Journal of Fluid Mechanics*, 109:25–43.

Davey, A. (1973). On the stability of plane couette flow to infinitesimal disturbances. *Journal of Fluid Mechanics*, 57:369–380.

Fornberg, B. (1998). Calculation of weights in finite difference formulas. *SIAM Review*, 40:685–691.

Frenkel, A. (1991). Stability of an oscillating Kolmogorov flow. *Physics of Fluids A: Fluid Dynamics*, 3:1718–1729.

Frenkel, A. and Xiaojing, Z. (1998). Large-scale instability of generalized oscillating Kolmogorov flows. *SIAM Journal of Applied Mathematics*, 58:540–564.

Garaud, P., Kumar, A., and Sridhar, J. (2019). The interaction between shear and fingering (thermohaline) convection. *The Astrophysical Journal*, 879:60.

George, W. D. and Hellums, J. D. (1972). Hydrodynamic stability in plane Poiseuille flow with finite amplitude disturbances. *Journal of Fluid Mechanics*, 51:687–704.

Holyer, J. Y. (1981). On the collective instability of salt fingers. *Journal of Fluid Mechanics*, 110:195â€“–207.

Holyer, J. Y. (1984). The stability of long, steady, two-dimensional salt fingers. *Journal of Fluid Mechanics*, 147:169â€“–185.

Howard, L. N. and Krishnamurti, R. (1986). Large-scale flow in turbulent convection: a mathematical model. *Journal of Fluid Mechanics*, 170:385–410.

Howard, L. N. and Veronis, G. (1987). The salt-finger zone. *Journal of Fluid Mechanics*, 183:1–23.

Hoyle, R. B. (2006). *Pattern Formation: An Introduction to Methods.* Cambride University Press.

Hughes, D. W. and Weiss, N. O. (1995). Double-diffusive convection with two stabilizing gradients: strange consequences of magnetic buoyancy. *Journal of Fluid Mechanics*, 301:383–406.

Huppert, H. E. and Moore, D. R. (1976). Nonlinear double-diffusive convection. *Journal of Fluid Mechanics*, 78:821–â€“854.

Huppert, H. E. and Turner, J. (1981). Double-diffusive convection. *Journal of Fluid Mechanics*, 106:299–329.

Johannessen, O. and Lee, O. S. (1974). A deep stepped thermo-haline structure in the mediterranean. *Deep Sea Research and Oceanographic Abstracts*, 21.

Kerr, O. S. (1992). Two-dimensional instabilities of steady double-diffusive interleaving. *Journal of Fluid Dynamics*, 242:99–116.

Kerr, O. S. and Tang, K. (1999). Double-diffusive instabilities in a vertical slot. *Journal of Fluid Dynamics*, 392:213–232.

Knobloch, E., Weiss, N., and Da Costa, L. (1981). Oscillatory and steady convection in a magnetic field. *Journal of Fluid Mechanics*, 113:25â€“43.

Lin, C. C. (1966). *The theory of hydrodynamic stability.* Cambridge University Press.

Linden, P. F. (1974). Salt fingers in a steady shear flow. *Geophysical Fluid Dynamics*, 6(1):1–27.

Lorenz, E. N. (1963). Deterministic nonperiodic flow. *Journal of the Atmospheric Sciences*, 20:130–141.

McKenzie, D. and Jarvis, G. (1980). The conversion of heat into mechanical work by mantle convection. *Journal of Geophysical Research*, 85:6093â€“–6096.

Merryfield, W. J. (2000). Origin of thermohaline staircases. *Journal of Physical Oceanography*, 30:1046–1068.

Meshalkin, L. D. and Sinai, I. G. (1961). Investigation of the stability of a stationary solution of a system of equations for the plane movement of an incompressible viscous liquid. *Journal of Applied Mathematics and Mechanics*, 25:1140â€“–1143.

Molcard, R. and Tait, R. (1977). The steady state of the step structure in the Tyrrhenian sea. *A Voyage of Discovery*, pages 221–233.

Noguchi, T. and Niino, H. (2010a). Multi-layered diffusive convection. Part 1: Spontaneous layer formation. *Journal of Fluid Mechanics*, 651:443–464.

Noguchi, T. and Niino, H. (2010b). Multi-layered diffusive convection. Part 2: Dynamics of layer evolution. *Journal of Fluid Mechanics*, 651:465–481.

Orszag, S. (1971). Accurate solution of the Orr-Sommerfeld stability equation. *Journal of Fluid Mechanics*, 50:659–703.

Paparella, F. and Hardenberg, J. (2014). A model for staircase formation in fingering convection. *Acta Applicandae Mathematicae*, 132:457â€“–467.

Pedlosky, J. (2013). *Geophysical Fluid Dynamics.* Springer-Verlag New York Inc.

Prikasky, I. (2007). Direct numerical simulations of the diffusive convection and assessment of its impact on arctic climate change. Master's thesis, Naval Postgraduate School, California, US.

Radko, T. (2003). A mechanism for layer formation in a double-diffusive fluid. *Journal of Fluid Mechanics*, 497:365–380.

Radko, T. (2005). What determines the thickness of layers in a thermohaline staircase? *Journal of Fluid Mechanics*, 523:79–98.

Radko, T. (2013). *Double-Diffusive Convection.* Cambridge University Press.

Radko, T. (2016). Thermohaline layering in dynamically and diffusively stable shear flows. *Journal of Fluid Mechanics*, 805:147–170.

Radko, T. (2019). Thermohaline-shear instability. *Geophysical Research Letters.*

Radko, T., Bulters, A., Flanagan, J. D., and Campin, J.-M. (2014a). Double-diffusive recipes. part 1: Large-scale dynamics of thermohaline staircases. *Journal of Physical Oceanography*, 44:1269–1284.

Radko, T., Flanagan, J., Stellmach, S., and Timmermans, M. (2014b). Double-diffusive recipes. part 2: Layer-merging events. *Journal of Physical Oceanography*, 44:1285–1305.

Radko, T. and Smith, P. (2012). Equilibrium transport in double-diffusive convection. *Journal of Fluid Mechanics*, 692:5–27.

Radko, T. and Stern, M. E. (2011). Finescale instabilities of the double-diffusive shear flow. *Journal of Physical Oceanography*, 41:571–585.

Rosenblum, E., Garaud, P., Traxler, A., and Stellmach, S. (2011). Turbulent mixing and layer formation in double-diffusive convection: Three-dimensional numerical simulations and theory. *The Astrophysical Journal*, 731(66).

Schmitt, R. W. (1994). Double diffusion in oceanography. *Annual Review of Fluid Mechanics*, 26:255–285.

Schmitt, R. W., Perkins, H., Boyd, J. D., and Stalcup, M. C. (1987). C-salt: An investigation of the thermohaline staircase in the western tropical north atlantic. *Deep Sea Research Part A. Oceanographic Research Papers*, 34:1697–1704.

Shampine, L. and Gordon, M. (1975). *Computer Solution of Ordinary Differential Equations: the Initial Value Problem.* W. H. Freeman.

Shampine, L. and Reichelt, M. (1997). The MATLAB ODE suite. *SIAM Journal on Scientific Computing*, 18:1–22.

Sparrow, C. (1982). *The Lorenz Equations.* Springer-Verlag New York.

Spiegel, E. and Veronis, G. (1960). On the Boussinesq approximation for a compressible fluid. *Astrophysical Journal*, 131(442).

Spiegel, E. and Weiss, N. (1982). Magnetic buoyancy and the Boussinesq approximation. *Geophysical and Astrophysical Fluid Dynamics*, 22:219–234.

Stellmach, S., Traxler, A., Garaud, P., Brummel, N., and Radko, T. (2011). Dynamics of fingering convection. Part 2: The formation of thermohaline staircases. *Journal of Fluid Mechanics*, 677:554–571.

Stern, M. E. (1960). The 'salt-fountain' and thermohaline convection. *Tellus*, 12:172–175.

Stern, M. E. (1967). Lateral mixing of water masses. *Deep Sea Research and Oceanographic Abstracts*, 14:747–753.

Stern, M. E. (1969). Collective instability of salt fingers. *Journal of Fluid Mechanics*, 35:209–218.

Stern, M. E. (1975). *Ocean Circulation Physics*. Academic Press.

Stern, M. E. and Simeonov, J. (2005). The secondary instability of salt fingers. *Journal of Fluid Mechanics*, 533:361–380.

Stern, M. E. and Turner, J. (1969). Salt fingers and convecting layers. *Deep Sea Research*, 16:497–511.

Stoker, J. (1950). *Nonlinear Vibrations*. Interscience, N.Y.

Stommel, H., Arons, A., and Blanchard, D. (1956). An oceanographical curiosity: the perpetual salt fountain. *Deep Sea Research*, 3:152–153.

Tait, R. and Howe, M. (1968). Some observations of thermo-haline stratification in the deep ocean. *Deep Sea Research*, 15:275–280.

Thess, A. (1992). Instabilities in two-dimensional spatially periodic flows. part i: Kolmogorov flow. *Physics of Fluids A: Fluid Dynamics*, 4:1385.

Turner, J. S. (1967). Salt fingers across a density interface. *Deep Sea Research*, 14:599–611.

Turner, J. S. (1968). The behaviour of a stable salinity gradient heated from below. *Journal of Fluid Mechanics*, 33:193–200.

Turner, J. S. (1980). A fluid-dynamical model of differentiation and layering in magma chambers. *Nature*, 285:213–215.

Veronis, G. (1965). On finite amplitude instability in thermohaline convection. *Journal of Marine Research*, 23:1–17.

Veronis, G. (1966). Large-amplitude Bénard convection. *Journal of Fluid Mechanics*, 26:49–68.

Veronis, G. (1968). Effect of a stabilizing gradient of solute on thermal convection. *Journal of Fluid Mechanics*, 34.

Veronis, G. (1987). The role of the buoyancy layer in determining the structure of salt fingers. *Journal of Fluid Mechanics*, 180:327–342.

Walin, G. (1964). Note on the stability of water stratified by both salt and heat. *Tellus*, 16:389–391.

Weiss, N. O. and Proctor, M. R. E. (2014). *Magnetoconvection.* Cambridge Monographs on Mechanics. Cambridge University Press.

Wood, T. S., Garaud, P., and Stellmach, S. (2013). A new model for mixing by double-diffusive convection (semi-convection). II. the transport of heat and composition through layers. *The Astrophysical Journal*, 768(157).

Xie, J. H., Julien, K., and Knobloch, E. (2019). Jet formation in salt-finger convection: A modified rayleigh-Bénard problem. *Journal of Fluid Mechanics*, 858:228–263.

Xie, J. H., Miquel, B., Julien, K., and Knobloch, E. (2017). A reduced model for salt-finger convection in the small diffusivity ratio limit. *Fluids*, 2(6).